# THE ADHESIVE SILK OF THE AQUATIC CADDISFLY LARVA:

# STRUCTURE, MECHANICS, AND FIBER SPINNING

by

Nicholas Nathan Ashton

A dissertation submitted to the faculty of
The University of Utah
in partial fulfillment of the requirements for the degree of

Doctor of Philosophy

Department of Bioengineering

The University of Utah

December 2016

**The University of Utah Graduate School**

# STATEMENT OF DISSERTATION APPROVAL

The dissertation of **Nicholas Nathan Ashton**

has been approved by the following supervisory committee members:

| | | |
|---|---|---|
| **Russell J. Stewart** | , Chair | **8/18/2016** Date Approved |
| **Vladimir Hlady** | , Member | **8/17/2016** Date Approved |
| **Richard D. Rabbitt** | , Member | **8/17/2016** Date Approved |
| **Brittany Coats** | , Member | **8/17/2016** Date Approved |
| **Robert B. Weiss** | , Member | **8/17/2016** Date Approved |

and by **Patrick A. Tresco** , Chair/Dean of

the Department/College/School of **Bioengineering**

and by David B. Kieda, Dean of The Graduate School.

# ABSTRACT

The aquatic caddisfly larvae (insect order Trichoptera) use their adhesive silk in diverse species-specific ways to construct shelters and procure food. Structural H-fibroin protein comprising the bulk of aquatic caddisworm silk is extensively phosphorylated (10-15 mol%), an attribute atypical of the terrestrial silks from the caddisfly sister order Lepidoptera. Mechanochemical characterization of caddisworm silk from a local genus (*Hesperophylax)* shows a definitive and central role for the peptidyl phosphates in the silk structure, mechanical properties, and during silk spinning. Phosphates, in the form of phosphoserines (pS), are in blocky serial alternating repeats throughout the H-fibroin. As the silk fibers are drawn from the contents of the silk gland, environmental sources of multivalent metal ions like $Ca^{2+}$ diffuse into the nascent silk fiber and together with the pSs form periodic structured complexes that stabilize insolubilizing β-secondary structures. Complexation with multivalent metal ions decreases the symmetry of the pS $–PO_3^{2-}$ moiety, as observed by changes in the number and frequency of IR-absorption bands. Under mechanical load, $Ca^{2+}$-pS domains rupture to reveal hidden length and dissipate mechanical energy. The fibers are therefore tough, requiring nearly twice the mechanical energy of tendon collagen to fracture: ~17.3 ± 6.2 $MJ/m^3$. Remarkably, silk fibers cycled to 20% elongation completely recover mechanically within 120 min because an elastic entropic network guides the post-yield refolding of the $Ca^{2+}$-pS domains. Various techniques were used to mechanochemically probe the $Ca^{2+}$-stabilized β-domains. Silk

fibers in solutions of descending pHs showed a drastic decrease in the force required to rupture the $Ca^{2+}$-pS networks coinciding with the $pK_a$ of the silk pSs (pH 4.5). Exchanging the intrinsic $Ca^{2+}$ ions in the silk with other species of multivalent metal ions modulates the initial stiffness and pseudo-yield stress of the silk fibers increasing in the order $Na^{+} << Mg^{2+} < Ca^{2+} < La^{3+} < Zn^{2+} \approx Fe^{2+}$. The integrated intensities of the $-PO_3^{2-}$ symmetric stretching IR-absorption bands, indicative of the metal ion's effect on transition dipole moment of the P-O bonds and thereby the strength of the phosphate metal complex, increase in the same order, establishing a link between P-O transition dipole moments and the silk fiber strength.

Volume 11 | Number 9 | 7 March 2015 | Pages 1649–1852

# Soft Matter

www.softmatter.org

ISSN 1744-683X

ROYAL SOCIETY OF CHEMISTRY

PAPER
Nicholas N. Ashton and Russell J. Stewart
Self-recovering caddisfly silk: energy dissipating, $Ca^{2+}$-dependent, double dynamic network fibers

"To see caddis larvae at eye level, I have crawled around in streams, pored over the downsides of rocks, and wadded in marshes and ponds…"

Glenn B. Wiggins, *Caddisflies the Underwater Architects*

TABLE OF CONTENTS

LIST OF TABLES

LIST OF FIGURES

# SYMBOLS

| | |
|---|---|
| pS | Phosphoserine |
| cm | Centimeter |
| mm | Millimeter |
| mL | Milliliter |
| pH | Potential Hydrogen |
| PAS | Periodic Acid-Schiff Reaction |
| TEM | Transmission Electron Microscopy |
| nm | Nanometer |
| csPxt | Caddis Silk Peroxinectin |
| csSOD3 | Caddis Silk Superoxide Dismutase |
| ROS | Reactive Oxygen Species |
| H-fibroin | Heavy Chain Fibroin |
| L-fibroin | Light Chain Fibroin |
| kg | Kilogram |
| mol | Mole |
| PCR | Polymerase Chain Reaction |
| wt% | Weight Percent |
| mol% | Mole Percent |
| µm | Micrometer |
| nT | Amino Terminus |
| cT | Carboxyl Terminus |
| P25 | Fibrohexamerin |
| Å | Angstrom |
| N | Newton ($kg \cdot m \cdot s^{-2}$) |
| m | Meter |
| h | Hour |
| L | Liter |
| PTFE | Polytetrafluoroethylene |
| g | Gram |
| DIC | Differential Interference Contrast |
| EtOH | Ethanol |
| PBS | Phosphate Buffered Saline |
| PBST | Phosphate Buffered Saline with Tween 20 |

| | |
|---|---|
| IgG | Immunoglobulin G |
| α-pSer | Anti-Phosphoserine Antibody |
| °C | Degrees Celsius |
| SEM | Scanning Electron Microscopy |
| AFM | Atomic Force Microscopy |
| NMR | Nuclear Magnetic Resonance |
| $LN_2$ | Liquid Nitrogen |
| RNA | Ribonucleic Acid |
| mRNA | Messenger Ribonucleic Acid |
| nt | Nucleotide |
| MS/MS | Tandem Mass Spectrometry |
| IMAC | Immobilized Metal Affinity Chromatography |
| LC | Liquid Chromatography |
| FT-ICR | Fourier Transform ion Cyclotron Resonance |
| ppm | Parts Per Million |
| M | Molar |
| mM | Millimolar |
| EDTA | Ethylenediaminetetraacetic Acid |
| kHz | Kilohertz |
| DI | Deionized |
| ATR | Attenuated Total Reflectance |
| FTIR | Fourier Transform Infrared Spectroscopy |
| IR | Infrared |
| NTV | Total of Constant Volume |
| MD | Molecular Dynamics |
| PME | Particle Mesh Ewald |
| NTP | Constant Pressure |
| kb | Kilobase |
| ns | Nanoseconds |
| RMSD | Root-mean-square Deviation |
| Pa | Pascal ($N \cdot m^{-2}$) |
| MPa | Megapascal |
| WAXD | Wide-angle X-ray Diffraction |
| $pK_a$ | Acid Dissociation Constant |
| HBTU | 2-(1H-benzotriazol-1-yl)-1,1,3,3-tetramethyluronium hexafluorophosphate |
| DMF | Dimethylformamide |
| TFA | Trifluoroacetic Acid |
| TIS | Triisopropylsilane |
| Tris | Tris(hydroxymethyl)aminomethane |
| Bis-Tris | 2,2-Bis(hydroxymethyl)-2,2',2''-nitrilotriethanol |

| | |
|---|---|
| ICP-OES | Inductively Coupled Plasma Optical Emission Spectrometry |
| UV | Ultra Violet Light |
| s.d. | Standard Deviation |
| $v_{as}$ | Asymmetric Stretching |
| $v_s$ | Symmetric Stretching |
| ARS | Alizarin Red S |

ACKNOWLEDGEMENTS

I am grateful to my advisor, Dr. Russell Stewart, for taking a chance on me as an undergraduate student by including me in the investigation of caddisworm silk. He encouraged me early to pursue a doctorate degree, for which I am thankful. I have learned much from Dr. Stewart, especially the importance of good scientific writing; I am thankful for his efforts to teach me this skill.

I thank the members of my supervisory committee, Dr. Vladimir Hlady, Dr. Richard Rabbitt, Dr. Brittany Coats, and Dr. Robert Weiss, for their willingness to mentor me and offer critical insights about this project. Dr. Robert Weiss is also a valued collaborator who enthusiastically took upon himself the de-novo reconstruction of the caddisworm silk-gland transcriptome. His contributions have become an intrinsic part of the caddisworm silk research and I am greatly appreciative. Additionally, I am thankful for the efforts of my collaborators, Dr. Daniel Row and Dr. Thomas Cheatham III, whose molecular dynamic modeling of caddisworm phosphopeptides have provided valuable insights into the caddisworm silk.

I express my gratitude to Dr. Frank Sachse for the considerable time he spent helping me image free $Ca^{2+}$ gradients within the silk gland cells. Although the results of these studies are unpublished, I am grateful for the selfless time he took to mentor me. Conversations with Dr. Sachse were invaluable, guiding subsequent phases of the caddisworm silk studies.

I have developed great friendships with current and former members of Dr. Russell Stewart's lab; I thank Monika Sima, Dr. Mahika Weerasekare, Dr. Sarbjit Kaur, Dwight Lane, Josh Jones, and Leland Prather for their support and feedback throughout my doctorate studies. Additionally, I would like to thank Dr. Ching-Sheuen Wang who was a graduate student senior to me. He is an expert biologist and mentor to me, providing guidance on countless occasions. I also thank Nancy Chandler, an expert histologist who patiently taught me embedding and sectioning techniques.

The Willits Foundation scholarship has been a great financial blessing to me and my family as I have pursued my studies in bioengineering here at the University of Utah. I openly thank the Willits committee, C. R. Bard, Inc., and those responsible for providing me the means to focus wholeheartedly on my studies.

Without the support from the Army Research Office, none of this research would have been possible. Their support is gratefully acknowledged.

Finally, I am deeply thankful for the understanding and support of my cherished family and friends too numerous to name here. I was blessed with dear Parents and Grandparents who enthusiastically encouraged my curiosity of the natural world. Above all I appreciate my wife, Katie, on whose constant encouragement and optimism I have relied throughout my studies.

# CHAPTER 1

# INTRODUCTION

## 1.1 Caddisfly Background

Caddisflies are the seventh largest insect order (Trichoptera). Larvae of their species (caddisworms) are the second most abundant aquatic insect, represented by ~14,291 extant species worldwide [1]. Caddisflies share a sister group relationship with moths and butterflies of the order Lepidoptera, together comprising the insect superorder Amphiesmenoptera. Trichoptera and Lepidoptera diverged ~234 million years ago (Fig. 1.1) [1,2]. Like moth and butterfly larvae, the caddisfly larvae (caddisworms) pull silk fibers from fluid precursors stored in a pair of large salivary glands, an attribute that both orders inherited from a common silk-spinning ancestor [1]. In tandem with this phylogenetic split, the larval caddisworms invaded aquatic ecosystems and nowadays can be found worldwide throughout numerous freshwater [3,4] and several marine habitats [5,6]. Caddisflies live most of their year-long lives feeding underwater as larvae. After pupating, the adult flies emerge, in mass, for a short 1-2 week period of mating and egg laying. The successful radiation of the order has been attributed, in part, to the underwater spinning of a sticky tape-like silk used by the worms in species-specific ways to exploit their diverse aquatic niches [4]. The inventive uses of larval silk to provide shelter and procure food are illustrated across the three caddisworm suborders which are loosely

differentiated by the types of silken structures they assemble: Integripalpia make mobile protective cases, usually incorporating adventitiously gathered materials like stones, plant matter, and mollusk shells; Annulipalpia typically build stationary retreats accompanied by suspended capture nets for filtering materials and food from flowing water; Spicipalpia are free-living and, except the occasional anchoring tether, spin silk only to construct a semipermeable cocoon just before pupation (Fig. 1.1) [1].

Despite several studies, the silk of the aquatic caddisworm is comparatively less understood, both structurally and mechanochemically, than lepidopteran silks. This disparity in knowledge is driven in part because of the commercial value of the textile silk harvested from the domesticated silkworm *Bombyx mori*. As such, the silk of the domesticated silkworm is the most extensively researched and understood of all arthropod silks. Comparisons between terrestrial Lepidopteran and aquatic Trichoptera silks are useful for understanding silk adaptations in relation to their functional applications and respective environments of use. Therefore, this introduction compares and contrasts the silks of the aquatic and terrestrial sister orders.

The caddisfly suborders branched early in their evolutionary history; all three were distinct by ~203 million years ago (Fig. 1.1). The different uses of silks across the three suborders suggest there may be significant variations in their molecular structure and mechanical properties. As is discussed subsequently in detail, the amino acid composition and structural silk sequences differ somewhat across the suborders as might be expected from over 200 million years of independent evolution; progress in understanding the mechanochemistry of silks in one caddisfly suborder does not necessarily translate to the silks in the other orders. This introduction focuses on relevant caddisworm silk studies

including research on all three suborders. This introduction does not reflect the current state of caddisworm research because data from the subsequent chapters of this dissertation are intentionally omitted.

## 1.2 Caddisworm Anatomy and Silk Spinning System

Caddisworms are bilaterally symmetric organisms with two identical silk glands. Each gland is a long, thin tube enclosed at the far posterior end [7,8]. The glands fold several times along the length of the ventral side of the alimentary canal. Together, the silk glands and the alimentary canal fill most of the larval abdomen. The unraveled silk glands are approximately twice the length of the larva. Each gland is anatomically divided into posterior and anterior regions; the two regions have distinct functions and cell types. A bulbous protrusion in the outer cell wall marks the transition from posterior to anterior silk gland. The posterior silk gland secretes and stores silk components; it makes up most of the gland length (~2-4 cm) and mass. The anterior silk gland is a short, 2-4 mm long, thin cuticle-lined conducting tube leading towards the spinneret. The anterior lumens of the paired silk glands fuse into a very short common duct at the silk press just before the spinneret [9,10]. Accessory silk glands, also known as Filippi's or Lyonet's glands, are typically connected to the anterior conducting channel in terrestrial Lepidopteran larvae [11,12]. Accessory glands have not been found accompanying caddisworm silk glands. The interior lumen of the silk press is thick chitin. Four muscular attachments are radially connected to the outside wall of the silk press and to the interior exoskeleton of the head [7]. The larva has voluntary control of the silk press muscles; when contracted, the press opens and allows the fiber to be freely drawn from the gland [7]; in the relaxed state the

press holds the nascent fiber firmly. It is thought that by modulating the contractile strength of the press muscles, the larva has variable control on the tension of the silk fiber during spinning [7]. The fiber leaves the larvae at a region designated by entomologist as the spinneret. It is located ventral to the mouthparts on the underside of the head [13,14].

The secretory cells of the posterior silk gland are morphologically similar in aquatic caddisworms and the terrestrial silkworm. In both orders, the posterior silk gland is covered in large hexagonal cells with interdigitated membranes and large extensively branched nuclei [7,15,9]. The cells sit atop a ~1 μm basement membrane lining the lumen of the gland [9]. Beams and Sekhon reported that the degree of nuclei branching seemed to be related to the secretory activity of the cell; more active cells had more extensively branched nuclei [8]. The silk gland of the commercial silkworm *B. mori* has distinct secretory regions corresponding to the core silk components in the extreme gland posterior and the silk sericin outercoat components more anteriorly. Engster observed only one type of secretory granule in the gland of the case-making caddisworm *P. guttifer* [9]. She also observed a peripheral layer component along the entire length of the silk gland lumen gradually increasing in thickness from ~0.25 μm at the extreme posterior to 3.0 μm more anteriorly. She suggested that the two components might be co-secreted and phase separate once in the lumen [9]. The peripheral component in the gland lumen was confirmed to be the same carbohydrate-rich material on the coating of the final silk fibers by the colorimetric periodic acid-Schiff (PAS) reaction for glycoproteins [9]. In TEM images, the peripheral layer appeared as a fine grained compact material [9]. Engster found that the stored core components in the posterior silk gland comprise many 26-90 nm granules; the granules appeared to be the same size and appearance as Golgi vesicles extruded by the

silk-producing cells. The uniform granular composition of the pre-fiber components therefore likely represents the fundamental secretory unit rather than structures driven by protein folding or higher order molecular arrangements. The granular spinning dope stored in the posterior silk gland is isotropic, as confirmed by sectioning in multiple directions [9]. During silk spinning, the contents of the two glands are drawn into a paired-fiber filament. The stimuli that lead to fiber formation and more broadly the silk-fiber spinning process are poorly understood for aquatic caddisworms.

## 1.3 Hierarchical Structure of Caddisworm Silks

Caddisworm silk is a sticky tape with the paired attributes of a fibrous backing material and a pressure-sensitive adhesive coating [9,16–18]. The silk comprises two core subfibers fused together and encased by a thin, fuzzy layer of adhesive (Fig. 1.2 A-B) [16]. This paired-subfiber arrangement is shared with terrestrial moth and butterfly silks because of conserved similarities in silk gland anatomy inherited from their common ancestor. The caddis silk core is an elliptical bundle of many axially aligned proteinaceous nanofibrils [16]. The core silk of a species of case-making caddisfly (suborder Integripalpia) has been studied in TEM cross-sections [16]. Nanoscale subfibrils of this case-maker's core-silk are evenly distributed. In contrast, a study on a species of web-spinning caddisflies (suborder Annulipalpia) show the core subfibrils are inhomogeneously distributed with two poorly understood concentric morphological regions [10]. The caddisworm makes an adhesive joint by drawing a silk fibers through its spinneret onto a substrate while moving its head back and forth. The nascent elliptical core subfibers flatten against the substrate, appearing to maximizing the adhesive contact area [19]. An inside view of a larval *Hesperophylax*

*occidentalis* case clearly shows paired sub-fiber ribbons securing the case components (Fig. 1.2 A, C). The adhesive coating of cross-laid fibers seamlessly meld together into cohesive bundles thought to strengthen the adhesive joint [19]. Both the sticky coating and the fibrous backing material inevitably function concertedly as an adhesive tape to produce strong joints underwater; understanding both components is required to thoroughly describe the silk adhesive system.

## 1.4 The Adhesive Coating

### 1.4.1 Composition of the Silk Coating

Engster's early histochemical characterization of case-maker caddisworm silk revealed that the adhesive peripheral layer is comprised of glycoproteins with neutral and acidic polysaccharides. She reached this conclusion because the silk coating of the caddis silk from *Pycnopsyche guttifer* and *Neophylax concinnus* labeled positive with the colorimetric PAS reaction that stains for vicinal diols in carbohydrates and with the general protein stains bromophenol blue and low pH fast green [9,16]. This work was repeated, in part, for sections of silk from case-maker *H. occidentals*. Labeling with the PAS reaction was strongest in the peripheral coating but was also observed in the fiber core to a much lesser extent, suggesting carbohydrates as a minor core constituent [17]. The thin carbohydrate-rich coating on caddisworm silk is functionally analogous to the sticky gum enveloping the silk of the domesticated silkworm (*B. mori*). The coating on *B. mori* silk is much thicker than that observed on caddisworm silk, comprising 19-28% of the silk mass [20]. In contrast, the sugar content of *P. guttifer* case silk was only ~1.2 weight% [9]. The peripheral coating is thin in comparison, only 0.3-0.5 μm in *H. occidentalis* silk sections.

The silk gum on terrestrial moth silk (*B. mori*) is almost entirely the glycoprotein sericin which can easily be removed with warm, slightly alkaline water to reveal the core subfibers. A sericin homologue has never been found for caddisworm silk even after exhaustive searches in mRNAs from several species in different suborders [17,18,21–23]. It is extremely difficulty to remove the peripheral coating or solubilize caddis silk fibers even with strong detergents, denaturants, reducing agents, elevated temperatures, and chelating agents pH [16,18]. In comparison, multiple researchers have been able to solubilize the caddisworm silk gland contents [17,21,24]. These observations strongly suggest that silk constituent irreversibly crosslink after they are drawn from the otherwise soluble silk gland precursors. Silk of the case-making caddisworm *H. occidentalis* was observed to redden over time. A similar observation was made by Rudall who found that some caddisworm cases appeared "like insect-tanned material" [16]. The extreme insolubility and reddening of the silk were early evidence of an active crosslink-forming enzyme co-drawn with caddisworm silk fibers.

### 1.4.2 Enzyme Catalyzed Cross-linking in the Peripheral Coating

A heme-peroxidase in the peroxinectin sub-family (Pxt) was identified by searching a de novo assembled *H. occidentalis* silk gland transcriptome with peptide sequences identified by LC-MS/MS of trypsin digested silk gland proteins. Heme-peroxidases catalyze the oxidation of various substrates by reducing $H_2O_2$ to water. Peroxidase activity in caddisworm silk was demonstrated with Amplex Red®, a peroxidase substrate that is converted to fluorescent resorufin in the presence of $H_2O_2$. Resorufin fluorescence in caddisworm silk did not require the addition of $H_2O_2$, although florescence was greatly

enhanced when added, evidence that endogenous $H_2O_2$ is produced in the fibers [18]. A superoxide dismutase enzyme (SOD3) identified in the silk gland transcriptome may be the source of endogenous $H_2O_2$. Super oxide dismutases are a broad category of enzyme, ubiquitous in living cells and tissues that convert reactive superoxides into more benign $H_2O_2$. Both the caddis silk peroxinectin (csPxt) and the caddis silk superoxide dismutase (csSOD3) were shown to be glycosylated by lectin column chromatography [17,18]. The csSOD3 enzyme may be co-drawn into the silk fiber where it uses reactive oxygen species (ROS) in natural water to generate $H_2O_2$ for the csPxt. There is a sink of ROS in surface waters that could feed the csSOD3 enzyme, including singlet dioxygen, superoxide, hydroxyl radical, and numerous peroxyl radicals. The concentration of ROS in natural waters is sustained primarily by photochemical reactions of sunlight with naturally occurring chromophores like humic acid [25].

To identify potential targets of csPxt, the free amino acids Tyr, Arg, His, Lys, and Gly were added to compete with the Amplex Red® assay [17]. Only Tyr competed appreciably, decreasing fluorescence by ~75%. Fluorescent imaging of silk fiber cross-sections revealed strong dityrosine fluroescence (415 nm) in the peripheral coating, confirming intrinsic tyrosine as a target for csPxt. The caddis silk Pxt itself is perhaps the most likely target for dityrosine crosslinking in the peripheral coating. Peroxinectins lack strong substrate specificity and instead achieve specificity through localization in proximity to their substrate [26]. Of the 24 Tyr residues in csPxt, five occur in the N-terminus outside of the active site. In some peroxidases, this region contains recognition binding sequences that localize the enzyme near their substrates, such as collagens in the extracellular matrix, basement membrane, or to integrins on the surface of cells [26]. Dityrosine crosslinks with

core components may covalently couple the peripheral coating to the fiber core. Dityrosine crosslinking occurs during or after the fibers are drawn since dityrosine fluorescence was not detected in the silk gland proteins before draw [17].

### 1.4.3 Mechanisms of Interfacial Adhesion

Successful attachment of caddisworm (*H. occidentalis*) silk fibers to foreign materials likely involves multiple adhesion mechanisms. The neutral and acidic polysaccharides in the fuzzy peripheral adhesive coating are adhesion promotors in their own right, as evident from their prevalence in aquatic bioadhesives. Examples include the glycosylated silk proteins of the aquatic midge larva [27], sulfated polysaccharides in the sandcastle worm adhesive [28], glycosylated anchoring plaques of sessile barnacles [29], and anionic exopolysaccharide bacterial biofilms, to name a few [30]. The carboxylate anion in acidic polysaccharides can form complexes on metal hydroxide surfaces typical of stony minerals [31]. Likewise, cooperative hydrogen bonding can occur with the numerous hydroxyl groups in polysaccharides by associating with the typically negatively charged hydroxide surfaces at the higher pH of the caddisworm's habitat: ~pH 8.2 [31]. Pristine surfaces do not exist in natural waters. Rather, phenolic macromolecules, like humic and fulvic acid or bacterial biofilms, foul natural surfaces. Caddisworm silks must therefore adhere to these fouled surfaces. Soluble humic acid, which fluoresces green (518 nm), became covalently bound within the peripheral coating of silk fibers in the presence of $H_2O_2$, providing evidence that csPxt can catalyze covalent interfacial crosslinking to external polyphenol macromolecules [17]. In the peripheral coating, csSOD3 may generate $H_2O_2$ from environmental ROS that is in-turn used by csPxt to catalyze dityrosine crosslinking within

the peripheral coating and with surface adsorbed polyphenolic compounds [17,18].

## 1.5 Structural Proteins of the Silk Core

### 1.5.1 The Fibroins

The primary structural component of both aquatic Trichopteran and terrestrial Lepidopteran silks is the homologous highly repetitive heavy chain (H) fibroin protein (>350 kg/mol) [21]. A smaller non-repetitive ~25 kg/mol light chain (L) protein is also widely found in Amphiesmenopteran silks except in the Lepidopteran order Saturniidae, the sister order to the commercial silkworm *B. mori* [32]. Of the known protein constituents secreted in the silk glands of the casemaker *H. occidentalis,* the L and H-fibroins were, by a wide margin, shown to be the highest expressed by quantitative PCR [17]. This is in agreement with studies on the silk gland contents of the web-spinning caddisworm *Stenopsyche marmorata* that showed H-fibroin was the major component ( ~45 wt%) of the silk gland contents [33]. In terrestrial *B. mori* silk , the L-fibroin is linked by a single disulfide bridge to the H-fibroin C-terminus in a 1:1 ratio [34]. Formation of this disulfide crosslink is essential for proper silk secretion; H-fibroins in the commercial silkworm *B. mori* with mutant L-fibroins lacking the disulfide-forming cysteine displayed thiol-mediated retention in the ER and did not properly secrete into the silk gland lumen [35]. Yonemura and colleagues showed that the position of the crossbridging cysteines were conserved in the H and L fibroins of species in all of the caddisfly suborders and therefore suggested that the disulfide bond is also conserved widely in the aquatic order [21]. The primary role of L-fibroins in both insect orders is likely the promotion of proper silk secretion by forming a disulfide bridge with the much larger H-fibroins. In contrast,

the repetitive H-fibroins primarily perform a structural role in the final silk fibers as is subsequently discussed.

### 1.5.2 Proteins Uniquely Identified in Only One Trichopteran Suborder

Other protein silk constituents have been uniquely identified in various caddisworm species for which no homologous equivalents have been reported in other suborders or terrestrial Lepidopteran silks. A repetitive 57 kg/mol structural protein was identified in the silk of the casemaker *H. occidentalis*; This protein was named PEVK-like because of its amino acid content and primary sequence similarities with the entropic spring-like spacer domains of the giant muscle protein titan which also contain abundant Pro, Glu, Val, and Lys [18]. Three repetitive cysteine-rich (7-14 mol%) proteins were reported for two species of the web-spinning caddisfly suborder (Annulipalpia), including both the smap-98 and smsp-72 from *S. marmorata*, named with their characteristic molar masses (kg/mol) [36,37], and the 37 kg/mol NF1 protein from *Hydropsyche sp*. [38]. These cysteine-rich proteins were hypothesized to strengthen the silk by forming insoluble macromolecular complexes through disulfide bridges. The cysteine-rich proteins might be unique to the suborder Annulipalpia because silk amino acid ratios in the case-making caddisworm *Pycnopsyche guttifer* show less than 1% Cys [39].

### 1.5.3 H-fibroin Primary Structure and Amino Acid Composition

Trichopteran and Lepidopteran H-fibroins share generic structural similarities. The bulk of their H-fibroins comprise highly repetitive structural motifs except for 5-7% of the protein mass that is non-repetitive N and C termini (Fig. 1.3-1.6). The primary sequence

repeats and amino acid composition of H-fibroins across the aquatic and terrestrial orders are so drastically different that homology can only be shown by the short non-repetitive termini (Fig. 1.3-1.6) [21]. The silkworm H-fibroin (*B. moir*) repetitive region comprises abundant poly (GA) repeats typically in GAGAGX motifs where X is usually Ser but sometimes Tyr. The GAGAGX motifs are highlighted in a representative sequence from the B. mori H-fibroin in Figure 1.3. The abundance of these GAGAGX repeats in the silkworm H-fibroin structural region is reflected by high amino acid rations of Gly, Ala, Ser, and Tyr: 47.6 and 31.3, 12.0, and 5.2 mol%, respectively (Table 1.1). In total, these 4 amino acids comprise 96.1 mol% of the H-fibroin structural region; charged amino acids only comprise 0.7 mol%. Posttranslational modifications are sparse in the silkworm H-fibroin structural region; 9 of the 598 Ser residues in this region might be phosphorylated [40], but attempts at labeling B. mori H-fibroin with anti-phosphoserine antibody were unsuccessful [19].

Trichopteran H-fibroin repeats contain similar molar ratios of Gly and Ser as the silkworm H-fibroin ranging from 21.8-30.7 and 12.8-16.5 mol%, respectively, for species in each of the three Trichopteran suborders (Table 1.1). In contrast, Ala in the caddisworm repeats are comparatively sparse (0.4-4.6 mol%) and there is an abundance of the charged acidic and basic residues Glu, Asp, Arg, and Lys (20.0-20.7 mol%). Extensive phosphorylation of serines in the the H-fibroin repeats has been reported for the case-making and web-spinning suborders (Integripalpia and Annulipalpia). In the case-making suborder, nearly all of the ~15.5 mol% Ser in the H-fibroin repeats are thought to be phosphorylated; in total, ~35 mol% of H-fibroin residues carry a charge in this suborder [19,23]. The Ser motifs identified as phosphorylated in species from Integripalpia and

Annulipalpia are conserved in the third suborder Spicipalpia, suggesting that peptidyl phosphorylation of H-fibroin repeats is widespread in the order (Fig. 1.6) .

The amino acid composition and variety of repeat motifs are more diverse in caddisworm H-fibroins than that of the silkworm. Except for the short termini, the caddisworm H-fibroins, across the order, are ampholytic with imperfectly alternating blocks of acidic and basic residues. The cationic blocks primarily contain repeats of Arg but sometimes are mixtures with Lys, and His depending on the suborder (Grey Shading Fig. 1.4-1.6). The anionic blocks comprise peptidyl phosphate motifs of the form $(pSX)_n$; In repeats where n is 4-6, X is usually aliphatic Val, Leu, or Ile, but sometimes Arg, and His; In repeats where n is 2, X is always Gly (Blue Shading Fig. 1.4-1.6). Yonemura and colleagues recognized imperfectly alternating repeating sequences in the H-fibroin of species from the web-spinning and case-making suborders which they designated as A-F repeats (Fig. 1.4-1.6) [22]. All except the B repeats contain at least one $(pSX)_n$ domain. The A-C repeats are unique to the web-spinning suborder (Fig. 1.4) and the E-F repeats are unique to the case-making and cocoon-making suborders (Fig. 1.5-1.6). In all suborders, the D-repeats are conserved imperfectly. In each D-repeat, there are two $(pSX)_{4-5}$ domains flanking a central Pro by 5-6 residues on either side (Fig. 1.4-1.6).

### 1.5.4 H-Fibroin Secondary and Higher Order Structure

Terrestrial Lepidopteran silks are semi-crystalline elastomers. The simple sidechains in the GAGAGS motifs form physical crosslinks by stacking into β-crystalline domains interspersed within an amorphous Gly-rich elastic matrix. These silks have a high degree of crystallinity. The alternating Gly and Ala residues in the poly(GA) domains end up on

opposite sides of the stacked antiparallel β-sheets. X-ray diffraction studies reveal alternating intersheet distances between the glycyl and the slightly more bulky alanyl faces: 3.70 and 5.27 Å, respectively [41]. Terrestrial spider silks independently converged on a similar mechanism for strengthening their silk; numerous poly (A) domains analogously stack into antiparallel β-crystallite crosslinks, except in this system, the intersheet spacing is 5.27 Å on either side of the sheet.

X-ray diffraction studies of case-making and cocoon-making caddisworm silks (suborders: Integripalpia and Spicipalpia) provide evidence of stacked antiparallel β-sheets albeit less crystalline than terrestrial lepidopteran silks [16,41–43]. Serial alternating residues like the caddisworm $(pSX)_n$ motifs are common in the primary sequence of β-sheets. Most notably are the poly(GA) repeats in the larval moth silks. Before the H-fibroin serines were known to be phosphorylated, multiple authors speculated that the caddisworm $(SX)_n$ domains would form β-sheets, a conclusion they reached from the alternating sequences alone [21,44,45]. With the discovery peptidyl phosphates in caddisworm H-fibroins, Stewart and Wang suggested that $(pSX)_n$ domains might still form rigid β-crystalline regions if the charge repulsion between the dianionic-pSs were stabilized through $Ca^{2+}$-crossbridging [19]. Indeed, the case-making caddisworm silk (*H. consimilis*) contains equimolar ratios of multivalent metal ions, predominantly $Ca^{2+}$, with intrinsic silk phosphates [19].

The two D-repeat $(pSX)_{4\text{-}5}$ domains are widely conserved in species from each of the three suborders (Fig. 1.4-1.6). The two D-repeat $(pSX)_{4\text{-}5}$ domains flank a conserved central Pro reside and in the case-making and cocoon-making suborders, Pro is paired with a Gly residue (Pro-Gly). The Pro-Gly sequence is typical of a tight turn [46]. This suggests

in the D-repeats that the peptide backbone doubles back on itself, making an antiparallel hairpin (Fig. 1.5 B). In a hypothetical D-repeat β-sheet, the aliphatic X residues and dianionic phosphates of the $(pSX)_{4-5}$ motifs would end up partitioned on opposite sides of the sheet surrounded by chemical similar or identical neighbors: the aliphatic residues on one side and the charged pS groups on the other. Hydrophobic effects typically dominate protein folding; association of the aliphatic X residues would be a strong driving force in the formation of the proposed β-structure [47]. $Ca^{2+}$-pS crossbridges on the reverse face would stabilize the β-structure. There is a 600-fold decrease in the solubility of dibasic phosphate salt with $Ca^{2+}$ vs. $Na^{+}$ (0.2 vs. 118 g/L), illustrating the strong affinity of multivalent metal ions for dianionic phosphate as well as their potential to stabilize the pS-face of the proposed $(pSX)_{4-5}$ β-sheets in a hydrated environment [48]. Steered molecular dynamic simulations were used to explore the unfolding forces for various hypothetical secondary structures of the phosphorylated and non-phosphorylated D-repeat, including variants with $Na^{+}$ or $Ca^{2+}$ counter ions arranged in an alpha helix or β-sheet secondary structure. A "dramatic increase in maximum unfolding force" was only observed for the phosphorylated $Ca^{2+}$-stabilized β-sheet model [49]. Without knowledge of post-translational silk phosphorylation, Rudall and Kenchinton reported that a 17 Å intersheet X-ray diffraction of the case silk (*Olinga feredayi*) was greatly reduced by treating with the chelating agent EDTA, prompting the prescient conclusion that within some of the sheets, "there are acidic groups binding an ion such as calcium [42]."

## 1.6 Motivation for This Study

Mechanochemical characterization of the caddisworm silk is lacking. Specifically, experiments have not been performed to determine the mechanical role of the caddisworm H-fibroins and the proposed $Ca^{2+}$-$(pSX)_n$ β-domains in the final silk fibers. In general, mechanical characterization of Trichopteran silks is sparse but there are two studies on the web-spinning caddisworm silks. First, the web silk of the caddisworm *Hydropsyche siltalai* was mechanically tested to failure underwater with a screw micrometer. In comparison with dry terrestrial silks, the authors concluded that the caddisworm silk was "one of the weakest natural silks so far reported [50]." In the second study, single molecules were picked with an AFM cantilever from the peripheral adhesive coating on the surface of caddisworm web-silk (*Hydropsyche angustipennis*) and mechanically tested by atomic force spectroscopy. The study authors observed saw-like force-displacement curves which they attributed to "a sacrificial bond mechanism that can serve as a mechanical buffer [49]." Despite these limited mechanical studies, mechanochemical characterization of the silk fibers is completely lacking. The motivations for the studies presented herein is to fill this knowledge gap. This includes experiments specifically designed to connect functional groups and secondary structures with their respective mechanical contributions in the bulk silk fibers.

The functional groups and repetitive domains within the caddisworm silk proteins must not be viewed as purely structural, as in the final silk fibers, but might also be described from their role in the silk fiber spinning process. By necessity, the silk constituents must also contain design features specifically for storing the pre-silk-fiber components as a dense liquid spinning dope. The caddisworm silk proteins are thus sophisticated precursors;

the silk starts as a concentrated fluid which is then deployed during the spinning process to become tough insoluble fibers; this is all done underwater at ambient temperatures and biologically benign conditions.

The silk spinning system of the terrestrial silkworm relies on mechanical shear to drive a structural silk-I to silk-II transition. In the fluid silk-I form, disorganized chains and type II β-turns promote weak intramolecular hydrogen bonds. During spinning, shear forces induce crystallization of the silk precursors (Silk-I); tough insoluble intermolecular β-crystallites crosslinks form from the Ala-dense poly(GA) H-fibroin repeats. As previously described, the caddisworm silk does not have the Ala-dense β-forming domains critical to fiber formation and insolubilization of terrestrial silks. Caddisworm silk must therefore rely on a fundamentally different mechanism to drive fiber formation during spinning. Understanding the liquid-solid phase transition during the caddisworm silk spinning process is another goal of the research presented herein.

The long-term motivation for these studies is to discover design principles to guide the future development of soft but tough materials intended for use in aqueous environments. The caddisworm silk spinning system might also hold important design principles for materials intended to be processed and/or deployed underwater in a liquid state but then set and insolubilize. Applications of such a material might include underwater paints and coatings, minimally invasive injectable embolics, and medical adhesives, to name a few.

Table 1.1 Amino acid molar ratios of Amphiesmenopteran H-fibroin repeats. (Columns 2-4) Amino acid composition of the partial H-fibroin repeat regions show in Figures 1.4-1.6 for representative species from each Trichopteran suborder. (Column 5) Amino acid composition for the complete H-fibroin repetitive region of the domesticated silkworm. Amino Acid ratios were deduced from sequences available in GenBank. The N and C termini were excluded in the amino acid analysis. (ACCN: BAF62092.2, BAH80182.1, BAH80184.1, BAH80179.1, P05790)

| Order | Trichoptera | Trichoptera | Trichoptera | Lepidoptera |
|---|---|---|---|---|
| Suborder | Integripalpia | Annulipalpia | Spicipalpia | Glossata |
| Species | *Hesperophylax occidentalis* | *Hydropsyche angustipennis* | *Rhyacophila obliterata* | *Bombyx mori* |
| Ala (A) | 0.5% | 4.6% | 0.4% | 31.3% |
| Arg (R) | 12.5% | 10.3% | 7.6% | 0.0% |
| Asn (N) | 0.1% | 0.1% | 0.3% | 0.1% |
| Asp (D) | 3.0% | 3.1% | 1.5% | 0.2% |
| Cys (C) | 0.0% | 0.0% | 0.0% | 0.0% |
| Gln (Q) | 0.1% | 0.2% | 2.4% | 0.0% |
| Glu (E) | 2.6% | 2.8% | 2.4% | 0.4% |
| Gly (G) | 30.7% | 21.8% | 28.6% | 47.6% |
| His (H) | 0.3% | 2.5% | 6.5% | 0.1% |
| Ile (I) | 4.6% | 5.7% | 9.4% | 0.0% |
| Leu (L) | 8.9% | 6.0% | 9.8% | 0.0% |
| Lys (K) | 1.7% | 1.3% | 2.7% | 0.0% |
| Met (M) | 0.0% | 0.0% | 0.0% | 0.0% |
| Phe (F) | 0.0% | 0.0% | 0.0% | 0.4% |
| Pro (P) | 3.7% | 9.9% | 3.1% | 0.2% |
| Ser (S) | 15.5% | 12.8% | 16.5% | 12.0% |
| Thr (T) | 1.3% | 1.8% | 1.8% | 0.6% |
| Trp (W) | 2.8% | 2.2% | 1.7% | 0.2% |
| Tyr (Y) | 4.3% | 6.5% | 2.0% | 5.2% |
| Val (V) | 7.5% | 8.5% | 5.5% | 1.5% |

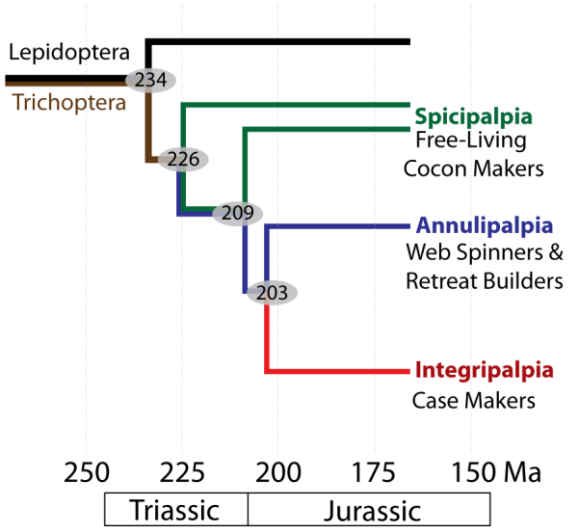


Figure 1.1. Phylogeny of caddisfly suborders. The relationship of the three caddisworm (Trichoptera) suborders to each other and terrestrial moths and butterflies (Lepidoptera), Spicipalpia (green), Annulipalpia (Blue), and Integripalpia (Red) are depicted in this phylogenetic tree. Approximates dates of divergence are depicted in the grey ovals. Units are millions of years ago (Ma). This diagram was created from data published in reference 1.

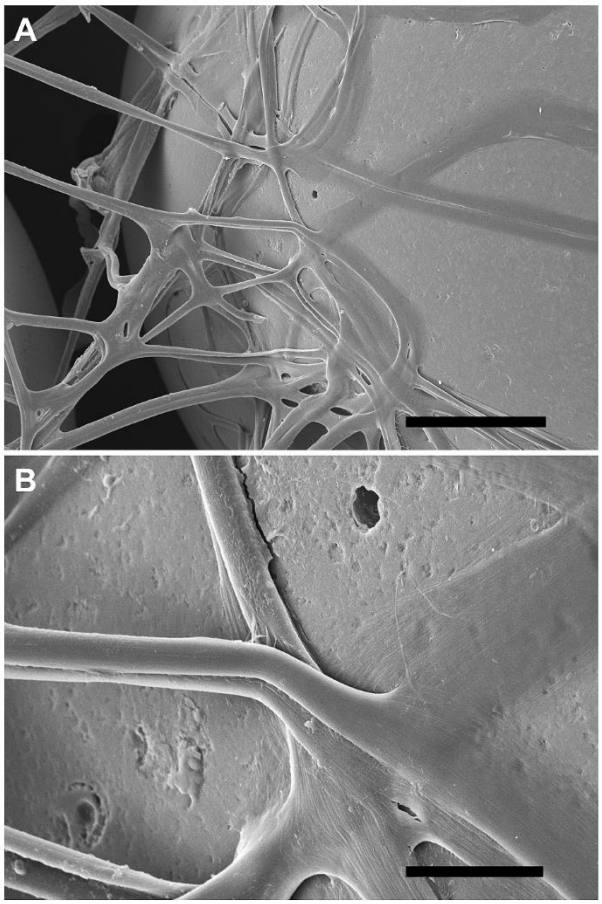


Figure 1.2. Scanning electron micrographs of the inside of a caddisworm case: (A) Inside view of the composite silk case constructed with 0.5 mm glass beads. (B) Close-up view of silk threads on the glass substrate. Scale bars are 100 and 20 μm, respectively.

nT:**MRVKTFVILCCALQYVAYTNA**NINDFDEDYFGSDVTVQSSNTTDEIIRDASGAVIE
EQITTKKMQRKNKNHGILGKNEKMIKTFVITTDSDGNESIVEEDVLMKTLSDGTVA
QSYVAADAGAYSQSGPYVSNSGYSTHQGYTSDFSTSAAV

GAGAGAGAAAGSGAGAGAGYGAASGAGAGAGAGAGAGYGTGAGAGAGAGYGAGAGA
GAGAGYGAGAGAGAGAGYGAGAGAGAGAGYGAGAGAGAGAGYGAGAGAGAGAGYGA
ASGAGAGAGYGQGVGSGAASGAGAGAGAGSAAGSGAGAGAGTGAGAGYGAGAGA
GAGAGYGAASGTGAGYGAGAGAGYGGASGAGAGAGAGAGAGAGAGYGTGAGYGAGA
GAGAGAGAGAGYGAGAGAGYGAGYGVGAGAGYGAGYGAGAGSGAASGAGSGAGAGS
GAGAGSGAGAGSGAGAGSGAGAGSGAGAGSGAGAGSGAGAGSGTGAGSGAGAGYGA
GAGAGYGAGAGSGAASGAGAGSGAGAGSGAGAGSGAGAGSGAGAGSGAGAGYGA
GAGAGYGAGAGAGYGAGAGVGYGAGAGSGAASGAGAGSGAGAGSGAGAGS
GAGAGSGAGAGS…
…GAGAGYGAGAGVGYGAGAGAGYGAGAGSGAGS
GAGAGSGSGAGAGSGSGAGSGAGAGSGAGAGSGAGAGSGAGAGSGAGAGSGAGAGS
GAGAGYGAGYGIGVGAGYGAGAGVGYGAGAGAGYGAGAGSGAASGAGAGSGAGAGS
GAGAGSGAGAGSGAGAGSGAGAGSGAGAGSGAGAGSGAGAGSGAGAGYGAGA
GVGYGAGAGSGAASGAGAGSGAGAGSGAGAGSGAGAGSGAGAGSGAGAGSGAGAGS
GAGSGAGAGSGAGAGYGAGYGAGVGAGYGAGAGYGAGYGVGAGAGYGAGAGSGAGS
GAGAGSGAGAGSGAGAGSGAGAGSGAGAGSGAGAGSGAGAGYGAGAGAGYGAGAGAGY
GAGAGSGAASGAGAGAGAGAGSGAGAGSGAGAGSGAGSGAGAGSGAGAGYGAGAGS
GAASGAGAGSGAGAGAGAGAGAGSGAGAGSGAGAGYGAGAGSGAASGAGAGAGAGT

cT:GSSGFGPYVANGGYSRREGYEYAWSSKSDFETGSGAASGAGAGAGSGAGAGSGAGA
GSGAGAGSGAGAGGSVSYGAGRGYGQGAGSAASSVSSASSRSYDYSRRNVRKNCGI
PRRQLVVKFRALPCVNC*

Figure 1.3. The silkworm H-fibroin (*Bombyx mori)*. Representative sequences from the silkworm H-fibroin N and C-termini. This sequence comprises 1200 of the 5263 amino acids in *Bombyx mori* H-fibroin. The non-repetitive N (nT) and C (cT) termini are indicated. The GAGAGX motifs of the repetitive core are highlighted in yellow (X=S or Y). The sequence is available in GenBank (ACCN: P05790).

```
nT:MRAAILLILFCSLQIHLTGAKIGHNAQKGIDDFLGGAHISKCGKHERILQGEDIIETNAKG
   ELIEKIVSRKEILTDDDSESFSVSYSSEDDSTETIVKTITIVQEIPKHGKGKGHAKEKIFE
   EETVIKKIGKGVAAPVVAPAVDIVGGGL

C: RRRPYGRYSASHSVSVEAPVVYHAPIVA
D:  RRPKISRSSSYSIERIVTPTVITRISASGSSSVEG
   RRGIYGP
   RRWVGPGGWGVA
A:     PAAYSASHSVSREGPRGWYGPRGLGPRGLGLGGLDSDILGHDLGPLGLGSRGHGPLGGL
C: RRRPYGGYSASHSVSVEAPVVYHAPII
D: RRRPKISKSSSYSVERIVKPAVITRIHHSASESVERPVYYRPPVVV
D:  RAPKVKKSASYSIERIVTPTVITRISGSHSVSAEG
    RRGVWGPHGVWGPHGVWGPSGLNGDSGIVDGVYGPGLVGTGGWG
A:  RRPYGGYSASGSVSAEGPRGWLGPRGHGPRGLGPLGLDSDIVGDGLGPLGLGDGYGPYGLGS
B:                                RGHGPLGGL
C: RRRPYGGYSASHSVSVEAPVVYHAPII
D: RRRPKISRSSSYSVERIVAPTVITRISGSHSVSAEG
    RRGVWGPHGVWGPSGLYGDSGIVDGVYGPGLVGPGGWG
A:  RRPYGGYSASRSVSAEGPRGWLGPR…

                …SGLYGDSGIVDGVYGPGLVGPGGWG
A:  RRPYGGYSASGSVSAEGPRGWYGPRGLGPRGLGPLGLDSDIIGDGYGPYGLGS
B:                                RGLGPLGLDSDIIGDGYGPRGLGPHGLGP
B:                                RGLGPLGLDSDIIGDGYGPYGLGPRGLGPLGGLG
A:  RRPYGGYSASGSVSAEGPRGWYGPRGLGGIGGW
C: RSRPYGGYSASHSVSVEAPVVYHAPII
D: RRAPKISRSSSYSVERIVTPTVITRISGSHSVSAEG
    RRGVWGPHGVWGPSGLYGDSGIVDGVYGPGLVGPGGWG
A:  RRPYGGYSASRSVSAEGPRGWYGPRGLGPRGLGPLGLDSDIIGDGYGPYGLGS
B:                                RGLGPLGLDSDIIGDGYGPRGLGP
B:                                RGLGPLGLDSDIIGDGYGPYGLGP
B:                                RGLGPLGGLG
A:  RRPYGGYSASGSVSAEGPRGWYGPRGLGGIGGWRS
C:   RPYGGYSASHSVSVEAPVVYHAPII
D:  RRAPKISRSASYSVERIVRPTVITKIHKSVSHSVEQPIYYRPPVVV
D:  RAPKVSKSESYSVERIVTPTVITRIHHSASDSVEQPIYYRPPVVV
D:  RRPKISRSASYSVERIVTPTVITRISGSHSVSAEG
   RRGVYGPRGVWGPSGLYGDSGILDGVYGPGLVGPGGWG
A:  RRPYGGYSASSSVSAEGPRGWYGPRGLGP
A: RRIGLGGYSASGSVSAEGPRGWYGPRGLGP
A:RRIGSLGGYSASGSVSAEG

cT:IRGVLRPSPGIVVPGVISSGVVAPGLVGGHGGLVNVGGTHVLPGTSVYTTHPDPRTVRSSC
   RTSPYNLLIKVGNARKLNGNC*
```

Figure 1.4. The web-spinning caddisworm H-fibroin (suborder Annulipalpia). Available sequences from *Hydropsyche angustipennis* H-fibroin. The Non-repetitive N (nT) and C (cT) termini are indicated. Imperfectly alternating repeats are labeled A-D. Cationic blocks in the repetitive region are in grey and Anionic $(pSX)_n$ domains are in blue. Conserved prolines are bolded. The sequences comes from GenBank (ACCN: BAF62092.2 and BAH80182.1).

```
nT:MRAILLLIVFCSWQVHRTGSSAVSNKVQDLFKHGRHLDSDGLH
   ERILEEEDIIETNSKGEIIEKIISRKEIISDDASNSWSDSDSS
   ESGSTEQIIKQIIIVQERPKHGHHHAKEKIYEEEIVIKKIGDV
   VHGVDVPIDTYGGIGRGR

D: RRGPN     ISISRSISIEQVVRPRVYTKISRSSSVSVEGG
E: RRHGPWGHGKGAWGPLGDL
                  SSSGDLDGLGGLGSIGG
F: RRGPWGRSVSASLSVSVERGI
D: RRGPWGRRGKVSISRSVSIER…
E:                    …DLDGYGGLGGYGGLGGL
                  SGSGDLDGLGGYGGLGGYGGLGGYGGLGG
F: RRGPWGRSVSSSLSVSVERGI
D: RRGPWGRRGKVSISRSVSIERIVTPGVYTKISRSSSVSIEGG
E: RR PWGYGRGLGGLSGSGDYDGLGGYGGLGGYGGLGG
F: RRGPWGRSVSVSLSVSVEGG
E: RR PWGYGRGLGGLSGSGDLDGLGGYGGLGGYGGLGG
F: RRGPWGRSVSSSLSVSVERGI
D: RRGPWGRRGKVSISRSVSIERIVTPGVYTKISRSSSVSVEGG
E: RR PWGYGRGLGGLSGSGDLDGLGGLGGLGGYGGLGG
E: RRGPWGRR GLGGLSGSGDLDGYGGLGGYGGLGGL
                  SGSGDLDGLGGYGGLGGYGGLGGYGGLGG
F: RRGPWGRSVSASLSVSVERGI
D: RRGPWGRRGKVSISRSVSIERIVTPGVYTKISRSSSVSVEGG
E: RR PWGYGRGLGGLSGSGDLDGLGGLGGLGGYGGLGGL
                  SGSGDLDGLGGYGGLGGYGGLGGYGGLGG
F: RRGPWGRSVSSSLSVSVERGI
D: RRGPWGRRGKVSISRSVSIERIVTPGVYTKISRSSSVSVEGG
E: RR PWGYGRGLGGLSGSGDLDGLGGYGGLGGYGGLGG
F: RRGPWGRSVSASLSVSVERGI
D: RRGPWGRRGKVSISRSVSIERIVTPSVYSKISRSSSVSVEGGI
   RRGPWG

cT:SFGGYDVSASSSLESVRPGRVLAGLGRVGALGRSGAVPVPSVY
   TNHPGINSVKSPCKLSDFNLLVKVGNVRKSNGNC*
```

Figure 1.5. The case-making caddisworm H-fibroin (suborder Integripalpia). Available sequences from *Hesperophylax occidentalis* H-fibroin. The Non-repetitive N (nT) and C (cT) termini are indicated. Imperfectly alternating repeats are labeled C-D. Cationic blocks in the repetitive region are in grey and Anionic $(pSX)_n$ domains are in blue. Conserved prolines are bolded. The sequences were previously published [23].

```
nT: MRAIFLLILVCSLQINIAGSSSVIDKLEDLLTHGHHGHHWEGTDGLHEKLLQEDDV
    IEANSKGEIIEKIISRREIITDDNSESESDSDSSEDSGSTEKIIKQIIIVQEKPKH
    GHHHAKEKIYEEEIIIKKIGDLPKKDCDENKPREVT

D:    SWRHTLPNRK  SISISKSISIEQIIKPHVITRIRTSKSSSLSISVE
     RPRRIISPIISG
D:    GWNRHKPRKYSASSSISKSISIERVITPAVWTRIHKSVSVSHSVSVE
F:  HRRRIAPIVVDYSISSSLSISGEGRGLG
E:  RGKHGWGGLGHGGLGGLGHGGLGGLGHGGLGGLGHGGLGGLGSDSGDL…


F:         …IIDYSISSSLSISGEGRGLG
E:  RGKHGWGGLGHGGLGGLGHGGLGGLGHGGLGGLGHGGLGGLGSGSGDLGGIGGLLGPGG
D:  RRGWGRRGPGKYSSSVSISQSISIERVITPGVYTSIHRSVSISHSVSVE
F:  HRRRIVPI IDYSISSSLSISGEGRGLGHG
E:    KHGWGGLGHGGLGGLGHGGLGGLGHGGLGGLGHGGLGGLGSGSGDLGGIGGLLGPGG
D:  RRGWGRRGPGKYSSSVSISHSISIERVITPGVYTSIHRSVSVSHSVSVE
F:  HRRRIVPI IDYSISSSLSISGEGRGLG
E:  RGKHGWGGLGHGGLGGLGHGGLGGLGHGGLGGLGHGGLGGLGSGSGDLGGIGGLLGPGG
D:  RRGWGKRGPGKYSSSVSISHSISIERVITPGVYTSIHRSVSVSHSVSVE
F:  HRRRIVPI IDYSISSSLSISGEGRGLG
E:  RGKHGWGGLGHGGLGGLGHGGLGGLGHGGLGGLGHGGLGGLGSGSGDLGGIGGLLGPGG
D:  RRGWGRRGPGKYSSSVSISHSISIERVITPGVYTSIHKSVSVSHSVSIE

cT: RSRRIIAPVVDYSISISASLSVSAEGGRRRRLPLSSGTIISDSSSNVGGLGRIGALH
    RLGGGRIPRPAIYTRHPGLKGLKPQCPLSNFNVHVKVGNIRKANGNC*
```

Figure 1.6. The cocoon-making caddisworm H-fibroin (suborder Spicipalpia). Available sequences from *Rhyacophila obliterata* H-fibroin. The Non-repetitive N (nT) and C (cT) termini are indicated. Imperfectly alternating repeats are labeled C-D. Cationic blocks in the repetitive region are in grey and Anionic $(pSX)_n$ domains are in blue. Conserved prolines are bolded. The sequences come from GenBank (ACCN: BAH80184.1 and BAH80179.1,).

## 1.7 References


[1] T. Malm, K.A. Johanson, N. Wahlberg, The evolutionary history of Trichoptera (Insecta): A case of successful adaptation to life in freshwater, Syst. Entomol. 38 (2013) 459–473.

[2] R.W. Holzenthal, R.J. Blahnik, A.L. Prather, K.M. Kjer, Order Trichoptera Kirby, 1813 (Insecta), Caddisflies, Zootaxa 698 (2007) 639–698.

[3] R.W. Merritt, K.W. Cummins, An introduction to the aquatic insects of North America, 2008 ed., Kendall Hunt Pub. Co., Dubuque, Iowa, 1996.

[4] G.B. Wiggins, Caddisflies: The underwater architects, University of Toronto Press, Toronto, 2004.

[5] E. Riek, The marine caddisfly family Chathamiidae (Trichoptera), Aust. J. Entomol. (1976) 405–419.

[6] P.W. Trichoptera, B.Y.J.P. Leader, Osmoregulation in the larva of the marine caddis fly , *Philanisus plebeius* (Walk.) (Trichoptera), J. Exp. Biol. 57 (1972) 831–838.

[7] J.P. Glasgow, Internal anatomy of caddis (*Hydropsyche colonica*), Q. J. Microsc. Sci. 79 (1936) 151–179.

[8] H.W. Beams, S.S. Sekhon, Morphological studies on secretion in the silk glands of the caddis fly larvae, *Platyphylax designatus* Walker, Zeitschrift Für Zellforsch. Und Mikroskopische Anat. 72 (1966) 408–414.

[9] M. Engster, Studies on silk secretion in the Trichoptera (*F. Limnephilidae*): I. histology, histochemistry, and ultrastructure of the silk glands, J. Morphol. 150 (1976) 183–212.

[10] T. Hatano, T. Nagashima, The secretion process of liquid silk with nanopillar structures from *Stenopsyche marmorata* (Trichoptera: *Stenopsychidae*), Sci. Rep. 5 (2015) 1-8.

[11] S. Patra, R.N. Singh, M. Raziuddin, Morphology and histology of Lyonet ’s gland of the tropical tasar silkworm , *Antheraea mylitta*, J. Insect Sci. 12 (2012) 1–7.

[12] E. Victoriano, E.A. Gregorio, Ultrastructure of the Lyonet’s glands in larvae of *Diatraea saccharalis* Fabricius ( Lepidoptera : Pyralidae ), Biocell 28 (2004) 165–169.

[13] M. Tszydel, S. Sztajnowski, M. Michalak, H. Wrzosek, S. Kowalska, I. Krucińska, B. Lipp-symonowicz, Structure and physical and chemical properties of fibres from the fifth larval instar of caddis-flies of the species *Hydropsyche angustipennis*, Fibres Text. East. Eur. 17 (2009) 7–12.

[14] B. Spanhoff, U. Schulte, C. Alecke, N. Kaschek, E.I. Meyer, Mouthparts, gut contents, and retreat-construction by the wood-dwelling larvae of *Lype phaeopa*, Eur. J. Entomol. 100 (2003) 563–570.

[15] A.S. Packard, A text-book of entomology, The MacMillan Company, New York, 1898.

[16] M.S. Engster, Studies on silk secretion in the Trichoptera (F. Limnephilidae): II. structure and amino acid composition of the silk, Cell Tissue Res. 169 (1976) 77–92.

[17] C.S. Wang, H. Pan, G.M. Weerasekare, R.J. Stewart, Peroxidase-catalysed interfacial adhesion of aquatic caddisworm silk, J. R. Soc. Interface. 12 (2015) 1-11.

[18] C.-S. Wang, N.N. Ashton, R.B. Weiss, R.J. Stewart, Peroxinectin catalyzed dityrosine crosslinking in the adhesive underwater silk of a casemaker caddisfly larvae, *Hysperophylax occidentalis*, Insect Biochem. Mol. Biol. 54 (2014) 69–79.

[19] R.J. Stewart, C.S. Wang, Adaptation of caddisfly larval silks to aquatic habitats by phosphorylation of H-fibroin serines, Biomacromolecules 11 (2010) 969–974.

[20] D. Naskar, R.R. Barua, A.K. Ghosh, S.C. Kundu, Silk biomaterials for tissue engineering and regenerative medicine, Woodhead Publishing, Cambridge, 2014.

[21] N. Yonemura, K. Mita, T. Tamura, F. Sehnal, Conservation of silk genes in Trichoptera and Lepidoptera., J. Mol. Evol. 68 (2009) 641–653.

[22] N. Yonemura, F. Sehnal, K. Mita, T. Tamura, Protein composition of silk filaments spun under water by caddisfly larvae, Biomacromolecules 7 (2006) 3370–3378.

[23] N.N. Ashton, D.R. Roe, R.B. Weiss, T.E. Cheatham, R.J. Stewart, Self-tensioning aquatic caddisfly silk: $Ca^{2+}$-dependent structure, strength, and load cycle hysteresis., Biomacromolecules 14 (2013) 3668–3681.

[24] K. Ohkawa, Y. Miura, T. Nomura, R. Arai, Isolation of silk proteins from a caddisfly larva , *Stenopsyche marmorata*, J. Fiber Bioeng. Informatics 5 (2012) 125–137.

[25] V. Blough, Neil, G. Ziepp, Richard, Reactive oxygen species in natural waters, 2nd ed., Chapman & Hall 1995, London, 1995.

[26] M. Soudi, M. Zamocky, C. Jakopitsch, P.G. Furtmüller, C. Obinger, Molecular evolution, structure, and function of peroxidasins, Chem. Biodivers. 9 (2012) 1776–1793.

[27] T. Hertner, H.M. Eppenberger, M. Lezzi, The giant secretory proteins of

*Chironomus tentans* salivary glands: the organization of their primary structure, their amino acid and carbohydrate composition, Chromosoma 88 (1983) 194–200.

[28] C.S. Wang, R.J. Stewart, Multipart copolyelectrolyte adhesive of the sandcastle worm, *Phragmatopoma californica* (Fewkes): catechol oxidase catalyzed curing through peptidyl-DOPA., Biomacromolecules 14 (2013) 1607–1617.

[29] J. Jonker, L. Morrison, E.P. Lynch, I. Grunwald, J. Von Byern, A.M. Power, A.M. Power, The chemistry of stalked barnacle adhesive (*Lepas anatifera*), Interface Focus 5 (2015) 1-13.

[30] K.E. Cooksey, B. Wigglesworth-Cooksey, Adhesion of bacteria and diatoms to surfaces in the sea: A review, Aquat. Microb. Ecol. 9 (1995) 87–96.

[31] R.J. Stewart, T.C. Ransom, V. Hlady, Natural underwater adhesives, J. Polym. Sci. B polym. Phys. 49 (2011) 757–771.

[32] F. Sehnal, M. Zurovec, Construction of silk fiber core in Lepidoptera, Biomacromolecules 5 (2004) 666–674.

[33] K. Ohkawa, Y. Miura, T. Nomura, R. Arai, K. Abe, K. Hirabayashi, Long-range periodic sequence of the cement/silk protein of *Stenopsyche marmorata* : purification and biochemical characterisation, J. Bioadhesion Biofilm Res. 29 (2013) 357–367.

[34] K. Tanaka, N. Kajiyama, K. Ishikura, S. Waga, a Kikuchi, K. Ohtomo, T. Takagi, S. Mizuno, Determination of the site of disulfide linkage between heavy and light chains of silk fibroin produced by *Bombyx mori*, Biochim. Biophys. Acta. 1432 (1999) 92–103.

[35] K. Mori, K. Tanaka, Y. Kikuchi, M. Waga, S. Waga, S. Mizuno, Production of a chimeric fibroin light-chain polypeptide in a fibroin secretion-deficient naked pupa mutant of the silkworm *Bombyx mori*, J. Mol. Biol. 251 (1995) 217–228.

[36] Y. Wang, K. Sanai, M. Nakagaki, A novel bioadhesive protein of silk filaments spun underwater by caddisfly larvae, Adv. Mater. Res. 79 (2009) 1631–1634.

[37] Y. Wang, H. Wang, T. Zhao, M. Nakagaki, Characterization of a cysteine-rich protein specifically expressed in the silk gland of caddisfly *Stenopsyche marmorata*, Biosci. Biotechnol. Biochem. 74 (2010) 108–12.

[38] J.H. Eum, S.M. Yoe, Y.R. Seo, S.W. Kang, S.S. Han, Characterization of a novel repetitive secretory protein specifically expressed in the modified salivary gland of *Hydropsyche sp*., Insect Biochem. Mol. Biol. 35 (2005) 435–441.

[39] S.T. Case, J. Powers, R. Hamilton, M.J. Burton, Silk and silk proteins from two aquatic insects, ACS Symp. Ser. 544 (1994) 80–90.

[40] W.Q. Chen, H. Priewalder, J.P.P. John, G. Lubec, Silk cocoon of *Bombyx mori*: Proteins and posttranslational modifications - heavy phosphorylation and evidence for lysine-mediated cross links, Proteomics 10 (2010) 369–379.

[41] J.O. Warwicker, Comparative studies of fibroins II. the crystal structure of various fibroins, J. Mol. Biol. 2 (1960) 350-362.

[42] K. Rudall, W. Kenchington, Arthropod silks: the problem of fibrous proteins in animal tissues, Annu. Rev. Entomol. 16 (1971) 73–96.

[43] J.B. Addison, W.S. Weber, Q. Mou, N.N. Ashton, R.J. Stewart, G.P. Holland, J.L. Yarger, Reversible assembly of β-sheet nanocrystals within caddisfly silk., Biomacromolecules 15 (2014) 1269–1275.

[44] Y. Wang, K. Sanai, H. Wen, T. Zhao, M. Nakagaki, Characterization of unique heavy chain fibroin filaments spun underwater by the caddisfly *Stenopsyche* marmorata (Trichoptera; Stenopsychidae), Mol. Biol. Rep. 37 (2010) 2885–2892.

[45] F. Sehnal, T. Sutherland, Silk produced by insect labial glands, Prion 2 (2008) 145–153.

[46] S.S. Zimmerman, H. a Scheraga, Influence of local interactions on protein structure. I. Conformational energy studies of N-acetyl-N'-methylamides of Pro-X and X-Pro dipeptides, Biopolymers 16 (1977) 811–843.

[47] C.M. Dobson, A. Šali, M. Karplus, Protein folding: A perspective from theory and experiment, Angew. Chemie-Int. Ed. 37 (1998) 868–893.

[48] A.F. Cotton, G. Wilkinson, M. Bochmann, C.A. Murillo, Advanced inorganic chemistry, Wiley, 1999.

[49] J.W. Strzelecki, J. Strzeleka, K. Mikulska, M. Tszydel, A. Balter, W. Nowak, Nanomechanics of new materials-AFM and computer modelling studies of Trichoptera silk, Cent. Eur. J. Phys. 9 (2011) 482–491.

[50] S.A. Brown, G.D. Ruxton, S. Humphries, Physical properties of *Hydropsyche siltalai* ( Trichoptera ) net silk, J. North Am. Benthol. Soc. 23 (2004) 771–779.

# CHAPTER 2

# SILK TAPE NANOSTRUCTURE AND SILK GLAND ANATOMY OF TRICHOPTERA



Authors Contributions: N.N.A. and D.S.T gathered and maintained caddisfly larvae in the lab. N.N.A. photographed the larvae, harvested the silk fibers, prepared samples for SEM, prepared samples for AFM, imaged silk fibers by AFM, immunolabled silk fibers, sectioned silk fibers, sectioned silk glands, performed laser scanning confocal microscopy, and performed DIC microscopy. D.S.T. Imaged silk fibers and glands by DIC, polarized light, and laser scanning confocal microscopy. N.N.A., D.S.T., and R.J.S. designed the experiments and interpreted the results. N.N.A. and R.J.S. prepared the manuscript. All authors proof-read the manuscript.

# Silk Tape Nanostructure and Silk Gland Anatomy of Trichoptera

Nicholas N. Ashton, Daniel S. Taggart, Russell J. Stewart
*Department of Bioengineering, University of Utah, Salt Lake City, UT 84112*

*Received 27 July 2011; accepted 13 September 2011*
*Published online 22 September 2011 in Wiley Online Library (wileyonlinelibrary.com). DOI 10.1002/bip.21720*

**ABSTRACT:**

*Caddisflys (order Trichoptera) construct elaborate protective shelters and food harvesting nets with underwater adhesive silk. The silk fiber resembles a nanostructured tape composed of thousands of nanofibrils (~ 120 nm) oriented with the major axis of the fiber, which in turn are composed of spherical subunits. Weaker lateral interactions between nanofibrils allow the fiber to conform to surface topography and increase contact area. Highly phosphorylated $(pSX)_4$ motifs in H-fibroin blocks of positively charged basic residues are conserved across all three suborders of Trichoptera. Electrostatic interactions between the oppositely charged motifs could drive liquid–liquid phase separation of silk fiber precursors into a complex coacervates mesophase. Accessibility of phosphoserine to an anti-phosphoserine antibody is lower in the lumen of the silk gland storage region compared to the nascent fiber formed in the anterior conducting channel. The phosphorylated motifs may serve as a marker for the structural reorganization of the silk precursor mesophase into strongly refringent fibers. The structural change occurring at the transition into the conducting channel makes this region of special interest. Fiber formation from polyampholytic silk proteins in Trichoptera may suggest a new approach to create synthetic silk analogs from water-soluble precursors.* © *2011 Wiley Periodicals, Inc. Biopolymers 97: 432–445, 2012.*

*Correspondence to:* Russell J. Stewart; e-mail: rstewart@eng.utah.edu
Contract grant sponsor: Life Sciences Division of the U.S. Army Research Office
Contract grant number: W911NF1010132


*Keywords: Trichoptera; silk; complex coacervates; adhesive tape; bioadhesives; polyampholytes; polyelectrolytes*

*This article was originally published online as an accepted preprint. The "Published Online" date corresponds to the preprint version. You can request a copy of the preprint by emailing the Biopolymers editorial office at biopolymers@wiley.com*

## INTRODUCTION

Larvae in the order Trichoptera (caddisflies) evolved an underwater, silk-based adhesive that bonds to diverse substrates, ranging from mineral particles to organic plant matter.[1] With the silks, the larvae build underwater composite structures for protection and food capture. The fossil record suggests a terrestrial ancestor diverged 200–250 million years ago, during the Triassic period, into the superorder Amphiesmenoptera, which includes terrestrial Lepidoptera (moths and butterflies) and aquatic Trichoptera.[2] In tandem with its divergence from Lepidoptera adaptation of its silk to aquatic environments allowed Trichoptera to infiltrate ecological niches ranging from freshwater lakes, rivers, and streams to wet grasslands.[2] Worldwide, more than 12,000 species have been classified into three suborders: Annulipalpia, Spicipalpia, and Integripalpia.[3] The silk constructions of species in each suborder are unique (Figure 1). The Integripalpia are mobile foragers that build cases around their soft larval bodies with stones, sticks, or leaves. The Annulipalpia build stationary retreats with stones or leaves and spin silk nets for collecting food. Spicipalpia make varied use of their silk but most are free living and only spin an underwater silk cocoon just before pupation.[3]

Trichopteran larval silk is extruded from a pair of silk glands that fold back and forth several times along the ventral side of the alimentary canal and terminate at the spinneret on the ventral side of the mouthparts and alimentary orifice.[4,5] This basic anatomical layout is shared by its terres-

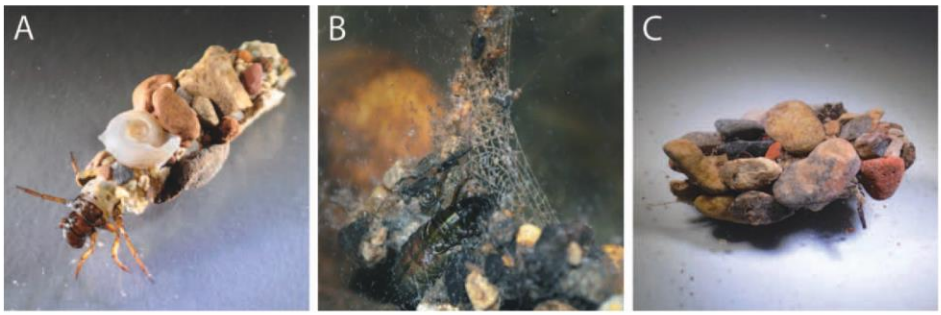


**FIGURE 1** (A) *H. consimilis* larvae and case naturally constructed with stones and debris from the riverbed. (B) Retreat and capture web built in a high-flow region of an artificial habitat by *A. grandis*. (C) Stone enclosure constructed by *Rhyacophila sp.* before pupation. Small rocks and debris protect an internal silk cocoon.

trial Lepidopteran cousins.[4] Caddisfly larval silk glands are functionally divided into three regions: a posterior region into which dense granules of silk precursors are secreted, a middle storage region, and an anterior conducting channel terminating at the spinneret.[6] In *Helicopsyche crispata*, the posterior and middle regions makes up about 80% of the gland's length.[7] The same regions in *Pycnopsyche guttifer* are 80–85% of the gland length.[5] (a distinct bulbous region occurs at the transition between the storage region and the anterior conducting channel of each gland) The gland lumen narrows dramatically at this transition; in *P. guttifer*, the cross-sectional area of the conducting channel is roughly 90% less than the lumen of the storage region.[5] The lumen of the anterior conducting channel is lined with a radially banded cuticle, a trait shared across the superorder Amphiesmenoptera.[4,5] In *P. guttifer*, a short, $\sim$ 1 mm, common duct region has also been reported.[5] A silk press, like that found in silkworms,[4] has not been observed in caddisfly larvae.[5] Several authors have worked on characterizing the mouthparts of various caddisflies species using scanning electron microscopy (SEM).[5,8,9] (Much remains to be learned about the anatomy and physiology of the caddisfly silk spinning system.)

The silks of Trichoptera larvae share several general features with the silks of their terrestrial Lepidopteran relatives, but there are distinct features that may have arisen during its adaptation to aquatic use. On the macroscale, silk fibers of both orders, originating from paired glands, are fused into a paired elliptical fiber at the spinneret.[5,10,11] Silkworm (*Bombyx mori*) silk has a central core surrounded with a sticky exterior sericin layer. Caddisfly silk has a central core covered with a much thinner, poorly characterized, peripheral layer.[5,10] On the molecular level, both Trichopteran and Lepidopteran silks are composed of heavy chain fibroin (H-fibroin) and light chain fibroin (L-fibroin). The H-fibroins are structurally organized similarly with highly repetitive central regions flanked with nonrepetitive terminal regions.[12,13] In silkworm silk, L and H-fibroin occur in a 1:1 ratio and are covalently linked by a single disulfide bond.[14] The locations of the cysteine residues are conserved in caddisfly L- and H-fibroins suggesting the intermolecular disulfide linkage and 1:1 ratio between H- and L-fibroin is conserved in the aquatic silks.[15] A perhaps significant molecular difference is the absence, in Trichopteran silks, of a homolog of fibrohexamerin (P25), a glycoprotein that occurs in 1:6 ratio to L- and H-fibroin dimers. P25 is postulated to be involved in the assembly of silk precursor micelles of silkworm silk.[12,15,16]

Comparison of H-fibroin amino acid compositions reveals the striking distinctions between terrestrial moth and aquatic caddisfly silks. First, moth silks contain 20–30 mol% alanine residues, whereas caddisfly silks contain less than 5 mol% alanine.[10,11,15,17] The alanine-rich regions of moth silks are widely considered to form rigid $\beta$-sheet structures dispersed within extensible, disordered glycine-rich matrices, a molecular design shared with spider silks.[13,16] Tensile strength and extensibility of dry silks are correlated with the proportions of ordered and disordered regions.[18] The comparative absence of alanine in caddisfly silks suggests either a fundamentally different molecular fiber design or that residues, other than alanine, contribute to rigid semicrystalline motifs functionally equivalent to the $\beta$-sheets of moth and spider silks. As revealed by X-ray diffraction, caddisfly silk from *P. guttifer* has a 21–22 Å periodic structure, whereas silkworm silk has a 17 Å periodic structure.[10] The intensity of the caddisfly silk diffraction pattern is considerably less than silkworm silk, suggesting less regularity in Trichopteran silk structure.[19] Perhaps consistent with less ordered silk, the mean tensile strength of hydrated net silk from the retreat


**FIGURE 2** Partial sequence of *L. decipiens* H-fibroin protein [AB214509]. Blue regions denote phosphorylated motifs $(pSX)_4$, yellow domains represent positively charged arginine-rich blocks, and pink segments highlight conserved glycine-proline pairs indicative of hairpin loops.

builder *Hydropsyche siltalai* (221 $mN/m^2$)[20] was among the lowest reported for arthropod silks and substantially lower than commercial silk ($\sim$ 300 $mN/m^2$) and spider dragline silk (1400–1800 $mN/m^2$).[18,20] That of *H. siltalai* net silk had a mean failure strain of 1.16.[20]

A second striking difference in amino acid composition is the abundance of charged residues in caddisfly H-fibroins compared to moths.[11] Around 16 mol% of caddisfly, H-fibroin residues are basic, with arginine (R) particularly well represented.[11,15,17] In contrast, basic residues make up less than 2 mol% of moth H-fibroin. Aspartic (D) and glutamic (E) acid residues are also more abundant in caddisfly than in moth H-fibroins. Serines (S) are well represented in the H-fibroins of both orders, ranging from 12 to 17 mol%. However, as many as 60% of the serines in caddisfly H-fibroins may be phosphorylated.[11] For comparison, 12 serine residues out of more than 5000 residues of silkworm H-fibroin were reported to be phosphorylated.[21] As a result of the high charge density, caddisfly H-fibroins are ampholytic in character, with alternating blocks of oppositely charged residues in the central H-fibroin region, whereas moth H-fibroins are amphiphilic consisting of alternating blocks of uncharged hydrophilic and hydrophobic residues.[16] Alternating oppositely charged residues also occur in the silk of aquatic black fly larvae (*Chironomus tentans*); the silk contains an estimated 8 mol% phosphoserine and a combined 25 mol% basic lysine and arginine residues.[17,22] Ampholytic silk precursors likely evolved independently in the two aquatic insect orders. The ampholytic character of caddis silk could drive liquid–liquid phase separation of silk proteins into complex coacervates: dense, amorphous, fluid networks of polyelectrolytes dynamically connected through intermolecular electrostatic interactions.[11] In some regard, this model is analogous to models in which the amphiphilic nature of moth and spider silks drives phase separation of silk fiber precursors into micelles or lyotrophic liquid crystals.[23,24] The comparatively high charge density acquired through phosphorylation of serines and accumulation of basic residues may be one of the molecular adaptations that allowed caddisflies to penetrate aquatic habitats with underwater silk.[11]

Caddisfly H-fibroin sequences are highly repetitive and comprise sets of unique repeats labeled A-F.[12,15] A majority of the caddisfly serines occur in $(SX)_4$ motifs, in which the Xs tend to be hydrophobic residues. The D repeats contain two $(SX)_4$ motifs separated by 11 residues with a central proline-glycine (PG) pair, which suggests a loop structure may lie between the motifs. The D repeat $(SX)_4$ pattern is conserved in the H-fibroins of all three families of caddisflies. A single $(SX)_4$ motif occurs in the F repeat. Mass spectrometry revealed that the serines in the D repeat $(SX)_4$ motifs are phosphorylated (Figure 2).[11] However, no evidence was found that the F repeat $(SX)_4$ motif was phosphorylated. H-Fibroins from all three caddisfly families have highly conserved D repeats, which suggested the phosphorylation pattern is also conserved. Three arginine-rich motifs separate each pair of D repeat $(pSX)_4$ motifs. Phosphates have high affinity for divalent cations like $Ca^{2+}$ and $Mg^{2+}$, which were also found in abundance in the caddisfly silk.[11] Returning to the absence of alanine-rich $\beta$-crystalline regions in caddisfly H-fibroins, it has been suggested that, in the presence of $Ca^{2+}$, the paired $(pSX)_4$ motifs, joined by a loop, could form a repeating structural domain functionally analogous to the

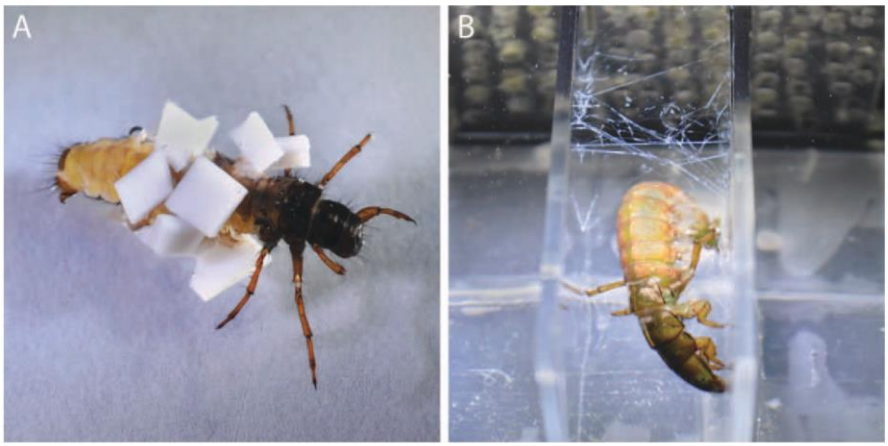


**FIGURE 3** The species-dependent methods for harvesting clean silk in controlled lab aquariums. (A) *H. consimilis* larvae with partially built PTFE case in a clean aquarium. (B) Artificial flow chamber retreat with *A. grandis* larvae spinning fibers across a narrow channel created with two parallel glass microscope slides.

$\beta$-crystalline regions of moth and spider silks providing tensile strength to the caddisfly silk fibers.[11] Molecular dynamic simulations in which a region of the D repeat containing the $(pSX)_4$ motifs was modeled in the presence and absence of $Ca^{2+}$ as a pair of antiparallel $\alpha$-helices or $\beta$-strands connected with a hairpin loop demonstrated the $\beta$-strands in the presence of $Ca^{2+}$ gave the highest predicted resistance to stretching.[25] The molecular dynamic simulations provide theoretical support for a $Ca^{2+}$ stabilized phosphoserine-rich structural domain in caddisfly silk.

The polyampholytic nature of Trichopteran silks may provide a unique model for investigating silk fiber formation. The ultimate goal is to identify the essential features of the silk component chemistry, mesophase structure, and the fiber forming machinery that must be replicated to create useful synthetic materials with the properties of the natural silk. Toward this end, the nanoscopic structure of adhesive underwater larval silks, as well as the anatomy of the silk spinning systems of species representing all three suborders of Trichoptera, are reported herein.

## METHODS

### Specimen Collection

During the early summer, fifth instar larvae from the genera *Arctopsyche*, *Rhyacophila*, and *Hesperophylax* (Figure 1) were collected from the Lower Provo River and upper Red Butte creek in Utah, USA. Larvae of the genera *Hesperophylax* and *Arctopsyche* were identified as *H. consimilis* and *A. grandis* (*H. consimilis* was mistakenly identified as *Brachycentrus echo* in an earlier report[11]). The *Rhyacophila* species could not be identified. They were transported in ice water to the lab. The three species were kept in separate filtered and bubbled aquaria chilled to 11°C. The tanks for *A. grandis* and *Rhyacophila* each had a circulation pump to simulate stream flow. The larvae were fed fish food pellets daily.

### Silk Harvesting

Before harvesting silk, clean aquaria were filled with tap water and bubbled for 24 h to remove chlorine. Larvae of the case maker *H. consimilis* were removed from their native cases and placed in a small dish inside a clean aquarium. The larvae were provided $\sim$ 1 $mm^3$ blocks of polytetrafluoroethylene (PTFE) for case rebuilding from which clean bulk silk fibers were harvested (Figure 3). For analytical techniques requiring silk on a substrate, the larvae were provided 0.5 mm diameter glass beads, shards of glass coverslip, or shards of silicon wafer. After 1–2 days, the newly constructed cases were removed, and the silk was gathered from the PTFE blocks with fine forceps under a dissecting microscope. Retreat building *A. grandis* larvae were removed from their native retreats and isolated between two standard glass microscope slides or silicon wafers in a clean aquarium. Water was circulated through the isolation chamber using a small aquarium pump to simulate stream flow. After 1–3 days, the larvae were removed from the chamber. Silk fibers spun between the two microscope slides were gathered with fine forceps (Figure 3).

### Gland Dissection

Caddisfly larvae were secured onto a silicone dissection plate by pinning the anterior and posterior regions with the insect's ventral side up. An incision was made along the ventral abdominal wall. After the first incision, the larva was bathed in insect Ringer's solution (10.93 g/L NaCl, 1.57 g/L KCl, 0.83 g/L $CaCl_2$ $2H_2O$, and 0.83 g/L

$MgCl_2$ 6 $H_2O$, adjusted to final pH 7.2).[26] The silk glands were then carefully teased out and unfolded. The ventral incision was continued through the thorax exposing the anterior gland region. The gland pair was traced to the posterior side of the head, and a radial cut was made in the sclerites, which form the head. The anterior conductive portion of the gland was exposed up to the mouthparts and spinneret by removal of the ventral side of the head sclerites. A circular cut was made around the mouthparts, thus, freeing the entire silk gland system.

### Optical Microscopy of Silk Gland

Dissected *H. consimilis* and *Rhyacophila* glands in Ringer's solution were sealed under a coverslip and examined with an Axiovert 100 microscope (Carl Zeiss AG, Oberkochen, Germany). Preparations were observed *in vitro* with crossed polarizing filters and a $\lambda/4$ wave plate set 45° and 30° to the slow axis of polarization. The same specimens were also observed by differential interference contrast (DIC) microscopy. Gland and lumen measurements were made by comparison with a calibrated slide standard.

### Confocal Laser Scanning Microscopy

Live glands were maintained in Ringer's solution and sealed under a glass coverslip. Specimens were viewed with a Fluoview FV1000 laser scanning confocal microscope (Olympus, Tokyo, Japan). Gland structure and contents were illuminated with 405- and 488-nm excitation wavelengths, and observed at emission wavelengths of 461 and 508 nm, respectively. Longitudinal optical sections were taken through fresh silk glands at the bulbous feature marking the boundary between the gland's storage and conductive regions.[5] Epifluorescent DIC and autofluorescent channels were combined into composite images using ImageJ software (National Institutes of Health, Bethesda, MD). Photos were merged into composite images using Photoshop software (Adobe Systems, San Jose, CA).

### Immunostaining

Silk, freshly harvested from PTFE substrates, was dehydrated with a graded ethanol series (50% EtOH/$H_2O$, 70% EtOH/$H_2O$, 95% EtOH/$H_2O$, and 100% EtOH). The dehydrated silk was imbedded in glycol methacrylate resin (Immunobed, Polysciences, Warrington, PA). The freshly excised silk glands of *H. consimilis* and *A. grandis* were promptly fixed in 4% paraformaldehyde in insect Ringer's solution at 4°C overnight. After dehydration using a graded ethanol series, the glands were carefully positioned and imbedded in glycol methacrylate resin (Immunobed, Polysciences, Warrington, PA). The resultant blocks were sectioned, using a glass knife on a Jung RM 2055 microtome (Leica Microsystems, Wetzlar, Germany), to a thickness of 3 $\mu$m and mounted on clean glass slides (Fisher Scientific, Hampton, NH). Glands from *H. consimilis* were sectioned longitudinally. Transverse sections of the *A. grandis* glands were collected in two regions of interest, posteriorly and anteriorly to the transition between the gland's storage region and conducting channel. The slides were treated with 0.25% trypsin in PBS + 0.05% Tween 20 (PBST) at 37°C for 15 min for antigen retrieval and subsequently blocked with 2 mg/ml bovine serum albumin in PBST, at 4°C overnight. The samples were then incubated overnight in primary anti-phosphoserine mouse antibody ($\alpha$-pSer) at 4°C (Abcam, #6729, 1:500 dilution). The primary antibody was labeled with a 1:5000 dilution of goat antimouse Alexafluor 647 IgG (H+L) at room temperature for 1 h. (Invitrogen, Carlsbad, CA). The samples were mounted in ProLong Gold Antifade mounting medium (Invitrogen, Carlsbad, CA) and capped with a clean glass coverslip. The primary ($\alpha$-pSer) antibody was omitted in control specimens. Samples were imaged using a Fluoview FV1000 confocal microscope with an excitation frequency of 650 and a 668-nm far-red filter (Olympus, Tokyo, Japan). On separate channels, the stained sections were excited under 405 and 488 nm wavelengths resulting in autofluorescence emission of 461 and 508 nm, respectively. A Fluoview FV1000 and an Axiovert 100 (Carl Zeiss AG, Oberkochen, Germany) were used to collect DIC images of silk sections.

### Scanning Electron Microscopy

Cases from *H. consimilis*, reconstructed with 0.5 mm glass beads, were mounted on carbon tape, cooled to −80°C, and lyophilized overnight. Samples were examined with a Quanta 600 FEG SEM (FEI Company, Hillsboro, OR). Images were collected at high vacuum (0.98 Torr) using accelerating voltages of 10 and 7 keV. Electron micrographs were produced using backscattered electron and low-vacuum detectors.

### Atomic Force Microscopy

Silk produced on silicon substrate by *A. grandis*, *Rhyacophilia*, and *H. consimilis* were lyophilized and mounted on steel stubs. Images were taken of all three silks using a Nanoscope II atomic force microscope in contact mode (Veeco, Plainview, NY). An ultrasharp cantilever (Mikromasch CSC21; San Jose, CA) was rastered obliquely to the long axis of the fiber to avoid artifacts.

### Optical Microscopy of Silk

*H. consimilis* and *Rhyacophila* silk on glass substrates were examined under polarized light using methods outlined for optical microscopy of the silk gland. Silk threads, attached to glass substrate, were observed for both species. Fiber diameter measurements were taken using a calibration slide standard.

## RESULTS

### Harvesting Silk

The silk and silk-spinning apparatus were studied for three species of caddisfly, one from each of the Trichopteran suborders: *Hesperophylax consimilis* (suborder Integripalpia), *Arctopsyche grandis* (suborder Annulipalpia), and an unidentified species of the genus *Rhyacophila* (suborder Spicipalpia) (Figure 1). The unidentified *Rhyacophila sp.* will be referred to as *Rhyacophila*. Controlled and clean artificial environments were designed for collecting silk for analysis. *H. consimilis*, as reported previously,[11] will attempt to rebuild its case with any material provided, including Teflon blocks, if its case is damaged or removed (Figure 3A). *A. grandis* will spin

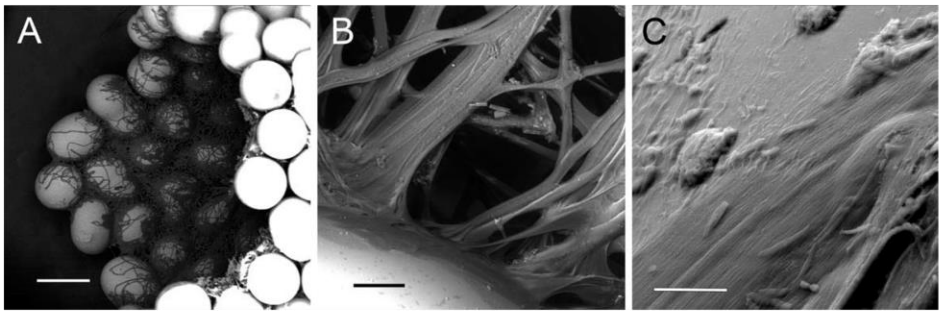


**FIGURE 4** (A) Electron micrograph of *H. consimilis* case reconstructed with 0.5-mm glass beads stitched together with silk fibers. Scale bar is 0.5 mm. (B) Increased magnification showing fusion of silk fibers and spreading of wet silk component over glass substrate; scale bar is 25 $\mu$m. (C) High-magnification electron micrograph showing fiber substructure. Nanofilaments are aligned with the fibers long axis. Scale bar is 5 $\mu$m.

a disorganized web when confined between two plates in a flow chamber (Figure 3B). The silk of the *Rhyacophila* species was difficult to collect because the species does not build silk structures until the beginning of pupation, at which point a stationary rock dome with a cocoon-like silk lining is constructed (Figure 1C). By careful monitoring of *Rhycophila* before pupation, isolated in a flow chamber like *A. grandis*, silk was successfully harvested.

## Silk Fiber Structure

Representative SEM micrographs of a *H. consimilis* case reconstructed with 0.5 mm glass beads are shown in Figure 4. The glass beads were taped together on the inside with a dense weave of paired fibers (Figure 4A). The fibers appear to have a fluid plasticity. Fibers that spanned between glass beads, for example, fused into thick cohesive bundles and reinforcing struts where they made contact (Figure 4B). At the substrate interface, the perpendicular bundles of fibers flattened into large adhesive contact areas. At high magnification in the SEM, nanoscopic subfibrils aligned with the long axis of the flattened tape, were apparent (Figure 4C).

Contact mode atomic force microscopy (AFM) of the silk on silicon wafer shards revealed repetitive nanoscale organization of surface features in silk fibers of all three species (Figure 5). The linear nanofilaments were assembled with spherical subunits about a hundred nm in diameter. The nanofilaments were occasionally observed to peel away from the bulk of the fiber bundle and adhere to the surface (Figure 5D). Similar nanofibrils have been observed in silkworm silk by AFM but the spherical subunit structure was not apparent.[27]

When examined under polarized light, the naturally extruded silk fibers of *H. consimilis* and *Rhyacophila* larvae were strongly refringent (Figure 6). Subfibers within each flat ribbon produce continuous parallel interference bands. Closely associated filaments within the fiber contribute to a range of transversely separated interference colors. Variations in color and transverse dispersion are both amplified when observing fibers that are curved or tilted (Figures 6B and 6C). The optical path length difference between longitudinal and transverse fiber axes increased with the $\lambda/4$ wave plate set $30^\circ$ to the slow vibration axis (Figure 6A).

Previously, the extruded silk of *H. consimilis* was shown to be extensively phosphorylated on H-fibroin serines.[11] To determine if H-fibroin phosphorylation is common to all three suborders of Trichoptera, an antibody against phosphoserine ($\alpha$-pSer) was used to immunolabel silk fibers that were embedded and sectioned. Representative images of mostly end-on sections are shown in Figure 7. The fibers are paired because they are drawn from paired silk glands. The presence of pSer was confirmed in all three species and thereby all three Trichoptera suborders. Phosphoserine was distributed across the entire cross section of the silk fibers of the casemaker, *H. consimilis,* although the interior appears to have a lower density and more granular labeling (Figure 7A). The uneven distribution of pSer is pronounced in *A. grandis*; a densely labeled annulus surrounds an unlabeled interior core (Figure 7B). The *A. grandis* silk fibers exhibited a wider range of fiber diameters than the other two species. *Rhyachophila* stained similarly to *H. consimilis* (Figure 7C). The filled tube structure of the *A. grandis* silk fibers was evident in DIC microscopy. In $\sim 45^\circ$ section of an *A. grandis* silk fiber, a fibrous longitudinal internal structure was visible (Figure 7F). The silk of *H. consimilis* was much less organized than that of *A. grandis,* with a granular structure consistent with its immunolabeling (Figure 7D). Silk sections were not autofluores-

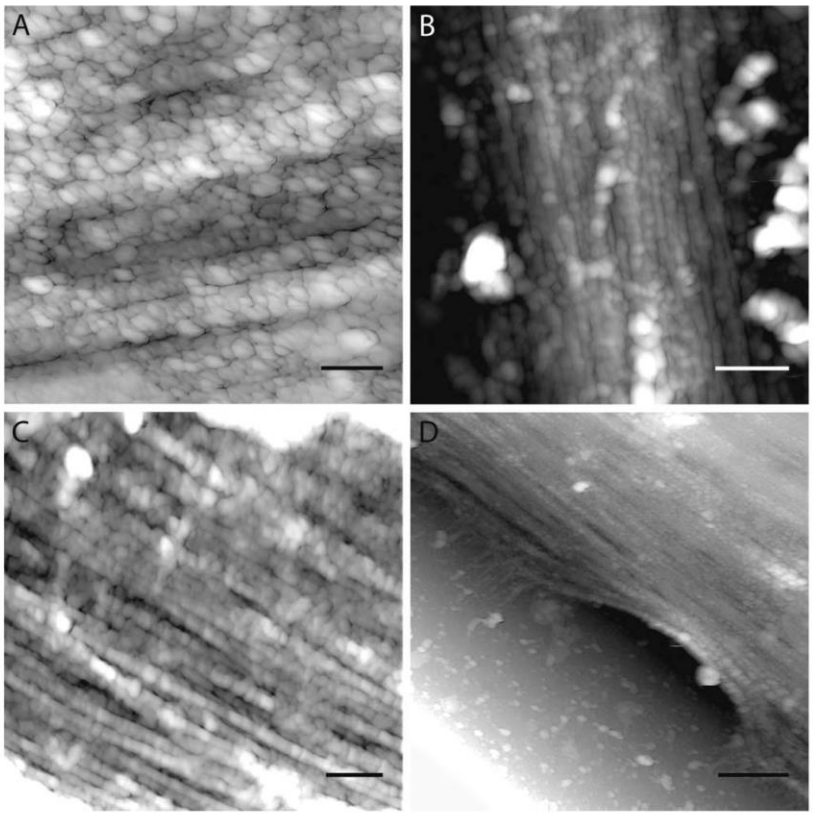


**FIGURE 5** Representative atomic force micrographs of silk from each of the three species studied. (A) Silk topography from *H. consimilis*. Scale bar is 300 nm. (B) Silk topography along the top of one of the two subfibers from *A. grandis*. Scale bar is 500 nm. (C) Silk topography from *Rhyacophila sp.* Scale bar is 500 nm. (D) AFM images showing silk-substrate (silicon) interface of silk from *H. consimilis*. Scale bar is 1 $\mu$m.

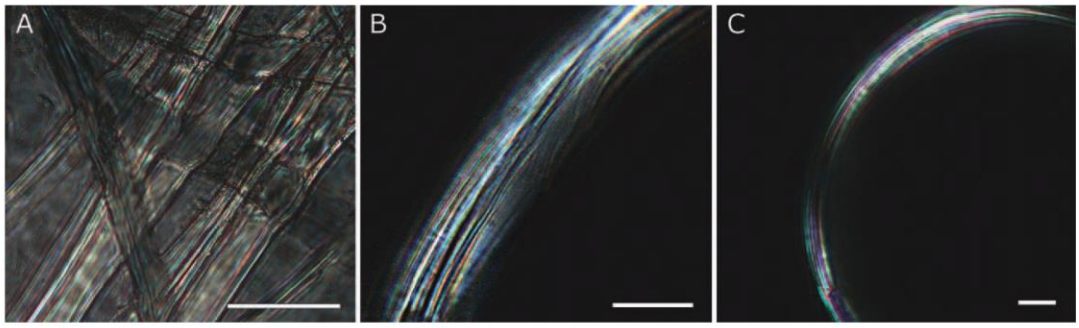


**FIGURE 6** (A) *H. consimilis* silk weave on glass substrate. Polarized light image with $\lambda/4$ plate. Multiple subfibers can be seen within the main thread as continuous parallel bands. Transverse color patterns may result from subfibrils being partially fused. (B) *H. consimilis* silk fiber on glass substrate under polarized light. Individual subfibrils are refringent. (C) *Rhyacophila sp.* silk fiber naturally extruded on glass substrate. Individual subfibrils are refringent. Scale bars in (B) and (C) are 10 $\mu$m.

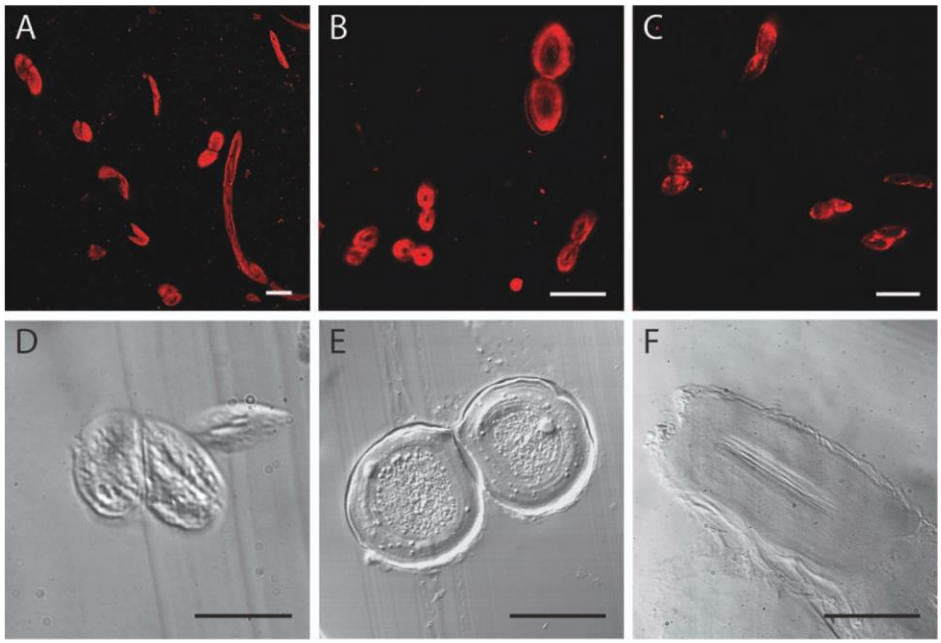


**FIGURE 7** (A–C) Phosphate distribution through transverse sections of silk using an anti-phosphoserine antibody. (A) *H. consimilis* (scale bar: 10 $\mu$m), (B) *A. grandis* (scale bar: 25 $\mu$m), (C) *Rhyacophila* (scale bar: 10 $\mu$m), and (D and E) representative DIC images of silk sections. (D) *H. consimilis* (scale bar: 10 $\mu$m), (E) *A. grandis* (scale bar: 20 $\mu$m), and (F) An $\sim 45^{\circ}$ transverse section an *A. grandis silk fiber* (scale bar: 20 $\mu$m).

cent in the far red (668 nm) using an excitation frequency of 650 nm. The silk and silk tissue is autofluorescent at 405 and 488 nm.

## Silk Gland Physiology and Anatomy

The silk spinning apparatus of caddisfly larvae is inseparable from, the final underwater silk fiber, and its adhesive attributes. As a first step toward understanding how the final adhesive fiber is formed, the anatomy of the silk gland was examined for all three Trichoptera suborder species. The silk glands fold several times along the length of the ventral side of the alimentary canal. Intact silk glands were carefully dissected into insect Ringer's solution to prevent dehydration of the tissue during dissection. Light microscopy revealed a distinct anatomical boundary, referred to previously as a bulbous prominence,[5] between the gland's middle silk storage region and the anterior conducting channel of all three species. In general, the bulbous region was characterized by a dramatic posterior narrowing of the silk gland internal lumen, a sharp transition to a cuticle lined anterior conducting channel that leads to the spinnerets, and the presence of distinct secretory cells lining the lumen before and after the transition. All three species of caddisfly larvae shared this basic anatomical layout.

The granular contents of prominent secretory cells were visible just before the transition in DIC images of the *H. consimilis* (Figure 8A). The contents of the granules are unknown. The lumen of the gland posterior to the bulbous transition contained two bicontinuous phases (Figure 9). A highly branched tracheole terminates at the transition from the gland's middle storage region to anterior conducting lumen (Figure 8A). The conducting channel is lined with a perpendicularly striated cuticle showing autofluorescence (blue: 405 nm excitation) in a longitudinal section through the transition region (Figure 8B). The tissue surrounding the lumen showed autofluorescence (green: 488 nm), while their granular contents did not. The silk fiber, apparent inside the lumen, decreased in diameter, pulling away from the cuticle lining, as though stretched as it passed through the transition. The forming silk fiber kinks back and forth inside the anterior lumen. This was not observed in live gland images, which suggested the

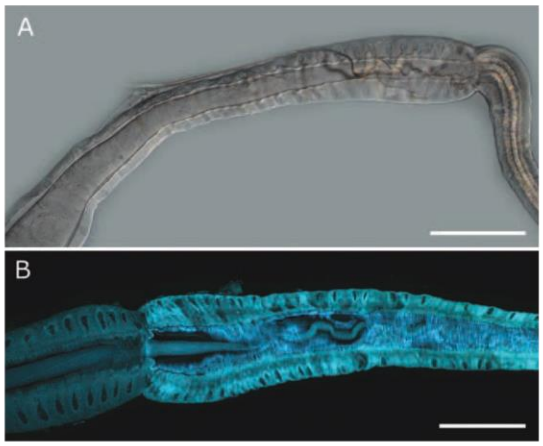


**FIGURE 8** (A) DIC micrograph of *H. consimilis* silk gland near transition from the middle storage lumen to cuticle lined anterior lumen (Scale bar is 300 $\mu$m). (B) Confocal autofluorescence image of *H. consimilis* silk gland from embedded longitudinal sections at the transition from the glands middle storage region to the cuticle lined anterior lumen. Gland tissue and secretory cell cytoplasm are fluorescent under 488 and 405 nm excitation (emission: 508 nm green and 461 nm blue). The cuticle lining of the anterior lumen is fluorescent under 405 nm excitation. Nascent silk fiber at the center of the organized cuticle is autofluorescent under 405 nm excitation (Scale bar is 100 $\mu$m.)

structure resulted from the process of fixation, dehydration, or embedding (Figure 8B).

Natural autofluorescence of the silk gland tissue facilitates confocal microscopy of unfixed glands. In longitudinal optical sections, dissected *Rhyacophila* silk glands narrow into anterior cuticle-lined conducting channels, much like *H. consimilis*, but the glands contained a larger, more pronounced bulbous structure and the lumen tapered more abruptly toward the transition to the anterior conducting channel (Figures 10A and 10B). The cuticle-lined conducting channel was autofluorescent (blue: 405 nm excitation) and had the same cross striated pattern as *H. consimilis*. The silk precursor contents of the lumen posterior to the transition did not autofluoresce. Under polarized light, posterior lumen contents were optically isotropic and extinct but became faintly refringent when they entered the tapered drawdown region just before the transition to cuticle-lined conducting channel (Figure 10B). The cuticle lining of the anterior conducting channel was strongly refringent with a perpendicular orientation to the long axis of the gland. Circumferential windings of the cuticle that gave rise to the refringence were apparent in DIC images, as were longitudinally oriented fibers within the lumen (Figure 10C). Within the refringent cuticle-lined anterior lumen, refringent silk fibers ran parallel to the long axis of the conducting channel, which suggested the structural transition that created the silk fiber refringence occurred during the transition from the middle lumen into the anterior conducting channel (Figure 10D).

Comparing the microscopic dimensions of the silk gland transition regions of *Rhyacophila* and H. *consimilis*, the mean taper lengths were 540 $\pm$ 100 $\mu$m and 2200 $\pm$ 200 $\mu$m, respectively. In this distance, *Rhyacophila* glands underwent a reduction in lumen diameter from 260 $\pm$ 35 $\mu$m to 11 $\pm$ 2 $\mu$m at the cuticle entrance. Similarly, *H. consimilis* glandular lumens tapered down from 230 $\pm$ 25 $\mu$m to 15$\pm$2 $\mu$m in diameter. Glands from both species remained roughly constant in diameter through the cuticle-lined conducting channels until they reached the gland orifice, a distance of $\sim$ 2500 $\mu$m.

If pSer is involved in the structural transition during fiber formation, its accessibility to the pSer antibody may change during the transition. To explore this possibility, thin sections of fixed and embedded silk glands of *H. consimilis* from before and after the transition into the conducting channel were probed with the pSer antibody (Figure 11A). In longitudinal sections, nascent silk fibers in the gland's anterior conducting channel were labeled more than silk fiber precursors distal to the transition point. Similar results were obtained using transverse gland sections of *A. grandis*. Silk fiber precursors in the middle storage region of the gland, before the transition, were poorly labeled by the pSer antibody (Figure 11B), while silk fibers in the anterior conducting channel were strongly labeled (Figure 11C).

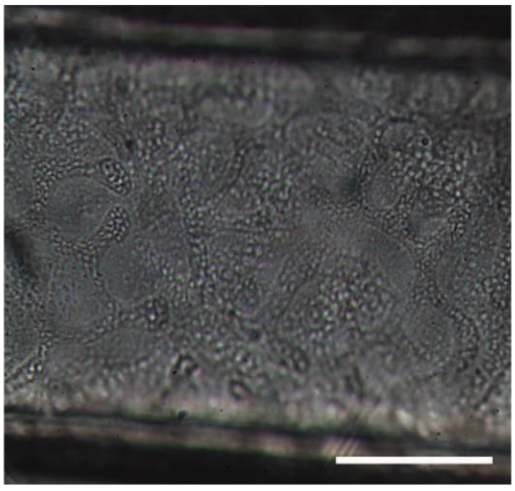

**FIGURE 9** DIC micrograph of the middle storage region of the silk gland of *H. consimilis* (Scale bar is 100 $\mu$m).

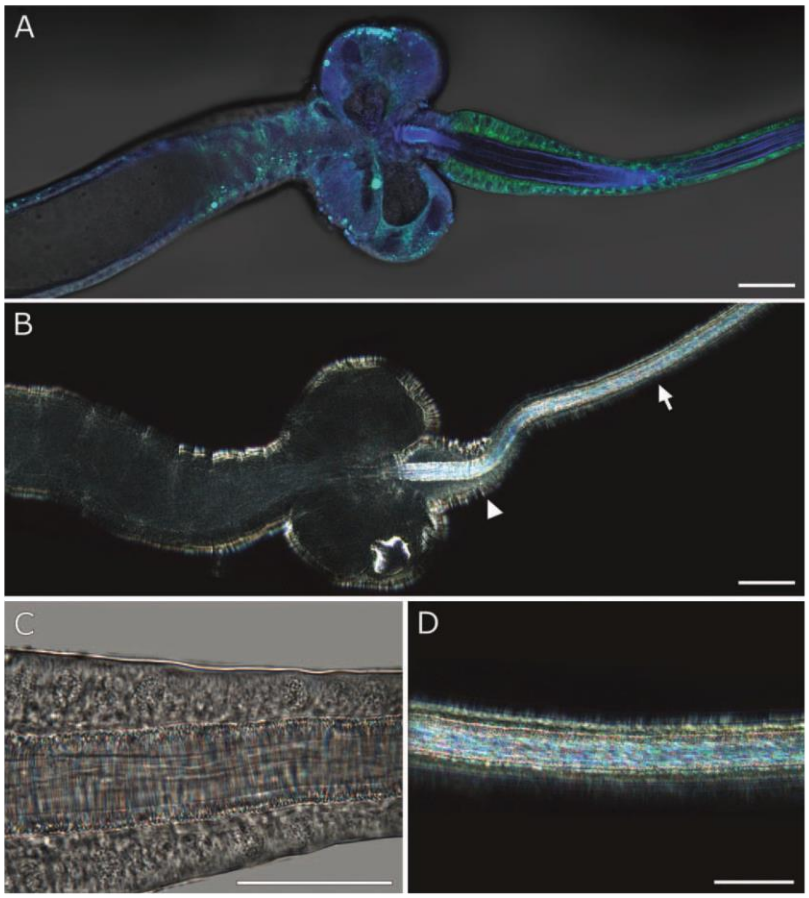


**FIGURE 10** (A) Confocal autofluorescence and DIC images of *Rhyacophila* silk gland at the transition from the gland's middle storage region to the anterior lumen. Gland tissue is autofluorescent (488 nm excitation and 508 nm emission). Organized structure at center of bulbous region and cuticle downstream of gland taper is strongly autofluorescent under 405 nm excitation (emission: 461 nm, blue). (B) Polarized microscope light image of *Rhyacophila* silk gland transition. (C) DIC image of *Rhyacophila* silk gland region indicated by arrowhead in B. (D) Region of *Rhyacophila* conducting channel under polarized light indicated by arrow in B. Scale bars in (A) and (B) 100 $\mu$m. Scale bars in (C) and (D) are 50 $\mu$m.

## DISCUSSION

### Underwater Adhesion Mechanisms

Caddisfly larvae construct elaborate composite underwater structures with their adhesive silks, including underwater capture webs reminiscent of orb-weaving spider webs (Figure 1B). The sophisticated underwater architectural applications distinguish caddisfly larvae from the terrestrial moths and butterflies, which construct comparatively simple silk cocoons for pupation on dry land. Setting the behavioral and architectural differences aside, what chemical differences between terrestrial and aquatic silks account for underwater adhesiveness of the later? One distinction is the lack of conclusive evidence for a sticky outer sericin layer, similar to that of the silkworm, which can be extracted with boiling water. Instead, there is a poorly characterized peripheral layer that was not extractable even under harsh conditions.[10]

A second major distinction between the aquatic and terrestrial silks is the presence of surface exposed phosphates in caddisfly silks, which have not been observed in moth

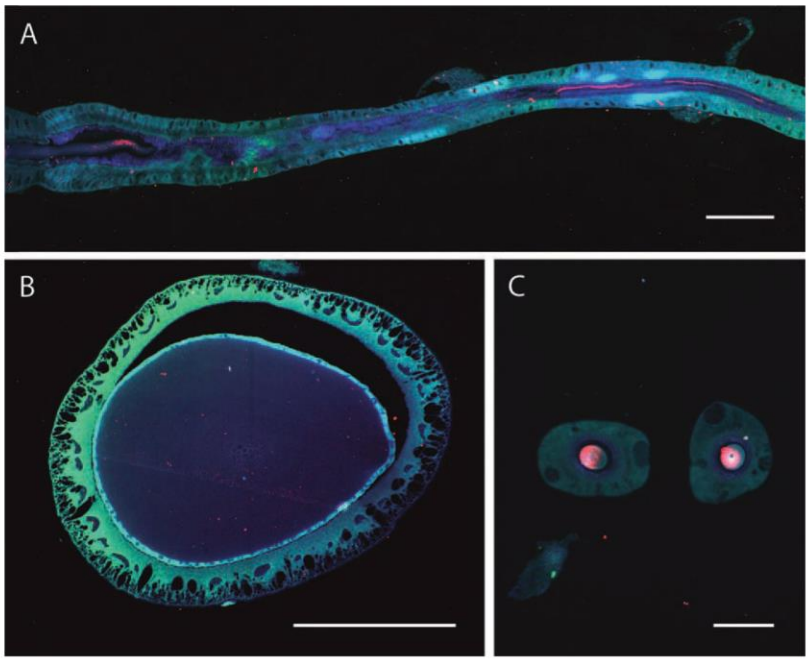


**FIGURE 11** (A) Longitudinal section of embedded *H. consimilis* silk gland at the transition from the gland's middle storage region to the anterior lumen. Gland tissue and cuticle lining are autofluorescent when excited with 405 nm (blue) and 488 nm (green) frequencies. Labeling α-phosphoserine antibody (red) under 650 nm excitation (Scale bar is 100 μm). (B) Transverse section of *A. grandis* silk gland posterior to bulbous feature at transition (Scale bar is 200 μm). (C) Transverse sections of *A. grandis* silk gland through the anterior conducting lumen (Scale bar is 50 μm).

silks.[11,21] The presence of peptidyl phosphate has now been confirmed for all three suborders of Trichoptera and is therefore an adaptation to aquatic life shared across the order. Polymeric phosphates are particularly well suited as adhesion promoters in aquatic environments. Phosphate side chains can displace water, hydroxides, and other surface-associated ions to form direct inner-sphere coordination complexes on metal-oxide surfaces.[28,29] Phosphates can also form indirect ternary complexes with metal ions coordinated with surface-associated polymers, as illustrated by the routine isolation of phosphopeptides in the laboratory by immobilized metal affinity chromatography.[30] In natural aquatic environments, most of the Fe and Al ions are bound by surface-associated biopolymers, such as the mixed polyelectrolytes known as humic and fulvic acids.[31] Such layers would serve as a primer for strong adsorption of polyphosphorylated proteins. In short, post-translational phosphorylation of serine provides a multitude of potential interfacial adhesion mechanisms. Indeed, several aquatic organisms, marine and freshwater, from diverse phyla exploit peptidyl phosphate in their underwater adhesives, presumably to promote interfacial adhesion.[32–34] As Lepidoteran silks contain a significant mol% of serines, one of the key molecular adaptations of a terrestrial ancestor silk to aquatic environments could have been a change as simple as a rogue kinase phosphorylating H-fibroin serines.

## Silk Fiber Nanostructure

The structure of the caddisfly silk fiber also contributes to underwater adhesion. Whereas other aquatic species generally apply aliquots of fluid adhesive to adherends that are in direct contact, or immediately brought into direct contact, caddisfly larvae apply their adhesive with a fiber backing, like tape, that can span large gaps between adherends (Figure 4). The design of the tape maximizes surface contact area; lateral associations between subfibrils are weaker than the longitudinal associations, a feature that provides plasticity for the elliptical fibers to flatten onto the surface (Figure 5D). Fine perpendicular projections from the fibers, which may be part of the thin peripheral layer described by Engster,[10] allow the tape to conform to even nanoscopic surface topographies to maximize the interfacial contact area. Peeling forces on the

silk fibers are proportional to only one dimension, the width of the fiber in contact with the surface; another reason flattening of the fiber into a tape was an adaptive advantage. As well as adhering to the substrate surface, individual silk fibers adhere to one another, fusing into large fiber bundles with reinforcing cross struts. This hierarchical arrangement, into bundles, increases the tensile strength of the connecting elements. As a result, the toughness of the construction may be considerably higher than would be predicted from mechanical measurements of single caddisfly silk fibers.[20]

## Silk Gland Structure and Fiber Formation

The middle storage region of the caddisfly larval silk gland contains stockpiles of silk fiber precursors that appear to be separated into two bicontinuous phases (Figure 9). Similar phenomena have been observed in moth silk glands and attributed to the organization of polyamphiphilic silk proteins into liquid crystals.[23,24] Caddisfly H-fibroin by comparison, is a polyelectrolyte containing alternating blocks of negatively charged $(pSX)_4$ motifs with positively charged arginine-rich motifs (Figure 2). Intermolecular electrostatic association between H-fibroins could drive formation of polyelectrolyte complexes followed by complex coacervation of the silk fiber precursors into the two bicontinuous phases observed in the silk gland lumen, one phase comprising a highly concentrated, yet fluid network of silk precursors, the other a dilute excluded aqueous phase. The biphasic storage of silk fiber precursors as complex coacervates could play an important role in fiber formation. The fiber precursors are concentrated into a high-viscosity fluid phase interspersed throughout a low viscosity fluid phase. Structural rearrangement of the phases could lead to dramatic shear thinning to facilitate extrusion of the silk fiber precursors. Bicontinuous phases have been observed in synthetic complex coacervates that also exhibit discontinuous flow behavior with sudden drops in viscosity at critical shear rates.[35,36]

The "bulbous prominence" of the caddisfly larval silk gland, occurring at the transition from the gland's middle storage region to the anterior lumen, appeared to be the critical region where silk fiber precursors were reorganized into insoluble fibers. In *Rhyacophila*, the bulbous anatomy was especially pronounced (Figures 10A and 10B). A dramatic drawdown occurred through this region as the lumen diameter decreased 10fold as it transitioned into the conducting channel. The steepness of the drawdown and hence the shear rate on silk precursors flowing through the transition zone varied significantly between species. Unique secretory cells lined the lumen in the transition zone and visibly secreted their granular contents into the gland lumen (Figure 8), which suggested the chemical composition of the silk precursors changed immediately before, during, and/or immediately after fiber formation. The presence of a highly branched tracheole terminating at the bulbous prominence suggests the tissue in this region is highly metabolically active. The conducting channel was circularly wound with a refringent cuticle. This anatomical feature is shared by species across the superorder Amphiesmenoptera.[4] The entrance to the conducting channel appeared to be especially important in fiber formation since shortly after entering the conducting channel the silk was fibrous and refringent. This region marked the beginning of an internal drawdown where the forming silk fiber pulled away from the lumen wall leaving a noticeable gap (Figure 8B). This was similar to the internal drawdown taper observed in the anterior narrowing of the spider and silkworm glands.[23,37] The role of the transition site in fiber formation merits further physiological and structural investigation.

The long-range structural order within the individual subfibrils, after passage through the transition zone, is evident from the refringence of extruded silk fibers (Figure 6). Optical anisotropy is a hallmark feature of silks in general.[37–39] There is a general agreement that the long-range ordered structures of both moth and spider silks arise from semicrystalline networks of antiparallel $\beta$-sheets within extensible glycine-rich matrices.[13] The conspicuous absence of alanines in caddisfly H-fibroins and the presence of repeating $(pSX)_4$ motifs, in which X tends to be hydrophobic, suggested a divergence from this shared molecular architecture.[11] Phosphorylated serines destabilize $\beta$-sheets due to charge repulsion.[40] However, the presence of divalent $Ca^{2+}$ ions could stabilize $(pSX)_4$ $\beta$-sheets.[25] Further, $Ca^{2+}$ could promote stacking of the $\beta$-sheets into semicrystalline domains (Figure 12B).

Formation of the silk fiber, in this model, would be highly dependent on the local pH and $Ca^{2+}$ concentration within the lumen, which would provide a biochemical trigger mechanism and driving force for large-scale structural reorganization of silk fiber precursors. Modulation of pH and $[Ca^{2+}]$ within the bulbous region, perhaps by the secretory cells lining the region, combined with shearing forces through the transition to anterior gland lumen, could create the long-range order within nanofibrils that give rise to the observed optical anisotropy. Gradients of pH and divalent cations have been reported in the *B. mori* silk gland and ascribed a role in the silk I to silk II transition as well as fiber insolubilization.[41–43] The effect of similar small ion gradients in the lumen of the caddisfly silk gland could have pronounced effects due to the comparatively high content of charged residues.[42]

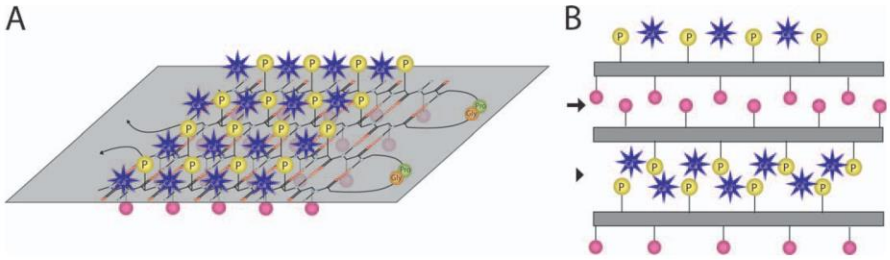


**FIGURE 12** A molecular model illustrating a possible mechanism of crystalline domain formation using the $(pSX)_4$ motifs conserved across all three Trichopteran suborders. (A) Two (pSX) motifs, equidistance from a central proline-glycine bend (Gly-Pro: green, and orange spheres), form an antiparallel $\beta$-sheet with another similar (pSX) pair. Phosphorylated serine residues (pS: yellow spheres) oriented upward are stabilized by divalent calcium ($Ca^{2+}$: blue stars) and hydrophobic domains (X: magenta spheres) are oriented downward. (B) Stacking of the $\beta$-sheets occurs from alternating hydrophobic association of the hydrophobic faces (arrow) and $Ca^{2+}$ stabilized phosphate face association (arrow head).

Two seemingly inconsistent roles for phosphoserine have been proposed. As a surface-exposed adhesion promoter, it may not play a role as the organizer of internal semicrystalline domains. Likewise, if phosphate is buried in a stacked $\beta$-sheet domain (Figure 12), it may not be accessible at the fiber surface as an interfacial adhesion promoter. Perhaps phosphoserine plays both roles. Immunolabeling suggests the phosphate becomes more surface accessible after silk fiber formation, which further suggests that at least some of the $(pSX)_4$ motifs may be reorganized as the silk precursors are squeezed through the die at the beginning of the conducting channel (Figure 7). The phosphoserine may be a useful probe for structural changes during fiber formation in future experiments.

Shear-induced fiber formation was first proposed in 1951[44] and is still an important feature of fiber assembly models. More recent models posit that shearing of liquid crystal silk fiber precursor drives protein alignment and staggered lateral association between H-fibroins with alternating hydrophobic and hydrophilic sequence blocks. A similar model for caddisfly silk fiber formation was proposed with alternating oppositely charged sequence blocks taking the place of alternating hydrophilic and hydrophobic blocks.[11] These models may not reconcile with the observed hierarchical organization of silk fibers as bundles of nanofibrils, which in turn are a chain of roughly spherical globular subunits (Figure 5).[27,45] Subunit interactions running longitudinal to the subfibrils appeared to be stronger than lateral interactions between subunits. Is there a head-to-tail organization of asymmetric subunits, like the tubulin subunits of microtubules, for example, that creates an overall fiber polarity? If so, polarized organization of the nanofibrils could have important implications for fiber assembly models.

## CONCLUSIONS

Caddisfly larvae build elaborate structures underwater with nanostructured tape. This is a unique strategy among the underwater bioadhesives that have been characterized in detail. Understanding how insoluble fibers are formed underwater from soluble precursors could lead to new approaches to form useful silk fiber analogs. Phase separation of polyelectrolytes, or polyampholytes, into complex coacervates, followed by shearing through a narrow orifice may be part of the solution.

The authors thank Dr. Christy Geraci for help with identifying the caddisfly species used in this work.

## REFERENCES

1. Merritt, R. W.; Cummins, K. W. An Introduction to the Aquatic Insects of North America; Kendall/Hunt Pub. Co.: Dubuque, Iowa, 2008.
2. Wiggins, G. B.; Canada Institute for Scientific and Technical Information; Royal Ontario Museum. Caddisflies: The Underwater Architects; University of Toronto Press: Toronto, 2004.
3. Morse, J. C. Ann Rev Entomol 1997, 42, 427–450.
4. Sehnal, F. Int J Insect Morphol 1990, 19, 79–132.
5. Engster, M. S. Morphology 1976, 183–212.
6. Beams, H. W.; Sekhon, S. S. Z Zellforsch Mikrosk Anat 1966, 72, 408–414.
7. Cianficconi, F.; Moretti, G. Aquat Insects 2000, 22, 58–65.
8. Tszydel, M.; Sztajnowski, S.; Michalak, M.; Wrzosek, H.; Kowalska, S.; Krucinska, I.; Lipp-Symonowicz, B. Fibres Text East Eur 2009, 17, 7–12.
9. Spanhoff, B.; Schulte, U.; Alecke, C.; Kaschek, N.; Meyer, E. I. Eur J Entomol 2003, 100, 563–570.
10. Engster, M. S. Cell Tissue Res 1976, 169, 77–92.
11. Stewart, R. J.; Wang, C. S. Biomacromolecules 2010, 11, 969–974.

12. Yonemura, N.; Mita, K.; Tamura, T.; Sehnal, F. J Mol Evol 2009, 68, 641–653.
13. Bini, E.; Knight, D. P.; Kaplan, D. L. J Mol Biol 2003, 335, 27–40.
14. Shimura, K.; Kikuchi, A.; Ohtomo, K.; Katagata, Y.; Hyodo, A. J Biochem 1976, 80, 693–702.
15. Yonemura, N.; Sehnal, F.; Mita, K.; Tamura, T. Biomacromolecules 2006, 7, 3370–3378.
16. Sehnal, F.; Zurovec, M. Biomacromolecules 2004, 5, 666–674.
17. Case, S. T.; Powers, J.; Hamilton, R.; Burton, M. J. ACS Symp Ser 1994, 544, 80–90.
18. Porter, D.; Vollrath, F. Adv Mater (Weinheim, Ger) 2009, 21, 487–492.
19. Wang, Y.-J.; Sanai, K.; Wen, H.-X.; Zhao, T.-F.; Nakagaki, M. Mol Biol Rep 2010, 37, 2885–2892.
20. Brown, S. A.; Ruxton, G. D. J N Am Benthol Soc 2004, 23, 771–779.
21. Chen, W. -Q.; Priewalder, H.; John, J. P. P.; Lubec, G. Proteomics 2010, 10, 369–379.
22. Galler, R.; Rydlander, L.; Riedel, N.; Kluding, H.; Edstroem, J. E. Proc Natl Acad Sci USA 1984, 81, 1448–1452.
23. Vollrath, F.; Knight, D. P. Nature (London, U K) 2001, 410, 541–548.
24. Jin, H.-J.; Kaplan, D. L. Nature (London, U K) 2003, 424, 1057–1061.
25. Strzelecki, J. W.; Strzelecka, J.; Mikulska, K.; Tszydel, M.; Balter, A.; Nowak, W. Cent Eur J Phys 2011, 9, 482–491.
26. Federle, W.; Brainerd, E. L.; McMahon, T. A.; Holldobler, B. Proc Natl Acad Sci USA 2001, 98, 6215–6220.
27. Miller, L. D.; Putthanarat, S.; Eby, R. K.; Adams, W. W. Int J Biol Macromol 1999, 24, 159–165.
28. Stumm, W.; Morgan, J. J. Aquatic Chemistry: Chemical Equilibria and Rates in Natural Waters; Wiley: New York, 1996.
29. Stewart, R. J.; Ransom, T. C.; Hlady, V. J Polym Sci Part B: Polym Phys 2011, 49, 757–771.
30. Kokubu, M.; Ishihama, Y.; Sato, T.; Nagasu, T.; Oda, Y. Anal Chem 2005, 77, 5144–5154.
31. Snoeyink, V. L.; Jenkins, D. Water Chemistry; Wiley: New York, 1980.
32. Waite, J. H.; Qin, X. Biochemistry 2001, 40, 2887–2893.
33. Stewart, R. J.; Weaver, J. C.; Morse, D. E.; Waite, J. H. J Exp Biol 2004, 207, 4727–4734.
34. Flammang, P.; Lambert, A.; Bailly, P.; Hennebert, E. J Adhes 2009, 85, 447–464.
35. Kaur, S.; Weerasekare, G. M.; Stewart, R. J. ACS Appl Mater Interfaces 2011, 3, 941–944.
36. Dubin, P. L.; Li, Y.; Jaeger, W. Langmuir 2008, 24, 4544–4549.
37. Asakura, T.; Umemura, K.; Nakazawa, Y.; Hirose, H.; Higham, J.; Knight, D. Biomacromolecules 2007, 8, 175–181.
38. Magoshi, J.; Magoshi, Y.; Nakamura, S. J Appl Polym Sci: Appl Polym Symp 1985, 41, 187–204.
39. Magoshi, J.; Magoshi, Y.; Nakamura, S. Polym Commun 1985, 26, 60–61.
40. Winkler, S.; Wilson, D.; Kaplan, D. L. Biochemistry 2000, 39, 12739–12746.
41. Foo, C. W. P.; Bini, E.; Hensman, J.; Knight, D. P.; Lewis, R. V.; Kaplan, D. L. Appl Phys A: Mater Sci Process 2006, 82, 223–233.
42. Zhou, L.; Chen, X.; Shao, Z.; Huang, Y.; Knight, D. P. J Phys Chem B 2005, 109, 16937–16945.
43. Azuma, M.; Ohta, Y. J Exp Biol 1998, 201, 479–486.
44. Mercer, E. H. Nature 1951, 168, 792–793.
45. Shen, Y.; Johnson, M. A.; Martin, D. C. Macromolecules 1998, 31, 8857–8864.

*Reviewing Editor: David Nate Breslauer*

# CHAPTER 3

## SELF-TENSIONING AQUATIC CADDISFLY SILK: $Ca^{2+}$-DEPENDENT STRUCTURE, STRENGTH, AND LOAD CYCLE HYSTERESIS

Reproduced with permission from, Nicholas N. Ashton, Daniel R. Roe, Robert B. Weiss, Thomas E. Cheatham III, and Russell J. Stewart, Self-Tensioning Aquatic Caddisfly Silk, $Ca^{2+}$-Dependent Structure, Strength, and Load Cycle Hysteresis, *Biomacromolecules,* 2013, 14, 3668-3681. 

Author Contributions: N.N.A. gathered and maintained caddisfly larvae in the lab, constructed the materials test system, performed single fiber mechancal tests, purified silk gland RNA, prepared silk samples for microscopy, and performed flow chamber experiments. D.R.R. and T.E.C. performed molecular dynamic simulations. R.B.W. assembled the H-fibroin N-terminal sequence. R.J.S. and N.N.A. designed the experiments, interpreted the results, and prepared the manuscript. All authors proofread the manuscript.

BioMACROMOLECULES

Article

pubs.acs.org/Biomac

# Self-Tensioning Aquatic Caddisfly Silk: $Ca^{2+}$-Dependent Structure, Strength, and Load Cycle Hysteresis

Nicholas N. Ashton,[†] Daniel R. Roe,[‡] Robert B. Weiss,[§] Thomas E. Cheatham, III,[‡] and Russell J. Stewart*,[†]

Departments of [†]Bioengineering, [‡]Medicinal Chemistry, and [§]Human Genetics, University of Utah, Salt Lake City, Utah 84112, United States

Supporting Information

**ABSTRACT:** Caddisflies are aquatic relatives of silk-spinning terrestrial moths and butterflies. Casemaker larvae spin adhesive silk fibers for underwater construction of protective composite cases. The central region of *Hesperophylax* sp. H-fibroin contains a repeating pattern of three conserved subrepeats, all of which contain one or more $(SX)_n$ motifs with extensively phosphorylated serines. Native silk fibers were highly extensible and displayed a distinct yield point, force plateau, and load cycle hysteresis. FTIR spectroscopy of native silk showed a conformational mix of random coil, $\beta$-sheet, and turns. Exchanging multivalent ions with $Na^+$ EDTA disrupted fiber mechanics, shifted the secondary structure ratios from antiparallel $\beta$-sheet toward random coil and turns, and caused the fibers to shorten, swell in diameter, and disrupted fiber birefringence. The EDTA effects were reversed by restoring $Ca^{2+}$. Molecular dynamic simulations provided theoretical support for a hypothetical structure in which the $(pSX)_n$ motifs may assemble into two- and three-stranded, $Ca^{2+}$-stabilized $\beta$-sheets.

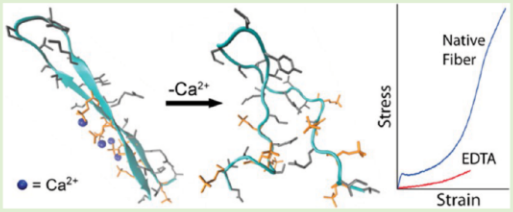


## INTRODUCTION

Caddisflies are an insect order (Trichoptera) represented by over 12000 species worldwide in three suborders.[1] The larval stages are spent feeding in freshwater streams, lakes, and wet grasslands. The success of the order in penetrating diverse freshwater habitats is due, at least in part, to the inventive underwater use of silk by their larvae. Casemaker larvae (suborder Integripalpia) are mobile foragers that use their silk-like adhesive tape to assemble transportable composite cases around their soft bodies with adventitiously gathered leaves, sticks, or stones in species-specific architectures (Figure 1A). Retreat builders (suborder Annulipalpia) assemble stationary composite shelters in fast flowing streams that are further elaborated with nets suspended in the current for capturing food. To complete their lifecycle, the cases or retreats are sealed to become closed pupation chambers. Winged adults emerge from the cases and race to the surface for a short season of terrestrial mating (Figure 1B).

Trichoptera is considered a sister order of Lepidoptera, which includes silk-spinning terrestrial moths and butterflies.[2] As expected from their shared ancestry, caddisfly silks share several general features with terrestrial moth silks. In both orders, the silks originate from a pair of modified salivary glands and are spun as a pair of fused fibers, each of which is a bundle of nanoscopic subfibrils.[3−6] The fibers are predominantly composed of H- and L-fibroin proteins (>300 and ~25 kg/mol, respectively). Conservation of the positions of H- and L-fibroin cysteine residues across the orders suggests the caddisfly fibroins, like silkworm moth silk,[7] may be covalently linked in a 1:1 ratio through disulfide bonds.[8,9] The H-fibroins of both orders have long, highly repetitive central regions flanked by short nonrepetitive termini. Silkworm H-fibroins contain blocks of poly(GAGAGS) that form ordered $\beta$-sheet domains, interspersed with order-disrupting blocks.[10,11] Caddisfly H-fibroins have a repetitive blocky structure of short conserved subrepeats.[8,9] The subrepeats vary in sequence and arrangement between the three caddisfly suborders, but one common feature is the presence of $(SX)_n$ motifs, where S is serine, X is usually an aliphatic amino acid larger than alanine, and $n$ is 2−6.[6,8,9,12]

Despite the general similarities, the differences between aquatic caddisfly and terrestrial moth silks are profound and may reflect molecular adaptations necessary for spinning and deployment of fibers underwater versus in air. The crystalline arrangement of poly(GAGAGS) $\beta$-domains within an extensible unordered matrix contributes to the strength and toughness of the terrestrial moth silk fibers, a structural theme shared with terrestrial spider silks.[13] Considering this key structural role of the alanine-rich $\beta$-domains in dry silks, one striking caddisfly divergence is that alanines comprise less than 5 mol % of retreat-builder H-fibroin residues and are nearly absent in casemaker H-fibroins (Figure 2).[8,14] Yet, early X-ray diffraction patterns of caddisfly silk fibers are consistent with an ordered crystalline component that was interpreted as a

Received: July 16, 2013
Revised: September 3, 2013
Published: September 19, 2013

  

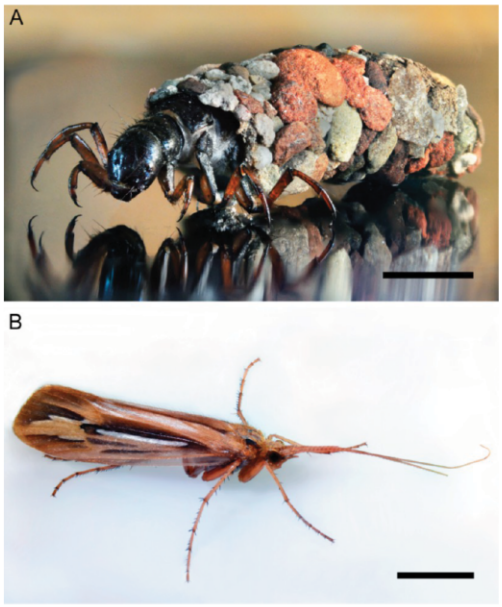


**Figure 1.** The caddisfly *Hesperophylax* sp. (A) The larvae are mobile foragers. The case protecting its body was constructed with silk and stones gathered adventitiously from the stream bed. Scale bar = 5 mm. (B) An *Hesperophylax* sp. adult. Scale bar = 5 mm.

repeating structure of three superposed $\beta$-sheets.[14,15] More recent X-ray diffraction studies of silk from the casemaker, *Hesperophylax* sp., were also consistent with ordered $\beta$-sheet structures comprising 7−8% of the fiber mass.[16]

A second distinguishing feature of caddisfly silks is extensive phosphorylation of H-fibroins and the presence of an approximately stoichiometric ratio of metals to phosphorus, predominated by calcium.[6] The phosphorus occurs as phosphate groups on the serines in the H-fibroin $(SX)_n$ motifs of *Hesperophylax* sp.[5,6] Phosphorylation of silk serine residues has been verified in species from each of the three suborders[5] and specifically identified on the H-fibroin $(SX)_n$ motifs of the net-spinning caddisfly *S. marmora*, demonstrating that the adaptation is shared across the caddisfly suborders.[17] The high negative charge density contributed to the H-fibroins by phosphate groups is accompanied by a high proportion of basic residues, which are nearly absent in terrestrial silks.[14] As a result, caddisfly H-fibroins are polyampholytic.[6]

Caddisfly silk fibers adhere strongly underwater to the case or retreat construction materials, flattening on the surface to increase contact area, and to one another to form suspended fiber bundles.[5,6] Phosphates can form several types of water-resistant bonds, which makes them highly effective and versatile adhesion promoters in wet environments.[18,19] The presence of phosphates in several natural underwater adhesives suggests nature has exploited this wet bonding versatility.[20] It followed that a logical function of the phosphate groups in caddisfly silk may be to promote interfacial adhesion in the submerged environment of the caddisfly larvae if they are exposed on the fiber surface. On the other hand, the alternating pattern of phosphoserines and hydrophobic residues in the $(pSX)_n$ domains and the presence of nearly stoichiometric $Ca^{2+}$ ions suggested a possible structural role in novel $Ca^{2+}$-stabilized $\beta$-sheet structures, which could also explain the reported $\beta$-crystallinity of caddisfly silk.[5,6] In support of the structural role, solid state $^{13}C$ and $^{31}P$ NMR studies of $^{13}C$-labeled *Hesperophylax* sp. silk were consistent with $Ca^{2+}$-stabilized phosphoserine $\beta$-sheet structures.[16] The roles are not mutually exclusive; phosphates may function dichotomously as interfacial adhesion promoters and in H-fibroin higher-order structure, contributing to adaptive mechanical properties of the silk fibers.

Our interest in caddisfly silk stems in part from its potential as a design resource for sophisticated synthetic materials. As a model material, casemaker larval silk uniquely lies at the intersection of two categories of natural materials that have inspired extensive efforts to replicate their properties in synthetic materials, underwater adhesives, and tough lightweight structural fibers: silks.[21−26] Caddisfly silk is also interesting as an example of molecular adaptation of structural biological materials. Comparison of caddisfly silk to terrestrial moth silks may provide a glimpse into modifications in the composition, molecular structure, and fiber formation processes of an ancestral silk to function in aquatic habitats (or vice versa). Toward these long-range objectives, the goal of the research described here was to further explore the role of phosphoserines and metal ions in caddisfly silk mechanical properties and structure. Assembly of the N- and C-terminal sequences of *Hesperophylax* sp. H-fibroin allowed identification of phosphopeptides corresponding to additional $(pSX)_n$ motifs using tandem mass spectrometry. The role of metal ions in silk mechanical properties and structure were evaluated by exchanging divalent metal ions with sodium, followed by single fiber mechanical analysis in a micromaterials test system, microscopic analysis of macroscale fiber structure, and infrared absorbance spectroscopy to investigate secondary structures. The theoretical stability of proposed $Ca^{2+}$-stabilized phosphoserine $\beta$-domains was evaluated using molecular dynamic simulations.

## ■ EXPERIMENTAL SECTION

***Hesperophylax* sp. Silk Gland Transcriptome Sequencing.** Approximately 20 gland pairs were dissected from fifth instar *Hesperophylax* sp. larvae gathered from Red Butte Creek in Salt Lake City, Utah, U.S.A. The glands were immediately rinsed in RNase free water, frozen in liquid nitrogen ($LN_2$), and ground in $LN_2$ with a mortar and pestle. Total RNA was isolated from ground tissue (30 $\mu$g) with an RNeasy kit (Qiagen, Venlo, Netherlands) following the manufacturer's instructions. Total RNA sample quality was analyzed using an Agilent Bioanalyzer RNA NanoChip before construction of an Illumina sequencing library using an Illumina TruSeq Stranded mRNA sample prep kit (Illumina, San Diego, CA) at the University of Utah Microarray and Genomic Analysis Core Facility. The quality and size range of the library created from oligo-dT selected mRNA was analyzed on an Agilent Bioanalyzer DNA chip and quantified by qPCR before 101 bp paired-end sequencing on an Illumina HiSeq 200 instrument.

**De Novo H-Fibroin Gene Assembly.** *Hesperophylax* sp. silk gland transcriptome Fastq files were trimmed for adapter sequence and filtered for low-quality reads using the FASTX-Toolkit (http://hannonlab.cshl.edu/fastx_toolkit). Approximately 42 million Illumina paired-end reads were assembled de novo using the Trinity software package[27] running default parameters and with -kmer_method jellyfish. A single Trinity contig (comp23970_c0_seq1, 465 nt.) was identified that aligned with 85% nucleotide identity to positions 1263−1711 from the partial cds and 3′ UTR of the *Limnephilus decipiens* H-fibroin mRNA (GenBank: AB214509.1). This C-terminal region of


**Figure 2.** Partial *Hesperophylax* sp. H-fibroin sequence. The continuous sequences are arranged to highlight the pattern of conserved D, E, and F subrepeats. The shared arginine-rich motif with a central proline is highlighted in gray. $(pSX)_n$ motifs are underlined. The hypothetical $[(pSX)_4]_2$ $\beta$-hairpin sequence is highlighted in turquoise. (A) N-terminus. Bold italics indicates the secretion signal peptide. (B) C-terminus; * = stop codon. (C) Schematic representation of the irregularly repeating pattern of conserved subrepeats.

AB214509.1 includes the stop codon at position 1552−1554 and the 3′ UTR from positions 1553−1711. A second Trinity contig (comp24865_c0_seq1, 405 nt.) aligned with 86−87% nucleotide identity to multiple N-terminal segments of *L. decipiens* H-fibroin (AB214509.1), including positions: 1−197, 172−409, 454−587, 562−793, 790−1094, and 1069−1298. Transcript abundance for these two contigs was estimated using the RSEM method included in the Trinity package: comp24865_c0_seq1 and comp23790_c0_seq1 accounted for ∼2 and ∼0.25% of the total RNA-Seq reads, respectively. Comp23970_c0_seq1 was assembled in the 5′ direction using 101 nt. collapsed reads. A collapsing algorithm from the FASTX-toolkit was used with a minimum read-depth of 200 required for inclusion in the directed assembly. Each assembly step required minimal extension (maximal overlap) with exact matching in the overlap. The contig was extended in 261 steps from the starting size of 465 nt. to 2390 nt. Estimating from the RNA-Seq depth of coverage, there are 12−18 DEF repeat units, which corresponds to a full transcript length in the 8 kb range.

**Tandem Mass Spectrometry (MS/MS) of Silk Proteins.** MS/MS analysis of tryptic peptides of silk proteins isolated from *Hysperophylax* sp. silk glands was described previously.[6] The caddisfly species in the earlier report was mis-identified as *Brachycentrus echo*; the local casemaker caddisflies used in the earlier and present studies (Figure 1) are in the genus *Hysperophylax*, suborder Integripalpia. The species has not been identified. Briefly, silk proteins isolated from dissected silk glands were heat denatured in 25 mM ammonium bicarbonate, immediately cooled on ice, and digested with a 1:25 ratio of trypsin to silk protein for 2 h at 37 °C. Immobilized metal affinity chromatography (IMAC) was used to enrich for phosphopeptides in a portion of the digested silk sample. Samples with and without IMAC enrichment were analyzed by LC/MS/MS in a LTQ-FT hybrid mass spectrometer (ThermoElectron Corp). Primary peptide molecular masses were determined by FT-ICR and peptide sequences by collision-induced dissociation in the linear ion trap of the LTQ-FT hybrid mass spectrometer. *Hysperophylax* sp. H-fibroin peptides were identified in the mass spec databases by searching the assembled ends of the *Hysperophylax* sp. H-fibroin DNA sequence (Figure 2) using the Mascot search engine (ver. 2.2.1, Matrix Science). Possible phosphorylation on S, T, and Y were included in the search. Mascot thresholds were set as primary mass errors of <3 ppm, MS/MS ion scores >20, and expect values <1.

**Elemental Analysis.** Silk fibers were manually harvested from Teflon blocks using previously described methods[5] and washed extensively with DI $H_2O$. Each measurement was performed in triplicate with silk from distinct larvae. Native silk samples were washed three times with DI $H_2O$ and lyophilized. Multivalent ion depleted samples were prepared in excess 1 mM EDTA buffered with 4.8 mM $NaHCO_3$ (pH 8.2 with NaOH) for 30 min. The samples were then washed three times in excess DI $H_2O$ and lyophilized. Calcium was restored by removing the EDTA solution, and washing with excess 1 mM $CaCl_2$ in 4.8 mM $NaHCO_3$ (pH 8.2 with NaOH) for at least 30 min, followed by three washes in excess DI $H_2O$ and lyophilization. After lyophilization, silk samples were dissolved in 40% nitric acid and analyzed for elements by ICP-OES (PerkinElmer, Optima 3100XL). Elements were quantified by comparison to standard curves prepared with commercial mixed metal standards (PerkinElmer).

**Mechanical Testing.** Fifth instar *Hesperophylax* sp. were collected from upper Red Butte creek (Salt Lake County, UT, U.S.A.) in the summer prior to pupating. Silk was harvested as previously described.[5] Under a dissection microscope, using a pair of fine forceps, the ends of single ∼3 mm silk fibers were attached to stainless steel (0.85 mm thick) fixtures of a custom microscale materials test system with a small amount of two-part epoxy. Fibers were loaded and unloaded at 0.033 $s^{-1}$ strain rate. The fixtures and mounted silk fibers were fully submerged in the test solution during mechanical testing. Test solutions consisted of either 1 mM $CaCl_2$, 5 mM $CaCl_2$, or 1 mM $Na^+$ EDTA each buffered in 4.8 $NaHCO_3$ (pH 8.2 with NaOH). The movable fixture was controlled with a Z812-motorized DC servo actuator (ThorLabs), attached to a 411-05S stage (Newport) using APTserver software (ThorLabs). The stationary fixture was connected to an FT03 force transducer (Grass Technologies) with a working range of 2 mg to 50 g. The system was calibrated with a 0.45 g/cm spring. A power supply and amplifier (A CP 122C, Grass Technologies) was used to power the bridge element and condition the signal with a −18 dB low pass filter. The analog signal was digitized with a NI USB-6008 data acquisition box and logged using SignalExpress software at 1 kHz (National Instruments). The data was processed and plotted using Matlab software (MathWorks). The fiber diameters could not be measured for each fiber before mechanical tests. To report the force−extension data as engineering stress−strain for convenient comparison to other silk fibers, the wide diameter of five hydrated native fibers from the same animal as those used for mechanical tests were measured under 100× magnification. Likewise, the diameter of swollen EDTA-treated fibers were measured to report engineering stress−strain in EDTA. The average fiber cross-sectional area was estimated, assuming paired cylindrical fibers of equal size. Stress was calculated by dividing force by the estimated average cross-sectional area.

**Silk Fiber Microscopy.** A single fiber was harvested from fifth instar *Hesperophylax* sp. using previously described methods.[5] The fiber was first loaded on the micromaterials test system described above and held taut while an isolated segment in the middle was anchored to the surface of a cover glass (22 × 40 mm) with two part epoxy on either end of the isolated segment. To accomplish this, two small quantities of epoxy were placed on a coverslip with a fine needle. The coverslip was then inverted and placed face down on the taut fiber thus submerging a portion of each end of the fiber in either of the two dabs of epoxy. Once cured, the coverslip was removed, breaking the fiber connection with the materials test system. Two strips of double-sided tape (62.5 $\mu$m thick) were placed parallel at ∼5 mm spacing on either side of the immobilized silk fiber. A second 1 oz cover glass (22 × 22 mm) was placed on the parallel double-sided tape to create a flow chamber around the isolated fiber. Chamber solutions were exchanged by adding a drop of solution to one side the flow chamber while wicking solution from the other side with filter paper. All fibers observed were submerged in either 1 mM $Ca^{2+}$ or 1 mM EDTA buffered with 4.8 mM $NaHCO_3$ (pH 8.2 with NaOH). DIC images of the silk were taken with a Zeiss Axiovert 100 microscope using a Zeiss Plan-Neofluar 100× oil immersion objective and a XLMC camera (Dage-MTI, Michigan City, IN). Images were captured using Exponent software (Dage-MTI). The fiber was first observed in simulated creek water (1 mM $Ca^{2+}$, 4.8 mM $NaHCO_3$, pH 8.2) followed by removing the $Ca^{2+}$ with excess 1 mM EDTA solution, then adding back excess 1 mM $Ca^{2+}$ solution. Each image collected is of the same fiber in the same location. Background images were collected from an empty region of the flow chamber. Matlab (MathWorks) was used to subtract background and adjust contrast of the DIC images.

Scanning electron micrographs of silk harvested from *Hesperophylax* sp. were obtained with a Quanta 600 FEG SEM (FEI Company, Hillsboro, OR). Micrographs were collected using an accelerating voltage of 5 KeV with a current of 0.22 nA. Fibers harvested from the same animal were divided into three groups and treated with (1) simulated creek water (1 mM $Ca^{2+}$) for 15 min; (2) with 1 mM $Ca^{2+}$ followed by 1 mM EDTA (pH 8.2) for 15 min each; and (3) 1 mM $Ca^{2+}$, 1 mM EDTA (pH 8.2), and 1 mM $Ca^{2+}$ for 15 min each. All samples were then rinsed 3× in DI $H_2O$, frozen at −80 °C, lyophilized, and sputter-coated with ∼5 nm of Au/Pd before imaging.

**Infrared Spectroscopy.** Silk was harvested from fifth instar *Hesperophylax* sp., as previously described.[5] Briefly, larvae diligently try to rebuild their case with almost any available material of the correct size, including millimeter-sized squares of Teflon, when their natural case is taken away. The silk fibers adhere poorly to Teflon and can be removed with fine forceps enabling the silk to be carefully cleaned of any visible particles.

For the analysis of the amide I (1575−1725 $cm^{-1}$) absorption band, metal ion depleted samples were prepared by soaking in either excess 1 mM or 100 mM EDTA buffered with 4.8 mM $NaHCO_3$ (pH 8.2 with NaOH) for 30 min. The samples were then washed three times in DI $H_2O$ and lyophilized. Calcium was restored by removing the EDTA solution, and washing with excess 1 mM $CaCl_2$ in 4.8 mM $NaHCO_3$ (pH 8.2), followed by three washes in DI $H_2O$ and lyophilization. As a standard for comparison, commercial *Bombyx mori* silk cocoons (Mulberry Farms, CA) were degummed by boiling in 0.25% aqueous $Na_2CO_3$ for 1 h, washed three times with DI $H_2O$, and lyophilized before analysis.

To analyze the effect of metal ions on the phosphate absorption bands (906−1182 $cm^{-1}$), a fibers were first rinsed three times in simulated creek water (1 mM $CaCl_2$ in 4.8 mM $NaHCO_3$, pH 8.2). The wet silk bundle was clamped to the ATR crystal. Excess solution was applied around the clamp to maintain hydration. The sample was removed and treated with excess 1 mM EDTA (pH 8.2 with NaOH) for 30 min to deplete metal ions. EDTA was removed by three washes with 4.8 mM $NaHCO_3$ (pH 8.2). The sample was again clamped wet to the ATR crystal with excess carbonate buffer around the clamp for the second recording. The sample was then treated in 100 mM EDTA buffered with 4.8 mM $NaHCO_3$ (pH 8.2 with NaOH) for 30 min and then rinsed three times in 4.8 mM $NaHCO_3$ (pH 8.2), and a third spectrum was recorded. The sample was incubated for 30 min in excess 1 mM $CaCl_2$ in 4.8 mM $NaHCO_3$ (pH 8.2) before the fourth spectrum was acquired.

The effect of pH on the phosphate absorption bands (906−1182 $cm^{-1}$) was studied by preparing 7 silk samples at the following pHs: 1.5, 3.0, 3.7, 4.0, 5.0, 8.2, and 10.5. Spectra were recorded from wet silk samples clamped to the ATR crystal with excess solution, of appropriate pH, around the clamp margins to prevent sample dehydration. The titration spectra reported were not normalized or baseline corrected.

ATR-FTIR absorbance spectra were collected using a Nicolet 6700 spectrometer (Thermo Scientific, FL) with a diamond Smart iTR accessory, a deuterated triglycine sulfate detector, and a KBr/Ge mid-infrared optimized beamsplitter. All spectra were recorded with a resolution of 4 $cm^{-1}$ and as 512 averaged scans. The area under the amide I region (1575−1725 $cm^{-1}$) and phosphate (906−1182 $cm^{-1}$) regions were normalized with Matlab software (MathWorks, MA) and decomposed with PeakFit software (Systat Software Inc., CA). Baselines were corrected by linear background subtraction with 3% tolerance. Local minima in the second derivative were used to identify peaks in the broad amide I region, which were fit as Gaussian curves. The peak position, height, and width were allowed to vary during an iterative least-squares method employed within the PeakFit software to minimize the residuals between reconstituted spectra and the experimental spectra.

**Modeling and Molecular Dynamic Simulations.** All systems were constructed using the Leap program from AmberTools 12, all analysis and structure manipulation was performed with the Cpptraj[28] program from AmberTools 12, and all molecular dynamics/minimizations were performed with either Sander or PMEMD from AmberTools 12.[29] All simulations were run at either NICS Keeneland or the Center for High Performance Computing, University of Utah.

A 30-residue section of the D-repeat (VpSIpSRpSVpSIERIVTPG-VYTKIpSRpSSpSVpSVE) was modeled as a $\beta$-hairpin using as an initial scaffold the backbone of a $\beta$-hairpin from the N-terminal domain of *B. mori* H-fibroin (PDB ID 3UA0, residues 76−105). Parameters were from Amber FF10 (protein FF99SB); parameters for pS (unprotonated phosphate, S2P) were from Homeyer et al.[29] The

**Table 1. Tryptic Peptides from F and E Sub-Repeats**[a]

| origin | peptide sequences | $M_{r(expt)}$ | $E$ (ppm)* | MS/MS score |
|---|---|---|---|---|
| F | R.**S**V**S**A**S**L**S**V**S**VERGIR.R (1) | 1619.4733 | 0.5 | 31 |
| E | R.GLGGLSG**S**GDLDGLGGYGGLGGYGGLGG.R (28) | 2525.1843 | −2.7 | 110 |
| E | R.GLGGL**S**GSGDLDGLGGYGGLGGYGGLGG.R (3) | 2525.1870 | −1.7 | 82 |
| E | R.GLGGL**S**G**S**GDLDGLGGYGGLGGYGGLGG.R (12) | 2605.1548 | −1.0 | 67 |
| E | G.L**S**G**S**GDLDGLGGYGGLGGYGGLGGR.R (6) | 2321.0078 | −0.5 | 39 |
| E | R.RPWGYGR.G (6) | 890.4511 | −0.02 | 25 |
| E | Y.GGLGGYGGLGGR.R (5) | 1019.5161 | 1.3 | 35 |

[a]Phosphorylated residues are bold and underlined. The numbers in the parentheses are the number of times the peptide was identified. Experimental relative molecular mass ($M_{r(expt)}$) errors, $E = (M_{expt} - M_{calc})/M_{calc}$, are presented in parts per million (ppm). The MS/MS ion score is $-10 \times \mathrm{Log}(P)$, where $P$ is the probability the observed peptide is a random match.

initial structure was energy minimized in 2000 steps of steepest descent minimization followed by 6000 steps of minimization with an implementation of the limited memory BFGS method[30] (XMIN in Amber) using the GBOBC implicit solvent model[31] with the salt concentration parameter set to 1.0 M and mbondi2 radii. The structure was then solvated (using Leap) with TIP3P[32] explicit water in a truncated octahedron unit cell using a buffer size of 10.0 Å. Seven $Ca^{2+}$ counterions were added to the system to neutralize the phosphate charges. The $Ca^{2+}$ ion parameters used were from Aqvist.[33]

The solvated system was then minimized at 300 K in two phases. The first phase used a combination of steepest descent minimization (4000 total steps), followed by 15 ps total of constant volume (NTV) molecular dynamics (MD) with restraints on solute heavy atoms to allow the initial relaxation of solvent. The MD used a step size of 1 fs, long-range interactions were handled using particle mesh Ewald[34] (PME) with a cutoff of 8.0 Å, Berendsen thermostat[35] with a coupling constant of 0.5 ps, and no bond constraints. The second phase consisted of several rounds of constant pressure (NTP) MD for a total of 30 ps with gradually decreasing restraints on heavy atoms. The same parameters as the NTV MD were used, except the Berendsen thermostat constant was 1.0 ps and bonds to hydrogen were constrained using the SHAKE algorithm.[36]

To create an extended $\beta$-sheet structure, the unminimized $[Ca^{2+}(pSX)_4]_2$ $\beta$-hairpin structure was replicated, translated, and rotated so that three antiparallel $\beta$-hairpins lay side-by-side in the same plane oriented end-to-end. The sheet was modeled by creating distance restraints between adjacent $\beta$-hairpin backbone atoms (carbonyl O to amide H of residues I3-V13, R5-R11, I9-V7, V29-T19, V27-I21, and S25-R23) and then minimizing for 500 steps with a steepest descent method, followed by 3500 steps of XMIN minimization using GBOBC implicit solvent with a salt concentration of 20.0 M and restraints within each individual hairpin to prevent the introduction of any structural artifacts from implicit solvent. The extended sheet was then further minimized for an additional 500 steps using XMIN with weak restraints on heavy backbone and pS phosphate atoms. The extended sheet structure was then solvated in the same manner as the unit sheet structure, except 21 excess $Ca^{2+}$ and 42 excess $Cl^-$ ions were added in addition to the 21 neutralizing $Ca^{2+}$ ions; the $Cl^-$ ion parameters were those of Joung and Cheatham.[37] The solvated system was then minimized using the same procedure as for the hairpin.

The two-layer structure was created by replicating and flipping the minimized sheet structure so that the pS groups pointed toward each other. The structure was solvated in the same manner as the sheet structure, with 42 neutralizing $Ca^{2+}$ ions and 21 $Ca^{2+}$ and 42 $Cl^-$ excess ions. The structure was then minimized in the same manner as the solvated hairpin structure; no additional restraints were required.

The "bottom" of the three-layer structure was created by taking the minimized two-layer structure and translating the "top" sheet layer down past the middle sheet layer so that the sides opposite the pSs in the middle and bottom layers were in contact. Distance restraints were used to align the sheets during minimization. There were six restraints between each $\beta$-sheet in opposite layers (C-$\alpha$ of pS4-I12, K20-pS28, pS8-pS8, pS24-pS24, I12-pS4, pS28-K20) for a total of 18 atom−atom restraints. Restraints were constructed to only activate beyond a distance of 12.0 Å. The structure was minimized for 500 steps using steepest descent with GBOBC and a salt concentration of 20.0 M while constraining the top two sheet layers. The structure was then minimized without restraints in the same manner as the $[Ca^{2+}(pSX)_4]_2$ $\beta$-hairpin structure. The system was further equilibrated using the 18 distance restraints described above for 20 ns with a force constant of 5.0 kcal/mol Å$^2$, followed by 10 ns with a force constant of 1.0 kcal/mol Å$^2$. Restraints were then removed for production MD.

Unless otherwise noted, production MD was performed at 300.0 K with a 2 fs time step, long-range interactions were handled using PME with a 8.0 Å cutoff, bonds to hydrogen were constrained using SHAKE, a Langevin thermostat was used with a 5 ps$^{-1}$ collision frequency, and an NTP ensemble was maintained using a weak coupling scheme with a 5.0 ps coupling constant. No restraints were used during production simulations.

Both coordinate root-mean-square deviation (RMSD) and secondary structure analysis were performed with Cpptraj. Secondary structure was assigned using the algorithm of Kabsch and Sander.[38] Cluster analysis of the first 40 ns of the hairpin trajectory was performed using an in-house version of Cpptraj. The DBSCAN[39] clustering algorithm was used. Clustering was performed on every fifth frame, with the remaining frames being added back in based on their distance to existing centroids. The distance metric was RMSD of C-$\alpha$ atoms from residues 3 to 28. The minimum number of points to form a cluster was 40 with an $\varepsilon$ (cluster distance cutoff) value of 0.7 Å. All molecular structure figures were generated with VMD 1.9.1.

## RESULTS

***Hesperophylax* sp. H-Fibroin Primary Structure and Phosphorylation.** Published N- and C-terminal sequences from the casemaker *L. decipiens*[8,9] were used to identify homologous contigs in a Trinity assembled transcriptome of the casemaker *Hesperophylax* sp. silk glands. The terminal sequences were then used as a starting point for assembling the *Hesperophylax* sp. H-fibroin sequence (Figure 2). A reliable assembly of the entire sequence (8−9 kb) was not possible because of the extreme repetitiveness of the central region. Nevertheless, the assembled terminal sequences are sufficient to reveal the blocky pattern of irregularly repeating conserved subrepeats, which likely span the entire distance between the relatively short terminal domains. In casemaker species, the subrepeats have been designated as D, E, and F (Figure 2).[8] Phosphorylated tryptic peptides from the *Hesperophylax* sp. D block were previously identified in the silk tyrptic peptide mass spectra by automated searching of published sequences.[6] Assembly of the *Hesperophylax* sp. H-fibroin sequence and automated searching allowed additional phosphorylated peptides to be identified in the mass spectra that contained $(pSG)_2$ and $(pSX)_5$ motifs from the E and F subrepeats, respectively (Table 1). Therefore, all three types of subrepeats in casemaker H-fibroins contain $(pSX)_n$ motifs. There may be heterogeneity in the extent of phosphorylation since not every serine was

phosphorylated in every $(SX)_n$ motif, a result of either incomplete phosphorylation during H-fibroin synthesis, or hydrolytic loss of phosphoester bonds during sample processing.

**Elemental Analysis.** In preparation to explore the effect of metal ion depletion on silk fiber mechanics and structure, elemental composition of silk fibers was analyzed before and after treatment with 1 and 100 mM sodium EDTA (pH 8.2). In untreated native fibers, Ca was by far the most abundant metal at a molar ratio of 0.88 to phosphate (Table 2), consistent with previous results.[6] The second most abundant metal, Mg, was less than 10% of the Ca. Small amounts of Fe and Zn were present. EDTA effectively depleted Ca and Mg from the fibers; 100 mM EDTA reduced the Ca and Mg by 84 and 92%, respectively. Adding excess $Ca^{2+}$ back to the EDTA treated fibers followed by washing in DI $H_2O$ restored the Ca/P ratio back to native levels.

**Table 2. Metal to Phosphorus Molar Ratios**[a]

| metal | native | EDTA 1 mM | EDTA 100 mM | $CaCl_2$ 1 mM |
|---|---|---|---|---|
| Ca | 0.83 ± 0.09 | 0.36 ± 0.11 | 0.13 ± 0.07 | 0.88 ± 0.17 |
| Mg | 0.12 ± 0.01 | 0.10 ± 0.02 | 0.01 ± 0.004 | 0.07 ± 0.02 |
| Fe | 0.01 ± 0.005 | 0.02 ± 0.01 | 0.04 ± 0.040 | 0.02 ± 0.003 |
| Zn | 0.09 ± 0.01 | 0.07 ± 0.01 | 0.02 ± 0.006 | 0.07 ± 0.01 |

[a]Averages of three independent samples (mean ± fractional total deviation).

**Single Fiber Mechanics.** Force was recorded as single fibers of *Hesperophylax* sp. silk were strained at a controlled rate to failure while submerged in simulated creek water (1 mM $CaCl_2$, 4.8 mM $NaHCO_3$, pH 8.2). Engineering stress is reported, calculated using an average fiber diameter for the two batches of silk used in these studies: 14.03 ± 1.08 and 14.78 ± 1.76 $\mu$m. Stress–strain profiles of five separate fibers were consistent (Figure 3A). Upon initial loading, the stress increased linearly with a modulus of 86.5 ± 19.2 MPa. At strains between 0.02 and 0.05, the fibers yielded, the stress plateaued, and in some cases, dropped slightly. At 0.1–0.2 strain, the stress gradually increased and became linear before failure at 32.7 ± 6.6 MPa. Strain at failure ranged from 0.9 to 1.7 (mm/mm).

Under controlled cyclical strains, the fibers revealed considerable hysteresis in the stress response (Figure 3B). When the strain was reversed at 0.5, stress dropped precipitously and the fiber went slack (zero load) at 0.25 strain. After a 15 min rest, the fiber had recovered to near its original resting length; at the beginning of a second strain cycle stress registered at 0.03 strain relative to the initial length (Video 1). The initial elastic modulus (108 MPa) was similar to the first cycle (123 MPa) as were the shape of the yield and stress plateau regions. After three strain cycles, silk fibers recovered ~95% of the initial resting length, and the stress at the yield point and at 0.5 strain were little changed from the previous cycles.

To explore the effect of divalent metal ion depletion on mechanical properties, silk fibers were tested while submerged in EDTA solutions. Five separate fibers, submerged in 1 mM EDTA solutions (4.8 mM $NaHCO_3$, pH 8.2 with NaOH), consistently failed below 1.0 strain and at an average of 0.325 ± 0.0065 MPa, only 1% of the native fiber peak loads (Figure 3A). The hysteresis during cyclic loading was also disrupted by $Ca^{2+}$ depletion. A fiber was first conditioned by cycling to 0.5 strain and back in native water conditions (1 mM $Ca^{2+}$, 4.8 mM $NaHCO_3$, pH 8.2). While the fiber was held at its initial length, the $Ca^{2+}$ solution was removed and replaced with a 100 mM EDTA solution. After 30 min in 100 mM EDTA, the fiber was again cycled to 0.5 strain and back in a 1 mM EDTA solution. The resulting stress–strain profile resembled that of a soft elastomeric rubber;[40] the initial modulus was reduced to 1.08 MPa, the distinct yield point observed in native fibers was gone, stress at 0.5 strain was reduced by 96%, and there was little hysteresis on return; the energy dissipated during cyclical loading of the fiber decreased by 98.8% (Figure 3C). With the fiber held at its initial length, the EDTA solution was replaced with a solution of 5 mM $CaCl_2$. After 24 h, a third strain cycle was performed in 1 mM $CaCl_2$ native water conditions. The mechanical response of the fiber was qualitatively recovered; the initial modulus recovered to 59 MPa, a yield point and stress plateau were apparent, and the energy dissipated by the fiber was 59.3% of the native fiber energy dissipation, as determined by comparing the area within the hysteresis loops (Figure 3C).

**Macroscale Structure.** To observe whole-fiber structural effects of metal ion exchange on caddisfly silk fibers, the ends of

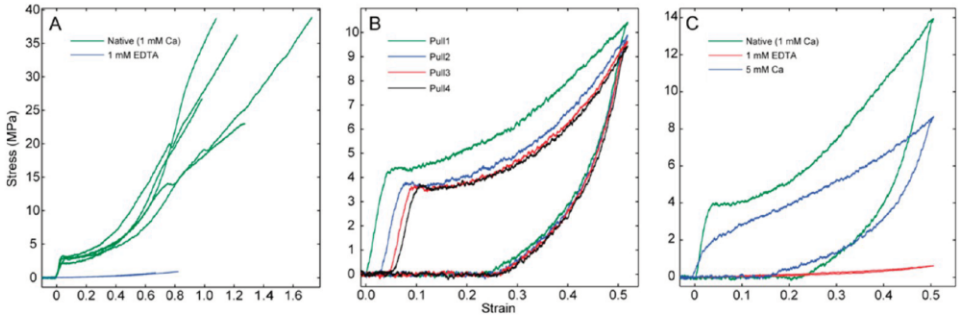


**Figure 3.** Single fiber mechanics. (A) Five fibers were stained to failure in 1 mM $Ca^{2+}$ (green) or in 1 mM EDTA (blue). (B) Force–extension profiles of a single native fiber cyclically loaded 4 times to 0.5 in 1 mM $Ca^{2+}$. The fiber was relaxed for 15 min between each strain cycle. (C) Green: force–extension profile from the third cycle of a single fiber cyclically loaded three times to 0.5 in 1 mM $Ca^{2+}$. Red: force–extension profile of a fiber cycled to 0.5 after 30 min in 1 mM EDTA. Blue: force–extension profile 24 h after replacing EDTA with 5 mM $Ca^{2+}$ and cycling to 0.5 strain.

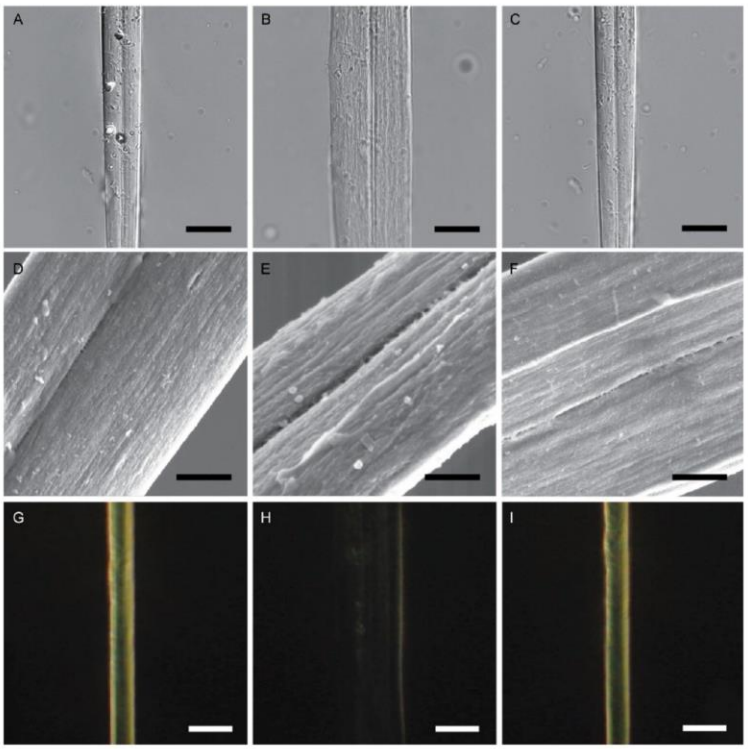


**Figure 4.** Macroscale structural effects of $Ca^{2+}$ depletion. Left column, native fibers; center column, fibers treated with 1 mM EDTA; right column, 1 mM $Ca^{2+}$ was added after EDTA was removed. (A−C) DIC images. Scale bar = 20 $\mu$m. (D−F) SEM images. Scale bar = 2 $\mu$m. (G−I) Birefringence under crossed polarizers. Scale bar = 20 $\mu$m.

a wet fiber, to fix its position, were secured with epoxy to the surface of a flow chamber, which was then filled with a 1 mM $CaCl_2$ solution (Figure 4A). When the $CaCl_2$ solution was washed out and replaced with a 1 mM EDTA solution the fiber swelled within a few minutes to approximately twice its initial diameter and the fibrillar substructure[5,14] became readily apparent by light microscopy (Figure 4B). When the EDTA solution was washed out and the chamber filled with a 1 mM $CaCl_2$ solution, the fiber shrank to its initial diameter in less than 5 s (Figure 4C). Scanning electron micrographs of an EDTA-swollen, $Ca^{2+}$-depleted fiber appeared more deeply corrugated than native fibers (Figure 4D−F). The surface topography of the fiber after returning $Ca^{2+}$ was similar to native fibers. Birefringence, indicative of long-range order, was lost when metal ions were depleted with EDTA, then rapidly and fully recovered when $Ca^{2+}$ was returned (Figure 4G−I). Despite the marked swelling pressure, metal ion depleted fibers did not dissolve entirely.

**Infrared Spectroscopy.** The IR spectral region from 1580 to 1700 $cm^{-1}$, the amide I region, corresponds to stretching modes of the peptide backbone C═O bonds and has been used extensively to study the secondary structure of silks.[41−43] As a baseline for comparison to caddisfly silk, the amide I spectral region of degummed commercial *B. mori* silk was decomposed into component absorbance bands by peak fitting (Figure 5A). The largest component, centered at 1616 $cm^{-1}$, corresponded to 37.6% antiparallel $\beta$-sheet conformations, consistent with published FTIR estimates of *B. mori* silk antiparallel $\beta$-sheet content.[42,44] The second largest component, centered at 1644 $cm^{-1}$, corresponded to 32.0% random coil, again consistent with literature values.[45,46] Two peaks, 1666 and 1682 $cm^{-1}$, occurred within the 1663−1694 $cm^{-1}$ region attributed to turn structures,[47,48] and corresponded to 12.1 and 7.4% of amide I absorbance, respectively. Peaks attributable to $\alpha$-helix were not present.

*Hesperophylax* sp. native silk fiber FTIR spectra, using identical methods, decomposed into component peaks similar to the *B. mori* silk fiber in the amide I region (Figure 3B). The strongest bands were centered at 1620 and 1646 $cm^{-1}$ and corresponded to 34.8% antiparallel $\beta$-sheet and 36.4% random coil, respectively. Two peaks centered at 1667 and 1681 $cm^{-1}$, within a region attributed to turns, corresponded to 13.7 and 7.5% of the amide I absorbance, respectively. Two absorbance bands centered at 1010 and 975 $cm^{-1}$, correspond to $Ca^{2+}$-complexed phosphate and dianionic phosphate, respectively (Figure 6A). These assignments were based on the pH dependence of the 975 $cm^{-1}$ absorbance that corresponded to titration of phosphate groups (Figure 7) and by comparison to literature precedents in which similar assignments were made in FTIR studies of the phosphoproteins, casein, and phosvitin.[49,50] The area ratio of these bands corresponded to 75% of the phosphate groups being complexed with $Ca^{2+}$ and

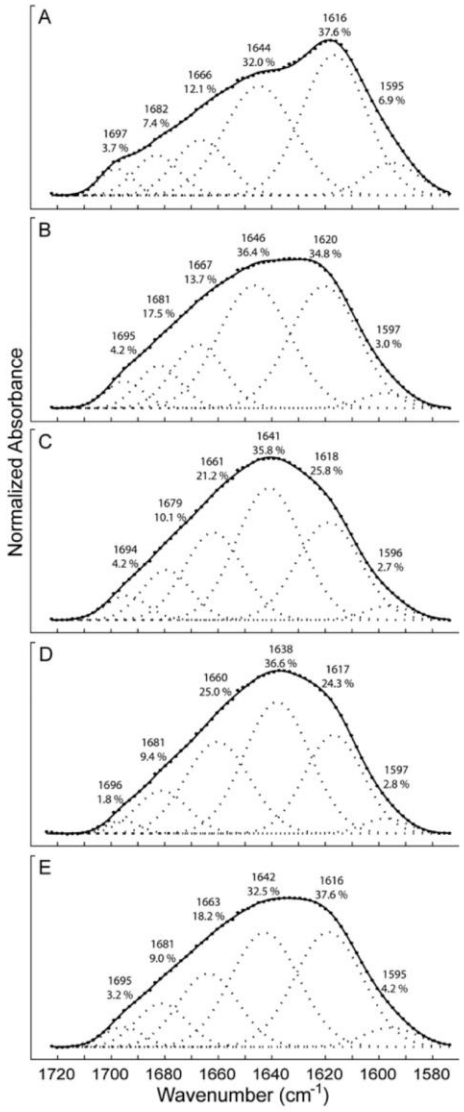


**Figure 5.** FTIR amide I region decomposition. (A) Degummed commercial *B. mori* silk. (B) Native *Hesperophylax* sp. silk. (C) *Hesperophylax* sp. silk treated with 1 mM EDTA (pH 8.2). (D) *Hesperophylax* sp. silk treated with 100 mM EDTA (pH 8.2). (E) EDTA was removed and replaced with an excess volume of 1 mM $Ca^{2+}$. Symbols: experimental spectra. Solid line: spectra calculated using fitted peaks. Dotted lines: Gausian bands identified by peak fitting.

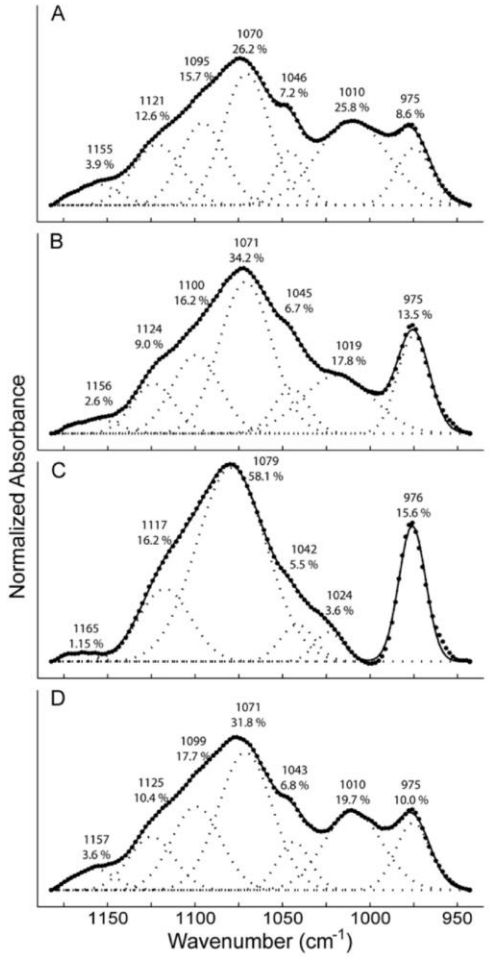


**Figure 6.** FTIR phosphoserines region decomposition. (A) Spectrum of native *Hesperophylax* sp. silk. (B) Spectrum in 1 mM EDTA (pH 8.2). (C) Spectrum in 100 mM EDTA. (D) Spectrum after 100 mM EDTA was removed and replaced with an excess volume of 1 mM $Ca^{2+}$. Symbols: experimental spectra. Solid line: spectra calculated using fitted peaks. Dotted lines: Gausian bands identified by peak fitting.

25% in the dianion form, assuming the two forms have equivalent extinction coefficients (Figure 6A).

Depletion of $Ca^{2+}$ with 100 mM sodium EDTA (pH 8.2) decreased the fiber $\beta$-sheet content from 34.8 to 24.3% (Figure 5D), as implied by the decreased area of the 1620 $cm^{-1}$ band, which was only slightly more than treatment with 1 mM EDTA (Figure 5C). The 1641 $cm^{-1}$ peak attributed to random coil components shifted to 1646 $cm^{-1}$, still within the random coil region, and its proportion of the total amide I band was nearly unchanged at 35.8% (Figure 5D). The 1667 $cm^{-1}$ peak appeared to shift to 1661 $cm^{-1}$, into a region usually attributed to $\alpha$-helices,[42,45] and its proportion increased to 21.2% from 13.7%. The $Ca^{2+}$- complexed phosphate peak appeared to shift from 1010 to 1024 $cm^{-1}$, and from its area ratio to the 975 $cm^{-1}$ band, the proportion of $Ca^{2+}$-complexed phosphate decreased to 19% and dianionic phosphate increased to 80% (Figure 6C).

When EDTA was washed out and excess $Ca^{2+}$ was added back, the proportion of the $\beta$-sheet 1616 $cm^{-1}$ peak increased back to 37.6%, only slightly lower than the value for native silk



dx.doi.org/10.1021/bm401036z | *Biomacromolecules* 2013, 14, 3668−3681

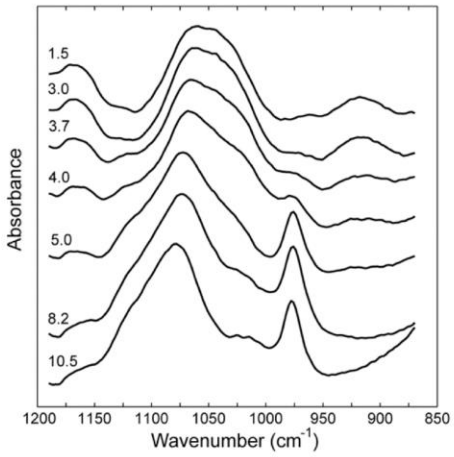


**Figure 7.** pH dependence of phosphoserine FTIR absorbance. Silk samples were depleted of $Ca^{2+}$ with EDTA prior to adjusting to the indicated pH.

fibers (Figure 5E). The random coil component, centered on 1642 $cm^{-1}$, decreased to 32.5%, somewhat lower than the native fibers. The 1661 $cm^{-1}$ band decreased in proportion and shifted back toward the native fiber 1667 $cm^{-1}$ band attributed to turn structures, although the proportion (18.2%) and peak position (1663 $cm^{-1}$) did not completely return to the native fiber proportion and position. The $Ca^{2+}$-complexed phosphate peak shifted back to 1010 $cm^{-1}$ and its proportion returned to ~66% with a proportionate decrease in the dianionic 975 $cm^{-1}$ band (Figure 6D).

**Molecular Dynamics Simulations.** The theoretical stability of a hypothetical $Ca^{2+}$-bridged $\beta$-hairpin formed by the pair of D subrepeat $(pSX)_4$ motifs[5,6] was evaluated by MD simulation. To model the $Ca^{2+}$-bridged $\beta$-hairpin, a $\beta$-hairpin from near the N-terminus of *B. mori* H-fibroin was used as an initial backbone scaffold. Within 15 ns, the $[Ca^{2+}(pSX)_4]_2$ $\beta$-hairpin adopted a slight twist from the initially bowed *B. mori* scaffold structure (Figure 8A), after which the coordinate root-mean-square displacements (RMSD) of the $\alpha$-Cs and the fraction of $\beta$-hairpin stabilized at 1.0−1.5 Å and 0.65, respectively (Figure 8C). After 40 ns, $Ca^{2+}$ ions were removed, whereupon the $\beta$-hairpin rapidly fell apart (Figure 8B). Within 15 ns of removing $Ca^{2+}$, the $\alpha$-C RMSD rose to ~7 Å and <10% of the residues remained in a $\beta$-sheet conformation (Figure 8C).

Hypothetically, the $[Ca^{2+}(pSX)_4]_2$ $\beta$-hairpin (Figure 9A) could further associate into $\beta$-sheets (Figure 9B) and stack through alternating $Ca^{2+}$-bridged and hydrophobic interfaces into $\beta$-domains (Figure 9C). A model for an extended $\beta$-sheet was created with three $[Ca^{2+}(pSX)_4]_2$ $\beta$-hairpins alternating in orientation (Figure 9B). This model was then extended perpendicularly by stacking two sheets with their pS residues oriented toward each other, creating a pS/$Ca^{2+}$ interface (not shown). The one- and two-sheet systems were simulated for 10 and 50 ns, respectively, and were both stable over this time frame with $\alpha$-C RMSDs of ~2.5 Å relative to their initial conformations and average fraction $\beta$ content of 0.74 ± 0.02 and 0.71 ± 0.03, respectively. The distance between layers in the $Ca^{2+}$-stabilized two-sheet structure stabilized at ~13 Å. A three-sheet model was created by adding a third sheet to the hydrophobic face of the two-sheet structure (Figure 9C). This model was simulated for 80 ns with no restraints. The $\alpha$-C RMSD relative to the structure of the most populated cluster remained below 2 Å. The average fractional $\beta$ content was 0.56 ± 0.03. The decreased $\beta$ content with respect to the 1- and 2-sheet structures arose from residues adjacent to the hairpin turns becoming more flexible over the course of the simulation; the core residues of the hairpins comprising each $\beta$-sheet remained stable over the course of the simulation. After 50 ns, the spacing between each layer had stabilized at 12−13 Å (not shown).

A three $\beta$-strand $Ca^{2+}$-bridged (FDD) structure can be created by associating the single F subrepeat $(pSX)_5$ motif (Figure 2) with the D subrepeat $[Ca^{2+}(pSX)_4]_2$ $\beta$-hairpin through a turn in the proline-containing R-rich motif that separates them (Figure 10A). During a 50 ns simulation without restraints, the average fraction of residues in the three-strand FDD structure that occupied a $\beta$-conformation was 0.56 ± 0.05, consistent with a stable structure (Figure 10B). This FDD structure may further assemble into stable semicrystalline $\beta$-domains with alternating hydrophobic and $Ca^{2+}$-stabilized interfaces, as suggested for the two-strand DD $\beta$-hairpin

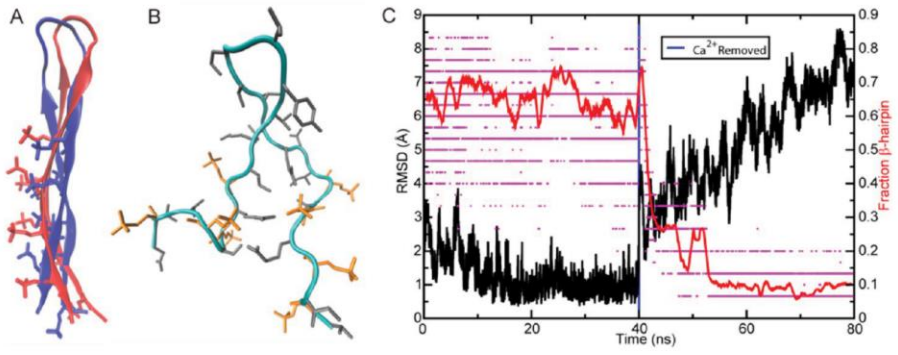


**Figure 8.** $[Ca^{2+}(pSX)_4]_2$ $\beta$-hairpin MD simulations. (A) Red backbone: initial structure. Blue backbone: stabilized structure. (B) Structure 40 ns after $Ca^{2+}$ removal. (C) Backbone $\alpha$-carbon RMSD (black line) and fraction of residues in $\beta$-hairpin conformation (red line) before and after $Ca^{2+}$ removal.

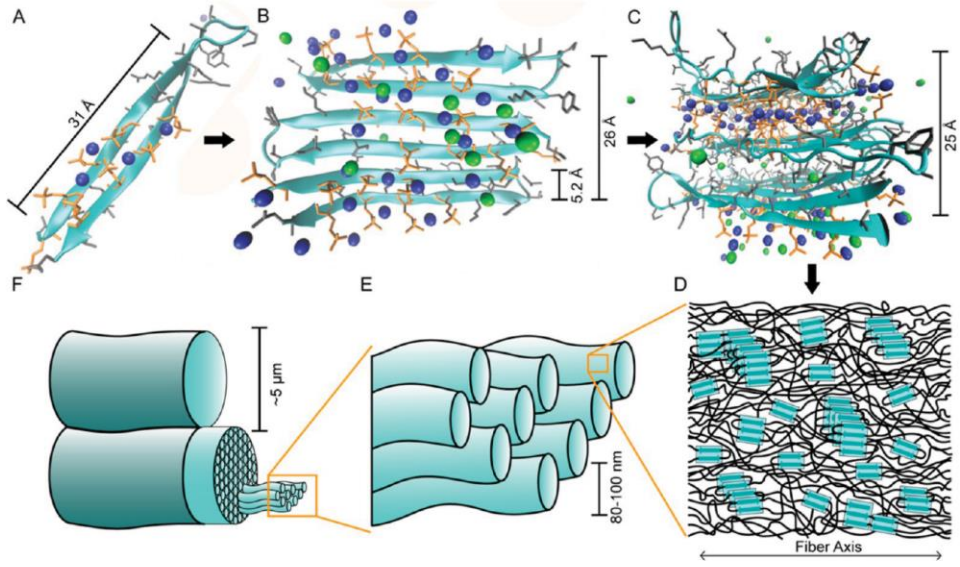


**Figure 9.** Hypothetical molecular structure of caddisfly H-fibroin $\beta$-domains and silk fibers. (A) Representative structure the D subrepeat $[Ca^{2+}(pSX)_4]_2$ $\beta$-hairpin from cluster analysis of a 40 ns MD simulation. $Ca^{2+}$ = blue spheres, $Cl^-$ = green spheres. (B) Representative structure after 10 ns of MD simulation of an extended $\beta$-sheet modeled with three antiparallel $[Ca^{2+}(pSX)_4]_2$ $\beta$-hairpins. (C) Representative structure of a three-sheet $\beta$-domain stabilized through alternating pS-$Ca^{2+}$ bridged interfaces and hydrophobic interfaces. Calculated dimensions of the domains are indicated. (D) Macroscale nanocomposite fiber model: semicrystalline $Ca^{2+}$-stabilized, pS-rich $\beta$-domains (turquoise) form interfiber cross-links connected by amorphous regions (black). (E) The core of the silk fiber consists of 100−80 nm nanofibrils (turquoise) running parallel with the macrofiber axis.[5] (F) The paired subfibers (turquoise) are fused together and have a thin, poorly characterized peripheral layer (blue).[14]

structure. These hypothetical FDD higher-order structures were not simulated.

## ■ DISCUSSION

**Silk Fiber Mechanics.** To extend its case, stones gathered from the stream bed are held in place while the end of a silk fiber, emanating from a spinneret just below its mouth, is pressed onto the stone. With a back-and-forth motion of its head, the larva draws the fiber out to crisscross the span between adjacent stones multiple times, adhering a loop of fiber to the substrate at each turn, to create tension-resisting ties between stones. Like an adhesive tape, the quality and effectiveness of the silk ties are as much a product of the backing material as they are of the adhesive interfacial anchors. Characterization of the mechanical properties of caddisfly silk fibers is therefore integral to understanding the silk's overall effectiveness as an underwater structural adhesive.

Well-characterized terrestrial silks vary widely in their response to tensile stresses, in ways that can be rationalized from their biological functions and molecular structures.[51−57] Compared to terrestrial silks, native *Hsyperophylax* sp. silk is at the low end of the range for initial elastic modulus and tensile strength, 86.5 ± 19.2 and 32.7 ± 6.5 MPa, respectively, and in the middle of the range for extensibility. There are few published reports of caddisfly mechanical testing. In one comparable study, the net fibers of a retreat-builder caddisfly, *Hydropsyche siltalai*, tested while fully submerged in water were also highly extensible, more than 100% at failure, and reportedly stronger than *Hysperophylax* sp. silk with a load at failure of 221 MPa.[58] We are unaware of any comparable testing of casemaker silk fibers. For its case construction purposes, the relatively low modulus and tensile strength of the casemaker *Hysperophylax* sp. silk may be compensated by the propensity of the fibers to cohere into bundles during case assembly, which would presumably increase both the modulus and tensile strength of the structural ties in the case.[6]

The force extension profiles of single native *Hesperophylax* sp. fibers displayed distinct yield points, force plateaus after yield, followed by strain stiffening, and considerable hysteresis during unloading. Similar profiles have been reported for several other types of biological materials, including terrestrial moth and spider silks,[59] hair and wool,[60,61] the proximal region of mussel byssal threads,[62−64] and marine snail egg capsules.[65,66] To generalize, the characteristic yield point and force plateau in these biological materials has been interpreted as macroscale evidence of a nanoscale toughening mechanism, whereby sacrificial rupture, or slippage, within repetitive domains exposes hidden length to dissipate strain energy and prevent brittle fracture.[67] Though the loading profile of caddisfly silk is characteristic, the unloading profile is more unique. The nearly full recovery of the initial modulus and yield point when the fiber was unloaded suggested the deformation of the stiff, yielding substructures was reversible. In this respect, caddisfly silk is distinct from terrestrial silks and keratinous fibers, which undergo permanent deformations when strained beyond their yield point in air[54,61] and more similar to the proximal region of aquatic mussel byssal threads, which also recover their initial length and elastic modulus when strained beyond their yield point underwater.[63,68,69] The area within the hysteresis loops represents strain energy dissipated as heat by

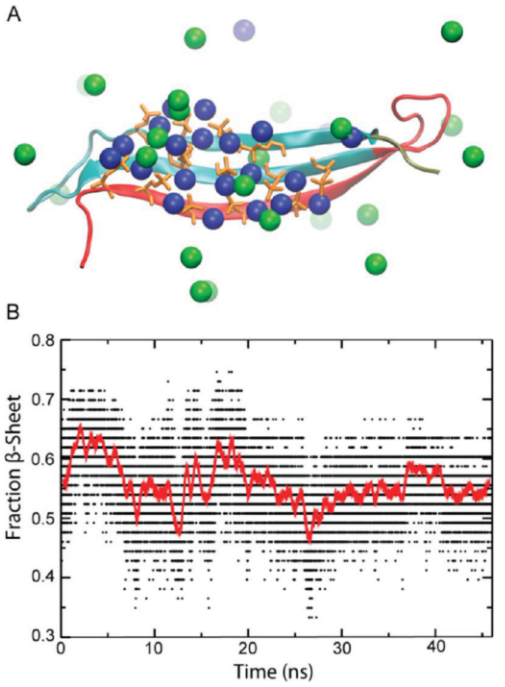


**Figure 10.** Hypothetical FDD domain $\beta$-structure. (A) The turquoise and red backbone are the D and F repeat contributions to the hypothetical $\beta$-sheet, respectively. Blue and green spheres are $Ca^{2+}$ and $Cl^{-}$ ions, respectively. (B) The fraction of $\beta$-sheet during a 50 ns simulation.

the fibers during the loading cycle. Slow recovery of the initial modulus and length (self-healing) retensions the silk fibers (Video 1), allowing repeated cycles of absorption and dissipation of transient stresses to keep the stone assembly tight. This may be highly adaptive for the caddisfly larval lifestyle near the high-energy margins of fast moving streams.

Exchange of divalent metal ions with $Na^{+}$ destroyed the stiffness, strength, energy-dissipating hysteresis, and caused the fibers to swell dramatically, effects which were at least partially reversed when $Ca^{2+}$ was returned. The mechanical effects of removing and restoring $Ca^{2+}$ are consistent with a stiff, repeating, energy-dissipating, $Ca^{2+}$-dependent structural domain. It follows that $Ca^{2+}$ may play a critical role in the formation of insoluble silk fibers from fluid silk precursors in caddisfly adhesive glands. The silk storage region of the gland is separated from the anterior conducting channel by a narrow, goblet-shaped, chitinous orifice.[5] Long-range order, as revealed by fiber birefringence, is created as silk proteins pass through the rigid constriction.[5] Addition of $Ca^{2+}$ to the silk proteins, or reorganization of $Ca^{2+}$ cross-links from intrafiber to interfiber, as the silk proteins are sheared through the orifice may insolubilize the waterborne silk fiber precursors and lock in strain as noncovalent interfiber cross-links. The loss of locked-in strain from the natural fiber drawing process may explain why the strength was not fully recovered when $Ca^{2+}$ was returned to EDTA-treated fibers in the absence of shear stress. Similar reversible effects on mechanical properties were reported for proximal byssal threads after metal ion depletion with EDTA in metal ion free seawater.[69] The effect was attributed to disruption of interstrand metal coordination bonds between histidine residues in the terminal region of blocky collagenous byssal thread proteins. It may be significant that metal ion-dependent caddisfly silk and byssal threads are both adapted to function while fully submerged in natural waters; metal bonding may be better suited for aquatic energy-dissipating structural fibers.

**Caddisfly Silk Structure.** Casemaker caddisfly H-fibroins are built from three types of irregularly repeating blocks (D−F) separated by highly conserved arginine-rich motifs with a central proline that can form a turn structure (Figure 2). The H-fibroins of all three suborders of caddisflies have highly similar D blocks, while the other blocks are less perfectly conserved, suggesting the D blocks may be of particular importance to the structure, formation, and mechanical properties of all caddisfly silk fibers. A structural model was previously proposed in which the pair of D repeat $(pSX)_4$ motifs (DD) form a $Ca^{2+}$-stabilized $\beta$-hairpin (Figure 8).[6] In theory, the DD hairpin could further associate laterally to form extended $\beta$-sheets and stack perpendicularly through alternating hydrophobic and $Ca^{2+}$−phosphate interfaces (Figure 9).[5] The discovery that F repeat serines are also phosphorylated suggests that its single $(pSX)_5$ could associate with the paired D $(pSX)_4$ motifs to form a FDD three-stranded $Ca^{2+}$-stabilized $\beta$-sheet (Figure 10), which in theory could also be extended laterally and stacked into $\beta$-domains. Note that not all F repeats are contiguous with D repeats. Noncontiguous F repeats may participate in intermolecular $\beta$-sheet cross-links that would strengthen the fibers. The casemaker E blocks, which vary in length and consist mostly of runs of GGY and GGL triplets, may form random coil spacers between the structured F and D blocks. Variations between casemakers and retreat builders in non-D block sequences and repeating block patterns may reflect adaptations for the distinct applications of the silks—composite body armor versus suspended capture nets.

The proposed structural model is consistent with the $Ca^{2+}$-dependent mechanical properties and also accounts for the high proportion of antiparallel $\beta$-sheet structures in native *Hesperophylax* sp. silk estimated by IR spectroscopy (Figure 5). Within the limitations of interpreting secondary structure by peak fitting FTIR amide I spectra, ∼35% of casemaker caddisfly silk residues appeared to be in antiparallel $\beta$-sheets, a similar proportion to degummed commercial *B. mori* silk fibers. Coincidently, if 100% of the F and D repeat $(pSX)_n$ motifs were present in the hypothetical FDD $\beta$-structures 100% of the time, the maximum amount of $\beta$-sheet in H-fibroin would be ∼35%. The fibers also contain L-fibroin and other proteins that may contain $\beta$-sheets. A significant fraction of the FTIR estimated $\beta$-structures are not part of H-fibroin FDD $\beta$-structures since the apparent $\beta$-sheet content was decreased by only 30.2% when 84.3% of the native $Ca^{2+}$ ions had been depleted with EDTA. Estimated antiparallel $\beta$-sheet returned to near native proportions when $Ca^{2+}$ was returned after removing EDTA. The high proportion of $\beta$-structure estimated by amide I peak fitting is at odds with WAXD estimates of only 7−8% crystallinity in *Hesperophylax* sp. silk fibers,[16] unless most of the $\beta$-structures are not in regular order.

The caddisfly silk phosphates are segregated into at least two populations in the FTIR spectra. In native fibers, ∼75% of the phosphates are in a tight $Ca^{2+}$-phosphate complex and ∼25% are in a dianionic form. As expected, EDTA treatment

substantially shifted the $Ca^{2+}$-complexed population to the dianionic form, and restoration of $Ca^{2+}$ shifted the populations back to near native fiber proportions. Clearly, not all of the silk fiber phosphates participate in the hypothetical H-fibroin $Ca^{2+}$-stabilized $\beta$-structures. Phosphates not in $Ca^{2+}$-stabilized $(pSX)_n$ structures may exist on the E block $(pSG)_2$, out-of-register D and F block $(pSX)_n$ motifs that cannot form stable $\beta$-structures, and phosphates on macromolecules other than H-fibroin. If surface exposed, this phosphate population may contribute to interfacial adhesion.

Reversible loss of birefringence and fiber swelling after $Ca^{2+}$ depletion with $Na^+$ EDTA is also consistent with reversible denaturation and entropic expansion of $Ca^{2+}$-stabilized domains. The effect is accompanied by increased osmotic pressure inside the fiber due to exchange of divalent cations with monovalent $Na^+$ and an influx of water. Despite the marked swelling pressure, metal ion depleted fibers did not dissolve entirely. The fibers may be cross-linked through conserved cysteines or other covalent bonds.[9,70] Freshly drawn fibers change from white to reddish brown over 24 h, indicative of quinonic cross-linking that would provide additional covalent fiber reinforcement. Precedents for quinonic tanning of moth silks are known from the dark brown silks of the Tussah moth and Saturniidae moths.[71]

X-ray diffraction studies of caddisfly silks, though few in number, have shown that caddisfly silks contain $\beta$-structures, but are much less ordered than other types of silk. The dimensions of the hypothetical $Ca^{2+}[(pSX)_4]_2$ $\beta$-domains (Figure 9A−C) are largely consistent with reported caddisfly silk X-ray diffraction data. The $Ca^{2+}[(pSX)_4]_2$ $\beta$-hairpin (Figure 3A), if they were oriented end-to-end within the fiber, would create a 31 Å periodicity. Indeed, weak diffraction peaks corresponding to a 30−31 Å periodicity along the fiber long axis were observed in the silk of the caddisfly *Pycnopsyche guttifer*.[14] The spacing between the hydrated $Ca^{2+}[(pSX)_4]_2$ $\beta$-sheets predicts an ∼25 Å periodicity perpendicular to the 31 Å periodicity (Figure 9C). Dehydrated *P. guttifer* silk displayed a radial axis periodicity of 21−22 Å, close to the predicted dimensions.[14] For comparison, the corresponding intersheet periodicity of terrestrial moth silks, with smaller side chain alanine-rich $\beta$-domains, is 9.2−12.5 Å.[72] Rudal and collaborators reported diffraction peaks corresponding to a 17 Å periodicity in the radial axis of silk fibers of the caddisfly *Olinga feredayi*. Treatment of the fibers with EDTA at pH 7.2 greatly diminished the intensity of the 17 Å diffraction peak, which led the authors to presciently suggest "that in every third pleated sheet there are acid groups binding an ion such as calcium."[15]

The initial MD simulations reported here provided supporting evidence that the hypothetical antiparallel $\beta$-hairpin structure was stable in the presence of $Ca^{2+}$. Simulated removal of $Ca^{2+}$ caused the $\beta$-hairpin structure to quickly disintegrate, consistent with the experimental loss of mechanical strength and antiparallel $\beta$-sheet content when $Ca^{2+}$ was exchanged with EDTA. The peptide backbone H-bonds are apparently insufficient to hold the $\beta$-hairpin together in the absence of $Ca^{2+}$ bridging between the phosphate side chains. The results are also consistent with earlier steered MD simulations that demonstrated the $Ca^{2+}$-bridged antiparallel $\beta$-sheet conformation was the most stable of several conformations investigated.[73] Enhanced sampling techniques[74,75] and steered MD[76,77] have been used with great effect to understand the relationships between nanoscale structure and mechanics of terrestrial moth and spider silks at several length scales.[78] In future simulations, similar computational techniques will be used to explore more fully the conformational landscape of the caddisfly H-fibroin $(pSX)_n$ domains and their response to loading.

One of the insights gleaned from computational studies of terrestrial silks is that clustering of a small number of H-bonds can overcome the intrinsic weakness of individual H-bonds. The highest shear strength was achieved when simulated silk $\beta$-strands contained 3−4 H-bonds that ruptured cooperatively. Beyond this number the strength decreased.[79] Likewise, the stiffness, strength, and toughness of $\beta$-sheet nanocrystals were subject to critical size effects. Smaller nanocrystals were stronger and tougher than larger nanocrystals. Optimal $\beta$-sheet dimensions were ∼3 nm.[80] Clustering of 4−6 H-bonds in $\beta$-sheet structures is found in a diverse array of proteins, which hints at the importance of this biological material design feature as a general mechanism for strengthening proteins.[81] The stiffness, strength, and toughness of caddisfly silk is contributed by $Ca^{2+}$ bridging between phosphate side chains rather than exclusively H-bonding. Nevertheless, it may be significant that the $Ca^{2+}$-phosphate bonds also occur as clusters of 4−5 in the $(pSX)_n$ domains, and that the dimensions of the proposed $\beta$-sheets are 3.1 × 2.6 nm (Figure 9A,B), near the theoretical optimal size for H-bonded silk nanocrystals.[80] Further work may reveal that clustered $Ca^{2+}$-phosphoserine bridges in caddisfly silk may work cooperatively to resist rupture in a manner analogous to clustered H-bonds in terrestrial silks, and that the size and proportion of the $(pSX)_n$ domains have been selected to maximize caddisfly silk strength, extensibility, and toughness in an aquatic environment.

## ■ CONCLUSIONS

Caddisfly larval silk has been adapted for duty in aquatic environments. In general terms, it appears that electrostatic interactions and metal ion-dependent bonding are more important for underwater fiber formation and stability than in terrestrial fibers. Caddisfly silk is a sophisticated underwater adhesive tape comprising an energy-dissipating silk fiber backing material with a pressure sensitive adhesive coating that sticks underwater. As such, it may be a unique source of design principles for tough, self-healing synthetic materials, fibers and fabrics, especially suited for underwater and wet-field biomaterial applications, as well as biomimetic processes for spinning water-borne polymers into fibers underwater.

## ■ ASSOCIATED CONTENT

### Supporting Information

The recovery of the self-tensioning caddisfly silk fiber is shown in supplemental Video 1 of a submerged single caddisfly silk fiber during a cyclic load cycle. The fiber is loaded at 0.1 mm $s^{-1}$ to a strain of 1.6 and unloaded at 0.5 mm/s. Load cycle hysteresis is visibly apparent in the delayed recovery of the silk thread to its initial length. This material is available free of charge via the Internet at http://pubs.acs.org.

## ■ AUTHOR INFORMATION

### Corresponding Author

*Tel.: 1-801-581-8581. E-mail: russell.stewart@utah.edu.

### Notes

The authors declare no competing financial interest.

## ■ ACKNOWLEDGMENTS

Support from the Army Research Office (W911NF1010132) is gratefully acknowledged. The authors thank Caleb Campbell for help with transcriptome assembly, Matt DeLong for SEM assistance, Dr. Krishna Parsawar for mass spectroscopy, and Hyung Kim for elemental analysis. The computational work was enabled by NSF XSEDE OCI-1053575 and allocation MCA01S027P and the Center for High Performance Computing at the University of Utah.

## ■ REFERENCES

(1) Wiggins, G. B. In *Caddisflies: The Underwater Architects*; Wiggins, G. B, Ed.; University of Toronto Press: Toronto, Buffalo, 2004; p xi, 292.
(2) Whalley, P. *Biol. J. Linn. Soc.* **1986**, *28*, 253−271.
(3) Sehnal, F.; Akai, H. *Int. J. Insect Morphol. Embryol.* **1990**, *19*, 79−132.
(4) Sehnal, F.; Sutherland, T. *Prion* **2008**, *2*, 1−9.
(5) Ashton, N. N.; Taggart, D. S.; Stewart, R. J. *Biopolymers* **2012**, *97*, 432−445.
(6) Stewart, R. J.; Wang, C. S. *Biomacromolecules* **2010**, *11*, 969−974.
(7) Tanaka, K.; Kajiyama, N.; Ishikura, K.; Waga, S.; Kikuchi, A.; Ohtomo, K.; Takagi, T.; Mizuno, S. *Biochim. Biophys. Acta, Protein Struct. Mol. Enzymol.* **1999**, *1432*, 92−103.
(8) Yonemura, N.; Sehnal, F.; Mita, K.; Tamura, T. *Biomacromolecules* **2006**, *7*, 3370−8.
(9) Yonemura, N.; Mita, K.; Tamura, T.; Sehnal, F. *J. Mol. Evol.* **2009**, *68*, 641−653.
(10) Colomban, P. *Adv. Nat. Sci.: Nanosci. Nanotechnol.* **2013**, *4*, 1−10.
(11) Ha, S.-W.; Gracz, H. S.; Tonelli, A. E.; Hudson, S. M. *Biomacromolecules* **2005**, *6*, 2563−2569.
(12) Wang, Y.-J.; Sanai, K.; Wen, H.-X.; Zhao, T.-F.; Nakagaki, M. *Mol. Biol. Rep.* **2010**, *37*, 2885−2892.
(13) Dunaway, D. L.; Thiel, B. L.; Viney, C. *J. Appl. Polym. Sci.* **1995**, *58*, 675−683.
(14) Engster, M. S. *Cell Tissue Res.* **1976**, *169*, 77−92.
(15) Rudall, K. M.; Kenchington, W. *Annu. Rev. Entomol.* **1971**, *16*, 73−96.
(16) Addison, J. B.; Ashton, N. N.; Weber, W. S.; Stewart, R. J.; Holland, G. P.; Yarger, J. L. *Biomacromolecules* **2013**, *14*, 1140−1148.
(17) Ohkawa, K.; Miura, Y.; Nomura, T.; Arai, R.; Abe, K.; Tsukada, M.; Hirabayashi, K. *Biofouling* **2013**, *29*, 357−367.
(18) Stewart, R. J.; Ransom, T. C.; Hlady, V. *J. Polym. Sci., Part B: Polym. Phys.* **2011**, *49*, 757−771.
(19) Stumm, W.; Morgan, J. J. *Aquatic Chemistry: Chemical Equilibria and Rates in Natural Waters*, 3rd ed.; Wiley: New York, 1996; p xvi, 1022.
(20) Flammang, P.; Lambert, A.; Bailly, P.; Hennebert, E. *J. Adhes.* **2009**, *85*, 447−464.
(21) Bré, L. P.; Zheng, Y.; Pêgo, A. P.; Wang, W. *Biomater. Sci.* **2013**, *1*, 239−253.
(22) Brubaker, C. E.; Messersmith, P. B. *Langmuir* **2012**, *28*, 2200−2205.
(23) Lewis, R. V. *Chem. Rev.* **2006**, *106*, 3762−3774.
(24) Vepari, C.; Kaplan, D. L. *Prog. Polym. Sci.* **2007**, *32*, 991−1007.
(25) Eisoldt, L.; Smith, A.; Scheibel, T. *Mater. Today* **2011**, *14*, 80−86.
(26) Vollrath, F.; Knight, D. P. *Nature (London, U. K.)* **2001**, *410*, 541−548.
(27) Grabherr, M. G.; Haas, B. J.; Yassour, M.; Levin, J. Z.; Thompson, D. A.; Amit, I.; Adiconis, X.; Fan, L.; Raychowdhury, R.; Zeng, Q. *Nat. Biotechnol.* **2011**, *29*, 644−652.
(28) Roe, D. R.; Cheatham III, T. E. *J. Chem. Theory Comput.* **2013**, *9*, 3084−3095.
(29) Case, D. A.; Cheatham, T. E.; Darden, T.; Gohlke, H.; Luo, R.; Merz, K. M.; Onufriev, A.; Simmerling, C.; Wang, B.; Woods, R. J. *J. Comput. Chem.* **2005**, *26*, 1668−1688.
(30) Liu, D. C.; Nocedal, J. *Math. Prog.* **1989**, *45*, 503−528.
(31) Onufriev, A.; Bashford, D.; Case, D. A. *Proteins: Struct., Funct., Bioinf.* **2004**, *55*, 383−394.
(32) Jorgensen, W. L.; Chandrasekhar, J.; Madura, J. D.; Impey, R. W.; Klein, M. L. *J. Chem. Phys.* **1983**, *79*, 926.
(33) Åqvist, J. *J. Phys. Chem.* **1990**, *94*, 8021−8024.
(34) Darden, T.; York, D.; Pedersen, L. *J. Chem. Phys.* **1993**, *98*, 10089.
(35) Berendsen, H. J. C.; Postma, J. P. M.; van Gunsteren, W. F.; DiNola, A.; Haak, J. R. *J. Chem. Phys.* **1984**, *81*, 3684.
(36) Ryckaert, J.-P.; Ciccotti, G.; Berendsen, H. J. C. *J. Comput. Phys.* **1977**, *23*, 327−341.
(37) Joung, I. S.; Cheatham III, T. E. *J. Phys. Chem. B* **2008**, *112*, 9020−9041.
(38) Kabsch, W.; Sander, C. *Biopolymers* **1983**, *22*, 2577−2637.
(39) Ester, M.; Kriegel, H.-P.; Sander, J.; Wimmer, M.; Xu, X. *Incremental Clustering for Mining in a Data Warehousing Environment*; Institute of Electrical and Electronics Engineers: New York, 1998; pp 323−333.
(40) Chaikumpollert, O.; Yamamoto, Y.; Suchiva, K.; Kawahara, S. *Polym. J.* **2012**, *44*, 772−777.
(41) Khan, M. M. R.; Morikawa, H.; Gotoh, Y.; Miura, M.; Ming, Z.; Sato, Y.; Iwasa, M. *Int. J. Biol. Macromol.* **2008**, *42*, 264−270.
(42) Hu, X.; Kaplan, D.; Cebe, P. *Macromolecules* **2006**, *39*, 6161−6170.
(43) Jin, H. J.; Park, J.; Karageorgiou, V.; Kim, U. J.; Valluzzi, R.; Cebe, P.; Kaplan, D. L. *Adv. Funct. Mater.* **2005**, *15*, 1241−1247.
(44) Zandomeneghi, G.; Krebs, M. R. H.; McCammon, M. G.; Fändrich, M. *Protein Sci.* **2004**, *13*, 3314−3321.
(45) Tretinnikov, O. N.; Tamada, Y. *Langmuir* **2001**, *17*, 7406−7413.
(46) Goormaghtigh, E.; Cabiaux, V.; Ruysschaert, J. M. *Eur. J. Biochem.* **1990**, *193*, 409−420.
(47) Dong, A.; Prestrelski, S. J.; Allison, S. D.; Carpenter, J. F. *J. Pharm. Sci.* **1995**, *84*, 415−424.
(48) Jung, C. *J. Mol. Recognit.* **2000**, *13*, 325−351.
(49) Sanchez-Ruiz, J. M.; Martinez-Carrion, M., A. *Biochemistry* **1988**, *27*, 3338−3342.
(50) Fernández, C.; Ausar, S. F.; Badini, R. G.; Castagna, L. F.; Bianco, I. D.; Beltramo, D. M. *Int. Dairy J.* **2003**, *13*, 897−901.
(51) Pérez-Rigueiro, J.; Viney, C.; Llorca, J.; Elices, M. *Polymer* **2000**, *41*, 8433−8439.
(52) Zhao, H.-P.; Feng, X.-Q.; Shi, H.-J. *Mater. Sci. Eng., C* **2007**, *27*, 675−683.
(53) Collin, M. A.; Garb, J. E.; Edgerly, J. S.; Hayashi, C. Y. *Insect Biochem. Mol. Biol.* **2009**, *39*, 75−82.
(54) Liu, Y.; Shao, Z.; Vollrath, F. *Biomacromolecules* **2008**, *9*, 1782−1786.
(55) Römer, L.; Scheibel, T. *Prion* **2008**, *2*, 154−161.
(56) Hayashi, C. Y.; Shipley, N. H.; Lewis, R. V. *Int. J. Biol. Macromol.* **1999**, *24*, 271−275.
(57) Blackledge, T. A. *J. Arachnol.* **2012**, *40*, 1−12.
(58) Brown, S. A.; Ruxton, G. D. *J. N. Am. Benthol. Soc.* **2004**, *23*, 771−779.
(59) Elices, M.; Plaza, G. R.; Pérez-Rigueiro, J.; Guinea, G. V. *J. Mech. Behav. Biomed. Mater.* **2011**, *4*, 658−669.
(60) Seshadri, I. P.; Bhushan, B. *Acta Mater.* **2008**, *56*, 774−781.
(61) McKittrick, J.; Chen, P. Y.; Bodde, S. G.; Yang, W.; Novitskaya, E. E.; Meyers, M. A. *JOM* **2012**, *64*, 449−468.
(62) Bell, E.; Gosline, J. *J. Exp. Biol.* **1996**, *199*, 1005−1017.
(63) Harrington, M. J.; Waite, J. H. *J. Exp. Biol.* **2007**, *210*, 4307−4318.
(64) Krauss, S.; Metzger, T. H.; Fratzl, P.; Harrington, M. J. *Biomacromolecules* **2013**, *14*, 1520−1528.
(65) Rapoport, H. S.; Shadwick, R. E. *Biomacromolecules* **2002**, *3*, 42−50.

(66) Miserez, A.; Wasko, S. S.; Carpenter, C. F.; Waite, J. H. *Nat. Mater.* **2009**, *8*, 910−916.
(67) Fantner, G. E.; Adams, J.; Turner, P.; Thurner, P. J.; Fisher, L. W.; Hansma, P. K. *Nano Lett.* **2007**, *7*, 2491−2498.
(68) Brazee, S. L.; Carrington, E. *Biol. Bull.* **2006**, *211*, 263−274.
(69) Vaccaro, E.; Waite, J. H. *Biomacromolecules* **2001**, *2*, 906−911.
(70) Takei, F.; Kikuchi, Y.; Kikuchi, A.; Mizuno, S.; Shimura, K. *J. Cell Biol.* **1987**, *105*, 175−180.
(71) Brunet, P. C. J.; Coles, B. C. *Proc. R. Soc. London, Ser. B* **1974**, *187*, 133−170.
(72) Marsh, R. E.; Corey, R. B.; Pauling, L. *Biochim. Biophys. Acta* **1955**, *16*, 1−34.
(73) Strzelecki, J. W.; Strzelecka, J.; Mikulska, K.; Tszydel, M.; Balter, A.; Nowak, W. *Cent. Eur. J. Phys.* **2011**, *9*, 482−491.
(74) Keten, S.; Buehler, M. J. *Appl. Phys. Lett.* **2010**, *96*, 153701−153701.
(75) Bratzel, G.; Buehler, M. J *J. Mech. Behav. Biomed. Mater.* **2012**, *7*, 30−40.
(76) Krishnaji, S. T.; Bratzel, G.; Kinahan, M. E.; Kluge, J. A.; Staii, C.; Wong, J. Y.; Buehler, M. J.; Kaplan, D. L. *Adv. Funct. Mater.* **2013**, *23*, 241−253.
(77) Bratzel, G.; Buehler, M. J. *Biopolymers* **2012**, *97*, 408−417.
(78) Buehler, M. J. *Acta Mech. Solida Sin. (Chin. Ed.)* **2010**, *23*, 471−483.
(79) Keten, S.; Buehler, M. J. *Nano Lett.* **2008**, *8*, 743−748.
(80) Keten, S.; Xu, Z.; Ihle, B.; Buehler, M. J. *Nat. Mater.* **2010**, *9*, 359−367.
(81) Buehler, M. J. *Nano Today* **2010**, *5*, 379−383.

# CHAPTER 4

## SELF-RECOVERING CADDISFLY SILK: ENERGY DISSIPATING $Ca^{2+}$-DEPENDENT, DOUBLE DYNAMIC NETWORK FIBERS

The subsequent work authored by Nicholas N. Ashton and Russell J. Stewart, Self-recovering caddisfly silk: energy dissipating, $Ca^{2+}$-dependent, double dynamic network fibers, *Soft Matter*, 2015, 11, 1667-1676, is reproduced with permission of The Royal Society of Chemistry.

Author Contributions: N.N.A. gathered and maintained caddisfly larvae in the lab, constructed the materials test system, performed single fiber mechanical tests, performed infrared spectroscopy, and processed the data. R.J.S. and N.N.A. designed the experiments, interpreted the results, and prepared the manuscript.

Soft Matter

PAPER

View Article Online
View Journal | View Issue



Cite this: *Soft Matter*, 2015, **11**, 1667

# Self-recovering caddisfly silk: energy dissipating, $Ca^{2+}$-dependent, double dynamic network fibers

Nicholas N. Ashton and Russell J. Stewart*

Received 3rd November 2014
Accepted 11th December 2014

DOI: 10.1039/c4sm02435d

www.rsc.org/softmatter

Single fibers of the sticky underwater larval silk of the casemaker caddisfly (*H. occidentalis*) are viscoelastic, display large strain cycle hysteresis, and self-recover 99% of their initial stiffness and strength within 120 min. Mechanical response to cyclical strains suggested viscoelasticity is due to two independent, self-recovering $Ca^{2+}$-crosslinked networks. The networks display distinct pH dependence. The first network is attributed to $Ca^{2+}$-stabilized phosphoserine motifs in H-fibroin, the second to $Ca^{2+}$ complexed carboxylate groups in the N-terminus of H-fibroin and a PEVK-like protein. These assignments were corroborated by IR spectroscopy. The results are consolidated into a multi-network model in which reversible rupture of the $Ca^{2+}$-crosslinked domains at a critical stress results in pseudo-plastic deformation. Slow refolding of the domains results in nearly full recovery of fiber length, stiffness, and strength. The fiber toughening, energy dissipation, and recovery mechanisms, are highly adaptive for the high energy aquatic environment of caddisfly larvae.



## Introduction

Aquatic caddisfly larvae (order Trichoptera) spin an adhesive silk that is used like pressure-sensitive tape for the underwater construction of species-specific composite structures, including stationary retreats and mobile cases assembled with adventitiously gathered stones or plant matter.[1] The diversity and adaptability of caddisfly silk architecture played a key role in the radiation of more than 12 000 species throughout freshwater habitats worldwide.[2] The underwater silk comprises a sticky thin peripheral layer[3,4] encasing an energy dissipating fiber.[5] Single silk fibers from the larvae of the casemaking genus *Hesperophylax*, are highly extensible underwater, more than doubling in length before failure.[5] The silk is elastic at low strains with an initial modulus between 80 and 140 MPa, strain softens dramatically (yields) between 0.02 and 0.05 mm $mm^{-1}$, following which the stress response plateaus before gradually strain hardening before failure around 30 MPa. Cyclically strained fibers displayed considerable load cycle hysteresis, going completely slack when unloaded before recovering within 15 min most of the initial fiber length, initial elastic modulus, and yield point stress.

For many materials, including most metals, moth silk,[6] and tendons,[7] permanent strain setting beyond the yield point limits their structural usefulness to stresses and strains within the pre-yield linear elastic region.[8] These materials efficiently store and transfer energy as reflected in minimal hysteresis during cyclical loading below the yield point. Some synthetic and natural materials that display post-yield strain stiffening are useful in applications where applied stresses are greater than the yield stress. Examples are polycarbonates used in bullet proof glass and spider web silks, both of which yield and plastically deform to absorb and dissipate kinetic energy to bring ballistic objects to a stop with minimized recoil.[9,10] These materials are single use because most of the post-yield deformation is permanent. Recovery of initial mechanical properties of these plastically deformed materials require reprocessing—a cycle of wetting and drying in the case of spider silks.[10] In contrast, spontaneous re-tensioning and yield domain recovery enables caddisfly silk to go through repeated cycles of energy dissipation in its natural watery environment. Self-tensioning repairs the silk composite structures with minimal metabolic investment in reprocessing and reconstruction.[5]

The caddisfly larval silks are similar to other highly extensible, energy-dissipating, self-recovering wet materials, both natural and synthetic. Examples of pseudo-plastic biological materials include the distal region of mussel byssal threads,[11,12] sea snail egg capsules,[13,14] and wet mammalian hair,[15] all of which display non-permanent yield behavior during cyclical extension. Several variations of toughened synthetic energy-dissipating double network hydrogels have been reported that provide insight into the behavior of the natural materials. The common design feature of self-recovering synthetic hydrogels is two independently cross-linked interpenetrating networks: a soft highly extensible elastic network and a stiff brittle sacrificial network formed through non-covalent reversible bonds.[16,17] Mechanical loading ruptures the non-covalent interactions in the stiff sacrificial network at a critical force and extension corresponding to a pseudo-yield point, which results in strain

*Department of Bioengineering, University of Utah, Salt Lake City, Utah 84112, USA. E-mail: russell.stewart@utah.edu; Tel: +1 801 581-8581*

softening as the elastic network is extended. When unloaded, the elastic network provides a restoring force that guides reformation of the non-covalent bonds, allowing the gels to recover their initial dimensions and stiffness. The hydrogels can undergo multiple highly hysteretic cycles to repeatedly dissipate strain energy. Non-covalent interactions used to create reversible sacrificial networks in self-recovering double network hydrogels include hydrophobic interactions,[18] electrostatic attractions between oppositely charged side groups,[19] metal ion complexes,[16,20] and reversible surface absorption to nanoparticles.[21]

The major structural component of caddisfly silk, the H-fibroin protein, comprises an imperfectly repeating pattern of three sub-repeats, designated D, E, and F in casemaker species.[22] Each repeat contains at least one $(pSX)_n$ motif in which pS is phosphoserine, X is usually an aliphatic amino acid or arginine, and $n = 2$–$6$.[5,23] Native caddisfly silk fibers contain exchangeable multivalent metal ions, predominantly $Ca^{2+}$ with lesser amounts of $Mg^{2+}$, $Fe^{2+}$, $Zn^{2+}$, and $Mn^{2+}$, in an approximately equimolar ratio with pS residues.[5,23] The D repeats, which contain two $(pSX)_4$ motifs separated by 11 residues with a central proline, have been modeled as a $Ca^{2+}$-stabilized β-hairpin structure that may further associate into nanoscale $Ca^{2+}$-stabilized β-domains.[5] The structural model is supported by molecular dynamic simulations, and by several experimental approaches: (i) FTIR spectroscopy revealed a decrease in silk fiber β-structure when $Ca^{2+}$ ions were depleted with EDTA,[5] (ii) solid state NMR on $^{13}C$ labeled silk showed the chemical shifts of V residues, which occur almost exclusively in the $(pSX)_n$ motifs of the H-fibroin D and F sub-repeats, are consistent with β-sheet conformations,[24] and, (iii) single fiber mechanical characterization showed exchange of $Ca^{2+}$ with $Na^+$ decreased the initial elastic modulus and tensile strength to approximately 1% of native values, and completely obliterated the yield point and load cycle hysteresis.[5] In the absence of metal ions caddisfly silk fibers behave as soft elastomers displaying little load cycle hysteresis.

Caddisfly larval silk is both an underwater adhesive, in a pressure sensitive tape format, and a tough energy-dissipating structural fiber, two categories of natural materials that are important models for synthetic materials design for use in aqueous environments. Full appreciation of the underwater adhesion of caddisfly silk requires a detailed understanding of both interfacial adhesion and the mechanical properties of the silk fiber backing material. Recoverable yield in the backing material absorbs and dissipates strain energy thereby protecting the adhesive interface from non-recoverable failure. Here, the response of individual caddisfly larval silk fibers to controlled strains combined with IR spectroscopy was used to probe the molecular structure of the silk fibers.

## Experimental section

### Silk harvesting

Final instar larvae of the casemaker *Hesperophylax occidentalis* were collected from the upper Red Butte Creek (Salt Lake County, UT, USA) in the late spring and early summer. Species were identified by larval reference mandibles.[25] Silk was harvested using previously published methods.[4] Briefly, when removed from their cases and provided with ~1 $mm^3$ blocks of PTFE, larvae compulsively attempt to rebuild their cases, which usually results in a disorganized PTFE-silk mass. With a pair of fine forceps, 3–5 mm long silk fibers can be detached from the PTFE blocks for mechanical testing.

### Mechanical testing

Stress–strain analysis of submerged single caddisfly silk fibers mounted in a custom micromaterials test system was previously described.[5] To convert force recordings into engineering stress, the cross-sectional area of five fibers from each of three animals was approximated by measuring the wide diameter of the silk and assuming two identical paired cylindrical subfibers. The average diameters were 14.4 ± 1.4, 15.2 ± 2.8, and 14.8 ± 0.3 μm. The initial length of mounted fibers at zero strain was determined by elongating the fibers until a measureable force was recorded. The actuator motor was programmed with the maximal reliable acceleration and deceleration (5 mm $s^{-2}$). To avoid acceleration artifacts at the beginning of the stress–strain profiles, elongation was initiated while fibers were slack to reach constant velocity before the predetermined initial length at zero strain. The effects of acceleration and deceleration are negligible at the turn around in cyclical stress–strain experiments in all cases except the fastest rates used in the strain rate experiments. Except for analysis of pH-dependent silk mechanical properties described later, all stress–strain experiments were carried out in 1 mM $CaCl_2$ buffered with 5 mM Tris (pH 8.0) to approximate natural water conditions. All test solutions were adjusted to the target pH with either NaOH or HCl using a UB-5 pH meter with a PerpHect Ross microcombination pH electrode standardized with Orion pH 2.0, 4.0, 7.0, and 10.0 reference solutions (Thermo Scientific, MA). Data were processed, analyzed, and plotted using Matlab software (MathWorks, MA). Initial silk fiber modulus was calculated from a linear regression of the elastic pre-yield region of the stress–strain curve. The pseudo-yield point was calculated as the stress and strain at 1% strain offset. Trapezoidal integration was used to calculate the areas under the forward and reverse stress–strain curves as well as compute cycle hysteresis.

### Strain dependence

To characterize the mechanical response to increasing strains at a constant strain rate, a single fiber was cyclically strained at 0.01 $s^{-1}$ with sequentially increasing cycle strains of 0.02, 0.04, 0.08, 0.12, 0.16, 0.20, 0.24, 0.28, 0.32, 0.36, and 0.40 mm $mm^{-1}$ without rest between cycles. The percent energy dissipated in each cycle was calculated from the area within the hysteresis loop divided by the total area under the forward curve. The residual strain of each cycle was determined by the strain at which force registered in the subsequent cycle.

### Strain rate dependence

A single silk fiber was first conditioned by cycling to a strain of 0.3 mm $mm^{-1}$ at 0.0005 $s^{-1}$, allowed to recover for 60 min, and

the initial length was re-measured. In each load cycle the fiber was strained to 0.2 mm mm$^{-1}$ at increasing strain rates of 0.001, 0.0025, 0.050, 0.010, 0.025, 0.05, and 0.10 s$^{-1}$. The yield stress of each cycle was plotted against the log of the strain rate, and fitted with a natural log function using the Matlab curve fitting toolbox (MathWorks, MA).

### pH dependence of mechanics

Fibers mounted on the micromaterials tests system were submerged in a flowchamber, which allowed the test solution to be changed without removing the fiber from solution. This arrangement avoids surface tension strains on the fibers as the test solutions are changed. Three independent fibers were cyclically strained to 0.2 mm mm$^{-1}$ at 0.03 s$^{-1}$ as the pH was progressively decreased between strain cycles. The test solutions contained 5 mM $CaCl_2$ and 1 mm of the following buffers: Tris–HCl (pH 8.0), ammonium bicarbonate (pH 7.0 and 6.0), acetic acid (pH 5.5 and 5.0), formic acid (pH 4.5 and 4.0) and glycine (pH 3.0). The solutions were adjusted to the desired pH with the addition of either NaOH or HCl. After each pH cycle the fiber was allowed to recover for one hour. The fibers were washed three times with an excess of the subsequent cycle test solution. The magnitude of the yield point (yield stress) and residual strain were computed for each cycle of the three fiber tested and normalized as a percentage of the first pH 8 cycle values.

### Recovery rate

A single fiber was repeatedly strained to 0.25 mm mm$^{-1}$ at 0.02 s$^{-1}$ with increasing rest periods between cycles of 0, 0.5, 1.0, 2.0, 5.0, 10.0, 15.0, 20.0, 30.0, 45.0, 60.0, 90, 150, 240, 360, 600, 900, 1440, and 2880 min. Three independent fibers for each resting period were used to determine the kinetics of fiber recovery. Two sets of fibers were strained to 0.20 mm mm$^{-1}$ at 0.03 s$^{-1}$ in either 1 mM $CaCl_2$, 5 mM Tris, pH 8.0 or in 1 mM $CaCl_2$, 5 mM formate, pH 3.5. At pH 8.0, recovery times were 0, 0.033, 0.166, 0.5, 1.0, 2.0, 5.0, 10.0, 15.0, 20.0, 30.0, 45.0, and 60.0 min. At pH 3.5, recovery times were 0, 0.5, 1.0, 2.0, 5.0, 10.0, and 20.0 min. The magnitude of the yield stress, the area of the hysteresis loop, and residual strain were computed for each cycle and normalized to the initial cycle values.

### Infrared spectroscopy

Silk phosphoserine dianionic and monoanionic vibrational modes between 953 and 1300 cm$^{-1}$, and an anionic carboxylate mode between 1305 and 1477 cm$^{-1}$ were used to titrate the respective functional groups using ATR-FTIR. A batch of silk fibers sufficient to fully cover the diamond ATR crystal was sequentially adjusted to lower pH after each scan by washing three times for 20 min with excess buffer solution of appropriate pH. The wet fiber bundle was then clamped to the diamond ATR crystal and wetted around the clamp margins with fresh buffer solution to maintain target pH and prevent dehydration during spectrum collection. Scans were done at pH 8.0, 7.0, 6.0, 5.5, 5.0, 4.5, 4.0, 3.5, 3.0, 2.0, 1.5, and 1.0. These solutions contained 5 mM $CaCl_2$ in 1 mM Tris–HCl (pH 8.0), ammonium bicarbonate (pH 7.0–6.0), acetic acid (pH 5.5–4.5), formic acid (pH 4.0–3.5) or glycine (pH 3.0–1.0).

The three major water absorbance bands, centered at 3500, 1635, and 2120 cm$^{-1}$, do not overlap with either the phosphate (952–1300 cm$^{-1}$) or carboxylate absorbance bands (~1392 cm$^{-1}$) of interest. A weak water absorbance from ~1100 to 953 cm$^{-1}$ overlaps with the phosphate absorbance region. To correct for water absorbance contributions across spectra a water baseline subtraction was performed. The water combination band centered at 2120 cm$^{-1}$ was used to determine water absorbance contribution because dehydrated silk does not absorb from 2500 to 1800 cm$^{-1}$. For each sample spectrum a water reference spectrum was scaled based on the area of the combination band in the hydrated silk sample. The scaled water spectrum was then subtracted from the sample spectrum.

The phosphate (953–1300 cm$^{-1}$) or carboxylate (1305–1477 cm$^{-1}$) absorbance region was isolated from the water corrected spectra and a linear baseline subtraction was applied. The intensity of all spectra were then normalized for the area of the spectra region from 1428–1475 cm$^{-1}$, which comprised absorption bands of pH insensitive side groups including Trp (CH) bending, Trp (CC) stretching, Trp (CN) stretching, and ($CH_3$) bending modes of aliphatic sidechains of Leu, Ile, Val, as well as the methyl groups of Ala, Thr, and Met.[26] For analysis of pS vibrational modes two sets of difference spectra were created by subtracting the pH 8.0 or pH 2.0 spectra from all other spectra. To analyze monoanionic vibrations the pH difference spectra created with respect to pH 8.0 was used whereas analysis of dianionic vibrations used the difference spectra created with respect to pH 2.0. The difference spectra for analysis of the carboxylate vibrational mode were generated by subtracting the pH 1.0 spectrum from all other spectra. The area of the peaks and troughs in the difference spectra were calculated by trapezoidal integration over the following regions: 953–1018, 1018–1061, 1061–1138, 1138–1250, and 1360–1417 cm$^{-1}$. The integrated intensity for each peak was then plotted as a function of sample pH and fitted with a logistic function using the Matlab curve fitting toolbox (MathWorks, MA).

ATR-FTIR absorbance spectra were collected using a Nicolet 6700 spectrometer (Thermo Scientific, FL) with a diamond Smart iTR accessory, a deuterated triglycine sulfate detector, and a KBr/Ge mid-infrared optimized beam splitter. All spectra were recorded with a resolution of 4 cm$^{-1}$ and 512 averaged scans.

## Results and discussion

### Strain dependence of mechanical response

Single native silk fibers display pseudo-yield points near 3.8 MPa stresses and 0.05 mm mm$^{-1}$ strains. It is a pseudo-yield point because the strain softening and deformation beyond the apparent yield is not permanent. Instead, given enough time, the fibers spontaneous recover their initial length and stiffness when unloaded. To further characterize their mechanical response pre- and post-yield, single fibers were cyclically and sequentially strained at 0.03 s$^{-1}$ to increasing strains without resting between cycles at 20 °C (Fig. 1A). During pre-yield strains

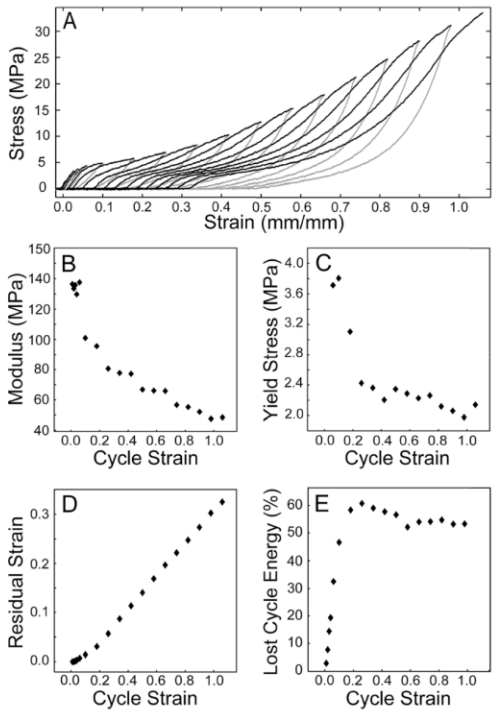


Fig. 1 Cyclical loading with increasing strain. (A) A single fiber was cyclically loaded with progressively increasing strain until failure. Forward (black) and reverse (grey) (B) Initial modulus for progressive cycles calculated by linear regression of the initial slope. (C) Yield stress for progressive cycles calculated using 1% strain offset. (D) Pseudo-plastic deformation represented by residual strain for progressive cycles. (E) The percent energy lost during progressive cycles calculated as the area within the hysteresis loop divided by the total area under the forward curve.

the initial modulus and fiber length changed little between cycles, and there was little hysteresis in the load cycle, which demonstrated the fiber responded elastically to small strains (Fig. 1B, D and E). Post-yield, the initial modulus declined sharply just beyond the yield strain, then decreased linearly as the strain increased (Fig. 1B). Yield-like strain softening was still apparent even in the shortest duration strain cycles after the first yield point. The second yield stress declined abruptly to ~65% of the first yield stress at a post-yield strain of 0.24 mm $mm^{-1}$, then gradually decreased ~12% over the remaining strain cycles (Fig. 1C). The change in fiber length at the beginning of each progressive cycle from the beginning length of the previous cycle was normalized to the initial fiber length and plotted as residual strain (Fig. 1D). Residual strain in the elastic region before the yield point is negligible, whereas post-yield pseudo-plastic deformation is linearly dependent on the degree of cycle strain. Strain energy dissipation rose rapidly from near 0% during the elastic cycles, to a peak of about ~60% by 0.15 mm $mm^{-1}$ strain, then declined slightly over the remaining cycles (Fig. 1E).

We interpret the response of the fibers to increasing strain, with two pseudo-yield points, as evidence of two distinct populations of yield domains, with different pre-yield moduli and yield stresses that comprise two parallel, pseudo-plastic networks. Accordingly, at low pre-yield strains, the elastic modulus of the fiber is dominated by the stiffer of the two networks. At a critical stress, the fiber yields when the weakest domains in the population rupture. At post-yield strains, the end of cycle stress initially plateaued as nearly identical members of the domain population sequentially ruptured and unfolded, then gradually increased with increasing strain as stronger members of the population were loaded. The less pronounced yield behavior in strain cycles beyond the first yield point was due to rupture of domains in the second network. Compared to the first network domains, the second network domains are less stiff, yield at lower stress, and recover rapidly when unloaded. Both networks are $Ca^{2+}$-ion dependent because EDTA exchange of $Ca^{2+}$ completely destroyed both yield behaviors leaving a soft elastic fiber with no yield or hysteresis in strain cycles.[5] Beyond the first yield point, the residual strain increased linearly with strain with a slope of ~0.33, which suggests a linearly proportionate number of domains ruptured for a given strain, with each domain revealing a consistent hidden length. The area within the forward and reverse curves peaked near 0.2 mm $mm^{-1}$ strain, then remained fairly constant with a slight downward trend until the fiber failed at over 1.0 mm $mm^{-1}$, which suggests the additive energy absorbed by the yield domains, then dissipated through rupture, was constant. The double $Ca^{2+}$-dependent network hypothesis will be further elaborated in the following discussion, and is diagrammed in Fig. 6.

### Strain rate dependence

To study the effect of strain rate on silk fiber mechanics, a single fiber was cyclically loaded to 0.2 mm $mm^{-1}$ strain at 20 °C with increasing strain rates ranging over two decades from 0.001–0.10 $s^{-1}$ (Fig. 2A). The fibers were allowed to fully recover between cycles. A strain of 0.20 mm $mm^{-1}$ was beyond the pseudo-yield point, well into the stress plateau region, and therefore sufficient to characterize the strain rate effect on initial modulus and pseudo-yield point. At high strain rates, velocity profiles at the end of the strain cycles (0.2 mm $mm^{-1}$) are distorted due to unavoidable deceleration/acceleration of the driver motor. The initial modulus and yield point regions of the forward stress–strain curves were not affected by acceleration effects (see Methods). Strain rate had little effect on the initial elastic modulus, which averaged 131.6 ± 19.5 MPa for all strain rate cycles. The yield stress, on the other hand, exhibited logarithmic dependence on strain rate, more than doubling from 2.5 to 5.6 MPa over the range of strain rates (Fig. 2B).

Similar to single caddisfly silk fibers, a number of thermoplastics, including polyvinyl chloride, polymethyl methacrylate,

 

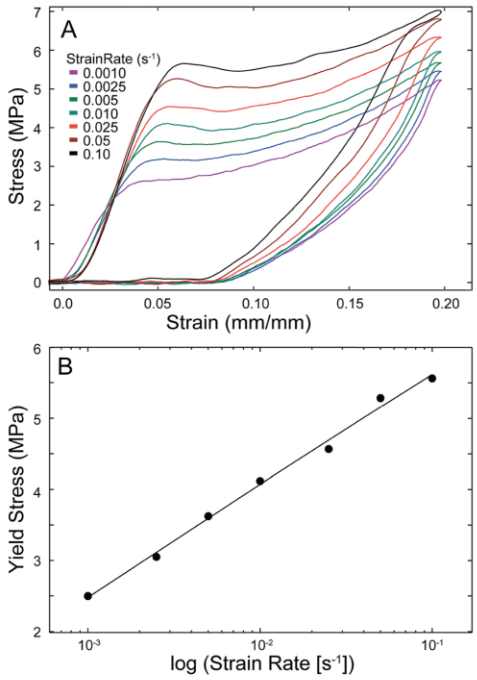


Fig. 2 Strain rate dependence of yield stress. (A) Stress strain profiles of a single fiber cyclically loaded to 0.2 mm mm$^{-1}$ strain with increasing strain rate with a 60 min rest period between cycles. (B) Logarithmic relationship of yield stress to strain rate. $R^2$ of fitted line >0.99.

and polycarbonate, display similar logarithmic relationships between yield stress and strain rate.[27,28] The mechanical responses of these materials to strain rate has been analyzed using Eyring's transition state theory of viscous flow.[29,30] Eyring's theory is predicated on pre-yield and post-yield molecular conformations with different energy states separated by an energy barrier. Mechanical strain provides the activation energy required to surmount the energy barrier between the two conformations. Eyring's equation can be expressed in terms of tensile yield stress ($\sigma_y$) and axial strain rate ($\dot{e}$), as

$$\frac{\sigma_y}{T} = \tilde{A}\left[\ln\left(2\tilde{C}\dot{e}\right) + \frac{\Delta G}{RT}\right], \quad (1)$$

where $T$ is absolute temperature, $R$ is the universal gas constant, $\tilde{A}$ and $\tilde{C}$ are lumped parameters, and $\Delta G$ is the transition energy.[28] The equation predicts the yield stress will depend linearly on the log of the strain rate for a transformation involving a single activated process, or, in other words, a single type of molecular transformation. The log relationship between strain rate and first yield stress (Fig. 2) is consistent with a single, consistent rupture mode of the first yield domain.

### pH dependence of mechanical properties

The functional groups responsible for the pseudo-plastic dynamic networks were probed by characterizing the pH dependence of silk fiber mechanical properties. Representative stress–strain curves for a single fiber cyclically loaded to 0.2 mm mm$^{-1}$ strain at successively lower pH starting at pH 8.0 is shown in Fig. 3A. The rest period between cycles was 60 min, sufficient time for nearly full recovery of native fiber mechanics between cycles (Fig. 3). The average yield stress, and residual strain for three independent silk fibers showed sigmoidal dependence on pH down to pH 3.0 (Fig. 3B and C). The residual strain is negative at low pH because the fibers shrank, resulting in measurable stress at lengths less than the initial pH 8.0 length. The inflection points of the sigmoidal plots, corresponding to the p$K_a$ of the protonated functional groups, were at pH 4.6 and 4.4, respectively. $R^2$ values for both fitted equations were >0.99. The tight fit to a single function suggested the mechanical transition between pH 8.0 and 3.0 was due to protonation of a single type of functional group in the silk fiber with an effective p$K_a$ of ~4.5.

During strain cycles at pH 3.5, where pSs are nearly all in the monoanionic form, yield behavior and strain cycle hysteresis were still obvious (Fig. 3A). The pH 3.5 strain cycles were reminiscent of the strain cycles beyond the first yield point where the first network domains begin to rupture (Fig. 1). In other words, at pH 3.5 network 2 appeared to be still mostly intact and retained ~35% of the pH 8.0 yield stress, whereas network 1 was mostly disrupted. During strain cycles at pH 2.0, yield behavior disappeared entirely and the initial modulus was reduced to ~10% of the pH 8.0 value. The mechanical behavior at pH 2.0 was similar to the effect of exchanging $Ca^{2+}$ with EDTA at pH 8.0, which completely obliterated yield behavior and reduced the initial modulus to about 1% of native fibers.[5] At pH 2.0 both networks were disrupted.

### pH dependence of IR spectra

ATR-FTIR spectroscopy was used to correlate mechanical pH response with protonation of silk fiber phosphate and carboxylate sidechains. The p$K_a$ of silk phosphates, absorbance region (953–1300 cm$^{-1}$), was determined using a single batch of silk fibers buffered at progressively lower pH from 8.0 to 2.0 (Fig. 4A). To accentuate bands in the phosphate spectral region that changed with pH, difference spectra were created by subtracting the pH 8.0 spectrum from the other spectra (Fig. 4B). As the pH was stepped from 8.0 to 2.0, two dianionic phosphate bands, one centered at 1095 cm$^{-1}$ and a double band in the region 975–1020 cm$^{-1}$, decreased in intensity as the intensity of two monoanionic phosphate bands centered at 1036 and 1177 cm$^{-1}$ increased. These peak assignments are consistent with assignments reported for other phosphoproteins, including phosvitin, ovalbumin, and α-casein.[31–33] The double dianionic symmetric stretching mode bands at 975 and 1010 cm$^{-1}$ in native caddisfly silk is due to two populations of pS, one population complexed with $Ca^{2+}$ and the other uncomplexed (Fig. 4).[5,32,33] Absorbance bands of both populations decreased proportionately as the pH was lowered, therefore the two bands

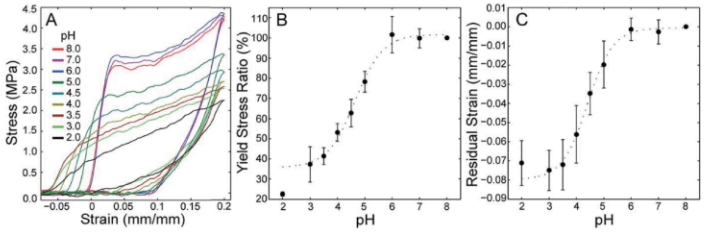


Fig. 3 pH-dependence of mechanical properties. (A) A representative stress–strain profile of a single silk fiber successively cycled in solutions of decreasing pH from 8.0 to 2.0 (B) the average percent change in yield-stress as pH is decreased from 8.0–2.0 (filled circles). Error bars represent the s.d, $n = 3$. The data, excluding pH 2.0, were fitted with a sigmoidal curve (dashed line). (C) The average residual strain of three separate silk fibers (filled circles) *vs.* pH. The data, excluding pH 2.0, were fitted with a sigmoidal curve (dashed line). Error bars represent the s.d, $n = 3$.

were integrated together from 953–1018 $cm^{-1}$. The integrated intensities of the four pS bands showed sigmoidal responses to changing pH (Fig. 4C). The fitted curves had $R^2$ values $\geq 0.98$. The inflection points, corresponding to the p$K_a$ of the phosphate groups of pS, ranged from pH 4.3 to 4.7 with an average of pH $4.4 \pm 0.15$.

The protonation of pS residues had a virtually identical sigmoidal response, over the same pH range, as the mechanical properties of single silk fibers. This result confirmed the functional group responsible for the first yield point was phosphate in the $(pSX)_n$ domains. The apparent p$K_a$ of the silk fiber phosphates is nearly three pH units below the p$K_{a2}$ of free phosphate, and more than one pH unit below the reported p$K_{a2}$ of pS in ovalbumin and phosvitin.[31,32,34] The acidic shift of the phosphate p$K_{a2}$, the resistance to protonation of pS in H-fibroin $(pSX)_n$ domains compared to free phosphate, is not due to complexation of phosphates and $Ca^{2+}$ ions. This is evident from the identical pH responses of the $Ca^{2+}$ complexed (995 $cm^{-1}$) and uncomplexed (976 $cm^{-1}$) dianionic peaks (Fig. 4). In addition, the phosphate p$K_{a2}$ was previously shown to lie between 4 and 5 in silk fibers largely depleted of $Ca^{2+}$ with EDTA.[5] Other factors in the local environment of the $(pSX)_n$ domains must be responsible for the p$K_a$ shift.

The p$K_a$ of silk carboxylate groups were similarly determined using ATR-FTIR spectroscopy for a single batch of silk fibers buffered progressively lower from pH 5.0 to 1.0 (Fig. 4D). Assignment of the carboxylate symmetric stretching mode, centered at 1389 $cm^{-1}$, was based on precedent literature.[26,35–38]

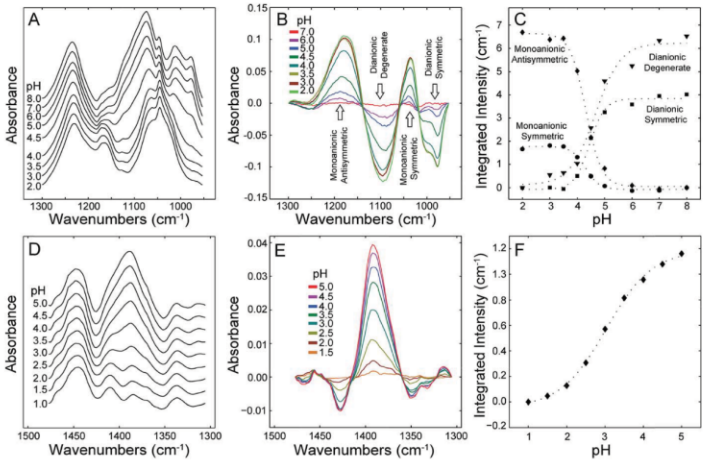


Fig. 4 Determination of silk phosphate and carboxylate p$K_a$s by ATR-FTIR. (A) Absorbance spectra of the silk phosphate region from 953–1300 $cm^{-1}$ in solutions of progressively decreasing pH from 8.0–2.0. (B) Phosphate difference spectra created by subtracting the pH 8.0 spectrum from all other spectra. Arrows and labels identify pH sensitive absorbance bands and are color coded to correspond with integrated intensities in C. (C) The integrated intensities of the indicated phosphate absorbance bands (symbols) fitted with sigmoidal curves (dashed lines). (D) Absorbance spectra of the silk carboxylate symmetric stretching mode centered at 1389 $cm^{-1}$ analyzed from pH 5.0–1.0. (E) Difference spectra of the carboxylate symmetric stretching mode created by subtracting the pH 1.0 spectrum from all other spectra. (F) The integrated intensity of the monoanionic carboxylate symmetric stretching mode (diamonds) fitted with a sigmoidal curve (dashed line).

Difference spectra were created to accentuate the carboxylate bands changing with pH by subtracting the pH 1.0 spectrum from the other spectra (Fig. 4E). The integrated intensity of the carboxylate absorbance band from 1360–1417 $cm^{-1}$ showed a sigmoidal pH dependence (Fig. 4F). The fitted curves had a $R^2$ values >0.99. The inflection point, corresponding to the p$K_a$ of silk fiber carboxylates, occurred at pH 3.0.

### Kinetics of mechanical recovery

Unlike the permanent strain setting observed for dry terrestrial silks strained past their yield points,[39] aquatic caddisfly silk display time-dependent strain and yield-point recovery.[5] The time-dependent recovery of caddisfly silk fiber mechanical properties at pH 8.0 is illustrated in Fig. 5A–C. To determine the kinetics of recovery at pH 8.0, three independent single silk fibers for each rest period were cycled to 0.20 mm $mm^{-1}$ strain at 20 °C. A total of 30 independent fibers were used to generate the recovery time courses (Fig. 5). A representative selection of stress–strain cycles at varying stages of recovery, normalized by the maximum stress of the first cycle, are shown in Fig. 5A. Silk fiber residual strain recovered with biphasic kinetics; a rapid recovery process was superimposed on a much slower recovery process (Fig. 5B). Likewise, cycle hysteresis increased with similar biphasic kinetics reaching 95% recovery within 120 min (Fig. 5C). The biphasic recovery kinetics is consistent with at least two parallel networks with substantially different recovery kinetics.

By testing fibers at a pH below the pS p$K_a$ and above the carboxylate p$K_a$, the contribution of the $Ca^{2+}$-bridged carboxylate network to fiber mechanics was characterized separately from the $Ca^{2+}$-bridged pS network. The recovery of residual strain and load cycle hysteresis for a series of fibers tested at pH 3.5 was much faster than full recovery of native fibers at pH 8.0 (Fig. 5D–F). Fig. 5D shows a representative selection of stress–strain cycles at varying stages of recovery when tested at pH 3.5. Full recovery occurred within 10–20 min compared to two hours for native fibers (Fig. 5E and F). At pH 3.5, the recovery profile of residual strain and hysteresis appeared to be consistent with a single process.

### Comparison to synthetic double network hydrogels

The underwater silks of caddisfly larvae have remarkable structural and mechanical similarities to synthetic super tough hydrogels designed with networks of reversible sacrificial bonds entwined with elastic networks to facilitate post-yield recovery. The synthetic double network hydrogel most similar to caddisfly silk in mechanical properties were prepared by random copolymerization of high concentrations of quaternary amine and sulfonate monomers to create an ionically crosslinked physical network of ampholytic polymers.[19] The pseudo-yield and hysteresis during strain cycles, imparting toughness, was attributed to the random ionic bonds having a wide distribution of bond energies. A population of stronger ionic bonds formed a static network that responded elastically to large strains, while a population of weaker ionic bonds formed a dynamic sacrificial network that yielded and deformed at a critical stress. The elastic network directed the reformation of the dynamic network during unloading. The initial modulus of the stiffest polyampholyte hydrogels was 8 MPa, failure stress of the strongest was 1.8 MPa. These values correspond to 140 and 33

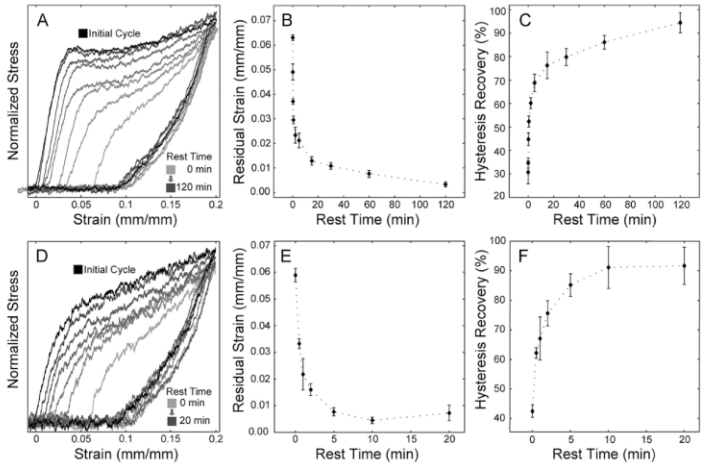


Fig. 5 Post-yield time-dependent recovery of silk mechanics. For each rest time data point (filled circles), 3 fibers were cycled to 0.2 mm $mm^{-1}$ strain at a strain rate of 0.03 $s^{-1}$. (A–C) Silk fibers were tested at a native pH 8.0. (A) Representative normalized stress strain curves at pH 8.0 with 0, 0.5, 5, 15, 30, 60, and 120 min rest periods. (B) Biphasic time dependent fiber length recovery. (C) Biphasic load cycle energy dissipation recovery. (D–F) Silk fibers were tested below the phosphoserine p$K_a$ and above the carboxyl p$K_a$ at pH 3.5. (D) Representative normalized stress–strain curves at pH 3.5 with 0, 0.5, 1, 2, 5, and 20 min rest periods. (E) Time dependent fiber length recovery. (F) Time dependent recovery of load cycle energy dissipation. Error bars represent the s.d, $n = 3$. The dashed line connecting the data points (diamonds) are to guide the eye.

MPa, respectively, for caddisfly silk, which is nearly 20-fold stiffer and stronger. Both materials recover their original strength and dimensions with similar biphasic kinetics, achieving nearly complete recovery within 120 min. The polyampholyte hydrogels, however, were much more extensible with strain at failure of 750%, compared to 100–150% for caddisfly silk fibers.[5] As a result, the work of extension to failure is similar, ~7 and ~17 MJ $m^{-3}$ for the hydrogels and caddisfly silk, respectively. Double network hydrogels with a static acrylamide network and dynamic hydrophobic lamella network had similar initial moduli, failure stress, and biphasic recovery kinetics as the polyampholyte hydrogels.[18] Other self-recovering double network hydrogels had initial moduli and stress at failure three orders of magnitude less than caddisfly silk, and fractional recoveries after much longer times.[16,20,21]

### A model

The results are consolidated in the mechanical model in Fig. 6. Caddisfly silk is conceptualized as a multi-network fiber, with two distinct dynamic networks of serial $Ca^{2+}$-stabilized domains acting in parallel (Fig. 6A and B). The stiffer and stronger dynamic network comprises phosphate complexed $Ca^{2+}$ domains, likely assembled from the $[(pSX)_4]_2$ β-hairpin motifs that are repeated approximately 100 times in each H-fibroin protein.[5] The $[(pSX)_4]_2$ motifs may assemble into nm-scale β-domains, on the order of ten per H-fibroin protein, creating intra- and intermolecular $Ca^{2+}$-bridged network connections. If so, molecular details of the rupture mode are difficult to predict because of the number of potential interactions within the $Ca^{2+}$-stabilized domains described earlier. Initial rupture could be due to delamination of stacked β-sheets, fraying of individual β-sheets, or unraveling of D-repeat $[Ca^{2+}(pSX)_4]_2$ β-hairpins. Rupture of the weakest interaction could lead to cooperative disintegration of other interactions and complete or partial unfolding. Mixed intra- and intermolecular rupture modes may account in part for the distribution of domain stabilities. Comparatively slow reformation of the domains upon unloading accounts for the slow phase of fiber recovery.

The second dynamic network in the model, with lower initial spring constant and pseudo-yield stress, comprises carboxylate complexed $Ca^{2+}$ domains (Fig. 6A and B). The $Ca^{2+}$-carboxylate network may be formed by a proline-rich protein, recently

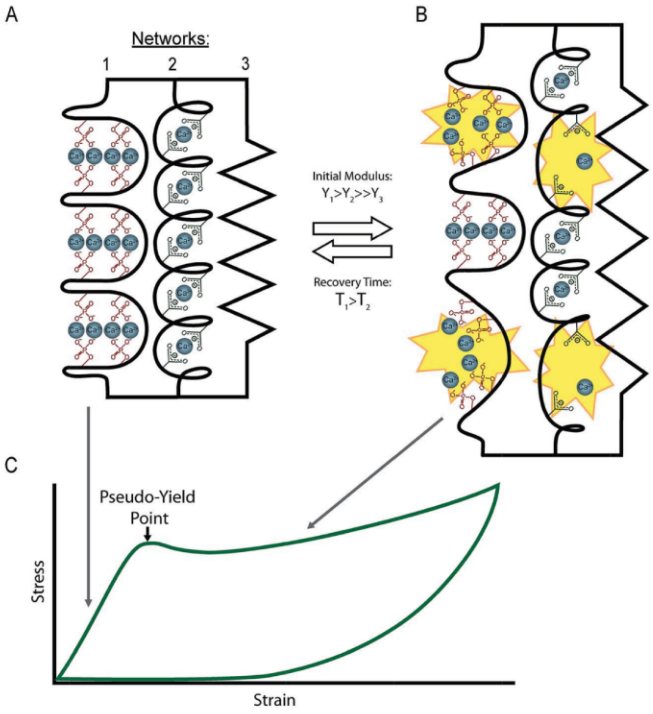


Fig. 6 Multi-network model of caddisfly silk. Silk fibers comprise two parallel $Ca^{2+}$-bridged non-covalent networks and a covalent elastic network. Spheres represent $Ca^{2+}$ ions. (A) Prior to yield, the $Ca^{2+}$-phosphate and $Ca^{2+}$-carboxylate networks respond elastically. (B) Beyond the first yield point, $Ca^{2+}$-crossbridged phosphate and carboxylate networks undergo sacrificial rupture (yellow symbols) and dissipate strain energy. When unloaded, the sacrificial networks gradually reform enabling multiple cycles of energy dissipation. (C) A schematic single cycle stress–strain curve, at pH 8.0, correlating silk fiber molecular structure with mechanical response to tensile load.

reported to be a component of caddisfly silk, that contains 18.9 and 2.4 mol% glutamic and aspartic acid residues, respectively.[40] The caddisfly silk proline-rich protein has an amino acid composition similar to the elastic PEVK region of the muscle protein, titin, which has been predicted to form a random coil entropic spring.[41,42] The titin PEVK region binds $Ca^{2+}$ ions, which affects the mechanical properties of the protein.[43,44] Another candidate component of the $Ca^{2+}$-carboxylate network is the non-repetitive N-terminus of caddisfly H-fibroin, which contains 10.2 and 7.5 mol% glutamic and aspartic acid residues, respectively.[5] The caddisfly silk PEVK-like protein may be networked with itself and/or the H-fibroin N-terminus through $Ca^{2+}$-mediated carboxylate crosslinking.

The model contains a soft and elastic third network. In the absence of $Ca^{2+}$, the fibers are weak and elastic, but do not completely disintegrate perhaps do to covalent crosslinks that may comprise the third network (Fig. 6A and B). The fibers are thought to contain disulfide crosslinks between H- and L-fibroins,[45] as well as a radially inhomogeneous distribution of dityrosine crosslinks that form a peripheral shell around the fiber core.[40] Dityrosine crosslinking is catalyzed by a peroxidase enzyme after the silk is drawn from the silk glands. In effect, the fibers may behave like an elastic, covalently crosslinked tube filled with viscoelastic, dynamically crosslinked material.

## Conclusion

Casemaker caddisfly species, such as *H. occidentalis* described in this study, spend most of their lifecycle at the margins of fast moving rivers and streams. The unique mechanical properties of their adhesive silk fibers are highly adaptive for construction of composite structures in their high energy niche. At low strains and high strain rates, the fibers are stiff to resist deformation. At higher strains, non-elastic deformation of the fiber beyond the pseudo-yield point absorbs strain energy to protect the interfacial adhesive bonds from non-recoverable failure. Spontaneous recovery of the initial stiffness and strength allows the silk fibers tying the structure together to undergo repeated cycles of strain dissipation without re-processing. The toughness and self-recovery of the best synthetic multi-network hydrogels approach the strength and toughness of natural caddisfly silk fibers. Perhaps incorporation of structural features from the natural silk fibers will lead to synthetic soft materials that far exceed the mechanical properties of the natural materials.

## Acknowledgements

The authors thank Professor Jeff Weiss for helpful discussions. Funding from the Army Research Office is gratefully acknowledged.

## References

1 G. B. Wiggins, *Caddisflies: The Underwater Architects*, University of Toronto Press, Toronto, 2004.
2 R. W. Merritt, K. W. Cummins and M. B. Berg, *An introduction to the aquatic insects of North America*, Kendall Hunt Pub. Co., Dubuque, Iowa, 4th edn, 2008.
3 M. S. Engster, *Cell Tissue Res.*, 1976, **169**, 77–92.
4 N. N. Ashton, D. S. Taggart and R. J. Stewart, *Biopolymers*, 2012, **97**, 432–445.
5 N. N. Ashton, D. R. Roe, R. B. Weiss, T. E. Cheatham and R. J. Stewart, *Biomacromolecules*, 2013, **14**, 3668–3681.
6 N. Du, Z. Yang, X. Y. Liu, Y. Li and H. Y. Xu, *Adv. Funct. Mater.*, 2011, **21**, 772–778.
7 M. Abrahams, *Med. Biol. Eng.*, 1967, **5**, 433–443.
8 B. D. Ratner, *Biomaterials science: an introduction to materials in medicine*, Academic Press, 2004.
9 N. A. Fleck, W. J. Stronge and J. H. Liu, *Proc. R. Soc. London, Ser. A*, 1990, **429**, 459–479.
10 M. Elices, G. V. Guinea, J. Pérez-Rigueiro and G. R. Plaza, *Mater. Sci. Eng., C*, 2011, **31**, 1184–1188.
11 S. Krauss, T. H. Metzger, P. Fratzl and M. J. Harrington, *Biomacromolecules*, 2013, **14**, 1520–1528.
12 M. J. Harrington, H. S. Gupta, P. Fratzl and J. H. Waite, *J. Struct. Biol.*, 2009, **167**, 47–54.
13 H. S. Rapoport and R. E. Shadwick, *J. Exp. Biol.*, 2007, **210**, 12–26.
14 F. D. Fischer, M. J. Harrington and P. Fratzl, *New J. Phys.*, 2013, **15**, 065004.
15 J. W. S. Hearle, *J. Mater. Sci.*, 2007, **42**, 8010–8019.
16 J.-Y. Sun, X. Zhao, W. R. K. Illeperuma, O. Chaudhuri, K. H. Oh, D. J. Mooney, J. J. Vlassak and Z. Suo, *Nature*, 2012, **489**, 133–136.
17 D. Myung, D. Waters, M. Wiseman, P.-E. Duhamel, J. Noolandi, C. N. Ta and C. W. Frank, *Polym. Adv. Technol.*, 2008, **19**, 647–657.
18 M. A. Haque, T. Kurokawa, G. Kamita and J. P. Gong, *Macromolecules*, 2011, **44**, 8916–8924.
19 T. L. Sun, T. Kurokawa, S. Kuroda, A. Bin Ihsan, T. Akasaki, K. Sato, M. A. Haque, T. Nakajima and J. P. Gong, *Nat. Mater.*, 2013, **12**, 932–937.
20 K. J. Henderson, T. C. Zhou, K. J. Otim and K. R. Shull, *Macromolecules*, 2010, **43**, 6193–6201.
21 S. Rose, A. Dizeux, T. Narita, D. Hourdet and A. Marcellan, *Macromolecules*, 2013, **46**, 4095–4104.
22 N. Yonemura, F. Sehnal, K. Mita and T. Tamura, *Biomacromolecules*, 2006, **7**, 3370–3378.
23 R. J. Stewart and C. S. Wang, *Biomacromolecules*, 2010, **11**, 969–974.
24 J. B. Addison, N. N. Ashton, W. S. Weber, R. J. Stewart, G. P. Holland and J. L. Yarger, *Biomacromolecules*, 2013, **14**, 1140–1148.
25 C. R. Parker and G. B. Wiggins, *Can. J. Zool.*, 1985, **63**, 2443–2472.
26 A. Barth and C. Zscherp, *Q. Rev. Biophys.*, 2002, **35**, 369–430.
27 E. Dogliotti and W. Yelland, *J. Appl. Polym. Sci.*, 1964, **8**, 211–235.
28 J. C. Bauwens, C. Bauwens-Crowet and G. Homes, *J. Polym. Sci., Part A-2*, 1969, **7**, 1745–1754.
29 H. Eyring, *J. Chem. Phys.*, 1936, **4**, 283.

30 D. Mulliken and M. C. Boyce, *Int. J. Solids Struct.*, 2006, **43**, 1331–1356.
31 J. M. Sanchez-Ruiz and M. Martinez-Carrion, *Biochemistry*, 1988, **27**, 3338–3342.
32 W. J. Goux and P. N. Venkatasubramanian, *Biochemistry*, 1986, **25**, 84–94.
33 C. Fernández, S. F. Ausar, R. G. Badini, L. F. Castagna, I. D. Bianco and D. M. Beltramo, *Int. Dairy J.*, 2003, **13**, 897–901.
34 H. J. Vogel and W. a Bridger, *Biochemistry*, 1982, **21**, 394–401.
35 K. J. Rothschild, Y.-W. He, D. Gray, P. D. Roepe, S. L. Pelletier, R. S. Brown and J. Herzfeld, *Proc. Natl. Acad. Sci. U. S. A.*, 1989, **86**, 9832–9835.
36 M. Mizuguchi, M. Nara, K. Kawano and K. Nitta, *FEBS Lett.*, 1997, **417**, 153–156.
37 M. Mizuguchi, M. Nara, Y. Ke, K. Kawano, T. Hiraoki and K. Nitta, *Eur. J. Biochem.*, 1997, **250**, 72–76.
38 G. B. Deacon and R. J. Phillips, *Coord. Chem. Rev.*, 1980, **33**, 227–250.
39 Y. Liu, Z. Shao and F. Vollrath, *Biomacromolecules*, 2008, **9**, 1782–1786.
40 C.-S. Wang, N. N. Ashton, R. B. Weiss and R. J. Stewart, *Insect Biochem. Mol. Biol.*, 2014, **54**, 69–79.
41 E. H. Lee, J. Hsin, O. Mayans and K. Schulten, *Biophys. J.*, 2007, **93**, 1719–1735.
42 A. Nagy, L. Grama, T. Huber, P. Bianco, K. Trombitás, H. L. Granzier and M. S. Z. Kellermayer, *Biophys. J.*, 2005, **89**, 329–336.
43 D. Labeit, K. Watanabe, C. Witt, H. Fujita, Y. Wu, S. Lahmers, T. Funck, S. Labeit and H. Granzier, *Proc. Natl. Acad. Sci. U. S. A.*, 2003, **100**, 13716–13721.
44 R. Tatsumi, K. Maeda, A. Hattori and K. Takahashi, *J. Muscle Res. Cell Motil.*, 2001, **22**, 149–162.
45 N. Yonemura, K. Mita, T. Tamura and F. Sehnal, *J. Mol. Evol.*, 2009, **68**, 641–653.

# CHAPTER 5

# CONNECTING CADDISWORM SILK STRUCTURE AND MECHANICAL PROPERTIES: COMBINED INFRARED SPECTROSCOPY AND MECHANICAL ANALYSIS



Authors Contributions: N.N.A. gathered and maintained caddisfly larvae in the laboratory, performed single fiber mechanical tests and infrared spectroscopy, and processed data. H.P. performed peptide synthesis and mass spectrometry. R.J.S. and N.N.A. designed the experiments, interpreted the results, and prepared the manuscript.

OPEN BIOLOGY

rsob.royalsocietypublishing.org

Research

**Cite this article:** Ashton NN, Pan H, Stewart RJ. 2016 Connecting caddisworm silk structure and mechanical properties: combined infrared spectroscopy and mechanical analysis. *Open Biol.* **6**: 160067.
http://dx.doi.org/10.1098/rsob.160067

Received: 18 March 2016
Accepted: 16 May 2016

**Subject Area:**
biochemistry/biophysics/structural biology

**Keywords:**
silk, bioadhesive, $Ca^{2+}$-phosphoserine complexes, caddisfly

**Author for correspondence:**
Russell J. Stewart
e-mail: russell.stewart@utah.edu

Electronic supplementary material is available at http://dx.doi.org/10.1098/rsob.160067.

THE ROYAL SOCIETY PUBLISHING

# Connecting caddisworm silk structure and mechanical properties: combined infrared spectroscopy and mechanical analysis

Nicholas N. Ashton, Huaizhong Pan and Russell J. Stewart

Department of Bioengineering, University of Utah, Salt Lake City, Utah 84112, USA

The underwater silk of an aquatic casemaking caddisfly larvae (*Hesperophylax occidentalis)* is viscoelastic, and displays distinct yield behaviour, large strain cycle hysteresis and near complete recovery of its initial strength and stiffness when unloaded. Yield followed by a stress plateau has been attributed to sequential rupture of serial $Ca^{2+}$-cross-linked phosphoserine (pS) β-domains. Spontaneous recovery has been attributed to refolding of the $Ca^{2+}$/pS domains powered by an elastic network. In this study, native $Ca^{2+}$ ions were exchanged with other metal ions, followed by combined mechanical and FTIR analysis to probe the contribution of pS/metal ion complexes to silk mechanical properties. After exchange of $Ca^{2+}$ with $Na^{+}$, the fibres are soft elastomers and the infrared spectra are consistent with $C_{v3}$ symmetry of the $-OPO_3^{2-}$ groups. Multivalent metal ions decreased the $-OPO_3^{2-}$ symmetry and the symmetric stretching modes ($v_s$) split in a manner characteristic of ordered phosphate compounds, such as phosphate minerals and lamellar bilayers of phosphatidic acid lipids. Integrated intensities of the $v_s$ bands, indicative of the metal ion's effect on transition dipole moment of the P–O bonds, and thereby the strength of the phosphate metal complex, increased in the order: $Na^{+} < Mg^{2+} < Sr^{2+} < Ba^{2+} < Ca^{2+} < Eu^{3+} < La^{3+} < Zn^{2+} < Fe^{2+}$. With a subset of the metal ion series, the initial stiffness and yield stress of metal ion-exchanged fibres increased in the same order: $Na^{+} \ll Mg^{2+} < Ca^{2+} < La^{3+} < Zn^{2+} \approx Fe^{2+}$, establishing the link between phosphate transition dipole moments and silk fibre strength.

## 1. Introduction

Aquatic caddisfly larvae (order Trichoptera) use sticky silk fibres like adhesive tape to construct protective shelters with species-specific designs using species-specific materials [1]. Casemakers, such as the species used in this study (*Hesperophylax occidentalis)*, tape together adventitiously gathered stones into transportable body armour. The silk comprises a thin adhesive coating on a tough nanofibrous core. The adhesive coating contains glycoproteins and a peroxidase enzyme, which can catalyze covalent cross-linking to natural surface-active polyphenolic compounds as part of the adhesion mechanism [2]. The fibrous core is stiff (80–200 MPa) at low strains but dramatically softens, or yields, at 2–4% elongation, after which the stress plateaus. The fibres stiffen again before fracture at 100%–120% elongation. The work of elongation to fracture of approximately $17.3 \pm 6.2$ MJ $m^{-3}$ is impressive for a fully hydrated biphasic material; the silk is tougher than tendon collagen [3], articular cartilage and the best synthetic double network hydrogels [4,5]. The abrupt softening at low strains is transient; silk fibres cyclically strained between 0% and 20% elongation fully and repeatedly recover their initial stiffness and yield stress within 120 min after unloading [6]. Significant for the caddisworm's lifestyle, the mechanical yield and stress plateau of the fibres shields the adhesive joints between fibre and substrate from irreversible damage, and repeated dissipation of strain energy without degradation of the silk's mechanical properties maintains the integrity of the composite case in its turbulent mountain stream environment.

The molecular basis for reversible yield of the silk fibres has been attributed to the sequential viscous unravelling of a serial network of $Ca^{2+}$-cross-linked phosphoserine (pS) domains [6,7]. When unloaded, the mechanically denatured domains refold, guided by the memory of an elastic covalent network, resulting in nearly complete spontaneous recovery of the fibre's initial stiffness and strength [6]. The major structural protein of the fibre core by molecular mass (greater than 300 kg $mol^{-1}$) and total mass, H-fibroin, comprises three imperfectly alternating repeats, which contain at least one $(pSX)_n$ motif, where pS is phosphoserine, X is usually an aliphatic residue or arginine and $n$ is usually 4 or 5 [6,8]. In total, casemaker H-fibroins contain approximately 13 mol% pS residues. The occurrence of phosphorylated H-fibroin serines in all three caddisfly suborders points to the importance of the modification to caddisworm underwater silk structure and function throughout the order [8–10]. The proposal that H-fibroin $(pSX)_n$ motifs form a network of $Ca^{2+}$-stabilized β-domains as the principal toughening mechanism of caddisworm silk is supported by multiple lines of experimental evidence. First, infrared (IR) and NMR spectroscopy, as well as X-ray scattering studies, showed decreased β-structure when $Ca^{2+}$ was exchanged with $Na^+$ [7,11,12]. Second, $Ca^{2+}$-depleted silk fibres behaved mechanically like weak elastomers, with the initial stiffness decreased to 1% of native silk fibres, with no yield-like strain softening and no strain cycle hysteresis [7]. Third, a sharp pH-dependent decrease in fibre stiffness and strength coincided with protonation of H-fibroin phosphate groups as measured by IR spectroscopy [6].

Here, we describe experiments intended to further probe the relationship between the molecular structure and viscoelastic properties of caddisworm silk wherein native $Ca^{2+}$ ions were exchanged with $Na^+$, $Mg^{2+}$, $Zn^{2+}$, $Fe^{2+}$, $Eu^{3+}$, $La^{3+}$, $Sr^{2+}$ and $Ba^{2+}$ ions. The stress response to controlled strains of fibres exchanged with a subset of these metal ions were correlated by Fourier transform infrared (FTIR) spectroscopy with effects on peptidyl-phosphate vibrational stretching modes, including frequency shifts, band splitting and integrated band intensities.

# 2. Material and methods

## 2.1. Silk harvesting

Fifth instar larvae of the casemaker *H. occidentalis* were collected just prior to pupation in the early summer in upper Red Butte Creek (Salt Lake County, UT, USA). Larvae were maintained in the laboratory and silk fibres were harvested from Teflon blocks as previously described [10].

## 2.2. Peptide synthesis

A $(pSX)_4$ sequence (VpSIpSRpSVpSI) from the H-fibroin D-repeat was synthesized by solid phase peptide synthesis using standard Fmoc chemistry on 2-chlorotrityl chloride resin [13]. HBTU (2-(1*H*-benzotriazol-1-yl)-1,1,3,3-tetramethyluronium hexafluorophosphate) was used as the coupling agent and 20% piperidine in dimethylformamide (DMF) as the deprotection agent for Fmoc protected amino acids. Trifluoroacetic acid (TFA), triisopropylsilane (TIS), piperidine and DMF were from Sigma-Aldrich (Milwaukee, WI). *N*-α-Fmoc protected amino acids (Fmoc-AA-OH), *N*-α-Fmoc-*O*-benzyl-L-phosphoserine (Fmoc-Ser(PO(OBzl)OH)-OH) and 2-Cl-trityl chloride resin (100–200 mesh, 1.27 mmol $g^{-1}$) were from EMD Biosciences (San Diego, CA). HBTU was from Advanced ChemTech (Louisville, KY). The peptide was cleaved from the resin with TFA/$H_2O$/TIS (95/2.5/2.5) for 2 h. Yield was 150 mg (81%). The mass of the peptide was 659.7 g $mol^{-1}$. A five wt% solution of the peptide in DI-$H_2O$ was adjusted to pH 9.0 with 6 M NaOH and lyophilized to obtain the $Na^+$ salt of the synthetic peptide. The $Ca^{2+}$ salt was prepared by adding $CaCl_2$ to precipitate the synthetic peptide, which was then lyophilized.

## 2.3. Metal ion exchange

To exchange native $Ca^{2+}$ with other metal ions, clean silk fibres were submerged for 1 h at ambient temperature in excess volumes of 10 mM solutions of the chloride salts of $Mg^{2+}$, $Zn^{2+}$, $Fe^{2+}$, $Eu^{3+}$, $La^{3+}$, $Sr^{2+}$ and $Ba^{2+}$ buffered with 1 mM Bis-Tris and adjusted to pH 7.0 with NaOH. Multivalent metal ion exchange was facilitated by including 50 mM NaCl in the exchange solutions. The exchanged fibres were then equilibrated for 1 h in excess solutions containing 1 mM of the test metal chloride, plus 1 mM NaCl, 1 mM Bis-Tris and adjusted to pH 7.0 with NaOH. Fibres exchanged with $Na^+$ were incubated for 1 h in 10 mM $Na^+$-EDTA, 50 mM NaCl and 1 mM Bis-Tris (pH 7.0), then equilibrated in 1 mM NaCl, 1 mM EDTA and 1 mM Bis-Tris (pH 7.0). For elemental and attenuated total reflectance (ATR)-FTIR analysis, bundles of fibres were exchanged in bulk. For mechanical testing, metal ions were exchanged after single fibres were mounted in a submersion chamber on the material test system.

## 2.4. Elemental analysis by ICP-OES

Bundles of fibres were rinsed thoroughly with DI-$H_2O$ after metal ion exchange, lyophilized, dissolved in 40% nitric acid, analysed in triplicate by inductively coupled plasma optical emission spectrometry (ICP-OES) and the metal ions and P quantified by comparison to commercial standards (PerkinElmer, Optima 3100XL). Metal ion concentrations are reported as molar ratios to P to normalize the mass of fibres in each sample. After normalization, the propagated error is given by the fractional total deviation.

## 2.5. Mechanical testing

Isolated single silk fibres, 3–4 mm in length, were mounted on the fixtures of a custom micromaterials test system with Loctite 3301 UV cure adhesive, then submerged in an immersion chamber [6,7]. As described earlier, metal ion exchange for mechanical testing was done after single silk fibres were mounted in the immersion chamber. During mechanical tests, fibres were submerged in excess solutions of 1 mM of the test metal chloride or 1 mM $Na^+$-EDTA. The test solutions contained 1 mM NaCl and 1 mM Bis-Tris and were adjusted to pH 7.0 with NaOH. The initial length of each mounted fibre was determined by pulling it taut until a measureable force was detected. The wide diameter of 10 fibres from each of the two larvae used in the study were optically measured under 100× magnification and used to approximate the cross-sectional area of the paired-fibre silk ribbons as 15.5 ± 1.4 and 13.6 ± 1.4 µm, for larva 1 and 2, respectively. Engineering stress was calculated assuming that the silk ribbons comprised two identical paired cylindrical sub-fibres. For all experiments the strain rate was 0.03 $s^{-1}$. The maximum reliable acceleration/deceleration for the actuator motor, 5 mm $s^{-2}$,

was used. Elongation was initiated while the fibres were slack so that constant velocity was reached before the fibres were loaded. The initial silk fibre modulus, pseudo-yield stress, cycle hysteresis and toughness were computed from the force-elongation profiles with MATLAB (MathWorks) software as previously described [6].

### 2.6. Single fibres strained to fracture

For each metal ion tested, five fibres were strained until complete rupture while submerged in the 1 mM metal ion test solutions described earlier (pH 7.0). The average of the five force–elongation profiles was plotted as a solid line with the standard deviation represented by shading. Mechanical tests were reported as force rather than engineering stress because $Na^+$-exchanged silk fibres swelled fourfold in cross-sectional area [7]. Although the volume of the biphasic fibres changed, the number of covalent load-bearing cross-links did not change and it was therefore not appropriate to divide the force by the cross-sectional area.

### 2.7. Cyclical strains

A single silk fibre was first conditioned by cycling to 20% elongation and back in 1 mM CaCl, 1 mM NaCl and 1 mM Bis-Tris (pH 7.0) to replicate the natural hard water habitat of caddisworms. After a 2 h recovery period, the initial length of the fibre was re-measured. After the conditioning cycle, the initial length changed by 0.4% elongation. When conditioned fibres were subsequently cycled four times to 20% elongation with a 2 h rest between each cycle, there were negligible changes in the initial modulus, yield stress and cycle hysteresis between progressive cycles. Therefore, all fibres were first conditioned by cycling to 20% elongation in 1 mM CaCl solution, allowed to fully recover for 2 h and the initial length was re-measured.

To determine the effects of metal ion exchange on fibre mechanical properties, conditioned fibres were first cycled to 20% elongation one time in 1 mM $CaCl_2$, 1 mM NaCl and 1 mM Bis-Tris (pH 7.0) solution to establish a mechanical baseline. Subsequent measurements of the mechanical parameters—initial stiffness, yield stress, cycle hysteresis and maximum stress at 20% elongation—after metal ion exchange are reported as percentage changes from the $Ca^{2+}$ baseline mechanical parameters for that individual fibre. Mechanical tests of ion-exchanged silk fibres were performed while the fibres were submerged in the 1 mM metal chloride test solutions buffered with Bis-Tris at pH 7.0. Mechanical measurements were repeated with three fibres for each metal ion species tested. To simplify the visual representation of the 15 different fibres tested, the area within the control cycle hysteresis loops was normalized to the average hysteresis loop for all 15 control cycles. The normalized exchange cycles were then averaged for each ion species ($n = 3$) and plotted $\pm$ s.d.

### 2.8. ATR-FTIR spectroscopy of silk phosphoserines

The effect of metal ion exchange on the dianionic phosphate symmetric ($\nu_s$) and ($\nu_a$) and asymmetric stretching modes, which occur between 914–1186 $cm^{-1}$, were monitored by ATR-FTIR. Metal ion-exchanged fibre bundles were clamped to the ATR crystal and excess solution was applied around the clamp to prevent dehydration. Multivalent metal ion-exchanged fibres were buffered at pH 7.0 with 1 mM Bis-Tris. At this pH the phosphates were fully deprotonated because monoanionic stretching modes were absent. $Na^+$ exchanged fibres were fully deprontonated at pH 9.0 (1 mM Tris-HCl).

ATR-FTIR absorbance spectra were collected using a Nicolet 6700 spectrometer (Thermo Scientific, FL) with a diamond Smart iTR accessory, a deuterated triglycine sulfate detector and a KBr/Ge mid-infrared optimized beamsplitter. All spectra were recorded with a resolution of 4 $cm^{-1}$ and 512 averaged scans. The silk spectra were corrected for water absorbance contributions and normalized using the area of the spectral region from 1428–1475 $cm^{-1}$ containing absorption bands of pH insensitive side groups including Trp (CH) bending, Trp (CC) stretching, Trp (CN) stretching and $CH_3$ bending mods of aliphatic sidechains like Leu, Ile, Val, Ala, Thr and Met using previously described methods [6]. The spectral region containing the serine phosphate symmetric and asymmetric absorbance modes, 914–1186 $cm^{-1}$, was deconvolved with Gaussian curves using PEAKFIT software (Systat Software Inc.). A linear baseline with a 3% tolerance was applied and local minima in the second derivative were used to place the initial Gaussian constituents. The peak position, height and width were allowed to vary during the iterative least-square method employed in the PEAKFIT software thereby minimizing the residuals between the fitted and experimental spectra. The $Na^+$ and $Ca^{2+}$ phosphoserine salt spectra were adjusted with a linear baseline and the two peak areas from 924–1211 $cm^{-1}$ were normalized to the average.

## 3. Results

### 3.1. Metal ion exchange

Silk fibres isolated from natural water contain multivalent metal ions in an approximately 1 : 1 molar ratio to phosphate groups [7,8]. $Ca^{2+}$ is most abundant, followed by $Mg^{2+}$, with much smaller ratios of $Fe^{2+}$ and $Zn^{2+}$. To exchange native metal ions with other multivalent ions, the fibres were incubated in a relatively high concentration, 10 mM, of the exchange ion. Inclusion of 50 mM NaCl in the exchange solution facilitated exchange. After metal ion exchange, the metal ion to P molar ratio was nearly 1 : 1 for Mg and Ca, higher for Zn and substantially higher for Fe (table 1). The high Fe/P ratios may have been due to iron hydroxide precipitation at pH 7.0 and entrapment within the fibres. To exchange the high affinity multivalent ions with low affinity monovalent $Na^+$, the fibres were incubated with the chelator sodium EDTA to compete with the high affinity phosphate binding sites for multivalent ions.

### 3.2. IR spectroscopy of silk phosphoserine/metal ion complexes

The region of the IR spectrum from 800–1200 $cm^{-1}$ contains absorption bands due to stretching modes of the P–O bonds of phosphate [14]. The number of IR-active P–O stretching vibrations is determined by the molecular symmetry of the phosphate group [15]. Changes in the number of bands upon metal complexation is indicative of changes in molecular symmetry and therefore provides information on the coordination environment of phosphate groups [16,17]. The frequencies and

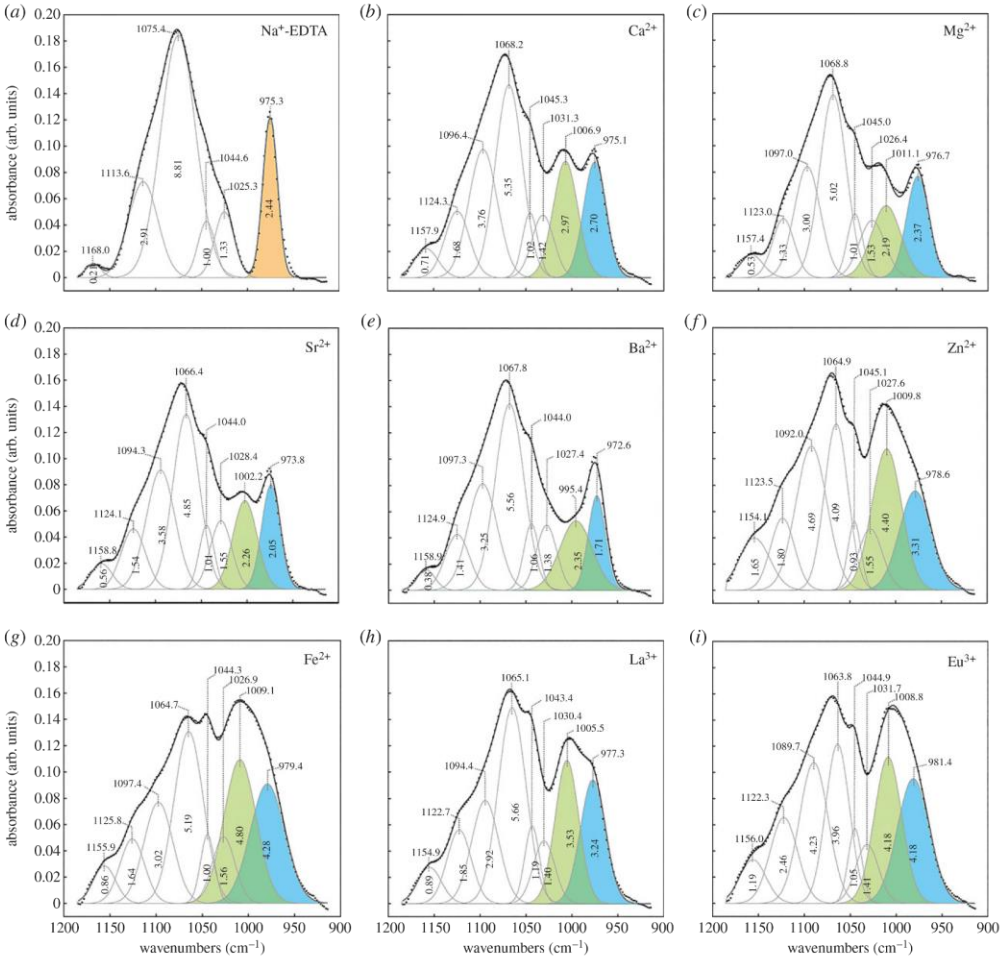


**Figure 1.** Effects of metal ions on peptidyl phosphate stretching modes. (*a–i*) Gaussian-fitted spectra of *Hesperophylax occidentalis* silk exchanged with the indicated metal ion and analysed in the hydrated state by ATR-FTIR. The split dianionic phosphate $\nu_s$ bands, $\nu_{s1}$ and $\nu_{s2}$, are shaded blue and green, respectively, for multivalent metal ions. All spectra were collected at pH 7.0 except (*a*), which was collected at pH 9.0.

**Table 1.** Metal to phosphorus molar ratios. Averages of three independent samples (mean ± fractional total deviation). Shaded values highlight the concentration of the intended exchange ion.

| | | exchange metal | | | | |
|---|---|---|---|---|---|---|
| measured metal | native silk[a] | Na[a] | Mg | Ca | Zn | Fe |
| Mg | 0.12 ± 0.01 | 0.01 ± 0.00 | 1.17 ± 0.06 | 0.02 ± 0.00 | 0.01 ± 0.00 | 0.02 ± 0.00 |
| Ca | 0.83 ± 0.09 | 0.13 ± 0.07 | 0.09 ± 0.04 | 0.90 ± 0.10 | 0.00 ± 0.03 | 0.17 ± 0.04 |
| Zn | 0.09 ± 0.01 | 0.02 ± 0.01 | 0.12 ± 0.00 | 0.12 ± 0.01 | 1.64 ± 0.13 | 0.11 ± 0.02 |
| Fe | 0.01 ± 0.01 | 0.04 ± 0.04 | 0.00 ± 0.00 | 0.01 ± 0.00 | 0.01 ± 0.00 | 5.14 ± 0.14 |

[a]Data from Ashton *et al.* [6].

intensities of the vibrational bands are sensitive to bonding interactions, such as (de)protonation, H-bonding and complexation with metal ions. Coupling of vibrational modes in periodic structures—factor group splitting—can change the number, frequency and intensity of the bands [18].

Fully deprotonated, the pyramidal $-PO_3^{2-}$ moiety of phosphoserine, with three resonance hybrid P–O bonds, has $C_{v3}$ symmetry with two IR-active stretching vibrations, a P–O symmetric stretch and a P–O doubly degenerate asymmetric stretch [14]. A normalized and background subtracted AT-FTIR spectrum from 900–1200 $cm^{-1}$ of hydrated silk fibres depleted of multivalent metal ions with $Na^+$ EDTA, at pH 9, is shown in figure 1*a*. Consistent with $C_{v3}$ symmetry, the 1075 $cm^{-1}$ band was assigned to the degenerate asymmetric

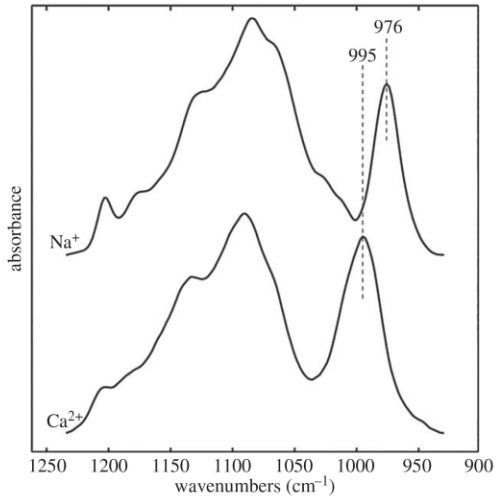


**Figure 2.** Phosphate IR spectra of $Na^+$ and $Ca^{2+}$ salts of synthetic $(pSX)_4$ peptide. The dianionic phosphate $v_s$ band shifted to higher frequency in the $Ca^{2+}$ salt relative to the $Na^+$ salt.

stretch ($v_{as}$) and the 975 $cm^{-1}$ band was assigned to symmetric stretch ($v_s$) [19]. The weaker bands at 1168, 1114, 1045 and 1025 $cm^{-1}$ were not assigned.

In $Ca^{2+}$-containing fibres, the frequency of the 975 $cm^{-1}$ $v_s$ band was unchanged and its integrated intensity increased (figure 1*b*). Two bands at 1068 and 1096 $cm^{-1}$, referred to as $v_{as1}$ and $v_{as2}$, appeared in place of the 1075 $cm^{-1}$ $v_{as}$ band. A new band appeared at 1007 $cm^{-1}$ with similar integrated intensity as the 975 $cm^{-1}$ $v_s$ band. The appearance of two asymmetric stretching modes was evidence that the $-PO_3$ symmetry of the phosphoserines was decreased to $C_{v2}$ or lower by $Ca^{2+}$ complexation. The similarity of the 1007 and 975 $cm^{-1}$ bands to phosphate compounds with periodic structures, discussed later, suggested that the 1007 $cm^{-1}$ band may have arisen from factor group splitting; the bands are therefore referred to as $v_{s1}$ and $v_{s2}$. A phosphopeptide (VpSIpSRpSVpSI) corresponding to a $(pSX)_4$ motif from H-fibroin was synthesized to investigate whether the unique IR spectra of caddisworm silk was due to local sequence effects, e.g. alternating phosphoserines. Similar to other phosphoproteins, the $v_s$ band shifted to 995 from 976 $cm^{-1}$ in $Ca^{2+}$ versus $Na^+$ without the appearance of new bands (figure 2).

ATR-FTIR spectra of fibres exchanged with $Mg^{2+}$, $Sr^{2+}$, $Ba^{2+}$, $Zn^{2+}$, $Fe^{2+}$, $La^{3+}$ and $Eu^{3+}$ were qualitatively similar to $Ca^{2+}$ fibres with regard to the number of IR bands, and therefore their qualitative effects on the symmetry of the $-PO_3^{2-}$ group were similar (figure 1*c–i*). The frequency of the $v_{s2}$ band had a nearly linear dependence on the ionic radius of the multivalent metal ions (figure 3*a*) [20]. By contrast, the integrated intensity of the combined $v_{s1}$ and $v_{s2}$ bands was not dependent on ionic radius, but rather depended on the electronegativity of the multivalent metal ions, with the exceptions of $Mg^{2+}$ and $Zn^{2+}$ (figure 3*b*).

ATR-FTIR spectra from 900–1800 $cm^{-1}$ of the metal ion-exchanged fibres (electronic supplementary material, figure S1) include the amide I region, which provides information on protein secondary structure. There was no discernible difference between the multivalent metal ions in the amide I region of the

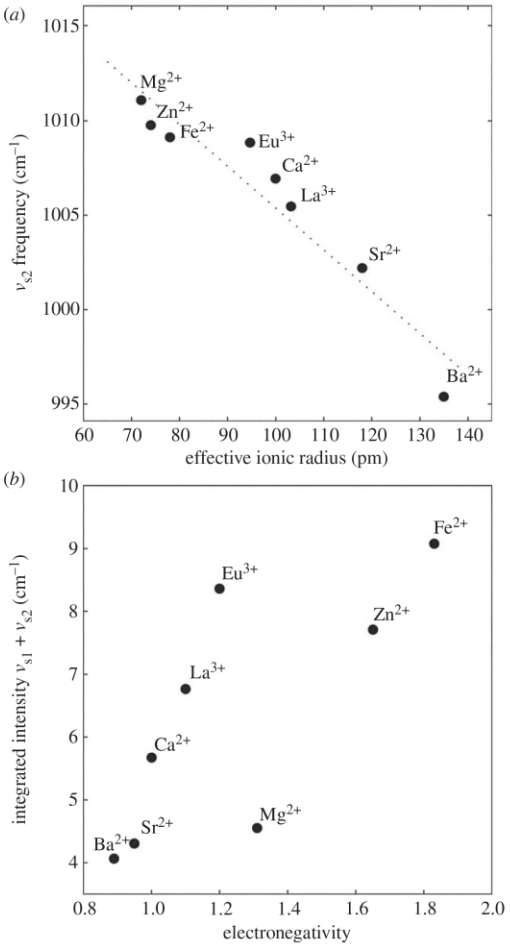


**Figure 3.** Dianionic phosphate $v_s$ mode frequency and integrated intensity versus metal ion properties. (*a*) Ionic radius versus the $v_{s2}$ band frequency. (*b*) Electronegativity versus the integrated area under the $v_{s1}$ and $v_{s2}$ bands.

normalized and water-corrected spectra. We conclude there was not a significant effect of the tested multivalent metal ions on caddisworm silk β-sheet content. The effect on secondary structure as discerned by deconvolution of the amide I region when $Ca^{2+}$ is exchanged with $Na^+$ was previously published [6].

## 3.3. Mechanical assay of metal ion exchange effects on silk fibre structure

Strong differential effects of multivalent metal ions on silk fibre mechanical properties were apparent in comparisons of the force–elongation profiles of silk fibres exchanged with $Na^+$ to fibres exchanged with divalent metal ions (figure 4*a*). All mechanical tests were done at pH 7.0. The average initial stiffness of the $Na^+$-exchanged fibres, 0.09 mN, was 1% of the stiffness of native and $Ca^{2+}$-exchanged fibres and 0.5% of the stiffest $Zn^{2+}$-exchanged fibres (figure 4*b*). The yield behaviour, interpreted molecularly as cooperative unfolding of serial H-fibroin domains comprising metal/phosphate complexes [6,7], was completely eliminated by depletion of multivalent

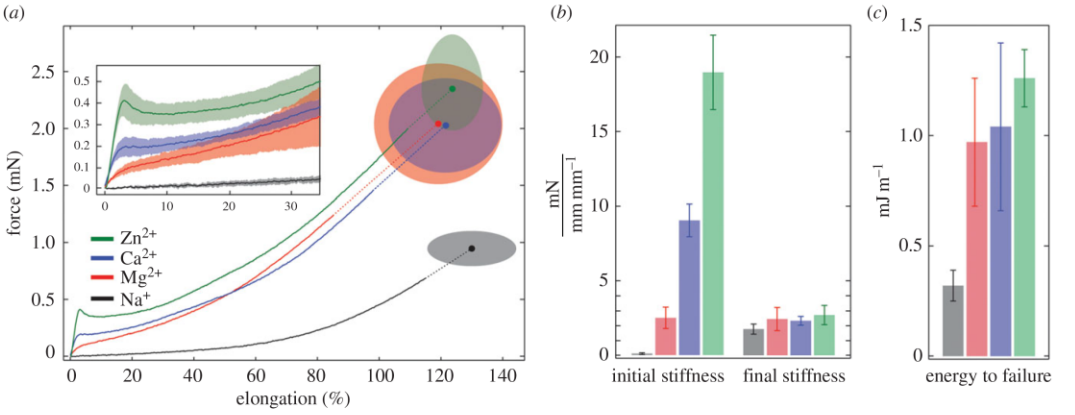


**Figure 4.** Metal ion-exchanged single silk fibres strained to fracture. (*a*) The average force–elongation profiles of fibres exchanged with the indicated metal ion then pulled to fracture (solid lines). The average fracture forces and strains are indicated by the symbol and $\pm 1$ s.d. by the shaded ellipses. $n = 5$ for each metal ion. Shading in the inset shows the standard deviations in the pseudo-yield region from 0% to 35% elongation. (*b*) The initial pre-yield stiffness and final stiffness just before failure are represented in units of force over strain. (*c*) The total energy absorbed before failure is reported per unit length of the fibre. In (*b*) and (*c*) the colours are the same as in panel (*a*).

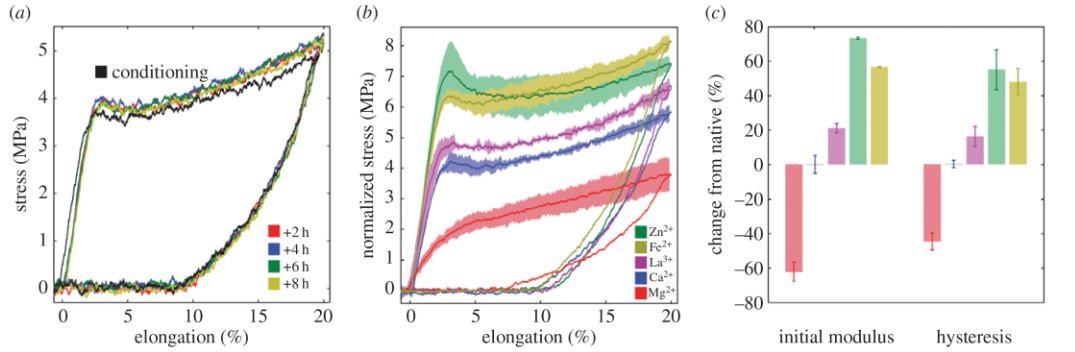


**Figure 5.** Cyclical strains of native and of ion-exchanged single silk fibres. (*a*) After the first conditioning cycle to 20% of a native fibre (black curve), subsequent cycles were superimposable on one another (coloured). The fibres were rested, unstrained, for 2 h between cycles. (*b*) The average cyclical force–elongation profile of three fibres exchanged with the indicated ion (solid lines). The shaded bands represent the s.d. ($n = 3$). (*c*) The percentage change in initial modulus and hysteresis from the control cycle values. Error bars represent the s.d. ($n = 3$).

cations. The $Na^+$-exchanged fibres progressively strain stiffened toward the end of elongation before fracture (figure 4*b*) similar to elastomeric rubbers [21], and broke at slightly higher average elongations, $130 \pm 14\%$, than divalent metal ion fibres, $119–124 \pm 10–21\%$ (figure 4*a*). Removing divalent metal ions revealed the covalent elastic network that provides a restoring force for spontaneous fibre recovery [4].

Comparing divalent metal ions to one another, the initial stiffness, yield force, and work to fracture (toughness) increased in the order of the expected stability of the metal ion/phosphates complexes: $Mg^{2+} < Ca^{2+} < Zn^{2+}$ [3,22]. The average initial stiffness increased 660%, from 2.5 to 9.0 to 19.0 mN, the average yield force increased 430%, from 0.08 to 0.19 to 0.40 mN and the average work to fracture increased only 29.8%, from 0.97 to 1.04 to 1.26 mJ $m^{-1}$ over the series (figure 4*a–c*). Work to fracture is presented for fibre length rather than fibre volume because the biophasic fibre cross-sectional area increases fourfold when divalent ions are exchanged with $Na^+$ [7]. The total amount of material and the number of load-bearing covalent bonds is unchanged in the $Na^+$ silk fibres swollen by an increase in the water phase. Beyond the yield point and force plateau, the divalent metal ion species had insignificant effects on the shape of the force–elongation profile. All three divalent cations displayed a similar magnitude of strain hardening before fracture, elongation at fracture, and fracture force (figure 4*a*,*b*). The final fibre stiffness was nearly independent of the metal ion, including $Na^+$, which demonstrated that the divalent metal/phosphate stabilized domains were completely unfolded toward the end of the force–elongation profile. The increasing work to fracture (toughness) over the divalent metal ion series (figure 4*c*) was due almost entirely to the pre-yield region of the force–elongation curves, which demonstrated the importance of the $Ca^{2+}$/phosphate domain structure on fibre toughness.

## 3.4. Cyclical strains

Single native fibres were strained to 20% elongation at 2 h intervals to evaluate recovery of the fibre's initial mechanical properties after repeated strains (figure 5*a*). At the beginning of the second cycle, the fibre's unstrained initial length

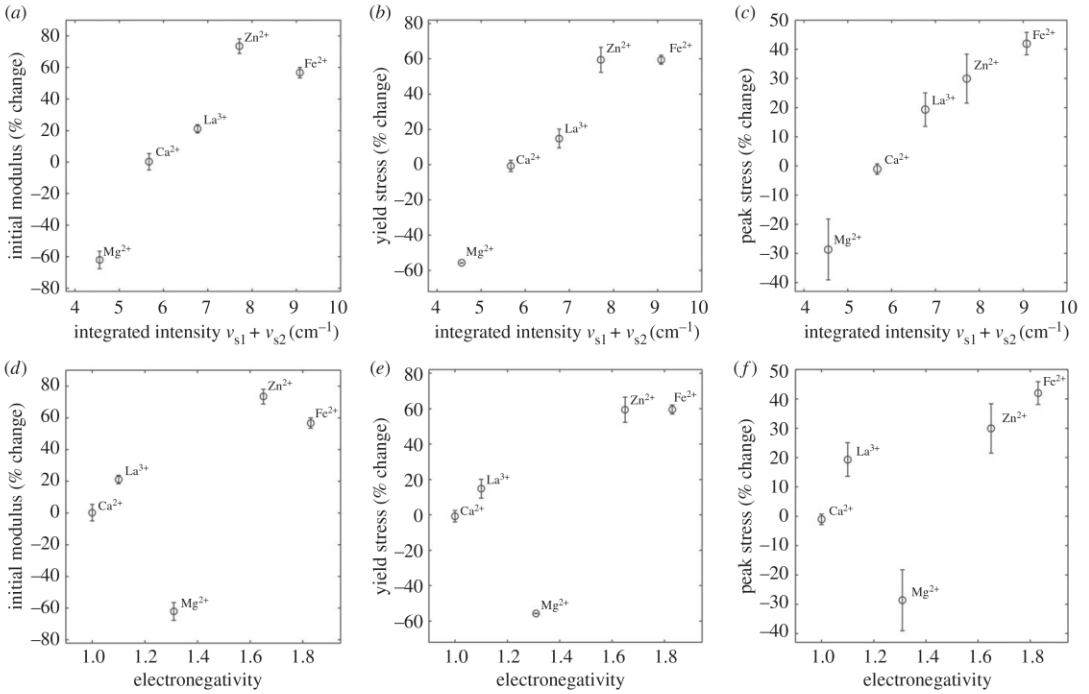


**Figure 6.** Correlating mechanical properties with phosphate vibrational spectra. (*a–c*) Mechanical properties of the silk including initial modulus, yield stress and maximum stress depend on the integrated intensity of the phosphate symmetric stretching modes. (*d–f*) The mechanical properties of the silk depend on electronegativity of the metal ion, with the exception of $Mg^{2+}$. Error bars represent the s.d. ($n = 3$). (*d–f*).

decreased by only 0.4% compared to the initial length at the beginning of the first cycle. After the first cycle, the initial stiffness and yield stress increased by approximately 7%. The second cycle and all subsequent cycles were nearly superimposable, demonstrating highly efficient recovery of the fibres from pseudo-plastic yield and repetitive energy dissipation during cyclical strains. Based on these observations, in all subsequent experiments native fibres were subjected to a single conditioning cycle before ion exchange. The highly reproducible mechanical response of conditioned single fibres to cyclical strains allowed baseline parameters to be established for an individual fibre in 1 mM $CaCl_2$ solution before evaluating the effects of metal ion exchange on the same fibre. This minimized effects of natural variability from fibre to fibre and animal to animal.

The initial stiffness, yield stress, maximum stress and magnitude of the hysteresis increased following the order: $Mg^{2+} < Ca^{2+} < La^{3+} < Zn^{2+} \approx Fe^{2+}$ (figure 5*b*,*c*). $Mg^{2+}$ exchange decreased the strength and toughness of the fibres relative to the $Ca^{2+}$ baseline, although reversible yield behaviour was still apparent and recovery of initial length was faster (figure 5*b*). Fibres exchanged with $Ca^{2+}$ changed by 1% or less in all parameters, as expected because native fibres contain mostly $Ca^{2+}$. Exchange of with $La^{3+}$, $Zn^{2+}$ and $Fe^{2+}$, on the other hand, all increased fibre strength and the magnitude of cyclical energy dissipation due to the hysteretic response to cyclical loads (figure 5*c*).

### 3.5. Correlating mechanics with IR spectroscopy

The effect of the multivalent metal ions on the frequency of the $v_s$ modes was uncorrelated with their effects on the mechanical properties of the fibres. Therefore, the ionic radius of the metal ions did not determine their mechanical effects on the fibres. On the other hand, the effect of the multivalent metal ions on the integrated intensities of both the $v_{s1}$ and the $v_{s2}$ bands paralleled their mechanical effect on the fibres (figure 6*a–c*). Integrated intensities of the $v_{s1}$ (blue peaks, figure 1) and $v_{s2}$ modes (green peaks, figure 1) more than doubled, increasing in the order $Mg^{2+} < Sr^{2+} < Ba^{2+} < Ca^{2+} < Eu^{3+} < La^{3+} < Zn^{2+} < Fe^{2+}$. Though the group of metal ions was smaller, the stiffness and strength of the fibres, as reflected in the initial modulus, yield stress and maximum stress, increased in the same order: $Mg^{2+} < Ca^{2+} < La^{3+} < Zn^{2+} \approx Fe^{2+}$.

## 4. Discussion

The effect of $Ca^{2+}$ on the phosphate IR spectra of caddisworm silk fibres, particularly the splitting of the $v_s$ band, is atypical of phosphoproteins, though there are only a few studies in the literature for comparison. When $Na^+$ was replaced by $Ca^{2+}$ or other multivalent metal ions in the phosphoproteins $\alpha_s$-casein [23,24] and hen egg yolk phosvitin [25], the $v_s$ bands corresponding to the 975 cm$^{-1}$ band of caddisworm silk shifted 10–20 cm$^{-1}$ higher, but a second band $v_s$ did not appear. These phosphoproteins have metal ion sequestration and storage functions; the metal ions do not have a structural role [26]. Similarly, the $-PO_3$ $v_s$ band of hexaphosphorylated inositol (phytic acid) shifted to 996 from 972 cm$^{-1}$ in $Ca^{2+}$ versus $Na^+$ without the appearance of new bands [27]. The $v_s$ band of the synthetic $(pSX)_4$ phosphopeptide also shifted to 995 cm$^{-1}$ from 976 cm$^{-1}$ without the appearance of a new

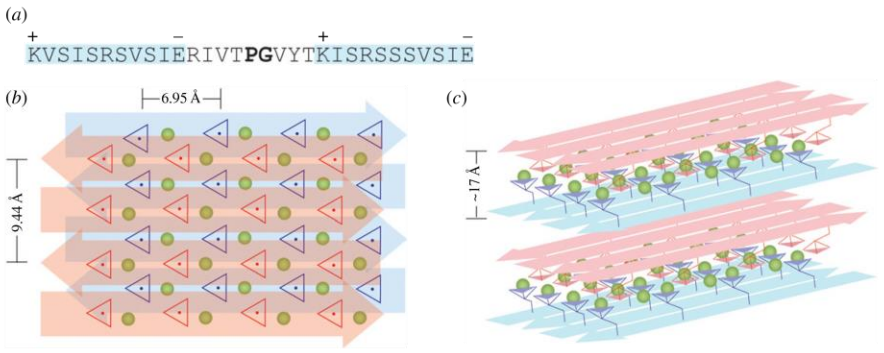


**Figure 7.** Hypothetical structures of periodic phosphates in caddisworm silk β-domains. (*a*) Primary sequence of a $[(pSX)_4]_2$ motif from the H-fibroin D-repeat. The Lys and Glu may align adjacent anti-parallel strands in a β-configuration as indicated by the + and − symbols. (*b*) Hypothetical arrangement of two anti-parallel $[(pSX)_4]_2$ β-hairpins in a β-sheet (blue arrows) stacked with an identical opposing β-sheet (red arrows) stabilized through $Ca^{2+}$/pS cross-bridging. The green spheres are $Ca^{2+}$ and the red and blue triangles are the orthographic projections of the $-PO_3^{2-}$ moieties. (*c*) The stacking of several anti-parallel sheets through $Ca^{2+}$ ion (green spheres) cross-bridging of phosphates (triangles) alternating with hydrophobic association of reverse face aliphatic sidechains (not shown).

band, which suggested that the unique $Ca^{2+}$-phosphate IR spectra of caddisworm silk (figure 2) is not due only to local sequence effects, like the alternating pattern of phosphoserines, but rather to the higher order structure of $[(pSX)_4]_n$ domains in the fibres.

The caddisworm silk fibre $Ca^{2+}$/phosphate IR spectra are strikingly similar to the spectra of phosphate compounds in which the phosphates occur in closely spaced, periodic arrangements. In these compounds, the $-PO_3$ $\upsilon_s$ band splits into two bands. The numerous examples of $\upsilon_s$ band splitting in periodic phosphate compounds include crystalline phosphate salts ($Na_2HPO_4{\cdot}2H_2O$) [28], the phosphate minerals brushite ($CaHPO_4{\cdot}2H_2O$) [29,30] and dittmarites (e.g. $NH_4MgPO_4{\cdot}H_2O$) [31], mononucleotides at high concentration in aqueous solution in which base stacking is thought to bring the phosphate groups into close regular order [32] and in dimyristoylphosphatidic acid lipid bilayers complexed with $Ca^{2+}$ [33]. In the latter case, based on the similarities of the IR spectra to calcium phosphate salts [29], the authors proposed that the decreased $-PO_3^{2-}$ group symmetry and splitting of the stretching mode bands into doublets was due to the periodic arrangement of $Ca^{2+}$-phosphate cross-bridges between lamellar bilayers. In their model, the lipid phosphate groups are fully deprotonated, each of the three P=O bonds has a similar partial negative charge (bond order) and each $Ca^{2+}$ ion in the two-dimensional network interacts with four phosphates, two from each of the stacked layers. Their model was consistent with the spacing between bilayers measured by small-angle X-ray diffraction.

Based on the dissimilarity of caddisworm silk metal ion-dependent phosphate IR spectra to casein and phosvitin and the similarity to periodic phosphate compounds, we propose that the $Ca^{2+}$ 1007 $cm^{-1}$ band is a $\upsilon_s$ mode that originates from factor group splitting of the $Na^+$ 975 $cm^{-1}$ $\upsilon_s$ band due to close proximity and periodic order of $Ca^{2+}$–phosphate complexes in $[(pSX)_4]_n$ domains. An ordered network of $Ca^{2+}$-cross-bridges between adjacent phosphatidic acid lipid bilayers is structurally similar to the previously proposed $Ca^{2+}$-cross-bridging of two opposing phosphoserine faces of $[(pSX)_4]_n$ β-sheets in caddisworm silk (figure 7) [7]. A detailed and definitive description of the coordination structure of the $Ca^{2+}$–phosphate complexes in caddisworm silk requires additional experimentation. Nevertheless, an illustrative example of a periodic, two-dimensional arrangement of $Ca^{2+}$–phosphate complexes is presented in figure 7. The two $(pSX)_4$ sequences separated by a short sequence with a central PG in the D-repeats of H-fibroin (figure 7*a*) are predicted to form β-hairpins. Lysine (K) and glutamic (E) sidechains, which flank the $(pSX)_4$ regions, may stabilize the registry of the anti-parallel β-strands through electrostatic interactions (plus and minus symbols, figure 7*a*). The phosphates are dianionic and in the centre of the sheet; each $Ca^{2+}$ ion interacts with four P=O ligands from one β-sheet and two from the opposing β-sheet. The phosphates at the edges of the β-sheets are in a different coordination environment from those in the centre. The model is consistent with previously reported solid-state NMR experiments that demonstrated the phosphoserines are in a β-sheet conformation with limited mobility and are uniformly and fully deprotonated (doubly anionic) [11].

The IR spectra of the other multivalent metal ions are similar to the $Ca^{2+}$ spectra with regard to the number of phosphate bands, indicating exchange with all of the metal ions tested resulted in a similar decrease in the symmetry of the phosphate groups. This suggests that the various multivalent metal ions do not affect the general structure of the $[(pSX)_4]_n$ β-domains. Variations in the frequencies and integrated intensities of the phosphate stretching modes, on the other hand, indicate subtle structural effects. The integrated band intensity ($I$) is related to the transition dipole moment ($\delta\mu/\delta Q$) of the vibrational mode by

$$I = \frac{l}{\upsilon}\frac{N\pi}{3c}\left(\frac{\delta\mu}{\delta Q}\right)^2, \tag{4.1}$$

where $\upsilon$ is the frequency of the vibration, $N$ is Avogadro's number, $l$ is the path length, μ is the dipole moment, $Q$ is the transition axis and $c$ is the concentration of the absorbing material [34]. Polar bonds with larger transition dipole moments absorb more IR radiation. The integrated intensities of the $\upsilon_{s1}$ and $\upsilon_{s2}$ bands increased in the order $Mg^{2+} < Sr^{2+} < Ba^{2+} < Ca^{2+} < La^{3+} < Zn^{2+} < Eu^{3+} < Fe^{2+}$. With a subset of metal ions, the stiffness and strength of the silk fibres increased in the order $Mg^{2+} < Ca^{2+} < La^{3+} < Zn^{2+} \approx Fe^{2+}$,

thereby establishing a direct correlation between the transition dipole moment of the metal ion–phosphate complexes and the mechanical properties of the silk fibres. The greater the electronegativity of the metal ion, the greater the transition dipole moment of the phosphate groups, the stronger the $[(pSX)_4]_n$ domain cross-bridges, the greater the stiffness and strength of the fibres.

$Mg^{2+}$ is an outlier in the series as its integrated intensities are lower and $Mg^{2+}$ fibres are weaker than $Ca^{2+}$ fibres despite the considerably greater electronegativity of $Mg^{2+}$ versus $Ca^{2+}$. Polyphosphate hydrogels were also mechanically weaker when cross-linked with $Mg^{2+}$ than with $Ca^{2+}$ and other divalent metal ions [3]. An octahedral coordination geometry is preferred by $Mg^{2+}$ ions, which in aqueous solution are strongly coordinated to six water molecules [35,36]. In nucleic acids, $Mg^{2+}$ ions are usually coordinated to outer-sphere phosphate ligands through an intact, or mostly intact, inner-sphere hydration shell [37,38]. The weak $Mg^{2+}$ cross-bridging in the $[(pSX)_4]_n$ domains, evident in the decreased stiffness and strength of the $Mg^{2+}$-exchanged fibres, may be due to indirect, outer-sphere coordination of $Mg(H_2O)_6^{2+}$ ions by phosphate sidechains or as a mix of outer- and inner-sphere coordination with only partial exchange of the hydration shell.

In conclusion, the integrated intensities of phosphate $\upsilon_s$ modes predict fibre stiffness and strength, providing definitive evidence that reversible phosphate/metal ion complexes are responsible for the toughness of caddisworm silk. Furthermore, the phosphate IR spectra have the split $\upsilon_s$ band characteristics of phosphate structures with regular periodic order, evidence the phosphate/metal ion complexes occupy a two- or three-dimensional periodic network, as predicted from the sequence of H-fibroin [6]. In the absence of multivalent metal ions, the $Na^+$ fibres are weak progressive springs with a final stiffness nearly the same as the final stiffness of the multivalent metal ion containing fibres (figure 4). The $Na^+$ fibres represent the isolated elastic covalent network that provides a restoring force to guide recovery of the $Ca^{2+}/(pSX)_4$ β-domains during unloading. Caddisworm silk is mechanically well adapted as an underwater structural material. Connecting features of its molecular structure with its toughness and unique mechanical response to strain will reveal further design principles for the development of tough synthetic materials specifically designed for wet environments [3].

Data accessibility. Extended data are provided in the electronic supplementary material (figure S1).

Authors' contributions. The manuscript was written through contributions of all authors. All authors have approved the final version of the manuscript. N.N.A. gathered and maintained caddisfly larvae in the laboratory, performed single fibre mechanical tests and ATR-FITR spectroscopy, and processed data. H.P. performed peptide synthesis and mass spectrometry. R.J.S. and N.N.A. designed the experiments, interpreted the results and prepared the manuscript.

Competing interests. The authors have no competing interests.

Funding. Funding from the Army Research Office, Life Sciences Division is gratefully acknowledged.

Acknowledgement. The authors thank Prof. Jack Simmons for helpful discussions.

## References

1. Wiggins GB. 2004 *Caddisflies: the underwater architects*. Toronto, Canada: University of Toronto Press.
2. Wang C-S, Pan H, Weerasekare GM, Stewart RJ. 2015 Peroxidase-catalysed interfacial adhesion of aquatic caddisworm silk. *J. R. Soc. Interface* **12**, 20150710 (doi:10.1098/rsif.2015.0710)
3. Gosline J, Lillie M, Carrington E, Guerette P, Ortlepp C, Savage K. 2002 Elastic proteins: biological roles and mechanical properties. *Phil. Trans. R. Soc. Lond. B* **357**, 121–132. (doi:10.1098/rstb.2001.1022)
4. Lane DD, Kaur S, Weerasakare GM, Stewart RJ. 2015 Toughened hydrogels inspired by aquatic caddisworm silk. *Soft Matter* **11**, 6981–6990. (doi:10.1039/C5SM01297J)
5. Miserez A, Weaver JC, Chaudhuri O. 2015 Biological materials and molecular biomimetics—filling up the empty soft materials space for tissue engineering applications. *J. Mater. Chem. B* **3**, 13–24. (doi:10.1039/C4TB01267D)
6. Ashton NN, Stewart RJ. 2015 Self-recovering caddisfly silk: energy dissipating, $Ca^{2+}$-dependent, double dynamic network fibers. *Soft Matter* **11**, 1667–1676. (doi:10.1039/C4SM02435D)
7. Ashton NN, Roe DR, Weiss RB, Cheatham TE, Stewart RJ. 2013 Self-tensioning aquatic caddisfly silk: $Ca^{2+}$-dependent structure, strength, and load cycle hysteresis. *Biomacromolecules* **14**, 3668–3681. (doi:10.1021/bm401036z)
8. Stewart RJ, Wang CS. 2010 Adaptation of caddisfly larval silks to aquatic habitats by phosphorylation of H-fibroin serines. *Biomacromolecules* **11**, 969–974. (doi:10.1021/bm901426d)
9. Ohkawa K, Miura Y, Nomura T, Arai R, Abe K, Hirabayashi K. 2013 Long-range periodic sequence of the cement/silk protein of *Stenopsyche marmorata*: purification and biochemical characterisation. *J. Bioadhesion Biofilm Res.* **29**, 357–367. (doi:10.1080/08927014.2013.774376)
10. Ashton NN, Taggart DS, Stewart RJ. 2012 Silk tape nanostructure and silk gland anatomy of Trichoptera. *Biopolymers* **97**, 432–445. (doi:10.1002/bip.21720)
11. Addison JB, Ashton NN, Weber WS, Stewart RJ, Holland GP, Yarger JL. 2013 β-Sheet nanocrystalline domains formed from phosphorylated serine-rich motifs in caddisfly larval silk: a solid state NMR and XRD study. *Biomacromolecules* **14**, 1140–1148. (doi:10.1021/bm400019d)
12. Addison JB, Weber WS, Mou Q, Ashton NN, Stewart RJ, Holland GP, Yarger JL. 2014 Reversible assembly of β-sheet nanocrystals within caddisfly silk. *Biomacromolecules* **15**, 1269–1275. (doi:10.1021/bm401822p)
13. Rejmanová P, Labský J, Kopeček J. 1977 Aminolysis of monomeric and polymeric 4-nitrophenyl esters of N-methacryloylamino acids. *Die Makromol. Chem.* **178**, 2159–2168. (doi:10.1002/macp.1977.021780803)
14. Deng H, Wang J, Callender R, Ray WJ. 1998 Relationship between bond stretching frequencies and internal bonding for $[^{16}O_4]$- and $[^{18}O_4]$-phosphates in aqueous solution. *J. Phys. Chem. B* **102**, 3617–3623. (doi:10.1021/jp973314q)
15. Wilson EB, Decius JC, Cross PC. 1955 *Molecular vibrations: the theory of infrared and Raman vibrational spectra*. New York, NY: Dover.
16. Nakamoto K. 2009 *Infrared and Raman spectra of inorganic and coordination compounds*. New York, NY: Wiley.
17. Tejedor-Tejedor M, Anderson M. 1990 The protonation of phosphate on the surface of goethite as studied by CIR-FTIR and electrophoretic mobility. *Langmuir* **6**, 602–611. (doi:10.1021/la00093a015)
18. Lagaron JM. 2002 The factor group splitting phenomenon: a vibrational spectroscopy approach to assess polymer crystallinity and crystalline density. *Macromol. Symp.* **184**, 19–36. (doi:10.1002/1521-3900(200208)184:1<19::AID-MASY19>3.0.CO;2-X)
19. Persson P, Nilsson N, Sjöberg S. 1996 Structure and bonding of orthophosphate ions at the iron oxide–aqueous interface. *J. Colloid Interface Sci.* **177**, 263–275. (doi:10.1006/jcis.1996.0030)
20. Shannon RD. 1976 Revised effective ionic radii and systematic studies of interatomic distances in

halides and chalcogenides. *Acta Crystallogr. Sect. A* **32**, 751–767. (doi:10.1107/S0567739476001551)

21. Chaikumpollert O, Yamamoto Y, Suchiva K, Kawahara S. 2012 Mechanical properties and cross-linking structure of cross-linked natural rubber. *Polym. J.* **44**, 772–777. (doi:10.1038/pj.2012.112)
22. Baumy JJ, Brule GG. 1988 Effect of pH and ionic strength on the binding of bivalent cations to β-casein. *Le Lait* **68**, 409–417. (doi:10.1051/lait:1988426)
23. Fernández C, Ausar SF, Badini RG, Castagna LF, Bianco ID, Beltramo DM. 2003 An FTIR spectroscopy study of the interaction between $\alpha_{s}$-casein-bound phosphoryl groups and chitosan. *Int. Dairy J.* **13**, 897–901. (doi:10.1016/S0958-6946(03)00115-8)
24. Ono T, Kaminogawa S, Odagiri S, Yamauchi K. 1976 A study on the binding of calcium ions to $\alpha_{s1}$-casein. *Agr. Biol. Chem.* **40**, 1717–1723.
25. Li B, Raff J, Barkleit A, Bernhard G, Foerstendorf H. 2010 Complexation of U(VI) with highly phosphorylated protein, phosvitin: a vibrational spectroscopic approach. *J. Inorg. Biochem.* **104**, 718–725. (doi:10.1016/j.jinorgbio.2010.03.004)
26. Samaraweera H, Zhang WG, Lee EJ, Ahn DU. 2011 Egg yolk phosvitin and functional phosphopeptides: review. *J. Food Sci.* **76**, 143–150. (doi:10.1111/j.1750-3841.2011.02291.x)
27. He Z, Honeycutt CW, Zhang T, Bertsch PM. 2006 Preparation and FT–IR characterization of metal phytate compounds. *J. Environ. Qual.* **35**, 1319–1328. (doi:10.2134/jeq2006.0008)
28. Chapman AC, Thirlwell LE. 1964 Spectra of phosphorus compounds: I the infra-red spectra of orthophosphates. *Spectrochim. Acta* **20**, 937–947. (doi:10.1016/0371-1951(64)80094-1)
29. Berry EE, Baddiel CC. 1967 The infra-red spectrum of dicalcium phosphate dihdrate (brushite). *Spectrochim. Acta Part A Mol. Spectrosc.* **23**, 2089–2097. (doi:10.1016/0584-8539(67)80097-7)
30. Hirsch A, Azuri I, Addadi L, Weiner S, Yang K, Curtarolo S, Kronik L. 2014 Infrared absorption spectrum of brushite from first principles. *Chem. Mater.* **26**, 2934–2942. (doi:10.1021/cm500650t)
31. Koleva VG. 2007 Vibrational behavior of the phosphates ions in dittmarite-type compounds M′M″$PO_4.H_2O$ (M′= $K^+$, $NH_4^+$; M″= $Mn^{2+}$, $Co^{2+}$, $Ni^{2+}$). *Spectrochim. Acta* **66**, 413–418. (doi:10.1016/j.saa.2006.03.015)
32. Hernández B, Gavira-Vallejo JM, Navarro R, Hernanz A. 2001 Splitting of infrared bands of mononucleotides in aqueous solution. *J. Mol. Struct.* **565–566**, 259–263. (doi:10.1016/S0022-2860(00)00816-4)
33. Laroche G, Dufourc EJ, Dufourcq J, Pizolet M. 1991 Structure and dynamics of dimyristoylphosphatidic acid/calcium complexes by $^2$H NMR, infrared, and Raman spectroscopies and small-angle X-ray diffraction. *Biochemistry* **30**, 3105–3114. (doi:10.1021/bi00226a018)
34. Steele D. 1971 *Theory of vibrational spectroscopy*. Cambridge, UK: Cambridge University Press.
35. Katz AK, Glusker JP, Beebe SA, Bock CW. 1996 Calcium ion coordination: a comparison with that of beryllium, magnesium, and zinc. *J. Am. Chem. Soc.* **118**, 5752–5763. (doi:10.1021/ja953943i)
36. Bock CW, Katz AK, Glusker JP. 1995 Hydration of zinc ions: a comparison with magnesium and beryllium ions. *J. Am. Chem. Soc.* **117**, 3754–3765. (doi:10.1021/ja00118a012)
37. Holbrook SR, Sussman JL, Warrant RW, Church GM, Kim S-H. 1977 RNA-ligand interactions:(I) magnesium binding sites in yeast $tRNA^{Phe}$. *Nucleic Acids Res.* **4**, 2811–2820. (doi:10.1093/nar/4.8.2811)
38. Robinson H, Gao YG, Sanishvili R, Joachimiak A, Wang AH. 2000 Hexahydrated magnesium ions bind in the deep major groove and at the outer mouth of A-form nucleic acid duplexes. *Nucleic Acids Res.* **28**, 1760–1766. (doi:10.1093/nar/28.8.1760)

# CHAPTER 6

# ENVIRONMENTAL $Ca^{2+}$ SETS THE NATURALLY-SPUN AQUATIC CADDISWORM SILK FIBERS

## 6.1 Introduction

Aquatic caddisfly larvae (insect order Trichoptera) use the process of fiber spinning to make an underwater adhesive silk tape [1]. Generically, fiber spinning describes both the natural and industrial process of drawing fluid precursors (spinning dope) into a solid filament by extrusion through a narrow passage called the spinneret [2]. In contrast with the relatively short commercial natural fibers such as cotton and wool, which are made by the slow process of growth, fiber spinning produces continuous filaments on-demand from stored precursors in a liquid reservoir. For hundreds of millions of years the only spun fibers were the proteinaceous silk secretions of arthropods such as those from caddisworms and their better known terrestrial relative the domesticated silkworm (*Bombyx mori*) [3]. In the late 1800s, the first commercial artificial fiber, rayon, was spun from a solution of processed wood pulp [4]. Nowadays, industrial fiber spinning is ubiquitous for making fibers from nearly all synthetic and natural polymers. Although the materials and processes used to make naturally and artificially spun fibers are diverse, shearing of the pre-fiber components through the spinneret is always closely accompanied by a liquid-solid or a gel-solid phase transition [2]. Shear-induced alignment of the polymer chains by the spinneret

imparts a superior mechanical advantage to the final fibers over the bulk polymer, typically an increase in modulus and toughness [2,5,6]. Industrially, a range of physical and chemical processes is used to solidify the nascent filament as it emerges from the spinneret: evaporation of organic solvents from suspended polymers (dry spinning), cooling of melted thermoplastics (melt spinning), and directly spinning into a chemical coagulation bath (wet spinning), to name a few.

In contrast, arthropod silks are naturally spun at a narrow range of ambient temperatures with only plasticizing water to solvate constituent proteins [7–9]. The natural silk of the domesticated silkworm *B. mori* (insect order Lepidoptera) was the first spun-fiber of commercial value and is consequently the most extensively studied and understood of all arthropod silks. The silkworm gland contents are liquid crystalline: compact proteinaceous constituents comprise many small spherical micron-sized granules [10]. By mass, the predominant structure silk protein of both silkworm and caddisworm silk is the large >350 kg/mol heavy chain (H) fibroin. The suspended H-fibroin proteins stored in the silkworm glands are in a chain conformation denoted silk I; they contain a repeated type II β-turn believed to promote intramolecular over intermolecular hydrogen bonding [11,12]. Shearing of the gland contents during spinning drives a silk I-silk II structural transition producing intermolecular β-crystallite crosslinks that insolubilize the nascent fiber. As a case in point, prior to tough synthetic nylon, fly fishing leaders were drawn manually from silkworm glands, mechanically set, by drawing between the angler's teeth [13]. The β-crystallites in silkworm silk arise from abundant poly (GA) repeats typically in GAGAGX motifs where X is usually S but sometimes Y. The abundance of these domains is reflected by a preponderance of the simple sidechain amino acids G, A, S, and Y in moth silk (~89.5

mol%).

Similarly, the unspun contents of the major ampulate silk gland of the golden orb-web spider lack analogous pleated β-sheets that are typical of the final silk fibers. The secondary structure of the spinning dope is ~30% α-helices, 40% random coil, and 30% β-turns [14]. The β-turns are likewise believed to promote a loose partially extended configuration much like the type II β-turns of the *B. mori* silk I spinning dope [8,14]. The phase transition of golden orb-web spider silk is also driven mechanically by the spinning process [8], except the analogous β-crystallite crosslinks arise from poly (A) domains and not poly (GA) motifs [15,16]. The silk spinning systems of the terrestrial silkworm and the golden orb-web spider are a striking case of evolutionary convergence. Both terrestrial silks are spun from concentrated liquid crystalline precursors stored in a specialized secretory gland; contain a preponderance of simple sidechain amino acids G, A, and S (over 60 mol%) [17–19]; and phase transition during spinning by shear-induced molecular rearrangement promoting interchain β-crystallite crosslinks.

The silk spinning process of the aquatic caddisfly larvae is comparatively less understood than that of its terrestrial relive the silkworm. Their silk lacks the alanine-dense β-sheet forming poly GA and poly A motifs critical to fiber spinning and insolubization of terrestrial silks. For comparison, *B. mori* H-fibroin contains 30.3 mol% Ala, whereas that of the caddisworm *H. consimilis* contains a sparse ~1.2 mol% [17,20]. Conversely, caddisworm H-fibroin (*H. occidentalis*) contains a preponderance of charged amino acids (~35 mol%) which are sparse in the commercial silkworm H-fibroins (1.7 mol%). These charged amino acids have a profound effect on silk structure and mechanical properties [20,21]. Except the short non-repetitive termini, caddisworm H-fibroins comprise 3

imperfectly alternating repeats designated D, E, and F [20,22]. The bulk of the H-fibroin is ampholytic with alternating blocks of acidic and basic residues. Each of the 3 repeats contains a positively charged block of 3-4 arginines and at least 1 negatively charged block of phosphorylated serines (pS) in motifs of the form $(pSX)_n$ [20]. In D and F repeats, X is usually aliphatic Val, Leu, or Ilu but sometimes Arg and n is 4 or 5, respectively. In E repeats, X is always Gly and n is 2. In the spun fibers, the ~15 mol% pSs are complexed with equal molar ratios of multivalent metal ions, predominantly $Ca^{2+}$ but lesser amounts of $Mg^{2+}$, $Fe^{2+}$, and $Zn^{2+}$ [21,23]. These $Ca^{2+}$ complexes affect the symmetry of the pS – $PO_3^{2-}$ IR-stretching modes in a way typical of compounds with periodic phosphates and metal ions [23].

The $(pSX)_n$ domains are believed to form extended β-structures somewhat analogous to the β-crystallites of terrestrial silks except that the sheets are stabilized by $Ca^{2+}$-pS complexes on the one side and by hydrophobic interactions between aliphatic Val, Leu, and Ilu residues on the opposite side [21]. Stacking of the β-sheets is thought possible by alternating intersheet associations of $Ca^{2+}$-pS and aliphatic groups, respectively [20]. Multiple molecular dynamic studies predicted $Ca^{2+}$-stabilized antiparallel β-sheets from the H-fibroin $(pSX)_n$ domains [20,24]. Corroborating studies showed the loss of β-secondary structures in $Na^+$-EDTA exchanged silk by ATR-FTIR, 13C solid state NMR, and X-ray diffraction [15,20,25,26]. $Na^+$-exchanged silk fibers swelled to over double their native diameter and displayed compromised mechanical properties, including a >98% decrease in initial modulus, toughness, and breaking stress [20,23]. The mechanical toughness of the caddisworm silk is attributed to the energy-dissipating rupture of the $Ca^{2+}$-

pS complexes [23,27]. When depleted of native $Ca^{2+}$, only a weakly elastic network remains intact [20,23].

It is unknown how and where the critical $Ca^{2+}$ enters the silk. Is it co-extruded with the fibers and stored as part of the gland contents? Or is it added during the spinning process either by the gland or directly from the hard water into which the fibers are spun? $Ca^{2+}$ promotes the proper folding of the mechanically important pS-containing β-structures, the addition of which might reasonably explain the liquid-solid phase transition of silk constituents during the underwater spinning of caddisworm silk. The goal of this study is to determine the role of $Ca^{2+}$ during the fiber spinning process. Included are comparisons between the silk fibers and silk gland contents by elemental analysis, ATR-FTIR analysis of the Amide I and phosphate modes. The ultrastructure of the gland and its contents were studied by DIC light microscopy and TEM to determine were the gland contents begin to form fibers. The gland and its contents were also studied with the $Ca^{2+}$-indicating dye alizarin S red to determine if internal $Ca^{2+}$ gradients induce fiber formation within the gland.

## 6.2 Experimental Section

### 6.2.1 Silk Harvesting

Fifth instar larvae of the case-maker *Hesperophylax occidentalis* were collected just prior to pupation in the early summer in upper Red Butte Creek (Salt Lake County, UT, USA) and maintained in the laboratory in chilled dechlorinated tap water. As previously described, isolated silk fibers were harvested from caddisworms which had been removed from their stone cases and given ~1 mm3 Teflon blocks as building material [1]. After

separating from the Teflon blocks, silk fibers were stored in the dechlorinated tap water from the caddisworm aquarium. Bundles of isolated silk fibers were used subsequently for analysis by ICP-OES, ATR-FTIR, and histologically with alizarin S red.

### 6.2.2 Silk Gland Dissection

Silk glands were dissected from fifth instar *H. occdentalis* larvae. The caddisworms were anesthetized with a 1% solution of diethyl ether in chilled water (~4 °C). The glands were removed using similar methods previously outlined [1]. The larvae were pinned ventral side up. A long cut was made from the inferior abdomen down the ventral midline to the base of the head exposing the posterior silk glands. The epicranial cuticle was radially cut and the ventral half was removed to expose the remainder of the silk gland, including the anterior portion and the silk press.

### 6.2.3 Isolating the Silk Gland Contents

Immediately after dissection, the silk glands were rapidly frozen by placing on a fresh glass coverslip glued atop a ~2 cm thick stainless steel plate which had been chilled in liquid nitrogen. The frozen glands were then lyophilized. With a pair of fine forceps, the stored contents of the posterior silk gland were isolated by carefully cracking away the brittle cellular layer. The lyophilized silk gland contents were analyzed by ICP-OES and ATR-FTIR as subsequently described. An intact lyophilized gland-pair, which did not have the cellular layer removed, was analyzed histologically with the alizarin red S (ARS) stain subsequently described.

### 6.2.4 Elemental Analysis by ICP-OES

An isolated bundle of native silk fibers was rinsed with dH2O then lyophilized. These lyophilized silk fibers and the previously described lyophilized silk gland contents were dissolved in 40% nitric acid, analyzed in triplicate by ICP-OES, and the metal ions and P quantified by comparison to commercial standards (PerkinElmer, Optima 3100XL). Metal ion concentrations are reported as molar ratios to P to normalize the mass of fibers in each sample. After normalization, the propagated error is given by the fractional total deviation.

### 6.2.5 ATR-FTIR Spectroscopy

An isolates bundle of silk fibers stored in the 1 mM $CaCl_2$ stream water analogue described above was blotted with a Whatman grade 50 filter paper then lyophilized. A bundle of $Na^+$-exchanged silk fibers was prepared by treating excess 10 mM EDTA, 50 mM NaCl, 1 mM Bis-Tris, pH 7.0 for 1 h, then treating in excess 1 mM EDTA, 1 mM EDTA, 1 mM Bis-Tris, pH 7.0 for 1 h. The sample was similarly blotted with a Whatman grade 50 filter paper then lyophilized. The lyophilized bundles of silk fibers and the lyophilized posterior gland contents described above were both analyzed by ATR FTIR including the amide I spectral region from 1576-1720 $cm^{-1}$ corresponding to the stretching mode of the C=O peptide backbone and from 875-1184 $cm^{-1}$ containing both the mono and dianionic phosphate stretching modes. ATR-FTIR absorption spectra were collected using a Nicolet 6700 spectrometer (Thermo Scientific, FL) with a diamond Smart iTR accessory, a deuterated triglycine sulfate detector, and a KBr/Ge mid-infrared optimized beamsplitter. All spectra were recorded with a resolution of 4 $cm^{-1}$ and 512 averaged scans.

The spectra containing the phosphate stretching modes from 875-1184 $cm^{-1}$ were normalized using the area of the spectral region from 1428-1475 $cm^{-1}$ containing absorption bands of pH insensitive side groups including Trp (CH) bending, Trp (CC) stretching, Trp (CN) stretching, and CH3 bending modes of the aliphatic sidechains Leu, Ile, Val, Ala, Thr, and Met using previously described methods [20]. A linear baseline subtraction was applied to the spectra of the amide I regions from 1576-1720 $cm^{-1}$ which were then normalized so all spectra had the same arbitrary integrated intensity using Matlab software (MathWorks). The amide I spectra were then fitted with Gaussian curves using PeakFit software (Systat Software Inc.) Local minima in the 2nd derivative were used to place the initial Gaussian constituents. The peak position, height, and width were allowed to vary during the iterative least-square method employed in the PeakFit software, thereby minimizing the residuals between the fitted and experimental spectra. Spectra were plotted using Matlab software (MathWorks).

### 6.2.6 IR-titration of the Silk Phosphoserines With and Without $Ca^{2+}$

To understand the effects of $Ca^{2+}$ on the silk phosphoserine titration curve, two separate phosphate curves were prepared using the absorption band assigned to the P-O(H) bond of the monoanion (888-946 $cm^{-1}$). One of the titration curves was performed on a bundle of native silk in buffers containing 5 mM $Ca^{2+}$ the other on a $Ca^{2+}$-depleted sample in buffers containing 5 mM of the chelator EDTA. The $Ca^{2+}$-depleted sample was prepared by washing for 1 h in excess 10 mM EDTA, 50 mM NaCl, and 1 mM Tris-HCl pH 8.0. The respective buffers were prepared from pH 8.0-2.0 with 1 mM (Tris-HCl) (pH 8.0), ammonium bicarbonate (pH 7.0-6.0), acetic acid (pH 5-4.5), forminc acid (pH 4.0-3.5), or

glycine (pH 3.0-2.0). IR spectra were collected sequentially on the same buddle of silk fibers at pH 8.0, 7.0, 6.0, 5.0, 4.5, 4, 3.5, 3, and 2 in the spectral region 881-1296 $cm^{-1}$ containing the phosphate mon- and di-anionic vibrations. The respective bundle of silk fibers was first treated in the appropriate buffer for 20 min then clamped to the diamond ATR window. The clamp margins were submerged with ~1 ml of the appropriate buffer to assure the fibers did not dry out during each scan. This was repeated for each one of the pHs. The spectra containing the phosphate stretching modes from 881-1296 $cm^{-1}$ were normalized using the area of the spectral region from 1428-1475 $cm^{-1}$ containing absorption bands of pH insensitive side groups, including Trp (CH) bending, Trp (CC) stretching, Trp (CN) stretching, and CH3 bending modes of the aliphatic sidechains Leu, Ile, Val, Ala, Thr, and Met using previously described methods [20]. A linear baseline subtraction and trapezoidal integration was applied to the region 888-946 $cm^{-1}$ containing the P-O(H) bond of the monoanion. The integrated intensities were fitted with a base 10 logistic function using Matlab software. The spectra, integrated intensities, and fitted curves were plotted using Matlab software (MathWorks).

### 6.2.7 The pH of the Silk Gland Contents

To find the approximate pH of the contents stored in the silk gland lumen, ~10 mg of the lyophilized gland contents were rehydrated in 0.5 ml of ASTM type I deionized water (Ricca Chemica). The pH of the solution was measured with a perpHect Ross micro-combination pH electrode standardized with Orion pH 4.0, 7.0, and 10.0 reference solutions (Thermo Scientific).

### 6.2.8 Differential Interference Contrast Microscopy (DIC)

An intact pair of silk glands were submerged for 12 h at 4 °C in a solution of 4 wt% paraformaldehyde in insect Ringer's containing 10.93 g/L NaCl, 1.57 g/L KCl, 3.6 g/L glucose, and 25 mM Tris, adjusted to pH 7.5 with HCl. The glands were then dehydrated in a graded ethanol series with insect Ringer's: 50, 75, and 100% EtOH at 2 h intervals. The silk gland were cleared for 12 h and imaged while submerged in wintergreen oil (Methyl Salicylate). DIC micrographs were collected with an Axiovert 100 microscope (Carl Zeiss AG) equipped with a Plan-Neofluar 100X oil immersion objective and a XLMC digital camera (Dage_MTI). Images were background corrected and contrast adjusted using Matlab software (MathWorks).

### 6.2.9 Transmission Electron Microscopy

The silk gland tissue was analyzed using previously published TEM preparation techniques [28,29]. Briefly, the glands were fixed in a solution of 2% glutaraldehyde and 1 % paraformadldehyde in 0.1 cacodylate buffer (pH 7.4) for 24 h. Silk samples were then treated with excess 2% OsO4 in cacodylate buffer then rinsed in DI-H2O. The samples were stained with 4% uranyl acetate then dehydrated with a graded ethanol series. After dehydration ethanol was exchanged with acetone and samples were embedded in epoxy Embed-812(Electron Microscopy Sciences). Blocks were sectioned to approximately 70 nm thickness with a diamond ultra 45o blade (Diatome). Sections were picked up on copper grids and stained with saturated uranyl acetate, rinsed with water, then stained with Reynold's lead citrate. A Tecnai 12 transmission electron microscope was used to collect

electron micrographs (FEI). Micrographs were analyzed with ImageJ software (National Institutes of Health).

### 6.2.10 Alizarin Red S Staining for $Ca^{2+}$

To determine where in the silk spinning process the silk constituents complex with $Ca^{2+}$, an alizarin red S (ARS) stain was applied to the previously described lyophilized gland pair. Lyophilized native caddisworm silk fibers were used as a positive control. Lyophilized $Ca^{2+}$-depleted silk was used as a negative control; the silk bundle was treated for 1 h in excess 10 mM EDTA, 50 mM NaCl, 1 mM Bis-Tris adjusted to pH 7.0 with NaOH. The lyophilized samples were submerged in a solution of 1.5 mM ARS, 60 mM Na2SO4 adjusted to pH 4.1 with 10% NH4OH for 15 min. Samples were destained in a solution of 60 mM Na2SO4 for 4 h, dehydrated in a graded series of ethanol, and imbedded in a glycol methacrylate resin following previously published techniques ( Immuno-Bed, Polysciencs, Inc.) [1]. Blocks were sectioned 10 um thick with a glass knife on a Jung RM 2055 rotary microtome (Leica Microsystems). The silk gland was serial sectioned from the spinneret towards the posterior gland. Samples were imaged by transmitted light micrsocopy using an Axiovert 100 microscope (Carl Zeiss AG) equipped with a Plan-Neofluar 100X oil immersion objective and a XLMC digital camera (Dage_MTI). Images were background corrected using Matlab software (MathWorks).

### 6.2.11 Scanning Electron Microscopy of the Caddisworm Case

Half of the stone case was removed from several caddisworms with a pair of fine forceps. The larvae were then given ~0.5 mm diameter round glass beads to rebuild their

cases. After several days, the rebuilt cases were removed, lyophilized, cut in half, and mounted inside-up to aluminum specimen stubs with carbon tape. Samples were Au/Pd coated then imaged with a Qunta 600 FEG scanning electron microscope (FEI).

### 6.2.12 Time-lapse Photography of Tanning Silk

A caddisworm larva, which had been given ~0.5 mm diameter round glass beads as case building material, was closely monitored. Immediately after incorporating a new bead into its case, the case was removed and cut in half to get a clear inside view of the freshly laid silk. The sample was submerged in the 1 mM $CaCl_2$ stream water analogue in a 10 ml culture plate with a transparent lid to eliminate evaporation. Photographs were taken at 5 min intervals for 40 h with a Nikon SMZ-U dissection microscope equipped with a Sony α7S camera body. The exposure was fixed for all images. The average blue channel intensity for all images was calculated inside a rectangular box drawn to encompassing the fresh silk. The blue channel intensity was fitted with an exponential decay function. Matlab software was used to process the data and make figure plots.

## 6.3 Results

### 6.3.1 Elemental Composition of the Gland Contents and the Silk Fibers

To understand the stimuli that leads to fiber formation, the elemental composition of the silk gland contents and the final fibers were analyzed by ICP-OES (Fig. 6.1). To facilitate comparison, the results were normalized by the concentration of the ~15 mol% intrinsic silk pS (Fig 6.1). The gland contents and the silk fibers also contain intrinsic S with molar ratios to P of 0.179:1 and 0.261:1, respectively (Fig. 6.1A, B). There are large

differences in the molar ratios of the metals Ca, Mg, and Fe; these are likely present in the silk as multivalent ions. $Mg^{2+}$ is the most abundant metal in the gland silk at a scant 0.031 per P (Fig. 6.1A). There are only trace amounts of Ca, Zn, and Fe totaling <0.001 per phosphate (Fig. 6.1A). In comparison, the silk fibers have nearly equimolar ratios of metal ions to P totaling 1.05:1; $Ca^{2+}$ predominates at 0.826:1 followed by Mg at 0.121:1 (Fig. 6.1B).

### 6.3.2 IR Spectroscopy of Silk Phosphoserine/Metal Ion Complexes

The IR-spectral region from 875-1184 $cm^{-1}$ contains the P-O stretching modes of the silk phosphoserines (Fig. 6.2) [30]. The number and location of phosphate absorption bands gives information about the pH and coordination environments of the silk phosphoserines [23,27]. The uncomplexed dianionic $–PO_3^{2-}$ moiety has $C_{3v}$ symmetry and two IR-active stretching modes: The weaker symmetric stretching ($\nu_s$) mode at ~975 $cm^{-1}$ and a stronger asymmetric ($\nu_a$) mode at ~1075 $cm^{-1}$ [23,30,31]. The native silk gland contents clearly displays these two modes, the $\nu_s$ mode at 967.9 $cm^{-1}$ and the $\nu_a$ mode at 1064.6 $cm^{-1}$ (Fig. 6.2A). In contrast, the $\nu_s$ mode of metal ion-complexed native caddisworm silk phosphates is split into modes designated $\nu_{s1}$ and $\nu_{s2}$ at 974.6 and 1010.5 $cm^{-1}$, respectively (Fig 6.2B). The spectrum of the gland contents treated in excess 1 mM $CaCl_2$ is qualitatively similar to that of the native silk fibers; a new absorption band emerges as the symmetric stretching modes splits into the characteristic $\nu_{s1}$ and $\nu_{s2}$ modes at 972.5 and 1010.2 $cm^{-1}$, respectively (Fig. 6.2A, B). Conversely, the spectrum of $Na^+$-EDTA exchanged silk fibers is qualitatively similar to that of the native silk gland contents with a solitary $\nu_s$ mode at 974.6 $cm^{-1}$ and the larger $\nu_a$ mode at ~1071.2 $cm^{-1}$ (Fig 6.2B).

In the spectra of native gland contents and $Na^+$-EDTA exchanged silk fibers, there is a much weaker absorption mode at 923.7 and 920.9 $cm^{-1}$ respectively associated with the P-O(H) stretching mode of the phosphate monoanion (Fig 6.2A, B) [32]. Although the dianonic mode predominates in the spectrum of the native gland contents, the 923.7 $cm^{-1}$ peak suggests that some of the phosphates are present as monoanions. This monoainion absorption band is not present in the native silk fibers (Fig 6.2B); the complexed phosphates have a purely dianionic character despite identical pH for both native and $Na^+$-EDTA exchanged fibers (pH 7.0).

### 6.3.3 IR-titration of the Silk Phosphoserines With and Without $Ca^{2+}$

The effect of $Ca^{2+}$ on the silk pS titration curve was investigated using the monoanionic absorption mode associated with P-O(H) stretching from 888-946 $cm^{-1}$. Other pH sensitive pS modes exist in the region 881-1296 $cm^{-1}$ and they are displayed in Figure 6.3A, B and have been discussed previously in great detail [23,27]. Because there is considerable overlap in most of the P-O stretching bands, the isolated band from 888-946 $cm^{-1}$ is particularly useful. Titration plots of the integrated intensities of the region 888-946 $cm^{-1}$ were prepared for silk samples with native $Ca^{2+}$ (Fig. 6.3A) and depleted of $Ca^{2+}$ with $Na^+$-EDTA (Fig 6.3B). There was very little difference in the $pK_a$ of the respective systems as determined by the inflection point of the fitted logistic functions: pH 4.53 and 4.58 for the native $Ca^{2+}$-containing sample, and the $Ca^{2+}$-depleted sample, respectively. The most notable difference between the two titration curves are their relative slopes a value quantified by the power term of the logistic fit: 1.50 for the native $Ca^{2+}$-containing sample, and 0.49 for the $Ca^{2+}$-depleted sample.

### 6.3.4 Secondary Structure and the IR-amide I Band

The IR-spectral region from 1576-1720 $cm^{-1}$, also known as the amide I band, corresponds to the stretching mode of the C=O peptide backbone. The frequency of the amide I vibrations in a protein are affected differently by the varied hydrogen bonds of the diverse protein secondary structures: β-structures from 1616-1637, random coils from 1638-1655, α-helices from 1656-1662, and turns from 1663-1669 $cm^{-1}$ [33,34]. Decomposition of the amide I band of the lyophilized native gland contents reveals a predominantly random coil composition at 41.5% followed by 22.3% β-sheets and lesser amounts of α-helices and turn structures (Fig. 6.4A). The $Ca^{2+}$-depleted silk fibers have a comparably similar structural profile with 42.8% random coils and 24.4% β-sheets (Fig. 6.4D). In native silk fibers and $Ca^{2+}$-treated gland contents, there is a considerable decrease in random coil composition by ~12% compared with samples without $Ca^{2+}$ (native gland contents, and EDTA-treated silk fibers); this accompanied by an equivalent increase in both β and turn structures in these samples (Fig. 6.4). The difference spectra (Fig. 6.4C, D) highlight the relative changes in secondary structure composition from native values; two difference spectra are effectively the inverse of one another. Judging from the chain conformation alone, the addition of $Ca^{2+}$ to the gland contents has the opposite effect as removing $Ca^{2+}$ from the spun silk fibers (Fig. 6.4C, F).

### 6.3.5 The pH of the Silk Gland Contents

The pH of the gland contents was approximated by rehydrating lyophilized gland contents in ASTM type I deionized water and measuring the pH of the solution. The pH of the solution is the approximate gland pH making the assumption that the buffering capacity

of the ASTM type I deionized water is negligible in comparison with the many functional groups within the lyophilized gland contents. The pH of the rehydrated gland contents is 7.19.

### 6.3.6 The Silk Gland and Its Contents

A ventral incision down the caddisworm midline exposes the bilaterally symmetric silk glands (Fig. 6.5A). Most of the space within the larval abdomen comprises the alimentary canal and the two silk glands. These long thin silk-producing organs fold several times within the larval body before passing up through the thorax and into the head (Fig. 6.5A, B). A bulbous protrusion in the outer wall of the glands marks the transition from the posterior to anterior regions; this feature is situated at the connection between the base of the head and the thorax (Arrowhead in Fig. 6.5B, C). The anterior portion of each silk gland passes through the head and fuse at a chitinous spinneret ventral to the mouthparts (Arrow in Fig. 6.5B, C). A silk gland was imaged by DIC at the locations indicated in Figure 5B: the posterior gland (Fig 6.5D), the bulbous transition (Fig 6.5E), and the anterior gland (Fig 6.5F). There is a dramatic narrowing in the silk gland contents as they are drawn into a fiber from ~50.7 μm in the posterior gland to ~12.6 μm at the gland transition and ~1.9 μm in the anterior gland. The inner wall of the gland lumen at the transition from posterior to anterior regions is marked by a chitinous annular narrowing (Arrowhead in Fig 6.5E). The annulus is the start of the anterior cuticle lining (Arrows Fig. 6.5E,F) with which it is continuous.

To provide greater morphological detail of the important gland anatomy, longitudinal physical sections of the silk glands were analyzed by transmission electron microscopy at

the bulbous transition and the anterior lumen. The annular narrowing at the bulbous transition (Arrowhead in Fig. 6.6A), and the cuticle lining of the anterior channel (Arrows in Fig. 6.6A, B) are clearly visible. There is a diffuse acellular material of unknown origin filling the void between the cuticle lining and the forming fiber in the anterior lumen (Stars in Fig. 6.6A, B). The silk dope in the lumen of the annular narrowing is relatively isotropic with large spherical inclusion appearing to elongate once drawn just past the narrowing (Triangles in Fig. 6.6A). Much farther into the anterior lumen, the gland contents develop a well-defined fibrous ultrastructure with dark globular inclusions (Fig. 6.5B).

To investigate, in greater detail, the morphological changes of the nascent silk fiber within the gland lumen, higher magnification transmission electron micrographs were taken of the silk gland contents at successive distances along a longitudinal gland section (the top panel of Fig 6.7). The stored contents in the anterior gland comprise many nanoscale spherical granules with a diameter of 53.9 ± 5.4 nm (n=10, ±S.D.) (Fig. 6.7A). There are much larger ~350 nm spherical inclusions with fuzzy diffuse contents within the granular silk dope (Fig 6.7A). Approximately at the annular narrowing, the granules appear to coalesce into a more disordered phase with faint dark banding perpendicular to the axis of the gland (Fig 6.7B). At progressive distances down the anterior lumen, the dark perpendicular banding becomes more pronounced with an apparent composition of ~80 nm coalesced uniformly dark globules (Fig 6.7D-F). Extended axially aligned fibrils progressively develop between the dark banding as the constituents progress towards the spinneret (Fig 6.7F).

The final silk fibers do not have the dark perpendicular banding nor the dark globules of the forming fiber inside the anterior silk gland (Fig 6.8A, B). The spun silk fiber is

comprised of axially oriented subfibrils of similar appearance to those that emerge between the dark banding in the anterior gland (Fig 6.6B, Fig 6.7F). The final silk fiber comprises the contents of the two glands fused by a thin fuzzy peripheral layer coating the two subfibers (Fig 6.8A).

### 6.3.7 Alizarin Red S Staining for $Ca^{2+}$

To determine where in the silk spinning process the $Ca^{2+}$ ions enter the silk and complex with phosphoserines, the $Ca^{2+}$-indicating dye, alizarin red S (ARS), was applied to lyophilized intact silk glands. The native $Ca^{2+}$-containing silk fibers serving as the positive control develops the deep crimson color associated with the ARS stain as shown in the representative silk fiber cross-section in Figure 6.9C. Conversely ARS-stained silk fibers depleted of $Ca^{2+}$ with $Na^{+}$-EDTA are transparent and devoid of color (Fig. 6.9D). The silk gland and its contents did not stain positive for $Ca^{2+}$. Representative sections from the posterior storage and anterior fiber-forming regions are colorless (Fig. 6.9A, B).

### 6.3.8 Scanning Electron Microscopy of the Caddisworm Case

Case-making caddisworms collected locally from the Red Butte Creek (Salt Lake City, UT) will repair their cases with the provided glass beads when artificially damaged and components are removed (Fig. 6.10A). Examination of the case interior by SEM shows how the caddisworm uses its silk underwater like an adhesive tape to adjoin the glass beads (Fig. 6.10B-F). The silk fibers have a flattened ribbon-like architecture with a clearly discernable seam between respective contributions of the two silk glands. These silk ribbons lay flat and spread out on the glass substrate appearing to maximize the interfacial

contact area. Higher magnification images show that the freshly drawn fibers plastically deform to accommodate the substrate topography and other previously spun fibers (Fig. 6.10E-F). A fibrillar silk substructure oriented along the fiber axis was observed in the higher magnification images (Fig. 6.10E-F).

### 6.3.9 Time-lapse Photography of Tanning Silk

Freshly spun silk is white and slightly transparent (Fig. 6.11A). The silk gradually turns red over the course of many hours as shown by the representative photographs from the time-lapse data set (Fig. 6.11A-F). The gradual redesigning of the silk was monitored by changes in the blue channel intensity of the photographs. The average blue channel intensity within the rectangular box was fitted with an exponential decay function with a goodness of fit (R-squared) of 0.986 (Fig. 6.11G). The time constant (T) for the reddening of the silk is 4.66 h.

## 6.4 Discussion

The results from this study are condensed into a model of caddisworm silk spinning presented in Figure 6.12. The silk glands do not contain the multivalent meatal ions typical of the final silk fibers (Fig. 6.1A); therefore $Ca^{2+}$, which is critical to the silk structure and mechanical properties, must necessarily be added to the silk fibers somewhere in the silk spinning process. The IR-spectra of the native silk phosphates in the posterior silk gland from 875-1184 $cm^{-1}$ is similar in appearance to the spectra of silk fibers exchanged with $Na^{+}$-EDTA confirming un-complexed phosphates in the precursors of the posterior silk gland (Fig. 6.2). The effect of multivalent metal ions on the phosphate IR spectra of

caddisworm silk has been discussed in detail in a previous study [23]. Briefly, the splitting of the phosphate symmetric stretching mode ($\nu_s$) into modes designated $\nu_{s1}$ and $\nu_{s2}$ as observed for the native caddisworm silk fibers is atypical of known metal-ion-binding phosphoproteins. For example, in the $Ca^{2+}$ sequestering phosphoproteins milk $\alpha_s$-casein and hen egg yolk phosvitin, complexation with $Ca^{2+}$ causes a 10-20 $cm^{-1}$ shift in the $\nu_s$ mode to higher wavenumbers but a second $\nu_s$ band does not emerge [35–37]. Splitting of the caddisworm silk phosphate $\nu_s$ mode is characteristic of phosphate compounds in periodic ordered arrangements such as crystalline phosphate salts, the phosphate minerals burshite and monitite, and phospholipid bilayers complexed with $Ca^{2+}$ [32,38–40]. It was thus proposed that the $\nu_{s1}$ and $\nu_{s2}$ modes of native caddisworm silk fibers are the result of factor group splitting of the solitary $Na^+$-975 $cm^{-1}$ peak due to periodic order of $Ca^{2+}$-phosphate complexes in the caddisworm H-fibroin $(pSX)_n$ domains [23]. The emergence of the second $\nu_{s2}$ peak at ~1010 $cm^{-1}$ is therefore an indicator of periodic ordered phosphates in complexes with multivalent metals like $Ca^{2+}$. Splitting of the gland contents $\nu_s$ mode by the addition of relatively low concentration 1 mM $CaCl_2$ indicates that the organized complexes are not driven by the process of shearing during spinning but rather the availability of free $Ca^{2+}$. At some point during silk processing, the fibers or pre-fiber components must be exposed to elevated concentrations of free multivalent metal ions like $Ca^{2+}$ which then diffuse in and complex with silk pSs.

It has been previously suggested that the formation of $Ca^{2+}$-pS complexes might be influenced by pH-dependent changes in the pS from the mono to dianionic form [21,41]. The IR spectrum of the gland contents reveals that the native gland pS are predominantly dianionic; the dianionic symmetric ($\nu_s$) mode at 968 $cm^{-1}$ predominates over the P-O(H)

stretching mode of the monanioinic species at 924 $cm^{-1}$ (Fig 6.2A). The pH of the gland contents is therefore above the $pK_a$ of the silk pSs. The $pK_a$ of the silk phosphates was measured at pH 4.53-4.58 (Fig 6.3). In good agreement with the IR spectrum of the gland pSs, the pH of the hydrated gland constituents measured well above the silk pS $pK_a$ at 7.19. Insect hemolymph pHs are reported from pH 6.4-7.5 depending on the species [42]. The pH of the silk gland contents likely reflects the worm's native internal physiology rather than indicating a special mechanisms for maintaining a separate $H^+$ gradient in the gland lumen. The pSs stored in the gland contents are already at a pH in which they will readily form complexes with multivalent metals like $Ca^{2+}$. A theoretical increase in pH during fiber processing would have a negligible effect on $Ca^{2+}$-pS complex formation. Although the titration curves recorded for the silk pSs with and without calcium showed no difference in $pK_a$, the steeper profile of the titration with $Ca^{2+}$ suggests that the addition of $Ca^{2+}$ to silk pSs above the $pK_a$ will promote the dianionic form. For example, in the gland contents at pH 7.19, the small monoanionic contribution would greatly diminish upon the binding of $Ca^{2+}$ even if there is no change in environmental pH.

The changes observed in chain conformation during native silk spinning, from the native gland contents to the native silk fibers, can primarily be explained by the addition of $Ca^{2+}$ without consideration of other processing aspects such as shear-induced alignment of the peptide chains (Fig 6.4). This does not mean that higher order structures are unaffected by shearing of the pre-fiber components during spinning. The amide I band (1576-1720 $cm^{-1}$) corresponding to the C=O stretching mode of the peptide backbone gives information about the protein secondary structure. The difference spectrum created by subtracting the amide I bands of native gland contents from the $Ca^{2+}$-treated gland contents

is effectively the inverse of the difference spectrum created by subtracting that of native silk from the $Ca^{2+}$-depleted silk fibers (Fig. 6.4). In terms of secondary structure and chain conformation, the removal of $Ca^{2+}$ from native silk is the opposite of adding $Ca^{2+}$ to the native gland contents.

In samples without $Ca^{2+}$, the random coil conformation predominates (~42%): either the native gland contents or EDTA treated silk (Fig. 6.4A, D). The addition of $Ca^{2+}$, either in native silk fibers or $Ca^{2+}$-treated gland contents, accompanies an increase in both the β (1616-1637 $cm^{-1}$ ) and turn (1663-1696 $cm^{-1}$) structures (Fig. 6.4B, E). The increase in β-structures is consistent with our proposed $Ca^{2+}$-stabilized $(pSX)_n$ β-domains. In the H-fibroin D-repeat there are two $(pSX)_4$ domains flanking a central Pro-Gly pair by 5 residues on either side. Experiments on small peptides containing a Pro-Gly pair have shown dihedral angels consistent with a bend in the protein chain [43]. Molecular dynamic simulations provide theoretical support for the antiparallel $Ca^{2+}$-stabilized β-hairpin from the D-repeat $(pSX)_4$ domains [20,24]. The formation of these $Ca^{2+}$-stabilized hairpins might explain, in part, the increase in both β and turn structures for $Ca^{2+}$ containing samples. The $Ca^{2+}$-dependent changes in silk secondary structure provide strong support for the theory of $Ca^{2+}$-induced setting of caddisworm silk during fiber spinning.

There is a relationship between liquid-phase separation in protein systems and disorder in the protein chain. All proteins known to liquid-phase separate are either partially or entirely intrinsically disordered [44]. The composition of the caddis silk proteins within the posterior silk gland lumen is primarily random coil consistent with the intrinsically disordered systems (Fig. 6.4A). The contents of the posterior gland have a ~54 nm granular composition. Similar observations were made previously for the gland contents of the case-

making caddisworm *Pycnopsyche guttifer* which was also comprised 26-90 nm granules [45]. The study author observed the small granular components to be the same size and appearance as Golgi vesicles extruded by the silk-producing cells. The uniform granular composition of the pre-fiber components therefore likely represents the fundamental secretory unit rather than structures driven by protein folding or higher order molecular arrangements.

In the absence of $Ca^{2+}$, there must be a counter ion to the predominantly dianionic pSs stored in the silk gland. The negatively charged $(pSX)_n$ domains in the caddisworm H-fibroin D, E, and F repeats alternate with positively charged blocks of 3-4 Arg residues [20]. The role of the Arg-rich blocks is poorly understood yet highly conserved in the H-fibroins of representative species in each of the three caddisworm suborders [20,22]. The caddisworm H-fibroin has generic similarities with known liquid-phase separating intrinsically disorder proteins [44]. For example, the intrinsically disordered N-terminal component of the nuage cellular protein Ddx4 is involved in phase-separation into membrane-less organelles. The ability of the the N-terminal tail of Ddx4 to liquid-phase separate was attributed to its block co-polymer structure of alternating positive and negative regions comprising 3-8 residues of like charge such as blocks of arginine [44,46]. The Arg-rich block in the caddisworm H-fibroin protein might condense the chain by interacting with the neighboring acidic $(pSX)_n$ domains. This is analogous, in some regard, to the arginine-rich proteins that bind DNA phosphodiesters to facilitating condensation in vertebrate sperm and certain viruses [47,48].

There is little doubt that fiber formation commences at the chitinous annular narrowing where the silk dope passes into the anterior gland lumen; here the granular silk precursors

lose anisotropy and axially aligned subfibrils begin to emerge (Fig 6.5-7). The annular narrowing appears to shear the fiber components much like the spinnerets used in industrial fiber spinning [2]. To see if fiber formation in this region is also accompanied by a $Ca^{2+}$-gradient, a rapidly dissected, frozen, and lyophilized gland pair was rehydrated in a solution of alizarin s red (ASR) at pH 4.1. Because the silk phosphates have a high affinity for multivalent metal ions like $Ca^{2+}$, this protocol was designed to eliminate extraneous sources that otherwise might have been introduced from dissection buffers and fixatives; this was done at the expense of preserving tissue morphology. ASR is typically used as an indicator for calcification in bone tissue. The abundant $H^{+}$ ions at the low pH of the alizarin s red stain (pH 4.1) protonate the phosphate ligands in hydroxyapatite bone mineral, thereby releasing the complexed $Ca^{2+}$ and lesser amounts of $Mg^{2+}$. An insoluble dye precipitate, known as a lake, is formed as ASR complexes with the multivalent ions [49,50]. This technique is sensitive to the relevant levels of $Ca^{2+}$ in the caddisworm silk because the native fibers develop the crimson color associated with ASR albeit somewhat weaker than bone tissue as might be expected because one is mineralized and the other only a $Ca^{2+}$-binding phosphoprotein (Fig. 6.9C). The samples were therefore intentionally sectioned unusually think at 10 μm to maximize the amount of dye within each section. The absence of color in ARS stained $Ca^{2+}$-depleted fibers confirms sensitivity to silk $Ca^{2+}$ rather than nonspecific binding with silk proteins. Sections of ARS strained silk glands collected through the anterior region are colorless both in the nascent silk fiber and in the cellular layer. Therefore, multivalent metal ions are absent in relevant concentrations in the nascent silk fiber and cellular layer of the anterior gland. Throughout the gland, the silk pSs are uncomplexed with multivalent metal ions.

The multivalent metal ions critical to the caddisworm silk structure and mechanical properties must come from an extraneous source once the fibers are drawn out of the larva. Dissolved multivalent metal ions like $Ca^{2+}$ and $Mg^{2+}$are typical of freshwater biomes; slightly acidic rain water and snowmelt leaches multivalent metal ions from surrounding bicarbonate minerals like calcite, aragonite, and dolomite. The water of the Red Butte creek from which the caddisworms in this study were collected has an average of 4.15 mM of $Ca^{2+}$ and 2.14 mM of $Mg^{2+}$, more than fourfold the concentration of $Ca^{2+}$ used in this study to artificially drive the formation of complexes with the pSs in the gland silk (Fig. 6.2A) [51]. Snapshots of the silk spinning process are captured in the high magnification SEMs of the interior of the caddisworm composite glass-bead case (Fig 6.10B-F). The now solidified silk fibers were apparently fluid immediately after drawing from the spinneret. For example, the freshly spun fibers contacting the glass beads spread out and flatten fluidly across the glass substrate; cross-laid fibers spanning the glass beads seamlessly fuse into cohesive bundles (Fig. 6.10E, F). We propose that caddisworm silk fibers are drawn from the gland in a fluid state and that the final phase of silk setting is triggered by the environmentally abundant multivalent metal ions as they diffuse into the silk and complex with the H-fibroin $(pSX)_n$ domains. The temporary fluid phase would provide the silk fiber a brief period to flow across the adhesive joint and maximizing interfacial adhesion.

The gradual reddening of post-drawn caddisworm silk fibers indicates the formation of internal covalent bonds by a complex process called tanning (Fig 6.11) [52]. Tanning is best characterized for the insect cuticles, a process also known as sclerotization, but has also been described for the silk cocoons of terrestrial Satturniid moths, among others possible examples [53,54]. Various types of metalloenzymes catalyze the oxidation of

diverse phenolic compounds forming covalent bonds within the proteins, carbohydrates, or chitin of the respective tanned materials. The covalent crosslinks formed during tanning alter the physical and chemical properties of tanned materials, making them highly insoluble and resistant to degradation [52,53]. Efforts to solubilize the spun caddis silk fibers have failed even with strong detergents, denaturants, reducing agents, elevated temperatures, chelating agents, and extremes in pH [55,56]. In comparison, multiple researchers were able to solubilize the caddisworm silk gland contents [57–59]. A heme-peroxidase in the peroxinectin sub-family (Pxt) is co-extruded with the silk fibers of the caddisworm *H. occidentalis* [56]. This enzyme catalyzes intrinsic di-tyrosine crosslinks and covalent linkages with exogenous polyphenolic compounds [58]. Pxt likely contributes to the tanning of the caddisworm silk fibers.

## 6.6 Conclusions

Our current understanding of the caddisworm silk spinning process is summarized as follows. The phosphoproteins stored in the posterior silk gland are intrinsically disordered and do not contain multivalent metal counter ions. During spinning, the silk fibers are sheared through an annular narrowing at the entrance into the anterior silk gland. In the anterior gland, shear induces the formation of a fibrous substructure but multivalent metal ions are not added to the silk. The nascent silk fibers are drawn out of the gland in a semi-fluid state flowing and deforming to accommodate the substrate surface. The silk fibers are quickly set when multivalent metal ions from the environment diffuse into the silk fibers and complex with silk pSs. $Ca^{2+}$-stabilized extended β-sheets spontaneously form from the silk $(pSX)_n$ domains and there is a decrease in random coil chain conformation. Tanning of

the silk fibers occurs over the next several hours and the silk fibers final conformation is irreversibly stabilized by covalent crosslinks.

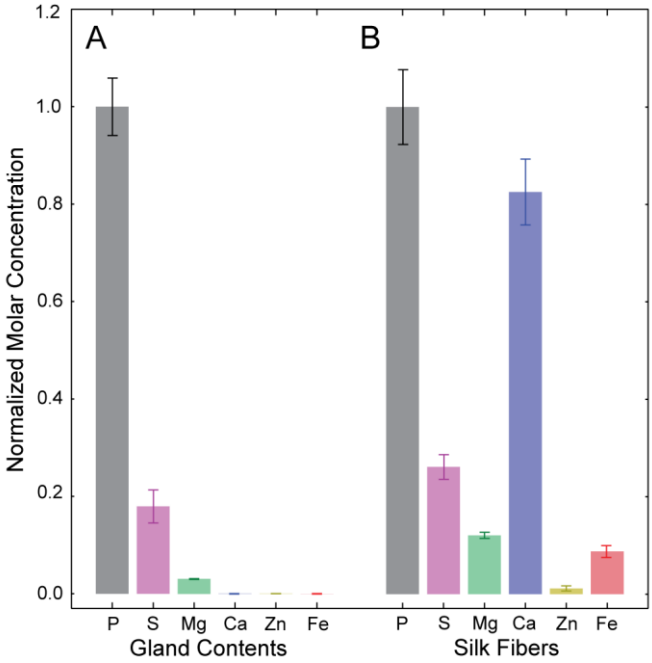


Figure 6.1. Elemental analysis by ICP-OES. (A) The contents of the posterior silk gland. (B) The final silk fibers. For comparison, the concentrations were normalized for the phosphorus of the intrinsic silk phosphoserines. The bars represent the average of three runs and the error bars are the fractional total deviation.

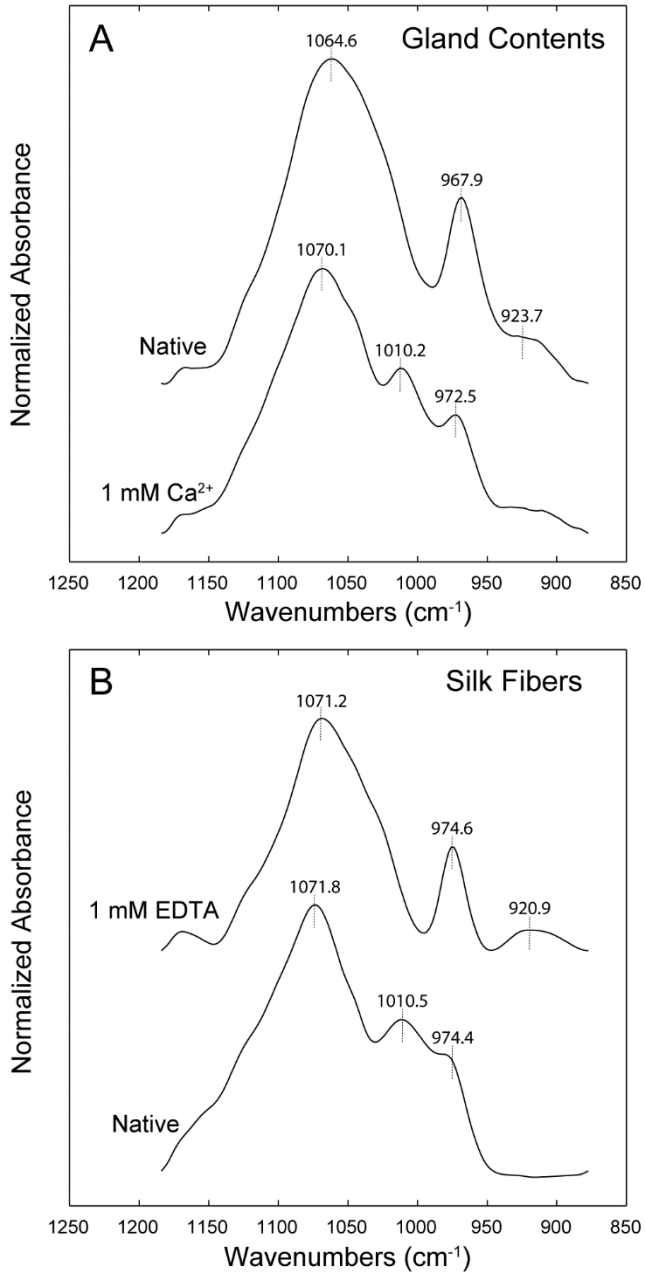


Figure 6.2. Peptidyl phosphate stretching modes (875-1184 $cm^{-1}$). (A) Lyophilized native gland contents (top), and lyophilized gland contents treated in excess 1 mM $CaCl_2$, pH 7 (bottom). (B) Lyophilized native silk (bottom), and the lyophilized silk fibers treated in excess 1 mM EDTA pH 7.0 (top).

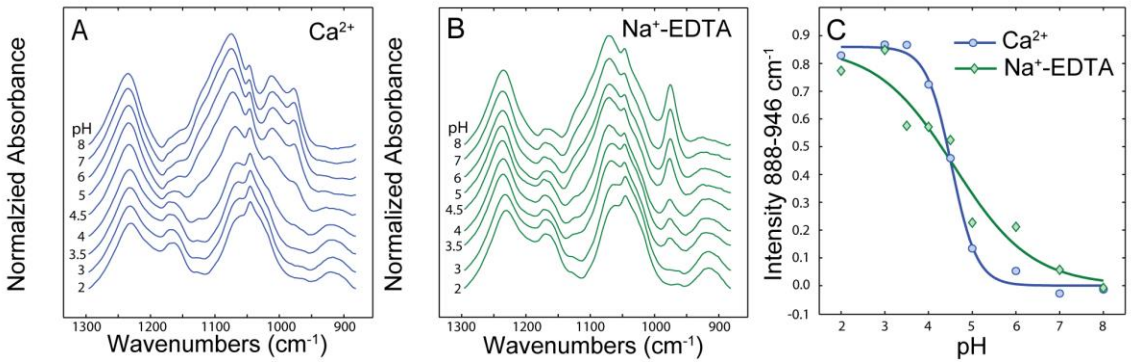


Figure 6.3. IR-Titration of silk phosphates with and without $Ca^{2+}$. Absorbance spectra of the silk phosphate region from 881-1296 $cm^{-1}$ in solutions of progressively decreaseing pH from 8.0-2.0 with either 5 mM $CaCl_2$ (A) or 5 mM $Na^+$-EDTA (B). (C) The integrated intensities of the P-O(H) bond of the monoanion from 888-946 $cm^{-1}$ (symbols) fitted with sigmoidal curves (solid lines).

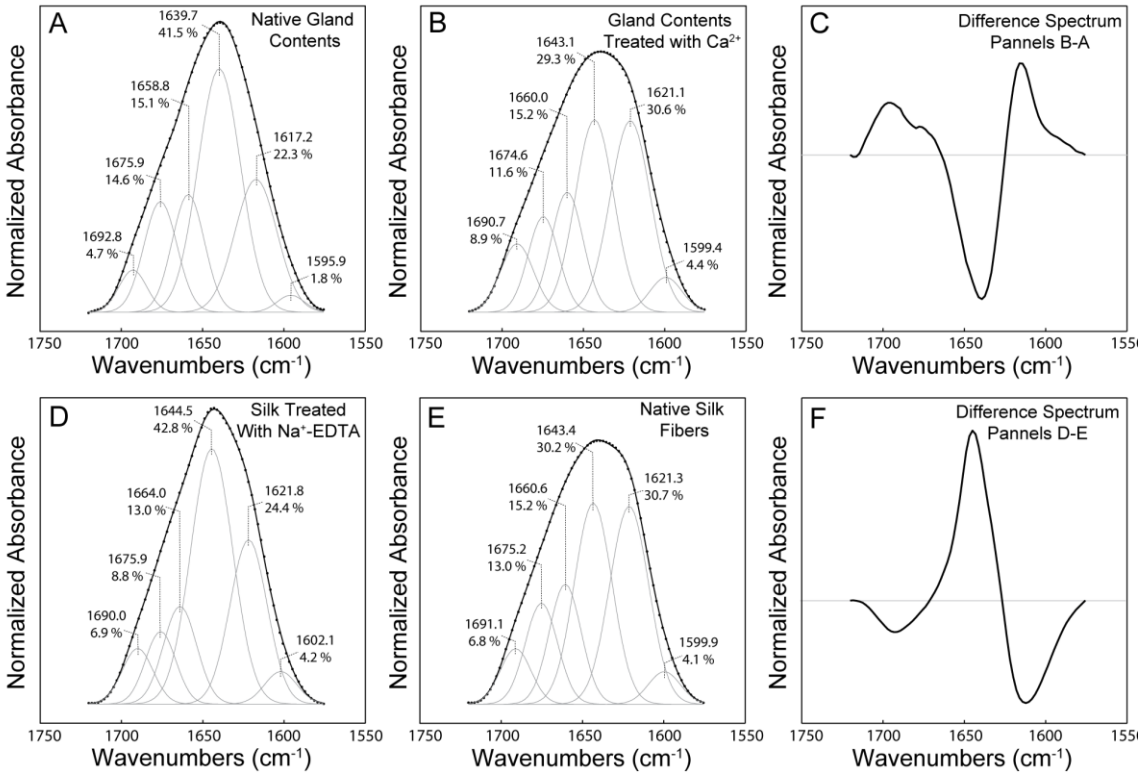


Figure 6.4. FTIR amide I decomposition. (A) Native gland contents. (B) Gland contents treated with excess 1 mM $CaCl_2$. (C) The difference spectra of panel A from B. (D) Silk Fibers treated in excess 1 mM $Na^+$-EDTA. (E) Native silk fibers. (F) Difference spectra of panel E from D.

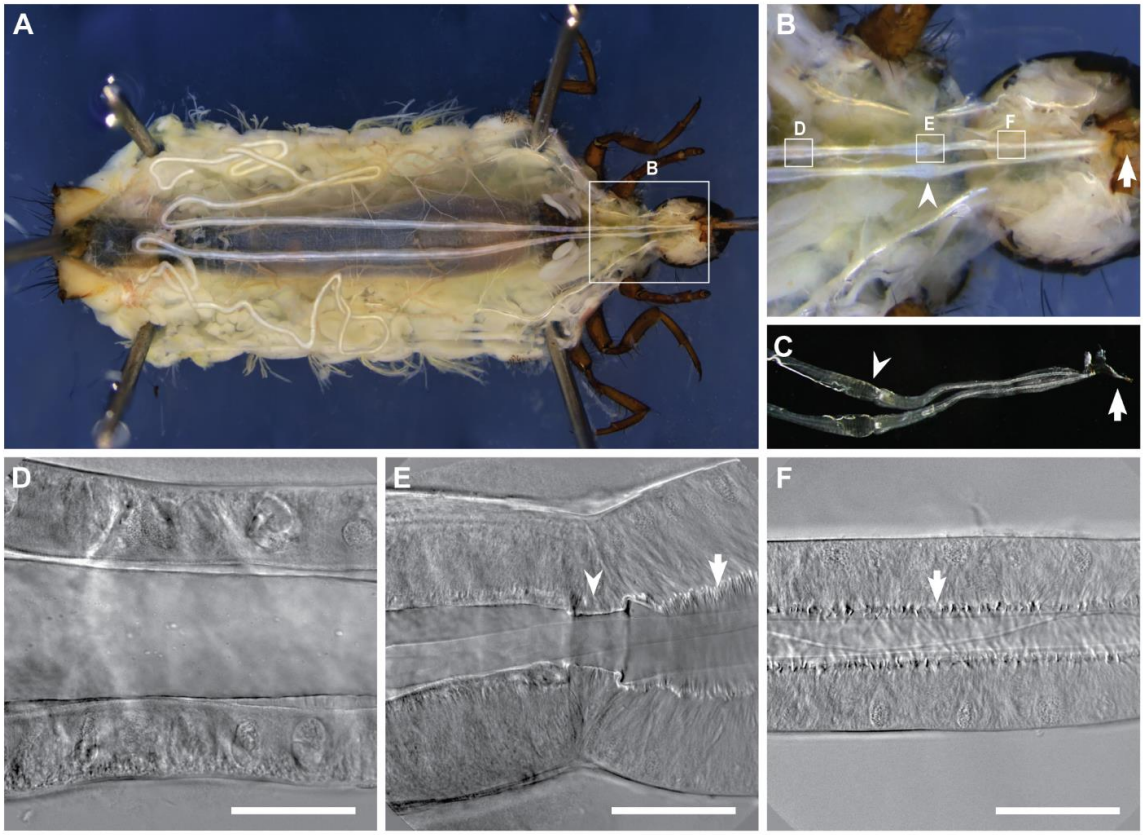


Figure 6.5. Caddisworm silk gland anatomy. (A) Ventral view of the silk gland pair. (B) A close up from panel A showing the transition from the posterior to anterior gland regions (arrowhead) and the spinneret (arrow). (C) An isolated gland pair also showing the transition from the posterior to anterior gland regions (arrowhead) and the spinneret (arrow). (D-F) DIC micrograph of the posterior gland (D), the transition from the posterior to anterior gland regions (E), and the anterior gland (F). There is a chitinous annular narrowing (arrowhead) at the transition continuous with the cuticle linin (arrow) of the anterior gland. Scale bars are 50 µm.

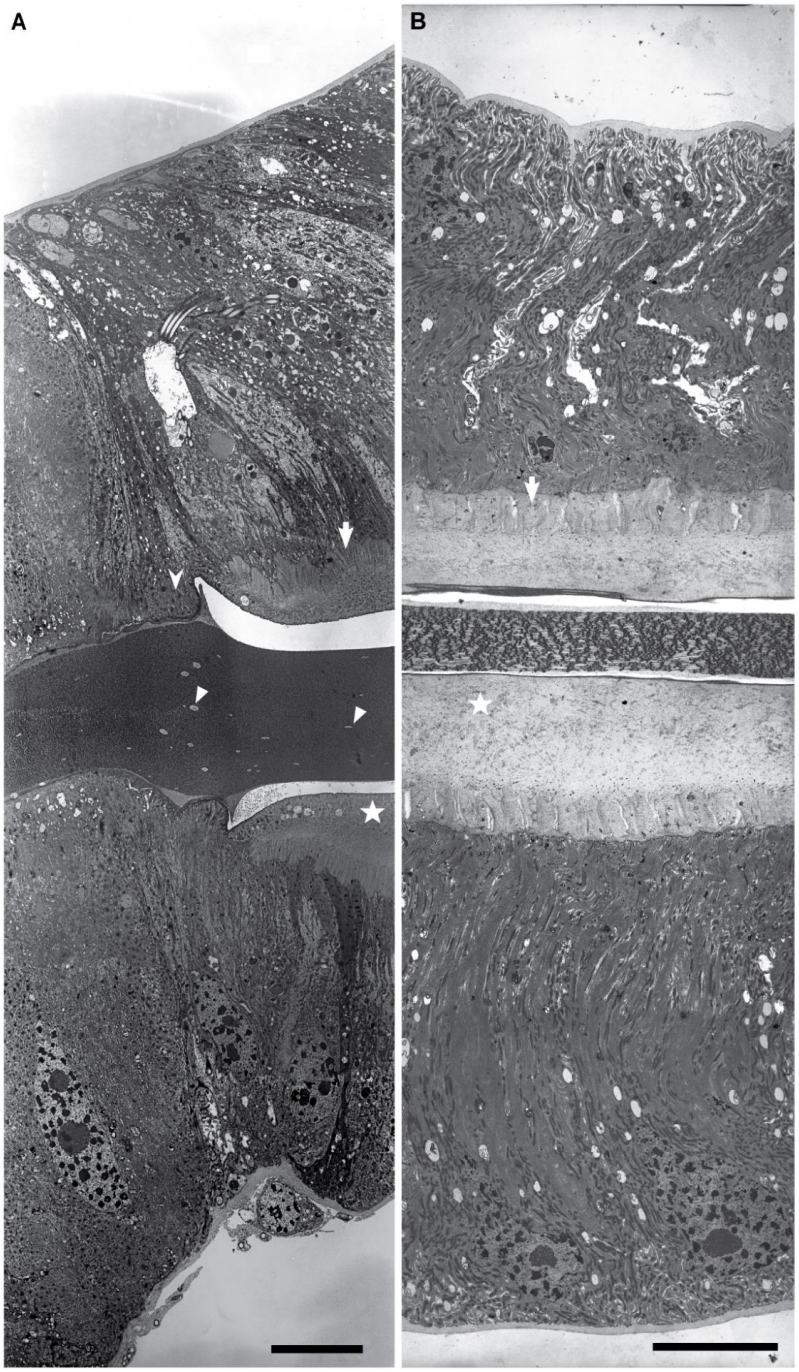


Figure 6.6. Transmission electron micrographs of silk gland longitudinal sections. (A) The transition from posterior to anterior gland showing the chitinous annular narrowing (arrowhead) and the cuticle lining (arrow). Round inclusions in the gland contents start to elongate in this region (triangles). (B) The cuticle-lined (arrow) anterior gland showing the formation of fibrous substructure in the nascent silk fiber. There is a diffuse acellular material surrounding the fiber in the anterior channel (stars). Scale bars are 10 μm.

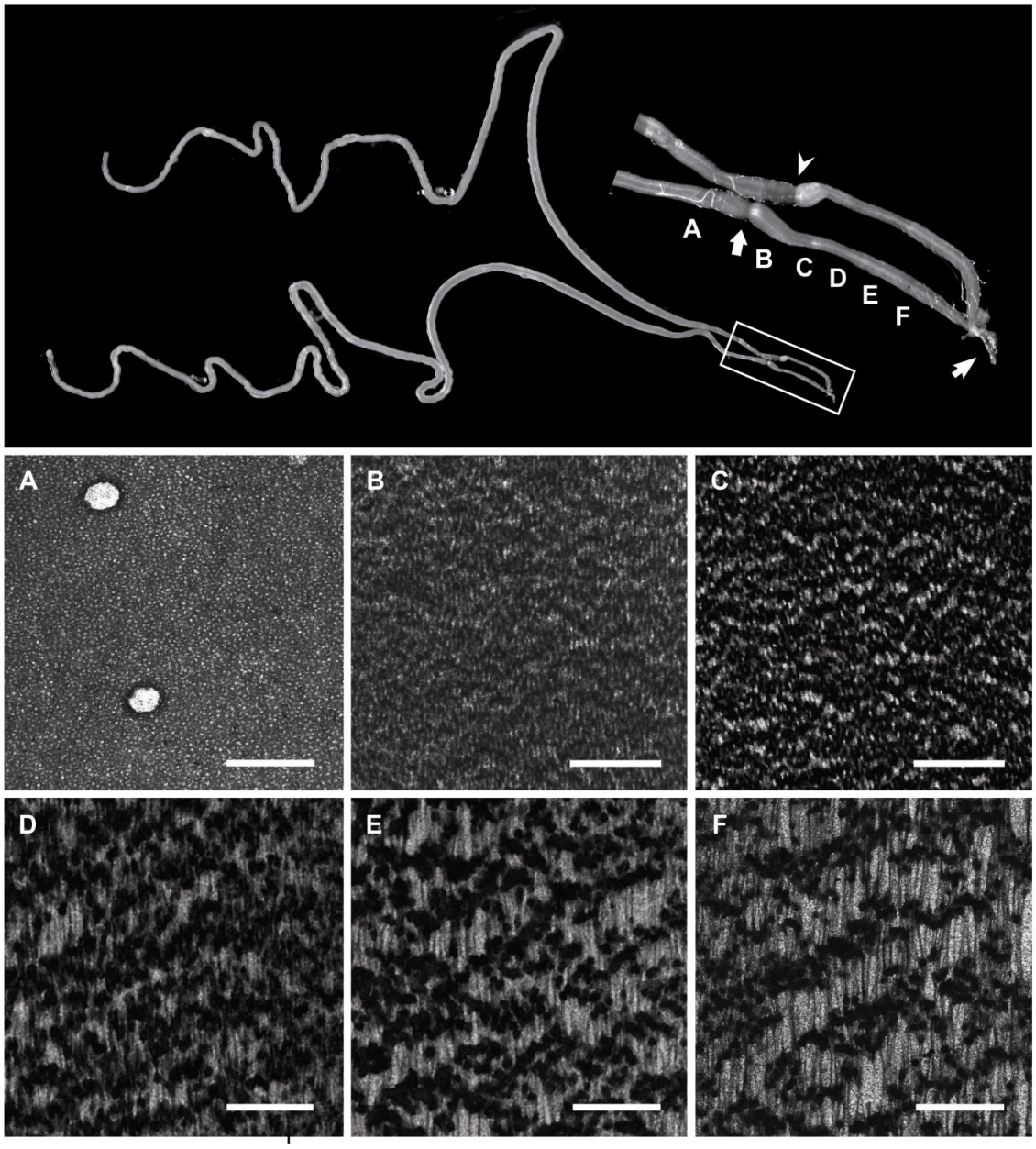


Figure 6.7. The formation of the silk fiber in the anterior silk gland lumen. (Top) An intact silk gland pair dissected from a fifth instar *H. occdentalis* caddisfly larva. The inset shows a close-up view of the anterior silk gland. The arrows mark the bulbous feature at the transition from the posterior to anterior silk glands. The arrowhead marks the silk press and spinneret. The approximate locations of the TEM in A-F are indicated. (A) Isotropic silk dope stored in the posterior silk gland lumen. (B-F) Gradual formation of the silk fiber as the precursors are drawn out of the gland (downward in the micrographs). Scale bars are 1 μm.

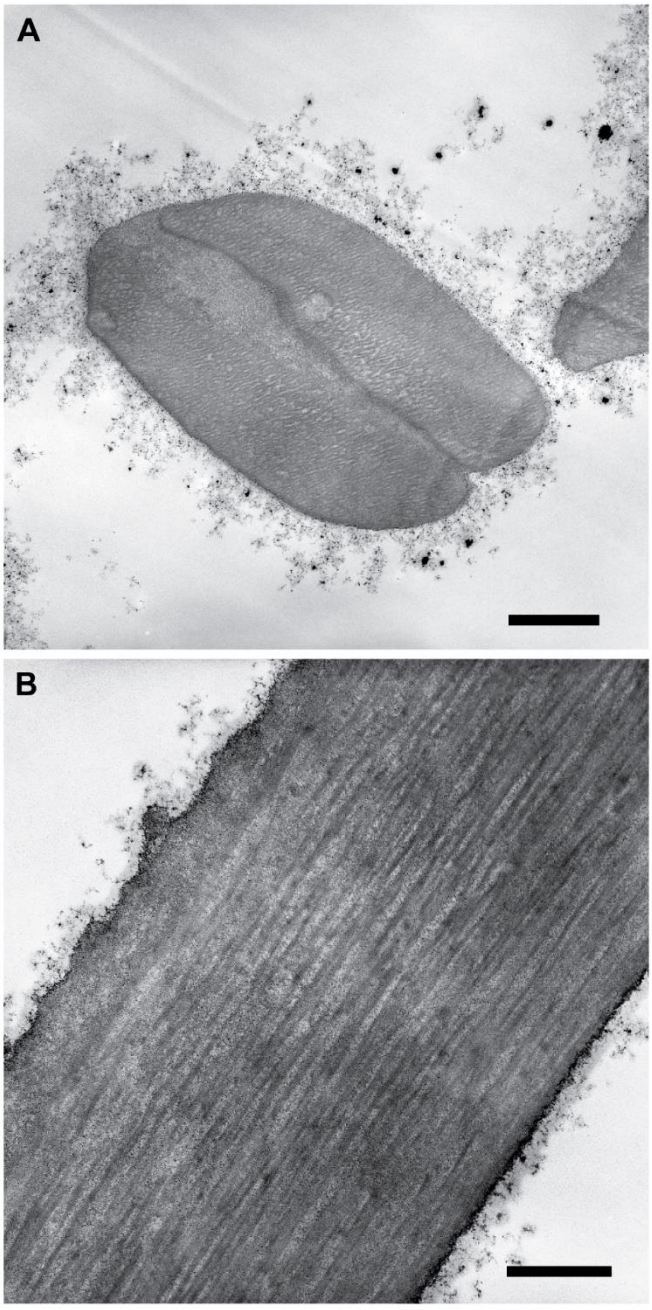


Figure 6.8. Transmission electron micrographs of silk sections. (A) Cross-section through the two silk sub-fibers. Scale Bar is 1µm. (B) Longitudinal section through a single silk sub-fiber. Scale Bar is 0.5µm.

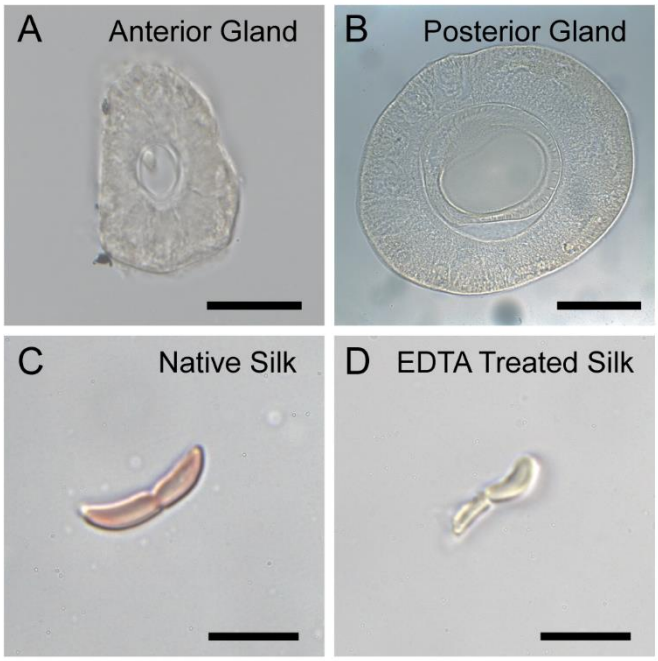


Figure 6.9. Alizarin S red staining for $Ca^{2+}$. Representative of alizarin s red stained cross-sections of the anterior silk gland (A), the posterior silk gland (B), a native silk fiber serving as a positive control (C), and a silk fiber treated in 1 mM $Na^{+}$-EDTA serving as the negative control. Scale bars are 20, 40, 10, and 10 μm, respectively.

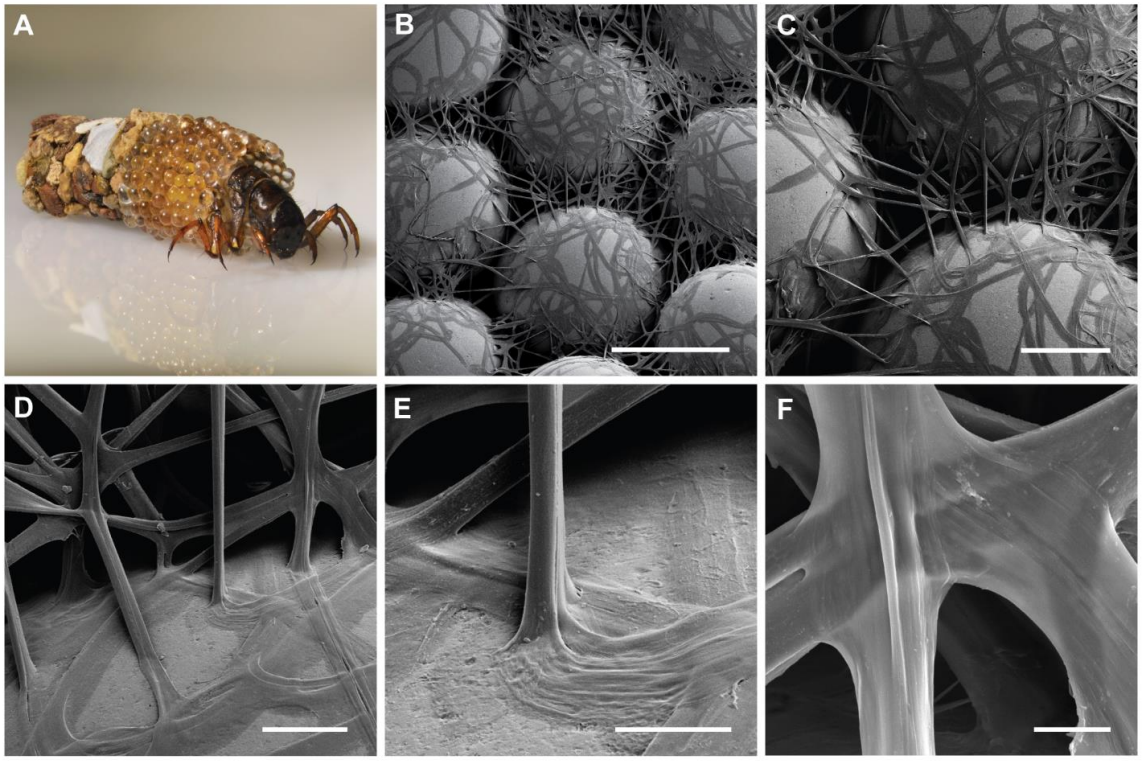


Figure 6.10. The caddisworm silk-stone composite case. (A) The caddisworm *Hesperophylax occidentalis* in a case partially constructed with glass beads. (B-F) SEMs of the inside of the glass bead portion of the case at increasing magnification (scale bars are 500, 200, 50, 20, and 10 μm, respectively.

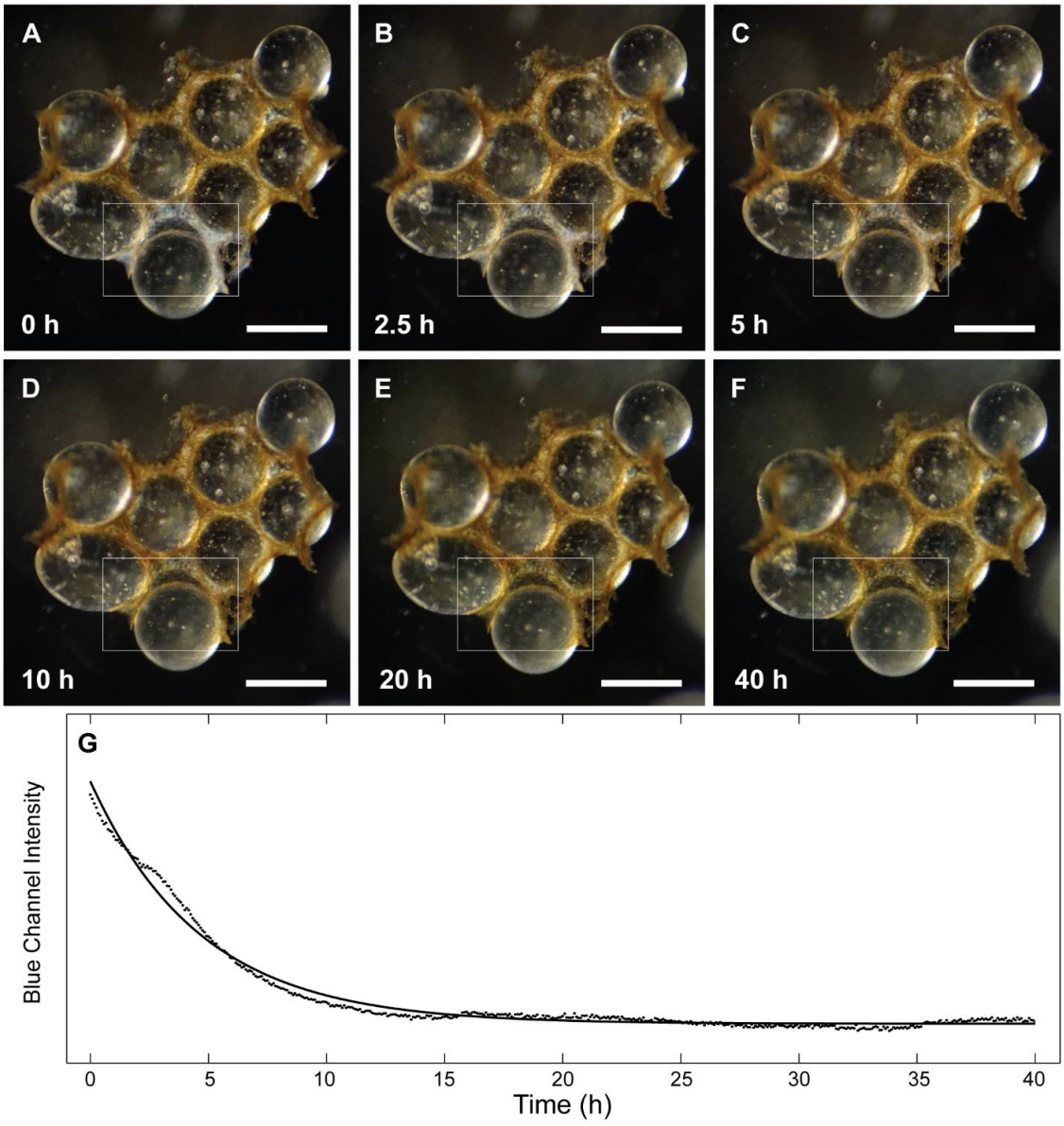


Figure 6.11. Time-lapse photography of silk reddening. (A-F) Successive photographs of freshly spun silk (boxed region) on the inside of a caddisworm case from 0-40 h. (G) The average value of the blue channel inside the boxed region (dotted line) fitted with an exponential decay function (solid line).

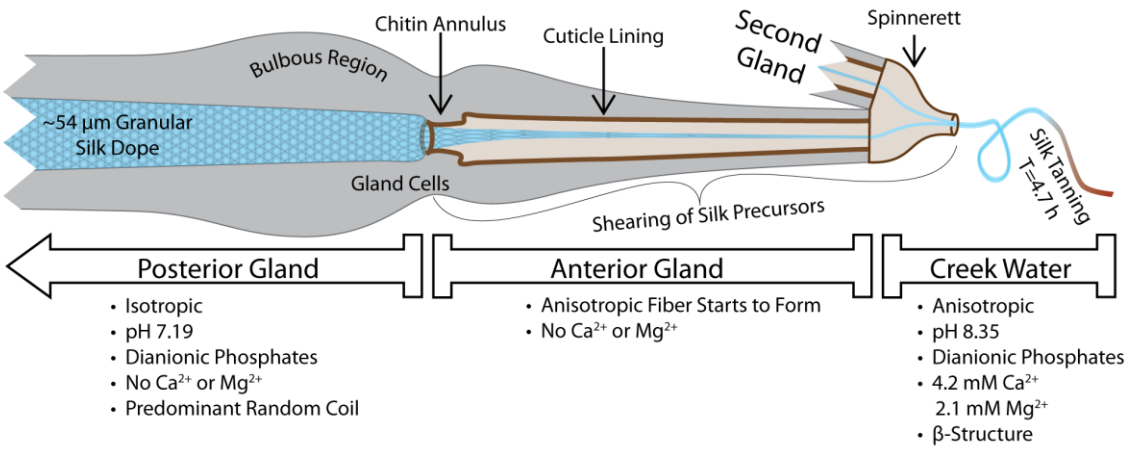


Figure 6.12. A model of caddisworm silk spinning. The results from this study are condensed in this model. As the silk precursors are spun into the final fiber, they pass through three distinct regions: the posterior gland, the anterior gland, and the creek water.

## 6.6 References

[1] N.N. Ashton, D.S. Taggart, R.J. Stewart, Silk tape nanostructure and silk gland anatomy of Trichoptera, Biopolymers 97 (2012) 432–445.

[2] K.K. Chawla, Fibrous materials, Cambridge University Press, New York City, 1998.

[3] C.L. Craig, Evolution of arthropod silks., Annu. Rev. Entomol. 42 (1997) 231–267.

[4] C. Woodings, Regenerated cellulose fibres, Woodhead Publishing, 2001.

[5] M.A. Wilding, Introduction: the structure of fibres, in: Chem. Text. Ind., Springer, 1995: pp. 1–45.

[6] J.P. O'Brien, S.R. Fahnestock, Y. Termonia, K.H. Gardner, Nylons from nature: synthetic analogs to spider silk, Adv. Mater. 10 (1998) 1185–1195.

[7] A. Ochi, K.S. Hossain, J. Magoshi, N. Nemoto, Rheology and dynamic light scattering of silk fibroin solution extracted from the middle division of *Bombyx mori* silkworm, Biomacromolecules 3 (2002) 1187–1196.

[8] F. Vollrath, D.P. Knight, Liquid crystalline spinning of spider silk, Nature 410 (2001) 541–8.

[9] H.-J. Jin, D.L. Kaplan, Mechanism of silk processing in insects and spiders, Nature 424 (2003) 1057–1061.

[10] H. Akai, The structure and ultrastructure of the silk gland, Experientia 39 (1983) 443–449.

[11] T. Asakura, T. Yamane, Y. Nakazawa, T. Kameda, K. Ando, Structure of *Bombyx mori* silk fibroin before spinning in solid state studied with wide angle X-ray scattering and C-13 cross- polarization/magic angle spinning NMR, Biopolymers 58 (2001) 521–525.

[12] H. Saitô, R. Tabeta, T. Asakura, Y. Iwanaga, A. Shoji, T. Ozaki, I. Ando, High-resolution 13C NMR study of silk fibroin in the solid state by the cross-polarization-magic angle spinning method. Conformational characterization of silk I and silk II type forms of *Bombyx mori* fibroin by the conformation-dependent 13C chemical shif, Macromolecules 17 (1984) 1405–1412.

[13] H.P. Wells, Fly-rods and fly-tackle, Harper & Brothers, Franklin Square, New York, 1885.

[14] D.H. Hijirida, K.G. Do, C. Michal, S. Wong, D. Zax, L.W. Jelinski, 13C NMR of *Nephila clavipes* major ampullate silk gland, Biophys. J. 71 (1996) 3442–3447.

[15] K. Rudall, W. Kenchington, Arthropod silks: the problem of fibrous proteins in

animal tissues, Annu. Rev. Entomol. 16 (1971) 73–96.

[16] J.O. Warwicker, Comparative studies of fibroins II. The crystal structure of various fibroins, J. Mol. Biol. 2 (1960) 350-362.

[17] F. Lucas, J.T.B. Shaw, S.G. Smith, Comparative studies of fibroins: I. The amino acid composition of various fibroins and its significance in relation to their crystal structure and taxonomy, J. Mol. Biol. 52 (1960) 339–349.

[18] X. Shi, G.P. Holland, J.L. Yarger, Amino acid analysis of spider dragline silk using 1H NMR, Anal. Biochem. 440 (2013) 150–157.

[19] S.J. Lombardi, D.L. Kaplan, The amino acid composition of major ampullate gland silk (dragline) of *Nephila clavipes* (Araneae, Tetragnathidae), J. Arachnol. 18 (1990) 297–306.

[20] N.N. Ashton, D.R. Roe, R.B. Weiss, T.E. Cheatham, R.J. Stewart, Self-tensioning aquatic caddisfly silk: $Ca^{2+}$-dependent structure, strength, and load cycle hysteresis, Biomacromolecules 14 (2013) 3668–3681.

[21] R.J. Stewart, C.S. Wang, Adaptation of caddisfly larval silks to aquatic habitats by phosphorylation of H-fibroin serines, Biomacromolecules 11 (2010) 969–974.

[22] N. Yonemura, F. Sehnal, K. Mita, T. Tamura, Protein composition of silk filaments spun under water by caddisfly larvae., Biomacromolecules 7 (2006) 3370–8.

[23] N.N. Ashton, H. Pan, R.J. Stewart, R.J. Stewart, Connecting caddisworm silk structure and mechanical properties : combined infrared spectroscopy and mechanical analysis, Open Biol. 14 (2016) 3668-3681.

[24] J.W. Strzelecki, J. Strzeleka, K. Mikulska, M. Tszydel, A. Balter, W. Nowak, Nanomechanics of new materials-AFM and computer modelling studies of Trichoptera silk, Cent. Eur. J. Phys. 9 (2011) 482–491.

[25] J.B. Addison, N.N. Ashton, W.S. Weber, R.J. Stewart, G.P. Holland, J.L. Yarger, β-Sheet nanocrystalline domains formed from phosphorylated serine-rich motifs in caddisfly larval silk: a solid state NMR and XRD study, Biomacromolecules 14 (2013) 1140–1148.

[26] J.B. Addison, W.S. Weber, Q. Mou, N.N. Ashton, R.J. Stewart, G.P. Holland, J.L. Yarger, Reversible assembly of β-sheet nanocrystals within caddisfly silk, Biomacromolecules 15 (2014) 1269–1275.

[27] N.N. Ashton, R.J. Stewart, Self-recovering caddisfly silk: energy dissipating, $Ca^{2+}$-dependent, double dynamic network fibers, Soft Matter 11 (2015) 1667–1676.

[28] V. Sandrin, W.I. Sundquist, ESCRT requirements for EIAV budding, Retrovirology 10 (2013) 1-14.

[29] S.J.D. Neil, V. Sandrin, W.I. Sundquist, P.D. Bieniasz, An interferon-α-induced tethering mechanism inhibits HIV-1 and ebola virus particle release but is counteracted by the HIV-1 vpu protein, Cell Host Microbe. 2 (2007) 193–203.

[30] H. Deng, J. Wang, R. Callender, W.J. Ray, Relationship between bond stretching frequencies and internal bonding for [$^{16}O_4$]- and [$^{18}O_4$] phosphates in aqueous solution, J. Phys. Chem. B. 102 (1998) 3617–3623.

[31] J.M. Sanchez-Ruiz, M. Martinez-Carrion, A Fourier-transform infrared spectroscopic study of the phosphoserine residues in hen egg phosvitin and ovalbumin, Biochemistry. 27 (1988) 3338–42.

[32] G. Laroche, E.J. Dufourc, J. Dufourcq, M. Pizolet, Structure and dynamics of dimyristoylphosphatidic acid/calcium complexes by $^2$H NMR , infrared , and Raman spectroscopies and small-angle X-ray diffraction, Biochemistry 30 (1991) 3105–3114.

[33] X. Hu, D. Kaplan, P. Cebe, Determining beta-sheet crystallinity in fibrous proteins by thermal analysis and infrared spectroscopy, Macromolecules 39 (2006) 6161–6170.

[34] J. Kong, S. Yu, Fourier transform infrared spectroscopic analysis of protein secondary structures, Acta Biochim. Biophys. Sin. 39 (2007) 549–559.

[35] C. Fernández, S.F. Ausar, R.G. Badini, L.F. Castagna, I.D. Bianco, D.M. Beltramo, An FTIR spectroscopy study of the interaction between $\alpha_s$-casein-bound phosphoryl groups and chitosan, Int. Dairy J. 13 (2003) 897–901.

[36] T. Ono, S. Kaminogawa, S. Odagiri, K. Yamauchi, A study on the binding of calcium Ions to $\alpha_{s1}$-casein, Agr. Biol. Chem. 40 (1976) 1717–1723.

[37] B. Li, J. Raff, A. Barkleit, G. Bernhard, H. Foerstendorf, Complexation of U(VI) with highly phosphorylated protein, phosvitin: A vibrational spectroscopic approach, J. Inorg. Biochem. 104 (2010) 718–725.

[38] A.C. Chapman, L.E. Thirlwell, Spectra of phosphorus compounds—I the infra-red spectra of orthophosphates, Spectrochim. Acta. 20 (1964) 937–947.

[39] E.E. Berry, C.C. Baddiel, The Infra-red spectrum of dicalcium phosphate dihdrate (Brushite), Spectrochim. Acta Part A Mol. Spectrosc. 23 (1967) 2089–2097.

[40] A. Hirsch, I. Azuri, L. Addadi, S. Weiner, K. Yang, S. Curtarolo, L. Kronik, Infrared absorption spectrum of brushite from first principles, Chem. Mater. 26 (2014) 2934–2942.

[41] T. Hatano, T. Nagashima, The secretion process of liquid silk with nanopillar structures from *Stenopsyche marmorata* (Trichoptera: Stenopsychidae), Sci. Rep. 5 (2015) 9237.

[42] J.F. Harrison, Insect acid-base physiology, Annu. Rev. Entomol. 46 (2001) 221–250.

[43] S.S. Zimmerman, H. a Scheraga, Influence of local interactions on protein structure. I. Conformational energy studies of N-acetyl-N'-methylamides of Pro-X and X-Pro dipeptides., Biopolymers 16 (1977) 811–843.

[44] V.N. Uversky, Protein intrinsic disorder-based liquid–liquid phase transitions in biological systems: Complex coacervates and membrane-less organelles, Adv. Colloid Interface Sci. (2016).

[45] M. Engster, Studies on silk secretion in the Trichoptera (*F. Limnephilidae*): I. histology, histochemistry, and ultrastructure of the silk glands, J. Morphol. 150 (1976) 183–212.

[46] T.J. Nott, E. Petsalaki, P. Farber, D. Jervis, E. Fussner, A. Plochowietz, T.D. Craggs, D.P. Bazett-Jones, T. Pawson, J.D. Forman-Kay, A.J. Baldwin, Phase transition of a disordered nuage protein generates environmentally responsive membraneless organelles, Mol. Cell. 57 (2015) 936–947.

[47] L.R. Brewer, Protamine-induced condensation and decondensation of the same DNA molecule, Science 286 (1999) 120–123.

[48] T.M. Cao, M.T. Sung, A protamine-like domain in basic adenovirus core protein, Biochem. Biophys. Res. Commun. 108 (1982) 1061–1066.

[49] Y. Fain, V., E. Zaitsev, B., A. Rayabov, M., Metal complexes with alizarin and alizarin red s: Electronic absorption spectra and structure of ligands, Russ. J. Coord. Chem. 5 (2004) 365–370.

[50] H. Puchtler, S.N. Meloan, M.S. Terry, On the history and mechanism of alizarin and alizarin red S stains for calcium, J. Histochem. Cytochem. 17 (1969) 110–124.

[51] M.A. Mast, D.W. Clow, Environmental characteristics and water quality of hydrologic benchmark network stations in the western United States, 1963-95, US Department of the Interior, US Geological Survey, Reston, Virginia, 2000.

[52] J. Kramer, T.D. Morgan, T.L. Hopkins, A. Christensen, J. Schaefer, Chapter 7 insect cuticle tanning enzymes and cross-link Structure, ACS Symposium Series, Washington DC, 1991.

[53] N.A. Mitchinson, Tanned silks, Proc. R. Soc. Lond. B. 187 (1974) 133–170.

[54] H.S. Rapoport, R.E. Shadwick, Reversibly labile, sclerotization-induced elastic properties in a keratin analog from marine snails: whelk egg capsule biopolymer (WECB), J. Exp. Biol. 210 (2007) 12–26.

[55] M.S. Engster, Studies on silk secretion in the Trichoptera (*F. Limnephilidae*): II.

structure and amino acid composition of the silk, Cell Tissue Res. 169 (1976) 77–92.

[56] C.-S. Wang, N.N. Ashton, R.B. Weiss, R.J. Stewart, Peroxinectin catalyzed dityrosine crosslinking in the adhesive underwater silk of a casemaker caddisfly larvae, *Hysperophylax occidentalis*, Insect Biochem. Mol. Biol. 54C (2014) 69–79.

[57] N. Yonemura, K. Mita, T. Tamura, F. Sehnal, Conservation of silk genes in Trichoptera and Lepidoptera., J. Mol. Evol. 68 (2009) 641–53.

[58] C.S. Wang, H. Pan, G.M. Weerasekare, R.J. Stewart, Peroxidase-catalysed interfacial adhesion of aquatic caddisworm silk, J. R. Soc. Interface. 12 (2015).

[59] K. Ohkawa, Y. Miura, T. Nomura, R. Arai, Isolation of silk proteins from a caddisfly larva , *Stenopsyche Marmorata*, J. Fiber Bioeng. Informatics. 5 (2012) 125–137.

# CHAPTER 7

# CONCLUSION

## 7.1 Study Discussion

The mechanochemical characterization of case-making caddisworm silk, discussed in this dissertation, functionally explains many of the unique adaptations conserved broadly in caddisworm silks, adaptions not found in their terrestrial relatives Lepidoptera. Trichoptera diverged from Lepidoptera ~234 million years ago, around the time of the first dinosaurs, and quickly became fully aquatic. By around ~203 million years ago, all three suborders were distinct [1]. Cross-suborder comparisons from representative species give us some idea of the early H-fibroin adaptations driven by the environmental pressures of the caddisworm's new habitat. One of the conserved features in the silks of all Trichopteran suborders are phosphorylated serines (pS) in blocky serial alternating repeats throughout the H-fibroin [2]. There are comparable amino acid ratios of Ser in the silks of both Trichoptera and Lepidoptera ~8-15 mol% [3]. One of the earliest adaptations of an ancestral dry silk to aquatic habitats might have been a rogue kinase indiscriminately phosphorylating silk serines [4]. The $(pSX)_n$ domains we now observe in the caddisworm silks are sophisticated sequences adapted to complex $Ca^{2+}$ ions and thereby spontaneously fold into stable β-domains. This level of primary sequence sophistication was likely not essential for the early caddisworms to benefit from indiscriminately phosphorylated

serines. A caddisworm silk inspired hydrogel was created using a synthetic phosphate-graft-methacrylate prepolymer as a "simple H-fibroin analogue" which was then copolymerized with a covalent elastic network of polyacrylamide [5]. The synthetic phosphate-graft-methacrylate prepolymer (H-fibroin analogue) is not sophisticated when compared to the caddisworm $(pSX)_n$ domains. Regardless, the disorganized polyphosphates in hydrogel formed complexes with multivalent metal ions like $Ca^{2+}$, displayed considerable load cycle hysteresis, and nearly complete recovery within 90 min when cycled to 50% elongation. These are all attributes of the caddisworm silk mechanics [6].

Abundant hydrophilic charged residues is another generic feature of all known caddisworm silks (20-35 mol%); their accumulation was probably an adaptation to the larvae's aquatic habitats; charged hydrophilic residues are sparse in terrestrial silks [3]. Caddisworm silk is more water than anything else; a preliminary experiment showed that the caddisworm silk is ~66 weight% water (unpublished). In contrast, water plasticizes the hydrogen-bonded yield domains of submerged terrestrial spider silks, leading to the loss of yield point and a considerable reduction in work of fracture [7,8]. Caddisworms evolved an analogous toughening mechanism, except the energy-dissipating $Ca^{2+}$-$(pSX)_n$ β-domains are water-stable and rely on water-resistant interactions to maintain their integrity: hydrophobic associations off the aliphatic X residues, and bridging of the pS residues through $Ca^{2+}$ coordination complexes. There is a growing number of characterized energy-dissipating self-recovering systems of both synthetic and natural origin, including natural materials like the caddisworm silk and the distal mussel byssal threads [9] and synthetic multi-network hydrogels like the caddis silk-inspired gel [5,10–12]. The types of

interactions that give rise to the pseudo-yield point in these self-recovering viscoelastic systems are varied but all of these systems are hydrated. An abundance of water is likely an indispensable mechanical component of the self-recovering caddisworm silk fibers even if it is only there to plasticize peptide domains.

## 7.2 Future Work

### 7.2.1 Mechanochemical Characterization of Silks from All Suborders

The caddisfly suborders branched early in their evolutionary history. The different uses of silks across the three suborders suggest there may be significant variations in their molecular structure and mechanical properties. The sequences of H-fibroin, the major silk structural protein, differ significantly between suborders. For example, a repetitive phosphorylated molecular sequence that toughens Integripalpia silk is less precise in Annulipalpia silk and Spicipalpia H-fibroin contains ~7 mol% histidine not found in the other suborders [13]. The independent adaptation of the silks means that progress in understanding the mechanochemistry of silks in one caddisfly suborder does not necessarily translate to the silks in the other orders.

The mechanochemical characterization of case-making caddisworm silk, presented in this dissertation, serves as a blueprint for studying the silk of representative species in the other two suborders. The studies presented herein relied heavily on correlating the results from two experimental techniques: mechanical testing of single silk fibers and FTIR analysis of the silk phosphoserine vibrational modes. Silk phosphates have strong transition dipole moments, the selection criteria for IR-spectroscopy. Moreover, the vibrational modes are sensitive to the formation of metal-ion complexes and protonation. These two

techniques are relatively inexpensive, require minimal sample preparation, and are quick. They would be ideal for a broad mechanochemical survey of caddisworm silks across the three suborders.

### 7.2.2 A Technique to Forcibly Silk Caddisworms

Methods to forcibly silk caddisworms need to be developed. Methods to forcibly silk spiders and silkworms already exist and are extensively used by experimental researchers [14,15]. Forcibly silking a spider is relatively simple; once the spider is anesthetized, silk fibers can be manually drawn with a pair of fine forceps. The fiber is then attached to a rotating spool with variable speed control. The silkworm, like the caddisworm, has a silk press. The silk press is controlled by four muscles that connect the silk press to the exoskeleton of the head [16]. In the relaxed state, the silk press is closed. When the muscles are contracted, the press opens and fibers can be drawn from the gland [16]. By modulating the contractile strength of the silk press muscles, the larva has control of the silk fiber tension during spinning [16]. In the commercial silkworm, a hormone is released upon the onset of cocoon spinning, the larvae loses voluntary control of the press muscles which permanently contract, and the press is maintained open. Researchers can then forcibly draw fibers from the worm. The caddisworms never loose voluntary control of their press muscles. When anesthetized, the press remains closed and the muscles are relaxed. One approach might be to identify a drug that induces involuntary muscle contractions in insects and apply it to the caddisworms.

The development of such a technique would benefit caddisworm research in numerous ways. First, in mechanical tests, there is a high degree of variation between fibers from the

same caddisworm. Fiber-fiber variation is even greater when comparing fibers from different larvae. Some of this variation comes from intrinsic properties within each fiber, likely because of variable spinning speed. Some of the observed differences might be from changing cross-sectional profiles that lead to inaccurate cross-sectional area estimates which are used to convert force to engineering stress. Only 3 mm of silk fiber are mounted to the micromaterials test system in a single test. A continuous uniform filament of 10 cm would be more than enough silk for a typical mechanics study. A representative silk fiber snippet cold be characterized in cross-section and used for all subsequent force-stress conversions. This would increase the accuracy of the caddisworm silk stress-strain profiles. Currently cross-sectional areas are optically measured across the wide diameter of the paired-fiber filament of 10 randomly selected fibers. The area is estimated by assuming two cylindrical subfibers. The standard deviation across the 10 fibers is typically 10% of the total fiber diameter. Cross-sections of fibers presented in this dissertation also show that the cylindrical subfiber assumption is only accurate for some of the fibers.

Currently, the silk adhesion force is uncharacterized. If the caddisworm could be forcibly silked, samples could easily be prepared by pressing nascent silk fibers onto a uniform substrate like a clean glass slide. With minor modifications to the micromaterials test system (see Chapter 3), the adhesion force could then be characterized by attaching the silk fiber end to one lead of the materials tester and the properly oriented substrate to the other lead.

Preparing oriented silk fibers for X-ray diffraction experiments with the *Hesperophylax sp.* case silk is very labor intensive. A single sample requires many manually-oriented fibers suspended across a ~3 mm gap. In unpublished studies, 20 aligned fibers were

insufficient to get a good signal. So far the most successful X-ray diffraction experiments on caddisworm silk were published in 1971 for the case of *Olinga feredayi* [17]. This species of caddisworm has the unique habit of making a case of pure silk with radially oriented fibers. To obtain many oriented fibers, the case only need to be sliced open and unfolded. If caddisworms could be forcibly silked, it would make sample preparations for X-ray diffraction experiments relatively simple. FTIR analysis of ion exchanged silk fibers showed that the frequency of the symmetric stretching mode ($\nu_{s2}$) was dependent on the ionic radius of the exchanged multivalent metal ion and not on the relative strength of the complex (Chapter 5) [18]. This implies the various metal ions sterically interact with the pSs of the $(pSX)_n$ domains. If multivalent metal ions stabilize intersheet stacking of the β-domains, X-ray diffraction might be useful to monitor changes in intersheet spacing corresponding to changes in ionic radius of the complexed multivalent metal ion.

Finally, The results presented in Chapter 6 suggest that silk fibers emerge from the gland in an uncomplexed state; environmental $Ca^{2+}$ then diffuse into the fibers from the stream water. The silk fibers of larvae, forcibly silked directly into air, could be used to confirm this conclusion. The air spun silk fibers would then be analyzed by elemental analysis and ATR-FTIR for the hallmarks of the $Ca^{2+}$ ion using the techniques outlined in Chapter 6. More broadly, silk from forcibly silked larvae could be used to study the process of silk fiber setting. From SEMs of the inside of larval cases, it is obvious that the silk fibers are spun in a liquid state [2,4]. The fluid silk fibers inevitably set over some undefined period of time. The setting process is likely driven by the binding of $Ca^{2+}$ to the silk pSs. Silk fibers from forcibly silked caddisworms could be useful in determining the amount of time the nascent silk fiber remains fluid.

## 7.3 A Source of Design Principles

The long-term goal of these studies was to discover design principles to guide the future development of materials intended for use in aqueous environments. The development of tough synthetic caddisworm silk-inspired hydrogels is partial fulfillment of this goal and also validates our current understanding of the $Ca^{2+}$-dependent toughening mechanism of the case-making caddisworm silk [5]. The silk-inspired hydrogels qualitatively replicated the self-recovering mechanical properties of the natural silk, but the initial modulus of the natural silk fibers is nearly 10-fold greater and the work of extension is double that of the silk-inspired hydrogels. The study authors observed that "it was possible to replicate the mechanical properties by copying only relatively simple and synthetically accessible structural features of the natural fiber [5]." The self-recovering mechanical properties of caddisworm silk are only one of the remarkable attributes worthy of replication. The caddisworm silk proteins should also be viewed as sophisticated precursors stored in the gland as a concentrated fluid. The H-fibroins have primary sequence similarities with liquid-phase separating intrinsically disordered proteins. Similarities include blocks of oppositely charged residues throughout the protein [19]. The liquid precursors are deployed during the spinning process becoming tough insoluble fibers; this is all done underwater at ambient temperatures and biologically benign conditions. Understanding this mechanism in detail might help in the design of materials like underwater surface coatings or paints, and injectable embolics that set by complexing with the low ~2-3 mM $Ca^{2+}$ in blood. Binding of $Ca^{2+}$ by the $(pSX)_n$ domains is currently thought to be the predominant driver of silk solidification during spinning. The $(pSX)_n$ domains remarkably have a dichotomous role to both mechanically toughen the silk fibers and insolubilize the nascent filament

during silk spinning.

## 7.4 References


[1] T. Malm, K.A. Johanson, N. Wahlberg, The evolutionary history of Trichoptera (Insecta): A case of successful adaptation to life in freshwater, Syst. Entomol. 38 (2013) 459–473.

[2] R.J. Stewart, C.S. Wang, Adaptation of caddisfly larval silks to aquatic habitats by phosphorylation of H-fibroin serines, Biomacromolecules 11 (2010) 969–974.

[3] F. Lucas, J.T.B. Shaw, S.G. Smith, Comparative studies of fibroins: I. The amino acid composition of various fibroins and its significance in relation to their crystal structure and taxonomy, J. Mol. Biol. 52 (1960) 339–349.

[4] N.N. Ashton, D.S. Taggart, R.J. Stewart, Silk tape nanostructure and silk gland anatomy of Trichoptera, Biopolymers 97 (2012) 432–445.

[5] D.D. Lane, S. Kaur, G.M. Weerasakare, R.J. Stewart, Toughened hydrogels inspired by aquatic caddisworm silk, Soft Matter 11 (2015) 6981-6990.

[6] N.N. Ashton, R.J. Stewart, Self-recovering caddisfly silk: energy dissipating, $Ca^{2+}$-dependent, double dynamic network fibers, Soft Matter. 11 (2015) 1667–1676.

[7] M. Elices, G.R. Plaza, J. Pérez-Rigueiro, G. V Guinea, The hidden link between supercontraction and mechanical behavior of spider silks., J. Mech. Behav. Biomed. Mater. 4 (2011) 658–669.

[8] N. Du, Z. Yang, X.Y. Liu, Y. Li, H.Y. Xu, Structural origin of the strain-hardening of spider silk, Adv. Funct. Mater. 21 (2011) 772–778.

[9] E. Vaccaro, J.H. Waite, Yield and post-yield behavior of mussel byssal thread: a self-healing biomolecular material, Biomacromolecules 2 (2001) 906–911.

[10] M.A. Haque, T. Kurokawa, G. Kamita, J.P. Gong, Lamellar bilayers as reversible sacrificial bonds to toughen hydrogel: hysteresis, self-recovery, fatigue resistance, and crack blunting, Macromolecules 44 (2011) 8916–8924.

[11] K.J. Henderson, T.C. Zhou, K.J. Otim, K.R. Shull, Ionically cross-linked triblock copolymer hydrogels with high strength, macromolecules. 43 (2010) 6193–6201.

[12] J.-Y. Sun, X. Zhao, W.R.K. Illeperuma, O. Chaudhuri, K.H. Oh, D.J. Mooney, J.J. Vlassak, Z. Suo, Highly stretchable and tough hydrogels., Nature. 489 (2012) 133–136.

[13] N. Yonemura, K. Mita, T. Tamura, F. Sehnal, Conservation of silk genes in

Trichoptera and Lepidoptera., J. Mol. Evol. 68 (2009) 641–653.

[14] M.M.R. Khan, H. Morikawa, Y. Gotoh, M. Miura, Z. Ming, Y. Sato, M. Iwasa, Structural characteristics and properties of *Bombyx mori* silk fiber obtained by different artificial forcibly silking speeds, Int. J. Biol. Macromol. 42 (2008) 264–270.

[15] R.W. Work, P.D. Emerson, An apparatus and technique for the forcible silking of spiders, J. Arachnol. 10 (1982) 1–10.

[16] J.P. Glasgow, Internal Anatomy of Caddis (*Hydropsyche colonica*), Q. J. Microsc. Sci. 79 (1936) 151–179.

[17] K. Rudall, W. Kenchington, Arthropod silks: the problem of fibrous proteins in animal tissues, Annu. Rev. Entomol. 16 (1971) 73–96.

[18] N.N. Ashton, H. Pan, R.J. Stewart, R.J. Stewart, Connecting caddisworm silk structure and mechanical properties : combined infrared spectroscopy and mechanical analysis, Open Biol. 14 (2016) 3668-3681.

[19] V.N. Uversky, Protein intrinsic disorder-based liquid–liquid phase transitions in biological systems: complex coacervates and membrane-less organelles, Adv. Colloid Interface Sci. (2016).